# Magnetic Fields and Accretion Processes in Young Stars:

## A case study of the classical T Tauri star DK Tau

Marie Nelissen

A thesis submitted to the University of Dublin

for the degree of Philosophiæ Doctor in Astrophysics

School of Physics, Trinity College Dublin, The University of Dublin
Astronomy & Astrophysics, Cosmic Physics, Dublin Institute for Advanced Studies

September 2023

Trinity College Dublin
Coláiste na Tríonóide, Baile Átha Cliath
The University of Dublin

DIAS
Institiúid Ard-Léinn | Dublin Institute for
Bhaile Átha Cliath | Advanced Studies

# Declaration

I declare that this thesis has not been submitted as an exercise for a degree at this or any other university and it is entirely my own work.

I agree to deposit this thesis in the University's open access institutional repository or allow the Library to do so on my behalf, subject to Irish Copyright Legislation and Trinity College Library conditions of use and acknowledgement.

I consent to the examiner retaining a copy of the thesis beyond the examining period, should they so wish (EU GDPR May 2018).

Name: Marie Nelissen

Signature: _____     Date: _____

# Abstract

Low-mass young stars that are a few million years old and called classical T Tauri stars (cTTs) experience magnetospheric accretion. They are surrounded by a circumstellar disk (which consists of an inner and outer disk) and accrete matter from it thanks to their magnetic fields. When the matter falls onto the star, it produces an accretion shock, which generates veiling in the stellar spectra. The shock also causes an accretion spot on the stellar surface. Misalignments between the stellar rotation axis and the outer disk axis are not predicted by standard theories of stellar formation, yet have been observed in several cTTs. This thesis studies one cTTs in particular, DK Tau, which is suspected of being among them. Additionally, it is an excellent subject to investigate the interaction between stellar magnetic fields and material accreting from the circumstellar disk, since it displays clear signatures of accretion. Focusing on a single object allows one to uncover the physics that governs its behavior, and the values derived from its analysis are important to constrain the models of star formation.

One goal of this thesis is to study DK Tau's average line-of-sight magnetic field in both photospheric absorption lines and accretion-powered emission lines. The second is to examine inconsistencies regarding the inclination of its rotation axis. The third aim is to investigate the accretion, particularly the mass accretion rate, using two different methods for comparison purposes. The last objective is to carry out a preliminary study of its large-scale magnetic field configuration.

For these purposes, archival data from the CFHT/ESPaDOnS and TBL/NARVAL spectropolarimeters were used. The observations probe two distinct epochs (i.e. 2010 and 2012), allowing one to study the evolution of DK Tau over time. Each dataset spans a few stellar rotation cycles and covers the optical range. First, stellar parameters were determined. Next, the veiling was measured across the spectra and its effects were removed. Then, least-squares deconvolution profiles of the photospheric absorption lines were obtained, before determining the average line-of-sight magnetic field from them. In addition, accretion-powered emission lines were investigated as tracers of the magnetic fields present in the accretion shocks. Next, the accretion luminosity was derived from multiple accretion-powered emission lines. This was done in order to calculate the mass accretion rate. This value was then compared to the one calculated from the fitting of accretion shock models onto the values of veiling. Finally, Zeeman-Doppler Imaging was applied to the photospheric absorption lines, in order to derive a first estimate of the photospheric brightness distribution and magnetic field configuration.

It was found that peak values of the veiling (defined as the ratio between the

accretion shock and photospheric fluxes) range from 0.2 to 1.8, with a steeper trend across the wavelength range for higher peak values. DK Tau shows a magnetic obliquity of $\sim 20°$. Based on the Heɪ line, in 2010, the average line-of-sight magnetic field reaches up to 1.77 kG. In 2012, it reaches up to 1.99 kG. The stellar rotation axis is inclined by 58° (+18)(-11), which is significantly different from the outer disk axis inclination of 21° given in the literature. Regarding the mass accretion rate, when using the accretion-powered emission lines, its values range from $\log(\dot{M}_{acc}[M_{\odot}\,yr^{-1}])$ = -8.20 to $\log(\dot{M}_{acc}[M_{\odot}\,yr^{-1}])$ = -7.40. This agrees with the values found in the literature, as well as the values calculated using the accretion shock models and the veiling. Moreover, a power-law correlation between the values of the accretion luminosity and the optical veiling is identified.

In conclusion, DK Tau's outer disk axis is likely misaligned compared to its rotation axis. In addition, both procedures of determining the mass accretion rate provide similar results. Furthermore, the correlation between the accretion luminosity and the veiling provides a helpful method of confirming accretion luminosity values by measuring the veiling at a single wavelength in the optical.

# Publications

- *Misalignment of the outer disk of DK Tau and a first look at its magnetic field using spectropolarimetry*
  **Nelissen, M.**; McGinnis, P.; Folsom, C. P.; Ray, T.; Vidotto, A. A.; Alecian, E.; Bouvier, J.; Morin, J.; Donati, J. -F.; Devaraj, R. (2023), Astronomy & Astrophysics, 670, A165.
  https://doi.org/10.1051/0004-6361/202245194

- *Correlation between the optical veiling and accretion properties: A case study of the classical T Tauri star DK Tau*
  **Nelissen, M.**; Natta, A.; McGinnis, P.; Pittman, C.; Delvaux, C.; Ray, T. (2023), Astronomy & Astrophysics, 677, A64.
  https://doi.org/10.1051/0004-6361/202347231

# Glossary

| Symbols | |
|---|---|
| $a$ | slope of a function |
| $A$ | perceived area of the accretion spot |
| $A_{\text{tot}}$ | true area of the accretion spot |
| $\alpha$ | angle between the visible stellar disk center and the accretion spot |
| $\alpha_{\ell,m}$ | radial component of the poloidal fraction of the magnetic field |
| $b$ | vertical intercept of a function |
| $B$ | magnetic field |
| $\langle B \rangle$ | mean magnetic field |
| $B_{\text{eq}}$ | magnetic field at the equator |
| $B_{\theta}$ | meridional magnetic field |
| $B_{\text{los}}$ | average line-of-sight magnetic field |
| $B_{\text{max}}$ | maximal magnetic field |
| $B_r$ | radial magnetic field |
| $B_{\varphi}$ | azimuthal magnetic field |
| $\beta$ | magnetic obliquity |
| $\beta_{\ell,m}$ | tangential component of the poloidal fraction of the magnetic field |
| $c$ | speed of light in vacuum |
| $\gamma_{\ell,m}$ | toroidal fraction of the magnetic field |
| $\bar{d}$ | equivalent line depth |
| $D$ | distance |
| $e$ | charge of the electron |
| $\text{EW}_{\text{line}}$ | veiling-corrected equivalent width |
| $\text{EW}_{\text{veiled}}$ | veiled equivalent width |
| $f$ | filling factor |
| $F$ | flux |
| $F_{\text{cont}}$ | continuum flux |
| $F_{\text{line}}$ | line flux |
| $\mathscr{F}$ | energy flux of the accretion column |
| $\log g$ | logarithmic surface gravity |
| $\bar{g}$ | equivalent Landé factor |
| $g_{\text{eff}}$ | effective Landé factor |
| $G$ | gravitational constant |
| $H$ | ratio between the extreme values of $B_{\text{los}}$ |
| $\theta$ | angle between the magnetic field and the line-of-sight |
| $i$ | inclination of the stellar rotation axis with respect to the line-of-sight |
| $I$ | amplitude of Stokes I |
| $I_c$ | level of the continuum in Stokes I |
| $I_L$ | perceived luminous intensity of the accretion spot |
| $I_{L,\text{tot}}$ | true luminous intensity of the accretion spot |
| $I_{\circlearrowright}$ | right circular polarization |
| $I_{\circlearrowleft}$ | left circular polarization |
| $J$ | total angular momentum |

| Symbols | |
|---|---|
| k | spectral order |
| $\kappa$ | absorption coefficient |
| $\ell$ | degree of the spherical harmonics |
| $L$ | geometrical depth |
| $L_\star$ | stellar luminosity |
| $L_\odot$ | solar luminosity |
| $L_{\mathrm{acc}}$ | accretion luminosity |
| $L_{\mathrm{line}}$ | line luminosity |
| $\lambda$ | wavelength |
| $\overline{\lambda}$ | equivalent wavelength |
| $\lambda_0$ | wavelength of the line center without a magnetic field |
| $\Delta\lambda_B$ | Zeeman broadening |
| $m$ | order of the spherical harmonics |
| $m_s$ | sonic Mach number |
| $m_e$ | mass of the electron |
| $M$ | line mask |
| $M_\star$ | stellar mass |
| $M_\odot$ | solar mass |
| $\dot{M}_{\mathrm{acc}}$ | mass accretion rate |
| $M_J$ | angular momentum projected onto a specific axis |
| $P$ | rotation period |
| $r$ | distance to the stellar surface |
| $r_{\mathrm{trunc}}$ | truncation radius |
| $r_{\mathrm{co\text{-}rot}}$ | co-rotation radius |
| $R$ | veiling |
| $R_\star$ | stellar radius |
| $R_\odot$ | solar radius |
| $R_{\mathrm{in}}$ | inner radius of the circumstellar disk |
| $\rho$ | density |
| $\sigma_{\mathrm{SB}}$ | Stefan-Boltzmann constant |
| $\sigma$ | standard deviation |
| $T_{\mathrm{eff}}$ | effective temperature |
| $\tau$ | optical depth |
| $v$ | radial velocity |
| $v_s$ | free-fall velocity |
| $v_{\mathrm{mac}}$ | macroturbulence velocity |
| $v_{\mathrm{mic}}$ | microturbulence velocity |
| $v \sin i$ | line-of-sight-projected equatorial rotational velocity |
| $V$ | amplitude of Stokes $V$ |
| $\varphi$ | rotation phase |
| $\Phi$ | latitude |
| $\chi^2$ | chi-squared distribution |
| $Y$ | observed spectrum |
| $Z$ | LSD profile |

| Acronyms | |
|---|---|
| APERO | A PipelinE to Reduce Observations |
| CADC | Canadian Astronomy Data Centre |
| CCD | charge-coupled device |
| CFHT | Canada-France-Hawaii Telescope |
| cTTs | classical T Tauri star |
| ESPaDOnS | Echelle SpectroPolarimetric Device for the Observation of Stars |
| ESpRIT | Echelle Spectra Reduction: an Interactive Tool |
| FWHM | full width at half maximum |
| IR | infrared |
| IRT | infrared triplet |
| LP | Large Programme |
| LSD | Least-Squares Deconvolution |
| MaPP | Magnetic Protostars and Planets |
| nIR | near-infrared |
| PDM | phase dispersion minimization |
| PMS | pre-main sequence star |
| HR | Hertzsprung-Russell |
| SED | spectral energy distributions |
| SLS | SPIRou Legacy Survey |
| S/N | signal to noise ratio |
| SPICE | Consolidating & Enhancing the SPIRou Legacy Survey |
| SPIP | SPectropolarimètre Infrarouge Pyrénéen |
| SPIRou | SPectropolarimètre InfraRouge |
| TBL | Télescope Bernard Lyot |
| TTs | T Tauri star |
| UV | ultraviolet |
| VALD | Vienna Atomic Line Database |
| wTTs | weak-lined T Tauri star |
| YSO | young stellar object |
| ZDI | Zeeman-Doppler Imaging |

# Contents

# List of figures

# List of tables

# Introduction 1

$\mathcal{I}$n this introductory chapter, the various concepts relevant to the study of magnetic fields and accretion processes in low-mass young stars (i.e. with $M_\star \leqslant 2\,M_\odot$) will be presented. To this end, the different stages of low-mass star formation will first be described in Sect. 1.1. Next, Sect. 1.2 will focus on the magnetic field aspect of young stars. The various techniques used in this work to study the stellar magnetic activity will be explained. Sect. 1.3 will then focus on the accretion processes, starting with a description of the current magnetospheric accretion paradigm. This will highlight the interaction between the stellar magnetic field and the accretion mechanism. This will be followed by a presentation of different accretion signatures. In Sect. 1.4, the spotlight will shift from the stars to their circumstellar disks. Finally, Sect. 1.5 will describe the characteristics of a particular young star, DK Tau, which is the focal point of this work.

## 1.1 Low-mass star formation

### 1.1.1 General picture of low-mass star formation

The formation of low-mass stars begins with cold, dark and gaseous molecular clouds in the interstellar medium (see panel a in Fig. 1.1). Their temperatures usually range from 10 to 20 K. In the Milky Way, molecular clouds vary largely in size and mass, ranging from about 100 pc and $10^6\,M_\odot$, to less than 10 pc and $10^3\,M_\odot$ (see e.g. Bergin and Tafalla 2007; Heyer and Dame 2015). The clouds are in an unstable equilibrium due to their high mass and subsequent significant self-gravity. Some forces work to maintain this equilibrium: centrifugal effects due to rotation, internal pressure gradients (due to turbulence and thermal processes) and forces due to the cloud's magnetic field; while events like a supernova explosion, or transit through a high-density zone can destabilize the clouds (see e.g. Feigelson and Montmerle 1999; Schulz 2005; Hartmann 2009).

When a part (of a few solar masses) of one of these clouds gravitationally collapses (see panel b in Fig. 1.1), it does so typically by a factor of a million in linear dimensions, and probably from the inside-out (see e.g. Shu 1977; Hartmann 2009). It then forms protostars surrounded by disks and dusty envelopes (see panel c in
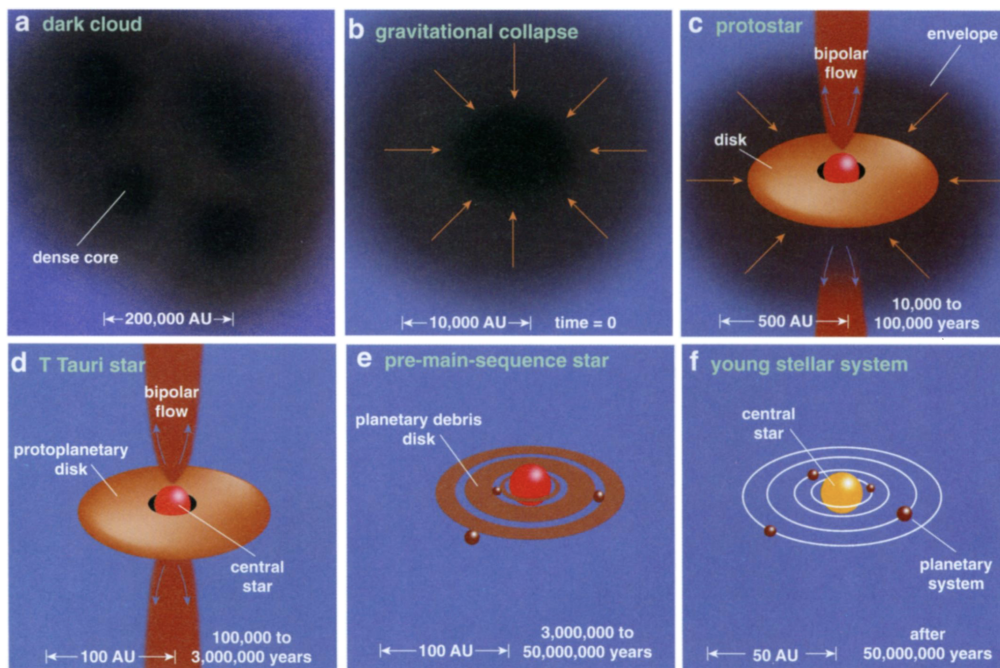
Figure 1.1 – Illustration of the stages of low-mass star formation (Greene 2001).

Fig. 1.1). Most low-mass stars form in binary or multiple star systems (see e.g. Hartmann 2009). For multiple systems, there can either be a disk around each protostar, a disk around the star system, or both. Because matter flows from the disk onto the forming star, it is called an accretion (or circumstellar, or protoplanetary) disk. The disk is originally gas-rich, with the dust accounting for about 1% of its mass.

As hydrostatic equilibrium is established in the protostar's core and the circumstellar envelope disperses, it transitions into a pre-main sequence star (PMS - see panel d and e in Fig. 1.1). At this stage, the forming star is producing radiation solely due to its gravitational contraction. Meanwhile, the circumstellar disk is losing matter through accretion onto the central star (mostly), outflows and evaporation of gas by high-energy stellar photons (see e.g. Feigelson and Montmerle 1999; Schulz 2005; Hartmann 2009).

Finally, when hydrogen fusion begins in the central object's core, it reaches the main-sequence (see panel f in Fig. 1.1). At this point, the circumstellar disk has disappeared. Some of its dust has agglomerated in the forming exoplanets and smaller bodies. Most of its gas has been accreted by the star, has agglomerated in exoplanets, and has photoevaporated (see e.g. Feigelson and Montmerle 1999; Schulz 2005; Hartmann 2009).

It can be noted that the discovery of gaps and rings in circumstellar disks around young stars (for instance around HL Tau) may indicate that planet formation has already begun in less than a million years (see e.g. ALMA Partnership et al. 2015; Bae et al. 2022). In other words, many millions of years before a star joins the main-sequence. Figure 1.2 is an interferometric image of HL Tau and its circumstellar disk,

showing multiple gaps and rings (see ALMA Partnership et al. 2015).
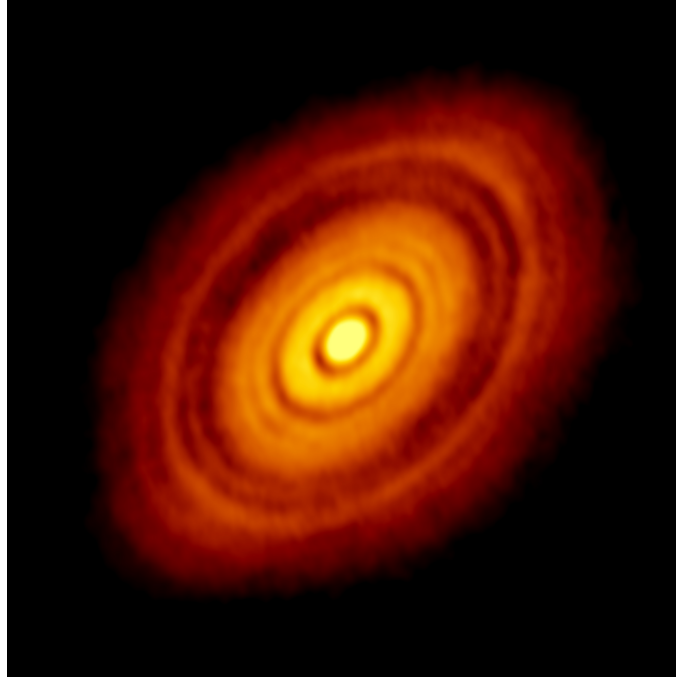


Figure 1.2 – 1.3 mm ALMA continuum image of HL Tau and its circumstellar disk (ALMA Partnership et al. 2015).

## 1.1.2 Stages of low-mass star formation

Protostars and PMS can be observationally classified into several categories, depending on their evolutionary stage. Historically (see e.g. Lada and Wilking 1984; Lada 1987; Andre et al. 1993), these classifications were morphological, depending on the shape of the spectral energy distributions (SEDs) of the young stellar objects (YSOs - i.e. the young stars and the surrounding material). More specifically, classes were defined in terms of $a$, the slope of the SED in the infrared (IR) between approximately 1 $\mu$m and 100 $\mu$m:

$$a = \frac{d\log(\lambda F_\lambda)}{d\log(\lambda)} \tag{1.1.1}$$

where $\lambda$ refers to the wavelength and $F$ to the flux (see Lada 1987). Figure 1.3 illustrates the morphological differences between the different categories (see Persson 2014).

The evolutionary stages are defined based on the IR excess of the object and the presence of strong emission lines, such as H$\alpha$. The IR excess corresponds to the level of IR emission produced by the YSO, compared to the emission of its stellar photosphere. This excess stems from thermal emission from the dust present in circumstellar envelopes and disks. The strong emission lines are due to accretion onto the central young star, as well as outflows (see e.g. Feigelson and Montmerle 1999; Schulz 2005; Hartmann 2009; Hartmann et al. 2016). In addition, different
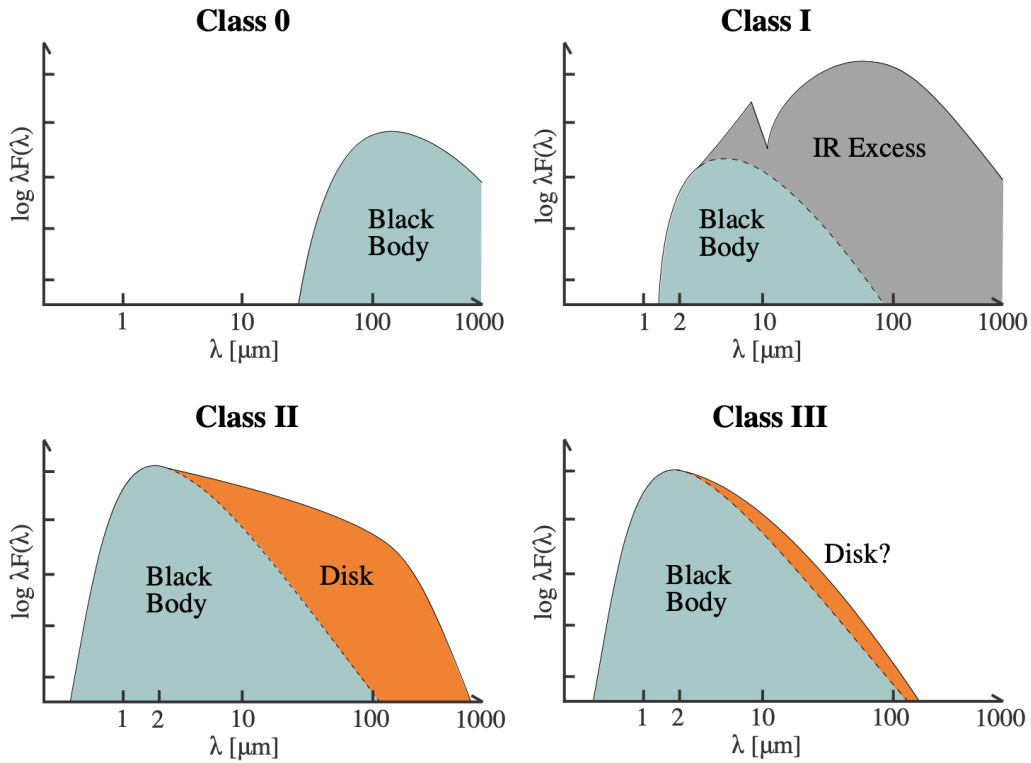
Figure 1.3 – Theoretical SEDs of YSOs of different classes (Persson 2014).

stages are characterized by different optical depths for the surrounding material. The optical depth ($\tau$) refers to the measurement of transparency of a medium as radiation passes through it. At the wavelength $\lambda$, it is defined as

$$\tau_\lambda \equiv \int \kappa_\lambda \, \rho \, dL \qquad (1.1.2)$$

with $\kappa$ the absorption coefficient at that $\lambda$, $\rho$ the density of the medium and $L$ its geometrical depth. The absorption coefficient contains contribution from the absorption and scattering of photons. In the optically thin regime, the intensity of the observed spectrum is directly proportional to the number of atoms along the line-of-sight that are absorbing the light at the wavelength of observation. While in the optically thick regime, not all the atoms are necessary to absorb all of the light at that wavelength. Consequently, the absorption observed is not directly proportional to the number of absorbing atoms. The transition between the optically thick and optically thin regimes corresponds to $\tau_\lambda = 1$ (see e.g. Tennyson 2005).

Figure 1.4 shows the various evolutionary stages (see Feigelson and Montmerle 1999). In particular, it provides the name of the category, displays a sketch of the situation, gives the age of the young star, provides the alternative name of the category and gives the status of the circumstellar disk.

Protostars with infalling envelopes (see the second column in Fig. 1.4), also called class 0 sources (see the top left panel in Fig. 1.3), correspond to young protostars deeply embedded in their parent molecular cloud. They are between $10^4$ and $10^5$
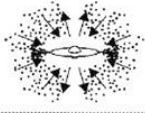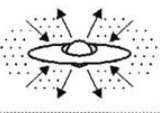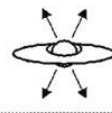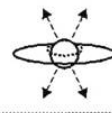
| PROPERTIES | Infalling Protostar | Evolved Protostar | Classical T Tauri Star | Weak-lined T Tauri Star | Main Sequence Star |
|---|---|---|---|---|---|
| SKETCH | | | | | |
| AGE (YEARS) | $10^4$ | $10^5$ | $10^6$ - $10^7$ | $10^6$ - $10^7$ | $> 10^7$ |
| mm/INFRARED CLASS | Class 0 | Class I | Class II | Class III | (Class III) |
| DISK | Yes | Thick | Thick | Thin or Non-existent | Planetary System |
| X-RAY | ? | Yes | Strong | Strong | Weak |
| THERMAL RADIO | Yes | Yes | Yes | No | No |
| NON-THERMAL RADIO | No | Yes | Yes | Yes | Yes |

Figure 1.4 – Types and properties of YSOs (adapted from Feigelson and Montmerle 1999).

years old. The protostars are invisible at optical wavelengths, but usually detected in the far-IR or millimeter bands, because the surrounding envelope of dust absorbs the stellar radiation and re-emits it at longer wavelengths. Most of the mass resides in the envelope. Their SED corresponds to a cold blackbody (see e.g. Andre et al. 1993; Feigelson and Montmerle 1999; Schulz 2005).

Evolved protostars (see the third column in Fig. 1.4), also called class I sources (see the top right panel in Fig. 1.3), are protostars surrounded by an optically thick disk and envelope, which is dissipating. They are about $10^5$ years old. They display strong IR excess. The mass of the protostar now dominates compared to the envelope. Their SED is broader than a blackbody distribution and rising after 2 microns (see e.g. Lada 1987; Feigelson and Montmerle 1999; Schulz 2005).

Classical T Tauri stars (cTTs - see the fourth column in Fig. 1.4), also called class II sources (see the bottom left panel in Fig. 1.3), are PMS. They are accreting from their optically thick circumstellar disk, which is slowly dissipating. They are between $10^6$ and $10^7$ years old. They present IR excess, are visible in the optical domain and are strong H$\alpha$ emitters. Their SED is again broader than a blackbody distribution, but this time decreasing after 2 microns. T Tauri stars (TTs) are named after the prototype T Tauri (see Joy 1945). They have spectral types ranging from M to F, which correspond to effective temperatures ranging from 3 000 to 7 000 K (see e.g. Lada 1987; Feigelson and Montmerle 1999; Schulz 2005).

Weak-lined T Tauri stars (wTTs - see the fifth column in Fig. 1.4), also called class III sources (see the bottom right panel in Fig. 1.3), are surrounded by a very optically thin disk or have exhausted it entirely. They are between $10^6$ and $10^7$ years old. They display weak (or non-existent) IR excess, are visible in the optical range and present weak H$\alpha$ emission. Their SED is similar to those of cool stars of similar spectral type (except in the UV), with little or no excess emission (see e.g. Lada 1987; Feigelson and Montmerle 1999; Schulz 2005).

The timescales for these different types of YSOs are theoretical. For protostars, as the dusty material falling inward is not supported against the gravitational collapse due to low-densities, the characteristic timescale corresponds to the free-fall time. In contrast, TTs are in hydrostatic equilibrium. As they have not yet started nuclear fusion, they are gravitationally contracting. Their timescale corresponds to the Kelvin-Helmholtz thermal time, i.e. the ratio between the stellar gravitational energy and luminosity (see e.g. Schulz 2005; Hartmann 2009; Krumholz 2015).

Observations have been used to infer large-scale magnetic fields for a multitude of TTs (see e.g. Donati et al. 2011, 2019, 2020a). In particular, many of them have complex field topologies, i.e. with considerable octupolar components and not only strong dipolar components like the Sun. It should however be noted that the strength of the higher order multipoles decreases quickly with an increased distance to the stellar surface. A dipolar component decreases with $r^{-3}$, whereas an octupolar component decreases with $r^{-5}$, with $r$ denoting the distance to the stellar surface. This means that on the stellar surface the octupolar component can dominate, while at a few stellar radii the dipolar component generally dominates (see e.g. Hartmann 2009; Johnstone et al. 2014). It should also be mentioned that the magnetic fields of TTs evolve with time (see e.g. Donati et al. 2008; Donati and Landstreet 2009; Donati et al. 2011, 2012, 2013, and Chap. 3) The importance of magnetic fields in star formation will be discussed in the following section.

## 1.2 Stellar magnetic fields

### 1.2.1 Roles of magnetic fields in star formation

Magnetic fields play several important roles in star formation. For instance, during the collapse of the parent cloud, most of its matter is deposited onto the outer part of the circumstellar disk, rather than onto the forming star. Despite this, the star will ultimately possess the majority of the mass of the system, in comparison to any exoplanets. This means that most of the material from the circumstellar disk must travel inward through the disk and be transferred to the forming star through accretion. Since it is believed that the stellar magnetic field is responsible for the existence of

accretion columns (see Sect. 1.3.1), it therefore plays a role in transferring mass from the innermost disk to the star (see e.g. Bouvier et al. 2007; Hartmann et al. 2016).

The magnetic fields of the star and circumstellar disk are also thought to play a role in stellar angular momentum evolution. Indeed, since molecular clouds experience a dramatic and rapid reduction in size, any initial rotation should be vastly amplified by the conservation of angular momentum during their contraction. However, observations show that TTs rotate much slower than what would be expected if all the angular momentum from the cloud were transferred to them (see e.g. Lynden-Bell and Pringle 1974). This indicates the existence of a mechanism transferring the angular momentum outward (see e.g. Bouvier et al. 2007; Hartmann et al. 2016). In addition, TTs are still contracting, and assuming angular momentum conservation, this would increase their spin. Accreting stars also experience additional spin-up effects due to accretion. Yet PMS display lower spins than what is predicted by these considerations. Consequently, these spin-up effects need to be counteracted by stellar angular momentum loss (see e.g. Rebull et al. 2004; Bouvier et al. 2014; Hartmann et al. 2016). Scenarios for the removal of stellar angular momentum are complex and depend on several processes (see e.g. Zanni and Ferreira 2013; Bouvier et al. 2014). These include angular momentum transport through the circumstellar disk, stellar and disk winds (see the next paragraph), magneto-rotational instability (linked to magnetic field lines threading the circumstellar disk - see Balbus and Hawley 1991), and magnetic influences. Through magnetic coupling, the star and the inner edge of the circumstellar disk (outside of the co-rotation radius, where the the disk rotates slower than the star - see Sect. 1.4.1) are synchronized to the same angular momentum, which helps spin-down the star (see e.g. Koenigl 1991; Hartmann et al. 2016). The disk subsequently carries the required amount of angular momentum outward.

The magnetic field is also believed to play a role in the launching of outflows (jets, stellar and disk winds - see e.g. Frank et al. 2014; Hartmann et al. 2016), although the different types of existing outflows and their exact production mechanisms are not yet well understood. Jets are composed of highly collimated gas travelling at velocities ranging from 100 to $1\,000\,\mathrm{km\,s^{-1}}$, while winds are slower and less collimated. As an example, regarding the origin of a type of wind called magnetospheric ejections, differential rotation between the star and its circumstellar disk cause differential rotation throughout the accretion columns. This leads to distortion of the magnetic field lines and consequently to disconnections and reconnections in order to recover the initial configuration. When this occurs, material can be ejected from the star-disk system. These outflows therefore remove angular momentum from the system (instead of transferring it back to the disk as in the previous scenario), also assisting in the regulation of the stellar spin (see e.g. Zanni and Ferreira 2013).

## 1.2.2 Zeeman effect

The Zeeman effect (see Zeeman 1896) can be used to observationally obtain information regarding the stellar magnetic field. This effect describes the impact of a magnetic field on a spectrum: its atomic (and molecular) lines are broadened or split (depending on the strength of the field and the sensitivity of the line in question). An atom has several quantum numbers, including the total angular momentum number $J$ and the azimuthal numbers $M_J$. $M_J$ is the angular momentum projected onto a specific axis, with $M_J = -J, -J + 1, \ldots, J - 1, J$. In the absence of a magnetic field, the quantum energy levels with set quantum numbers (including $J$), but different $M_J$, are identical. This means that there are $2J + 1$ degenerate sub-levels. However, in the presence of an external magnetic field, the degeneracy is removed. Consequently, spectral lines that were previously blended will broaden or split (see e.g. Tennyson 2005; Donati and Landstreet 2009; Oswalt and Bond 2013; Hussain and Alecian 2014). Figure 1.5 illustrates the Zeeman effect for J = 2 and J = 3. The left side shows the degenerate sub-levels in the absence of a magnetic field. The right side presents the $2J + 1$ sub-levels that have split in the presence of an external magnetic field.
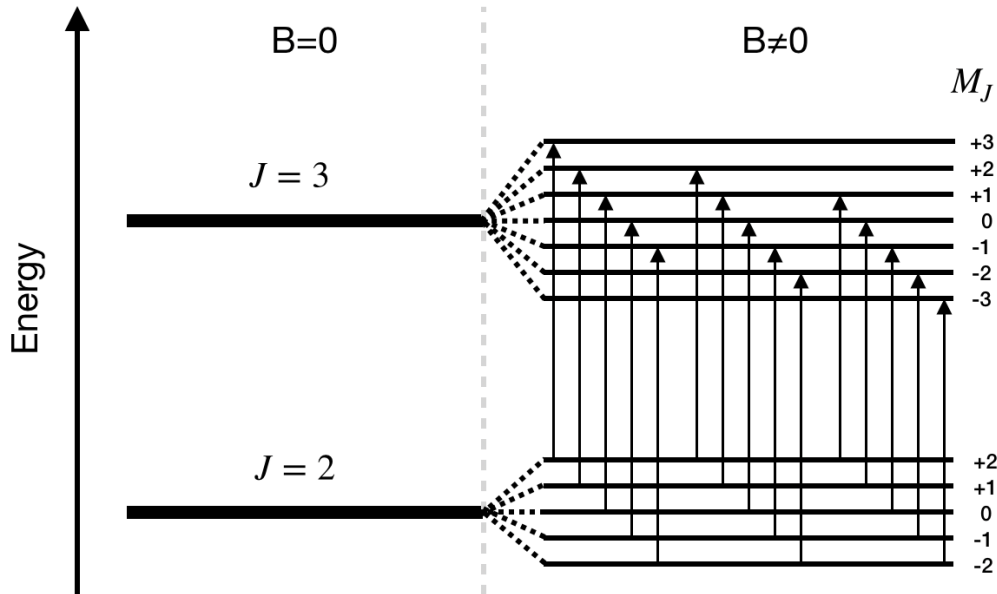


Figure 1.5 – Schematic view of the Zeeman effect. On the left side, without an external magnetic field, the quantum energy levels are degenerate. On the right side, with a magnetic field, the energy levels split into $2J + 1$ sub-levels.

Working in the CGS unit system, the Zeeman effect is characterized by

$$\Delta \lambda_B = \frac{\lambda_0^2 \, e \, g_{eff} \, B}{4\pi \, m_e \, c^2} = 4.67 \times 10^{-12} \, \lambda_0^2 \, g_{eff} \, B, \qquad (1.2.1)$$

where $\Delta \lambda_B$ refers to the wavelength broadening, $\lambda_0$ is the central wavelength of the

line without a magnetic field (in nm), $e$ refers to the charge of the electron, $B$ is the modulus of the stellar magnetic field (in G), $m_e$ is the mass of the electron and $c$ is the speed of light in vacuum. Finally, $g_{eff}$ is the dimensionless effective Landé factor of the line. It quantifies the sensitivity of the line to the Zeeman effect, with magnetically sensitive lines usually having Landé factors of 1 or higher. Because the wavelength broadening scales with the square of the central wavelength of the line, the Zeeman effect is more pronounced at longer wavelengths for a given magnetic field strength (see e.g. Donati and Landstreet 2009; Schulz 2005; Morin 2012; Hussain and Alecian 2014).

The study of the Zeeman broadening/splitting of lines originating in the stellar atmosphere gives information on the intensity of the stellar magnetic field, and even on its topology. These studies rely on spectropolarimetric observations (see the next section).

## 1.2.3 Spectropolarimetry & Stokes parameters

As stated in the previous section, magnetic fields can be examined using spectropolarimetric data. Spectropolarimetry consists in measuring the polarization of light, as well as its intensity as a function of wavelength. Stokes (1852) showed that the polarization properties of light can be described using four parameters, known as I, Q, U and V. Stokes I (see the first row of Fig. 1.6) corresponds to unpolarized light. It may be recovered by adding the right and left circular polarization for example. Stokes Q and U (see the second row of Fig. 1.6) are measures of linear polarization. Stokes V (see the last row of Fig. 1.6) quantifies net circular polarization. It is recovered by subtracting the right and left circular polarization (see e.g. Kochukhov et al. 2011; Morin 2012). In this work, unpolarized light will be referred to as Stokes I, and circularly polarized light as Stokes V.

Depending on the orientation of the stellar magnetic field compared to the line-of-sight of the observer, the observed polarization will differ. In particular, Stokes V is only sensitive to $B_{los}$ (see Sect. 1.2.5), the field along the line-of-sight integrated over the visible stellar hemisphere (since the star is not resolved). This integration potentially produces a cancellation effect (e.g. if the hemisphere harbors two spots of opposite polarities, their signature will have opposite signs and the magnetic field modulus might tend toward zero). This means that, in practice, Stokes V is only sensitive to the (strength and geometry of the) large-scale magnetic field. Stokes I, on the other hand, does not provide information on the vectorial properties of the magnetic field (and therefore its geometry). However, it is not undergoing any cancellation effect, meaning that it will provide a correct estimate of the average magnetic field value at the surface of the star. The information provided by Stokes I and Stokes V can be
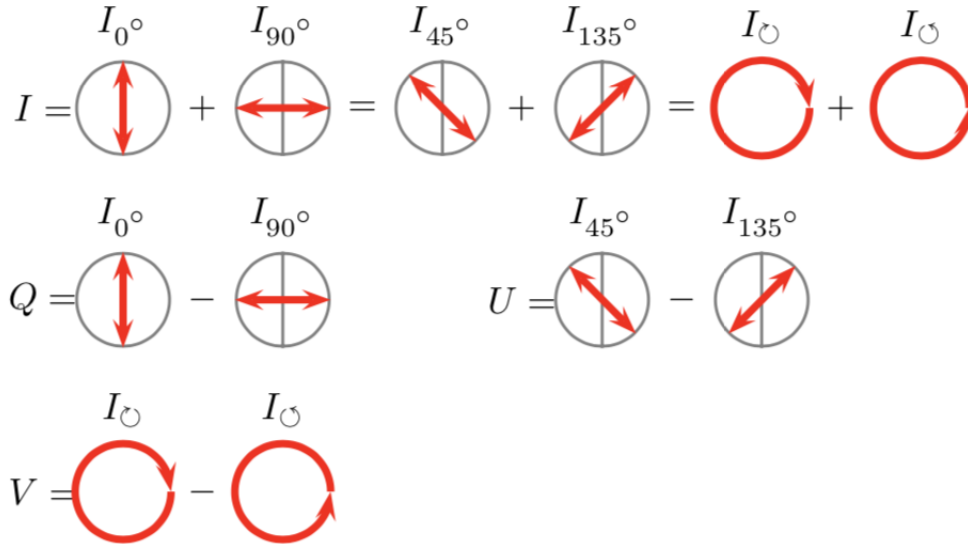
Figure 1.6 – Definition of the Stokes parameters (Morin 2012). The red arrow represents the polarization, with a straight arrow symbolizing linear polarization and a round arrow symbolizing circular polarization. The vertical gray line represents the direction of reference for the measurements of linear polarization. The angle mentioned above it refers to the angle between the direction of polarization and the direction of reference.

used simultaneously to reconstruct the true strength and geometry of the magnetic field (see e.g. Morin 2012; Tessore et al. 2017).

In the weak-field approximation, i.e. when the magnetic field is less than a few kG, it can be shown that

$$V = -g_{eff}\,\Delta\lambda_B\,\cos\,\theta\,\frac{dI_0}{d\lambda} \tag{1.2.2}$$

where $V$ refers to the amplitude of Stokes V, $g_{eff}$ is the effective Landé factor of the line, $\Delta\lambda_B$ is the value of the Zeeman splitting, $\theta$ is the angle between the line-of-sight and the magnetic field (with $V$ being maximal when $\theta = 0$), and $dI_0/d\lambda$ is the derivative of the intensity (i.e. of Stokes I, in the absence of a magnetic field) with respect to the wavelength. This equation shows that the amplitude of Stokes V is a function of the strength of the magnetic field, through the Zeeman effect (see Donati et al. 1997).

Unfortunately, at the scale of individual spectral lines, the Zeeman effect is often quite weak. This is where the technique described in the next section is particularly useful.

## 1.2.4   Least-Squares Deconvolution

Least-Squares Deconvolution (LSD) is a technique used to obtain the mean line profile of a stellar spectrum (see Donati et al. 1997). The stellar magnetic field signature often cannot be detected for a single line, as it is weak. This stems from the fact that

the Zeeman effect is not resolved, it is smaller than the intrinsic width of the lines. To get around this problem, LSD, a cross-correlation technique, can be used to add the signatures from hundreds of photospheric absorption lines in order to obtain an LSD profile, which can be seen as a summary of the chosen lines. This leads to a better signal to noise ratio. It is possible under the hypothesis of self-similarity of the selected lines. In the weak-line regime, it is assumed that the lines have essentially the same shape, only at a different wavelength and rescaled as a function of depth in the case of Stokes I, and as a function of depth and Landé factor in the case of Stokes V. In addition, LSD works in the weak-field regime (see e.g. Donati et al. 1997; Kochukhov et al. 2010).

The self-similarity hypothesis implies that the observed spectrum ($Y$) can be viewed as the convolution between a line pattern function ($M$) and the mean line profile ($Z$):

$$Y = M * Z \tag{1.2.3}$$

where $Z$ is also called the LSD profile and $M$ the line mask. The latter is a weighted Dirac comb, containing the information on the position and depth of the chosen lines. It is paramerized by the Landé factor $\overline{g}$, the depth $\overline{d}$ and the central wavelength $\overline{\lambda}$ of the lines (see e.g. Kochukhov et al. 2010; Tessore et al. 2017). Figure 1.7 illustrates the operating principle of LSD, with the bottom panel depicting the observed spectrum (in black) as the convolution of the LSD profile (in red) with the line mask (in blue).
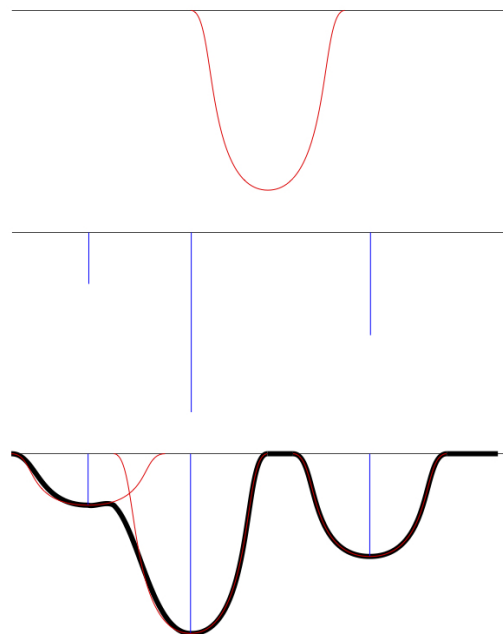


Figure 1.7 – Schematic view of the operating principle of LSD. The top panel symbolizes the mean line profile, $Z$. The middle panel symbolizes the line pattern function, $M$. The bottom panel symbolizes the observed spectrum, $Y$. The x-axis represents the wavelengths and the y-axis the intensity of the spectrum (by C. Delvaux).

In summary, the essence of LSD is to solve an inverse problem corresponding

to Eq. 1.2.3, i.e. to estimate the mean line profile for a given observed spectrum and an assumed line pattern function. In other words, to deconvolve. Iteratively, LSD searches for the mean line profile that, once convolved with the line pattern function, gives a spectrum which is the closest to the observed spectrum in the least square sense (i.e. by $\chi^2$ minimization - see e.g. Kochukhov et al. 2010).

Figure 1.8 shows an example of an LSD profile. The Stokes I profile (i.e. the unpolarized spectrum) normalized to the continuum ($I_c$) is on the bottom panel and the Stokes V profile (i.e. the circularly polarized spectrum) normalized to $I_c$ and scaled by a hundred is on the top panel. As Stokes V corresponds to the subtraction of the left and right circular polarization (with each one undergoing a wavelength shift due to the Zeeman effect), this explains the shape of the profile: the signature has a peak and a trough. Because the amplitude of Stokes V is a function of the magnetic field strength, the greater the signature, the greater the magnetic field. It should however be noted that the shape of the Stokes V profile differs depending on how the magnetic field is distributed on the surface of the star. It does not necessarily have this simple shape, but can be more complex (see e.g. the Stokes V profiles in Fig. 1.9).
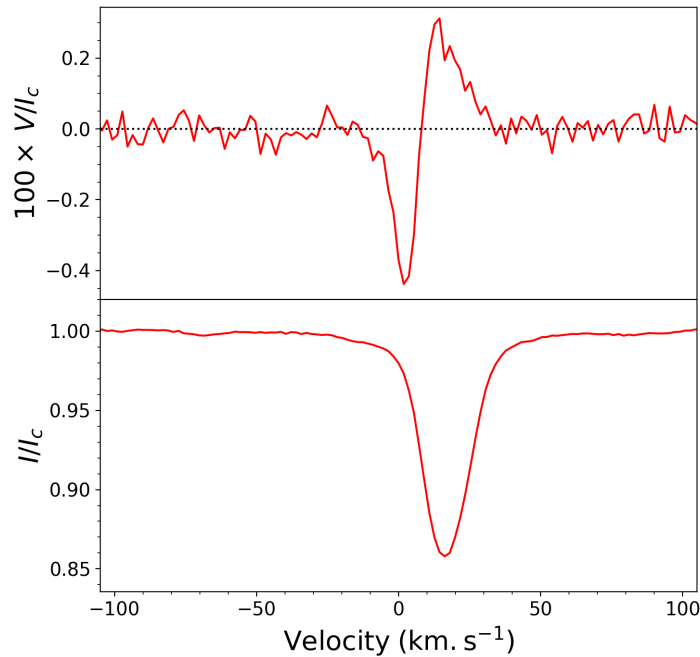


Figure 1.8 – Example of an LSD profile for DK Tau (see Sect. 3.2.5). The top panel shows the Stokes V profile (scaled by a hundred), while the bottom panel shows the Stokes I profile. Both are normalized to the continuum ($I_c$) and shown as a function of the velocity.

## 1.2.5  Average line-of-sight magnetic field

$B_{\mathrm{los}}$[1], the magnetic field along the line-of-sight and integrated over the visible stellar hemisphere, can be derived from the Stokes parameters. This is done by using the following equation on the LSD profiles for each night (see e.g. Rees and Semel 1979; Donati et al. 1997; Wade et al. 2000; Morin 2012):

$$B_{\mathrm{los}} = -2.14 \times 10^{11} \frac{\int v\, V(v)\, \mathrm{d}v}{\lambda_0\, g_{\mathrm{eff}}\, c\, \int [I_c - I(v)]\, \mathrm{d}v} \tag{1.2.4}$$

where $B_{\mathrm{los}}$ is expressed in G, $v$ refers to the radial velocity in the rest frame of the star, $V$ refers to Stokes V, $\lambda_0$ is the wavelength of the line center in nm, $g_{\mathrm{eff}}$ is the effective Landé factor of the line, $c$ is the speed of light in vacuum and is expressed in the same units as $v$, $I$ refers to Stokes I and $I_c$ to the level of the continuum in Stokes I. This yields a value of $B_{\mathrm{los}}$ for each LSD profile. In other words, for each observation.

It should be noted that, since $B_{\mathrm{los}}$ represents a signed average over the visible stellar hemisphere, regions of opposite polarities partly cancel out. Consequently, a magnetic field with significant magnitude but a complex geometry might correspond to an average line-of-sight magnetic field that is too weak to be detected.

## 1.2.6  Magnetic obliquity

$B_{\mathrm{los}}$ can be used to calculate the magnetic obliquity ($\beta$). This is defined as the angle between the stellar rotation axis and the magnetic field axis. Assuming a pure dipole, Preston (1967) gives an estimate of $\beta$ via the following equation:

$$i = \arctan\left[\left(\frac{1-H}{1+H}\right)\cot\beta\right] \tag{1.2.5}$$

where $i$ is the angle between the rotation axis of the star and the line-of-sight (and is determined observationally) and where

$$H = \frac{B_{\mathrm{los}}(\max)}{B_{\mathrm{los}}(\min)} \tag{1.2.6}$$

with $B_{\mathrm{los}}(\max)$ and $B_{\mathrm{los}}(\min)$ the extreme values for the average line-of-sight magnetic field (out of the various values for the different nights).

For TTs, obliquities ranging from 5° to 60° have been measured (see e.g. Johnstone et al. 2014; Alencar et al. 2018; McGinnis et al. 2020; Pouilly et al. 2020; Donati et al. 2020a; Finociety et al. 2023).

---

[1]$B_{\mathrm{los}}$ is also referred to as the longitudinal field, with the symbol $B_\ell$. This term was not used in this work in order to avoid confusion with its homonym $B_\varphi$, the field along the east-west direction, also called the azimuthal or longitudinal field (see e.g. Vidotto 2016).

## 1.2.7 Zeeman-Doppler Imaging

In addition to $B_{los}$ derivation, spectropolarimetric data can also be used to obtain magnetic field maps with Zeeman-Doppler Imaging (ZDI). ZDI is a tomographic technique used to determine the large-scale magnetic field configuration of a star and its photospheric brightness distribution. The ZDI code was originally developed by Semel (1989). It was subsequently updated by Donati and Brown (1997). Further implementations of the code were produced, for instance by Donati et al. (2006b) and Folsom et al. (2018).

ZDI uses Stokes I LSD profiles to model the brightness map of the studied star by fitting them with a synthetic photospheric line based on a Voigt profile (i.e. the convolution between a Gaussian and a Lorentzian profile). In addition, as stated in Sect. 1.2.3, Stokes I allows one to recover the total magnetic flux (through the Zeeman effect) without being sensitive to the geometry of the magnetic field. ZDI also uses Stokes V LSD profiles, which are mainly sensitive to $B_{los}$, but are subject to the cancellation effect of opposite polarities. In cases where the evolution of the magnetic field with time is longer than the stellar rotation period, it is possible to map the entirety of the visible large-scale field (i.e. excluding the parts of the field that are constantly hidden by the star from the line-of-sight). This is done by obtaining high-resolution spectra covering the full rotation period of the source. Indeed, they capture the modulation of $B_{los}$ due to the rotation only (and not intrinsic variations, as $B_{los}$ is expected in this case not to vary during the timescale of a stellar rotation period), because magnetic regions cross the projected image of the stellar disk (see e.g Semel 1989; Brown et al. 1991; Donati and Brown 1997; Donati et al. 2006b; Folsom et al. 2018).

This projected image is divided into strips of apparent equal line-of-sight radial velocity. This corresponds roughly to the longitude on the stellar surface. The light originating from a particular area carries a certain Doppler shift (i.e. a receding lane will be redshifted, while a lane that is coming toward the observer will be blueshifted). This means that the polarized signature of a potential magnetic spot (also called cold or dark spot, as they appear dark since they are cooler than the surrounding photosphere) will occur at a specific wavelength position ruled by its Doppler shift. This will provide the longitude of the spot. In addition, by using a time series of spectra sampling the entire stellar rotation, it is possible to determine the latitude of the spot. Indeed, as the equator rotates faster than the poles, it will impact the evolution of the Doppler shift with time: near the pole, the Doppler shift will only distort the center of the LSD profile; at the equator the distortion will reach the wings. Ultimately, ZDI allows the localization of the magnetic spots in latitude, longitude and relatively to each other, but also the determination of the orientation of the magnetic field vector because of its impact on Stokes V (see e.g Semel 1989; Hussain et al. 2002; Clarke

2010; Morin 2012).

Figure 1.9 illustrates the operating principle of ZDI (see Morin 2012). A simulated star (and its respective spectrum) are shown at two different epochs. Three magnetic spots on the surface of the star (in blue, green and red) produce a signal (which is integrated over the visible hemisphere and projected onto the line-of-sight) simultaneously in the Stokes I (bottom part of the plots) and Stokes V (top part of the plots) measurements. The symbol $\varphi$ denotes the rotation phase. As the star rotates, the positions of the spots (compared to the line-of-sight of the observer) shift and with it the orientation of the stellar magnetic field. Because the observed polarization is sensitive to the orientation of the magnetic field, the Stokes V signatures (which quantify the circular polarization) will also vary with the stellar rotation. In contrast, there is no impact on the unpolarized spectrum (Stokes I - see e.g Semel 1989; Morin 2012).
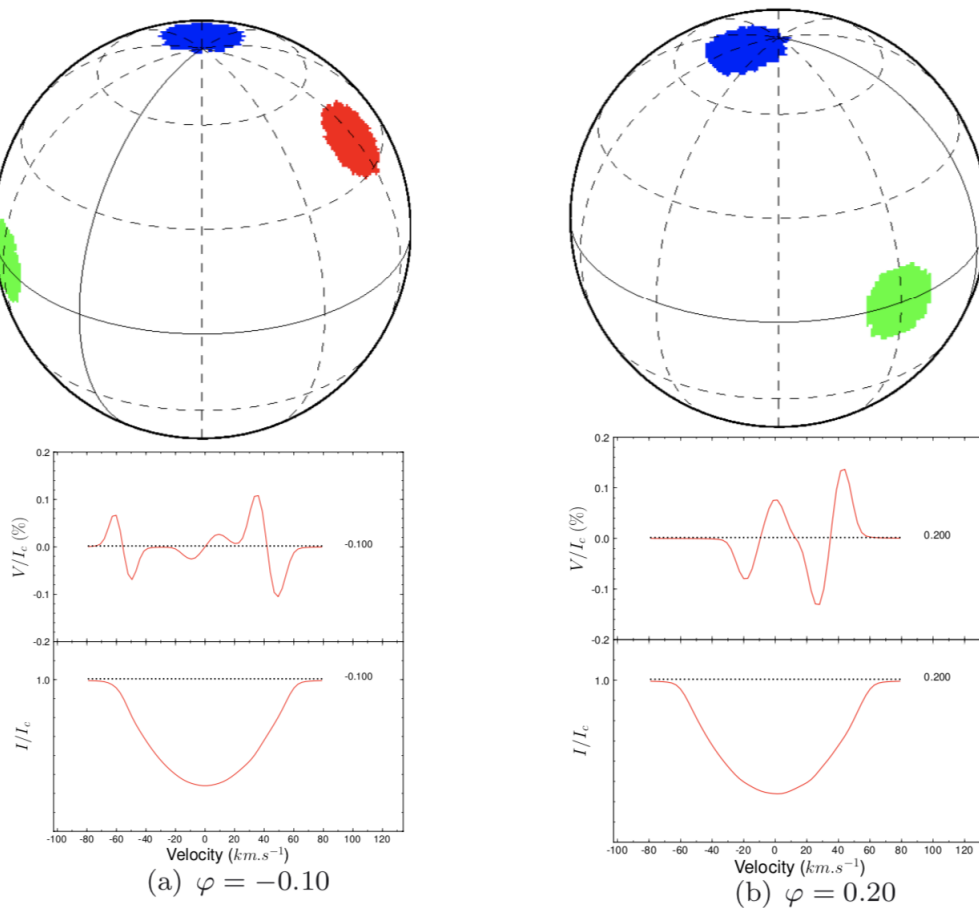


Figure 1.9 – Schematic view of the operating principle of ZDI (Morin 2012). The top panels show two representations of the surface of a star at different rotation phases, with three magnetic spots (in blue, green and red). The bottom panels show the corresponding LSD profiles, with Stokes V and Stokes I normalized to the continuum ($I_c$) and shown as a function of the velocity. $\varphi$ denotes the rotation phase.

Starting from a basic model (a homogeneous photosphere in the case of Stokes I and a zero-field map in the case of Stokes V), the ZDI code iteratively increases the information on the model. It checks at each step if the polarized spectrum computed

from the model fits the observed data (i.e. the LSD profiles). It stops when the fit reaches a given reduced $\chi^2$ (provided by the user). This yields a brightness map and a magnetic map (see e.g Morin 2012; Folsom et al. 2018; Donati et al. 2020a).

## 1.2.8 Magnetic field description

ZDI maps (see Sect. 5.2.1) usually display the different vector components of the stellar magnetic field (see e.g. Vidotto 2016):

- The radial field ($B_r$) which is the field radially away from the center of the star.

- The azimuthal or longitudinal field ($B_\varphi$) which is the field along the east-west direction.

- The meridional or latitudinal field ($B_\theta$) which is the field along the north-south direction.

These components can be related to the decomposition of the magnetic field into poloidal and toroidal components. The latter are expressed in terms of spherical harmonics, following Donati et al. (2006b):

- The poloidal component corresponds to field lines that connect the poles (composed of radial, azimuthal and meridional components).

- The toroidal component corresponds to field lines encircling the stellar rotation axis (composed of azimuthal and meridional components only).

When producing the ZDI magnetic maps, the ZDI code reconstructs spherical harmonic coefficients. This means that the magnetic field reconstruction is saved in a file listing those coefficients. They are the free parameters in the iterative fitting of the Stokes V LSD profiles (see Sect. 1.2.7). They describe the complexity of the magnetic field and are called $\alpha_{\ell,m}$, $\beta_{\ell,m}$ and $\gamma_{\ell,m}$:

- $\alpha_{\ell,m}$ characterizes the radial component of the poloidal fraction of the magnetic field.

- $\beta_{\ell,m}$ characterizes the tangential component of the poloidal fraction of the magnetic field.

- $\gamma_{\ell,m}$ characterizes the toroidal fraction of the magnetic field.

$\ell$ and $m$ are respectively called the degree and the order of the spherical harmonics coefficients, with $\ell \in \mathbb{N}$ and $m \in \{0, \ldots, \ell\}$. $\ell_{\max}$ is fixed by the user in the ZDI code.

Figure 1.10 is a schematic view of a spherical harmonic decomposition. Each rectangle represents a stellar surface. The different colored sections represent opposite field polarities. The illustration depicts $\ell$ ranging from 0 to 3 and $m$ reaching

up to 3. It shows that the higher the degree $\ell$, the more complex the magnetic field is. Though it should be noted that ZDI is only sensitive to the large-scale magnetic field and does not provide information on the magnetic field at the granulation scale, for instance. The $\ell$ = 1 components represent dipole fields (see the left panel in Fig. 1.11), the $\ell$ = 2 components represent quadrupole fields (see the right panel in Fig. 1.11) and the $\ell$ = 3 components represent octupole fields. When $m$ = 0 (see the first columns in Fig. 1.10), the magnetic field is axisymmetric about the rotation axis. As $m$ increases (see the second, third and fourth columns in Fig. 1.10), the number of nodes connecting the poles increases as well.
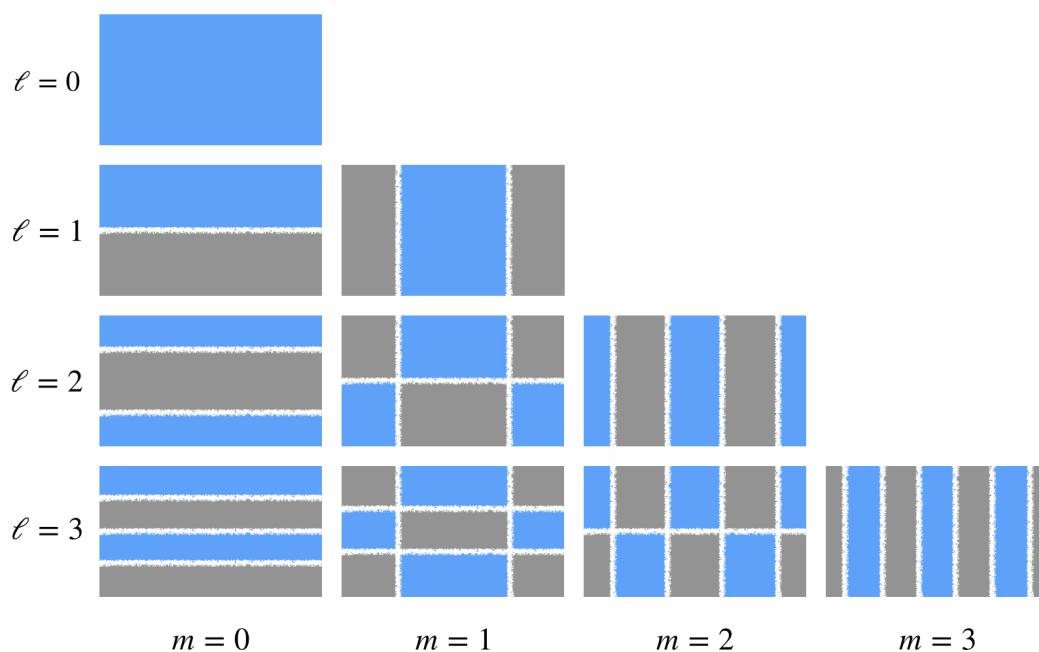


Figure 1.10 – Schematic view of a spherical harmonic decomposition. The stellar spherical surface is shown as a strip of the latitude as a function of longitude. The blue and gray sections represent opposite field polarities.

Describing the magnetic field as a combination of spherical harmonics provides direct access, for instance, to the percentages of poloidal and dipolar magnetic energy and to the level of axisymmetry of the magnetic field. In addition, it allows one to compare with theoretical and numerical studies.

In the following section, accretion processes will be discussed. For this purpose, the current magnetospheric accretion paradigm is first described. The term "magnetosphere" refers to the area surrounding the star dominated by the stellar magnetic field. The paradigm explains the interplay of the stellar magnetic field and accretion mechanism.
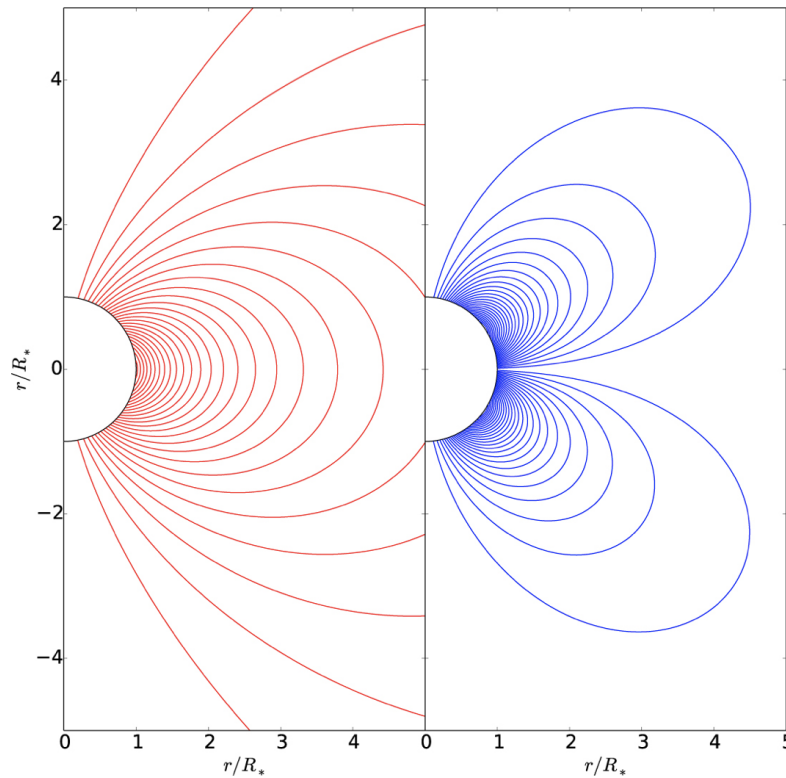
Figure 1.11 – Schematic view of a dipolar (left panel) and quadrupolar field (right panel - adapted from Finley and Matt 2017).

## 1.3 Accretion processes

### 1.3.1 Magnetospheric accretion paradigm

According to the current magnetospheric accretion paradigm (see e.g. Shu et al. 1994; Hartmann et al. 1994; Bessolaz et al. 2008; Kurosawa and Romanova 2013; Hartmann et al. 2016), the magnetic field of cTTs (see the red lines in Fig. 1.12) is thought to be strong enough to interact with the circumstellar disk and produce a magnetospheric gap. This truncation occurs at a distance of a few stellar radii, where the pressure from the matter in the disk is roughly equal to the pressure from the magnetic field. Because of this, the circumstellar matter that was migrating toward the star through the plane of the disk can no longer do so. It is forced to flow in the vertical direction and begins to follow the magnetic field lines into accretion columns (see the yellow lines with black arrows in Fig. 1.12) in order to reach its destination. Inside the accretion columns, the matter is gravitationally accelerated and heated up. When it finally arrives at the stellar photosphere at near free-fall velocities (i.e. on the order of $300\,\text{km}\,\text{s}^{-1}$), it merges with the photosphere (at rest) through a shock, in which kinetic energy is converted into thermal energy. The shocks in turn generate emission lines and an excess continuum (see e.g. Calvet and Gullbring 1998). This excess continuum is superimposed on the photospheric spectrum, inducing veiling

of the photospheric absorption lines (see Sect. 1.3.3).
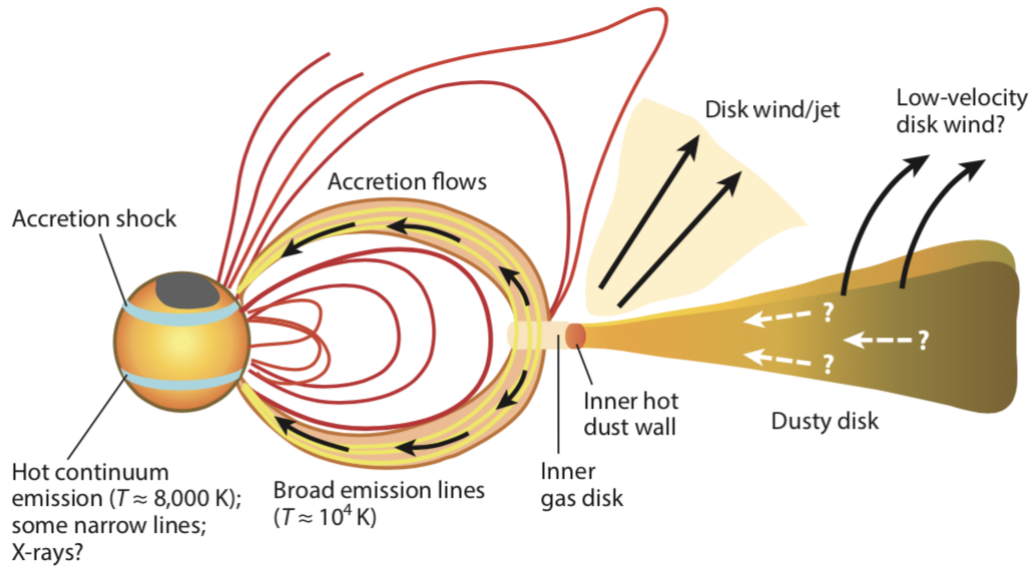


Figure 1.12 – Sketch of the magnetospheric accretion for cTTs (Hartmann et al. 2016). It shows the truncation of the inner circumstellar disk caused by the magnetic field (represented in red), together with the ensuing flow of matter in accretion columns, following the field lines. The matter is accelerated and generates broad emission lines (e.g. H$\alpha$). When it arrives near the stellar surface, it produces accretion shocks, and consequently accretion spots.

The shocks also cause the emergence of localized spots at the chromospheric level (see e.g. Calvet and Gullbring 1998; Hartmann 2009; Hartmann et al. 2016). These are called accretion spots (or hot spots, or bright spots). Espaillat et al. (2021) have found that accretion spots display a radial density gradient: they have a denser core that is surrounded by a lower-density region.

## 1.3.2 Accretion regimes

Magnetohydrodynamics simulations (see e.g. Kulkarni and Romanova 2008, 2009; Kurosawa and Romanova 2013; Romanova et al. 2013) have proposed two accretion regimes for cTTs: stable (see the left panel in Fig. 1.13) or unstable (see the right panel in Fig. 1.13). In the stable regime, the dipolar component of the magnetic field is the dominant component at the inner edge of the circumstellar disk and the dipole axis is misaligned compared to the rotation axis[2]. Consequently, the accreted matter follows the magnetic field lines and falls onto the star via two main accretion columns (that produce two accretion spots), one in each hemisphere, near the magnetic poles. This configuration is stable over several rotation cycles. Observations have shown that most cTTs are in the stable regime (see Gregory et al. 2012; Thanathibodee et al. 2023).

---

[2]The simulations consider that the rotation axis of the star coincides with the inner disk axis.
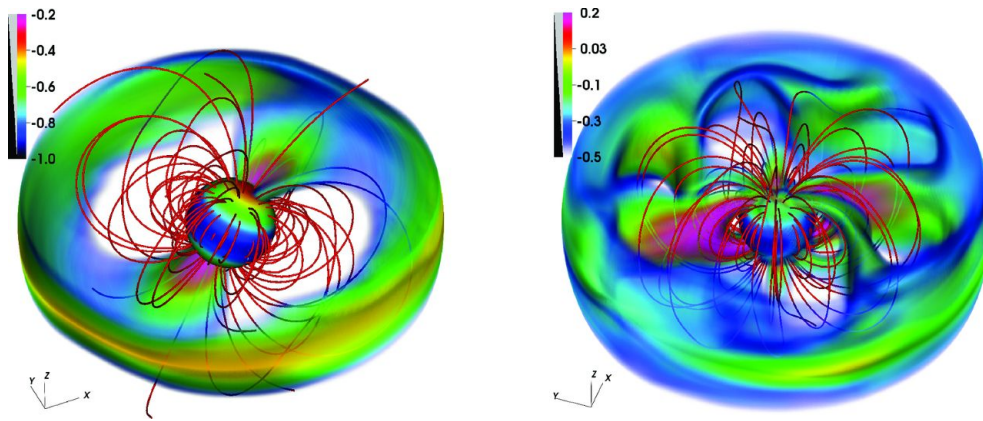
Figure 1.13 – 3D magnetohydrodynamics simulations of the stable (left panel) and unstable (right panel) accretion regimes (Kurosawa and Romanova 2013). The magnetic field lines are shown in red. The colors in the background represent the density.

In the unstable regime (see e.g. Kulkarni and Romanova 2008; Kurosawa and Romanova 2013), either the strength of the magnetic dipolar component at the inner edge of the circumstellar disk is too weak, or the dipole axis is aligned with (or only slightly titled compared to) the rotation axis, or both. This leads to accretion in the equatorial plane through several sporadic accretion tongues (the shape and number of which vary with time - producing multiple randomly distributed accretion spots) that penetrate the magnetosphere. This is due to Rayleigh-Taylor instabilities between the disk and the magnetosphere. Rayleigh-Taylor instabilities (see e.g. Chen 1984) arise when the plasma is not uniform (e.g. presenting with a density gradient or a sharp boundary) and an external non-electromagnetic force is applied to it. In this case, the matter from the disk has a high density and is supported against gravity by the magnetospheric plasma which has a low density. The timescale of the unstable regime is a few times shorter than the stellar rotation period.

In addition to the dipole strength and to the magnetic obliquity, the geometry of the accretion flow is affected by several physical parameters (see e.g. Kulkarni and Romanova 2008; Kurosawa and Romanova 2013; Romanova and Owocki 2015). For instance, higher accretion rates onto the stellar surface are associated with the unstable regime. Another example is the ratio between the truncation radius and the co-rotation radius (which are defined in Sect. 1.4.1), which can be used to estimate the boundary between the stable and unstable accretion regimes. Additional parameters that influence instability include the stellar rotation rate and the viscosity in the disk. If one or a few of these factors change, there can be a transition between the regimes. The mass accretion rate can experience both short term (i.e. days or weeks) and long term changes (i.e. years) of the same intensity (see e.g. Venuti et al. 2014; Costigan et al. 2014). The stellar magnetic field configuration is not expected to vary on timescales of days, but it can change significantly over the years (see e.g. Donati et al. 2011).

### 1.3.3 Veiling

The accretion shocks are at a higher temperature than the stellar photosphere and add an extra continuum to the photospheric continuum of the cTTs. This veils the photospheric lines (such as Liɪ lines) by decreasing their depth (see e.g. Calvet and Gullbring 1998; Hartmann et al. 2016). Indeed, due to the presence of this extra continuum, the continuum of the whole spectrum is shifted to a higher intensity. When the spectrum is then normalized, the intensity is divided by a value that is higher than the stellar continuum. The absorption lines consequently appear shallower (see an example of a veiled and deveiled line in Fig. 1.14).
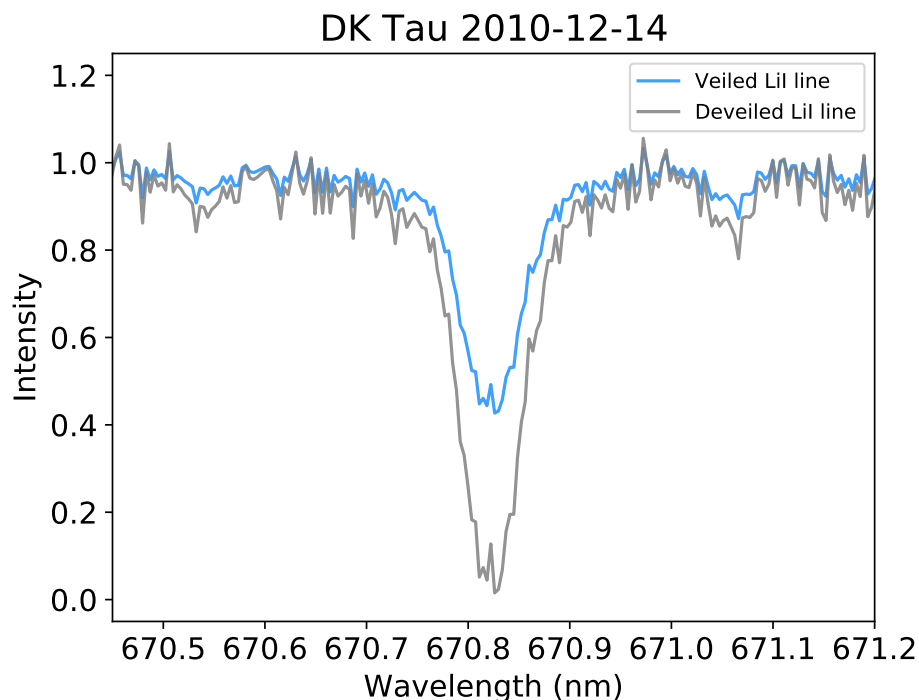


Figure 1.14 – Illustration of veiling of the Liɪ line. The veiled line is represented in blue, the veiling-corrected line is in gray. Both are normalized to the continuum.

The veiling ($R$) is defined as the ratio between the flux coming from the accretion shock and the flux coming from the stellar photosphere at a given wavelength (see e.g. Hartigan et al. 1991; Fischer et al. 2011). In other words, if $R = 1$, the accretion shock and photospheric flux are equal; if $R = 0.2$, the accretion shock flux is five times weaker than the photospheric flux. Because of its nature, the value of the veiling varies with wavelength: the accretion shocks emit most in the ultraviolet (UV) range, then their emission decreases in the visible. Furthermore, as the star rotates, the accretion shocks appear to be migrating with respect to the line-of-sight of the observer, giving a temporal variation to the veiling. In addition, as the accretion rate varies in time, the intensity of the veiling varies as well. The veiling can therefore be used as a tracer of accretion activity and variability. The photospheric absorption lines and their decrease in depth can be resolved using high-resolution spectra (by

comparing with the spectrum of the stellar photosphere), and the amount of veiling can therefore be measured.

Determining the values of the veiling allows one not only to examine accretion processes, but it is also necessary in order to study the stellar magnetic field. Indeed, the decrease of the spectral line depths prevents accurate measurements of the magnetic field. Therefore, the effect of veiling needs first to be removed before starting the magnetic field analysis. Fig. 1.15 illustrates the impact of veiling on Stokes I LSD profiles, with the different nights in gray and their average in red. The bottom left panel shows the veiled LSD profiles, at different depths. The bottom right panel shows the deveiled LSD profiles, at the same depth, which is deeper than for the veiled nights.
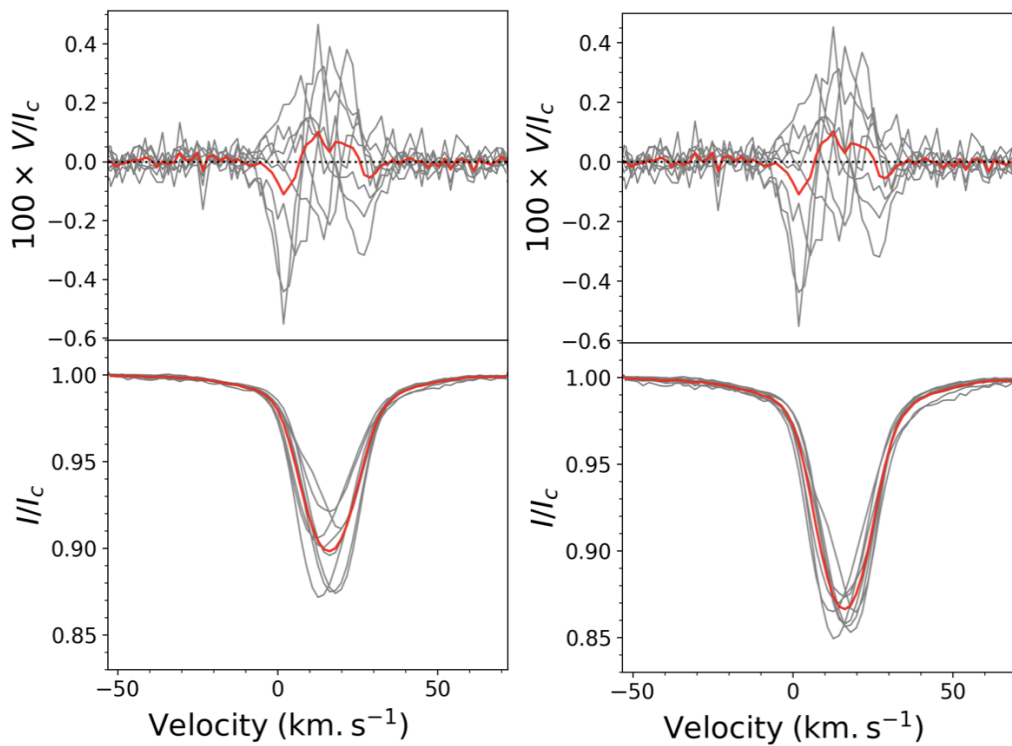


Figure 1.15 – Impact of veiling on Stokes I LSD profiles. Average LSD profiles with veiling (left panel) and without veiling (right panel). The LSD profiles from different nights are represented in gray. The average LSD profiles over the total number of nights are in red.

## 1.3.4   Accretion luminosity

The mass accretion rate onto a star ($\dot{M}_{\mathrm{acc}}$) is an important parameter when studying accretion. For instance, it is a factor in determining the stability of accretion, as instability is associated with higher accretion rates (see e.g. Kulkarni and Romanova 2008). In turn, the study of accretion and its variability from night to night is valuable in investigating disk evolution and stellar formation. $\dot{M}_{\mathrm{acc}}$ can be derived from the

accretion luminosity ($L_{\text{acc}}$) via the following equation from Gullbring et al. (1998):

$$L_{\text{acc}} \simeq \frac{GM_{\star}\dot{M}_{\text{acc}}}{R_{\star}} \left(1 - \frac{R_{\star}}{R_{\text{in}}}\right) \tag{1.3.1}$$

where $G$ is the gravitational constant, $M_{\star}$ denotes the mass of the star, $R_{\star}$ is the stellar radius and $R_{\text{in}}$ is the inner radius of the circumstellar disk and is typically set at the commonly used value for the truncation radius of $5\,R_{\star}$.

The accretion luminosity can be calculated from the luminosity of many different accretion-powered emission lines (see e.g. Natta et al. 2006; Biazzo et al. 2012; Manara et al. 2015). For example, in this work the H$\alpha$, H$\beta$, H$\gamma$, the He I lines at 447.1 nm, 501.6 nm, 587.6 nm, 667.8 nm and 706.5 nm, as well as the Ca II infrared triplet at 849.8 nm, 854.2 nm and 866.2 nm were used. Alcalá et al. (2017) present the following empirical relations between the accretion luminosity and the line luminosity ($L_{\text{line}}$):

$$\log\left(L_{\text{acc}}/L_{\odot}\right) = a \cdot \log\left(L_{\text{line}}/L_{\odot}\right) + b \tag{1.3.2}$$

where $a$ and $b$ are parameters varying with the spectral line in question and $L_{\odot}$ is the solar luminosity. To obtain these relations, they worked with a large sample of cTTs from the Lupus star forming region. They first fitted each spectrum with the sum of a photospheric template and the emission of a slab of hydrogen (to simulate the continuum excess emission due to accretion). They took the luminosity emitted by the slab as the accretion luminosity. Then they plotted the various values of $\log\left(L_{\text{acc}}\right)$ obtained from their sample as a function of $\log\left(L_{\text{line}}\right)$, and fitted a linear relation through the points (see Fig. 1.16 for an example for the H$\alpha$ line). These relations have been found to apply to a large number of star formation regions (see e.g. Natta et al. 2006; Manara et al. 2012, 2016; Alcalá et al. 2021; Gangi et al. 2022).
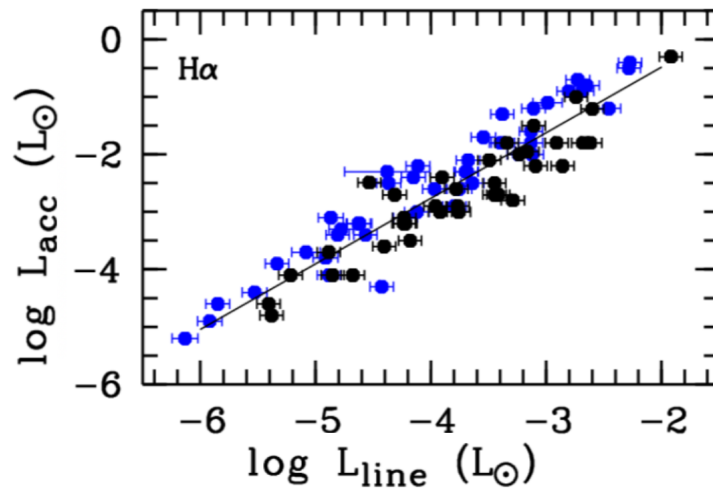


Figure 1.16 – Empirical relation between the accretion luminosity and line luminosity for the H$\alpha$ line (Alcalá et al. 2017).

The line luminosity itself can be derived from line flux ($F_{\text{line}}$) through the following

formula:

$$L_{\text{line}} = 4\pi D^2 F_{\text{line}} \tag{1.3.3}$$

where $D$ denotes the distance to the star. The line flux is based on the deveiled and flux-calibrated (in the case of non-flux-calibrated spectra - see Sect. 2.1) equivalent width (EW) of emission lines. The flux-calibration uses a template of the stellar photospheric continuum:

$$F_{\text{line}} = \text{EW}_{\text{line}} \cdot F_{\text{cont}} \tag{1.3.4}$$

where $\text{EW}_{\text{line}}$ is the veiling-corrected EW of the line and $F_{\text{cont}}$ is the flux of the continuum of the template at the wavelength of the line in question. The EW is deveiled using the following formula:

$$\text{EW}_{\text{line}} = \text{EW}_{\text{veiled}} \cdot (1 + R) \tag{1.3.5}$$

with $\text{EW}_{\text{veiled}}$ denoting the veiled EW and $R$ the veiling.

## 1.3.5 Accretion shock models

A second approach for estimating the mass accretion rate uses accretion shock models. First introduced by Calvet and Gullbring (1998), these models simulate the base of an accretion column at the surface of a star (see also Lamzin 1995, 1998). They are based on a geometry that is one-dimensional and plane-parallel and does not distinguish between a single or a multitude of accretion spots.

The models are defined by the accretion energy flux ($\mathscr{F}$) and filling factor ($f$). $\mathscr{F}$ corresponds to the flux of energy carried by the accretion column into the shock, while $f$ corresponds to the fraction of the stellar surface that is covered by the accretion spots.

The accretion energy flux is defined by Calvet and Gullbring (1998) with the following equation:

$$\mathscr{F} = \frac{1}{2}\rho\, v_s^3 \tag{1.3.6}$$

with $\rho$ denoting the density of the material in the accretion column and $v_s$ the free-fall velocity of that material at the stellar surface. The free-fall velocity depends on the stellar mass and radius via the following equation (see Calvet and Gullbring 1998):

$$v_s = \left|\frac{2GM_\star}{R_\star}\right|^{1/2} \left|1 - \frac{R_\star}{R_{\text{in}}}\right|^{1/2} \tag{1.3.7}$$

where $M_\star$ refers to the stellar mass, $R_\star$ to the stellar radius and $R_{\text{in}}$ is the radius where the magnetosphere truncates the circumstellar disk. It is assumed that $R_{\text{in}} = 5\,R_\star$, as stated in the previous section. It follows from Eq. 1.3.6 that, for a particular

young star, low/high values of $\mathscr{F}$ correspond to low/high densities of the material in the accretion columns.

Each energy flux is scaled by a corresponding filling factor, which represents the fractional surface coverage of the accretion spots. Its value ranges from 0 to 1, the former corresponding to a non-existent spot, the latter to a spot of the size of the star. If, for instance, $f = 0.1$, this signifies that 10 % of the surface of the star is covered by accretion spots (either a single large spot or several smaller spots).

In addition to $\mathscr{F}$ and $f$, the models depend on stellar parameters: the distance, the luminosity ($L_\star$), the radius, the effective temperature ($T_{\mathrm{eff}}$) and the mass of the star. Once obtained, the models can be compared to observed spectra in order to determine the values of $\mathscr{F}$ and $f$ that give the best fit. It should be noted that decreasing the filling factor value will downscale the emission of the accretion column independently of wavelength. On the contrary, changing the energy flux values will shift the peak of the emission in wavelength (see Sect. 4.2.4).

Historically, the models were characterized by a single pair of $\mathscr{F}$ and $f$. Ingleby et al. (2013) updated them to allow for multiple accretion columns, by using multiple energy fluxes, each one with its corresponding filling factor, to fit a single observation. In such a case, each energy flux is better constrained by different regions of the spectrum. In general, the higher energy fluxes (i.e. higher densities accretion column) peak in the UV and the lower energy fluxes peak in the optical. Figure 1.17 (see Espaillat et al. 2022) illustrates this aspect. It shows three models (in cyan, sea-green and brown), each one fitting a different region of the observed spectrum (in black) best. Further improvements continue to be made to the models (see e.g. Robinson and Espaillat 2019; Espaillat et al. 2022; Pittman et al. 2022).

An alternative to comparing shock models to observed spectra is to derive modeled values of veiling from the shock models. This is achieved by dividing the modeled accretion shock fluxes with a photospheric template, since the veiling is defined as the ratio between the accretion shock flux and the photospheric flux. The modeled veiling can then be fitted to the observed veiling in order to determine the values of $\mathscr{F}$ and $f$ characterizing the data (see Sect. 4.2.4).

The mass accretion rate can be calculated using the obtained values of $\mathscr{F}$ and $f$ in the following equation from Calvet and Gullbring (1998):

$$\mathscr{F} = 9.8 \times 10^{10} \text{ ergs s}^{-1} \text{ cm}^{-2} \left( \frac{\dot{M}_{\mathrm{acc}}}{10^{-8} M_\odot \text{ yr}^{-1}} \right)$$
$$\times \left( \frac{M_\star}{0.5 M_\odot} \right) \left( \frac{R_\star}{2 R_\odot} \right)^{-3} \left( \frac{f}{0.01} \right)^{-1}$$

(1.3.8)

where $\dot{M}_{\mathrm{acc}}$ is the mass accretion rate, $M_\star$ is the mass and $R_\star$ is the radius of the
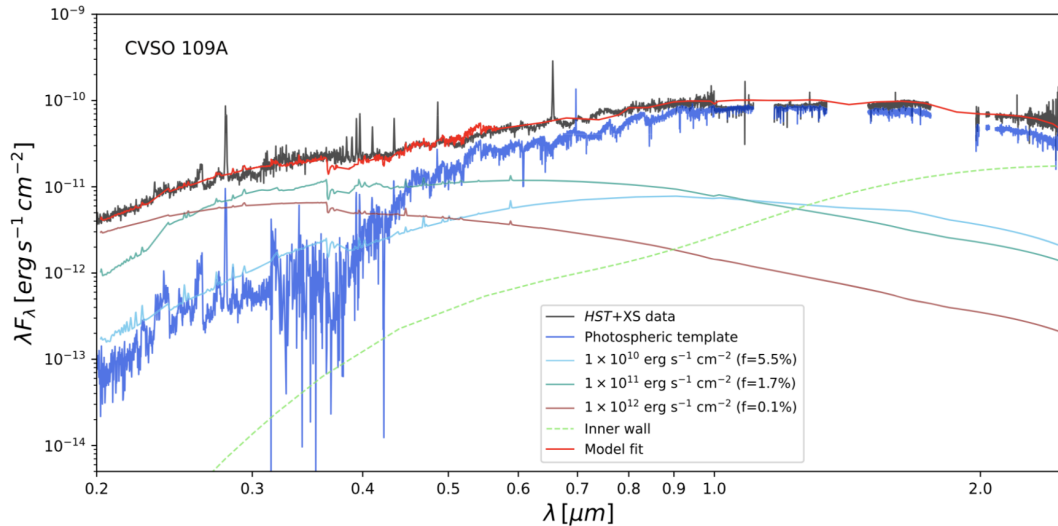
Figure 1.17 – Fitting the continuum of CVSO 109A with accretion shock models ([Espaillat et al. 2022]). The continuum ranges from the near-UV to near-IR. The observed spectrum is in black, the photospheric template is in dark blue. The best-fitting model is in red and is a combination of three accretion shock models (in cyan, sea-green and brown). These models have energy fluxes of $1 \times 10^{10}$, $1 \times 10^{11}$ and $1 \times 10^{12}$ erg s$^{-1}$ cm$^{-2}$. The corresponding filling factors are 0.055, 0.017 and 0.001.

star.

As accretion processes involve not only the star but also its circumstellar disk, the next section will focus on disks.

## 1.4 Circumstellar disks

The circumstellar disks of cTTs are composed of gas (mostly) and dust. They have a life time on the order of a few million years (see [Manara et al. 2023]). They can be divided into two parts: the inner disk and the outer disk. The inner disk is usually considered to be at a distance smaller than 0.1 au from the star. It is the location of the star-disk interactions and can reach temperatures higher than 1 000 K, as a result of heating by the stellar radiation field and viscous dissipation. The outer disk stretches to further distances, its radius ranging from a few tens of au to more than 1 000 au. There, the temperatures range from 10 to 30 K (see e.g. [Mamajek 2009]; [Dullemond and Monnier 2010]; [Hartmann et al. 2016]).

In the next section, two particular radii (namely the truncation and co-rotation radii) located in the circumstellar disk will be presented. This will be followed by a discussion of misalignments of the outer disk axis with respect to the stellar rotation axis.

## 1.4.1 Truncation & co-rotation radii

The radius where the circumstellar disk is truncated by the magnetic field is called the truncation (or magnetospheric) radius ($r_{trunc}$). Bessolaz et al. (2008) expressed its theoretical value for an axisymmetric dipolar magnetic field as:

$$\frac{r_{trunc}}{R_\star} \simeq 2m_s^{2/7} B_{eq}^{4/7} \dot{M}_{acc}^{-2/7} M_\star^{-1/7} R_\star^{5/7} \qquad (1.4.1)$$

where $m_s \sim 1$ is the sonic Mach number (i.e. the ratio between the flow velocity and the local speed of sound) measured at the mid-plane of the circumstellar disk. $B_{eq}$ is the intensity of the magnetic field at the stellar equator expressed in units of $140\,\mathrm{G}$. $\dot{M}_{acc}$ is expressed in units of $10^{-8} M_\odot \,\mathrm{yr}^{-1}$, $M_\star$ is in units of $0.8\,M_\odot$ and $R_\star$ in units of $2\,R_\odot$ [3]. In the present case of a dipolar field, $B_{eq}$ is equal to half of the magnetic field intensity at the pole of the star (see Gregory 2011).

The radius where the Keplerian period of the disk is equal to the rotation period of the star is called the co-rotation radius ($r_{co\text{-}rot}$) and can be calculated using Kepler's third law:

$$r_{co\text{-}rot}^3 = GM_\star \left(\frac{P}{2\pi}\right)^2 \qquad (1.4.2)$$

with $P$ the stellar rotation period (see e.g. Bouvier et al. 2007).

Under the assumption of a dipolar magnetic field aligned with the rotation axis of the system, in order for the accreted matter to fall on the star, it needs to lose angular momentum, which implies that the accretion column has to be connected to the disk inside the co-rotation radius, which transfers angular momentum to the star. However, in order to avoid accelerating the stellar rotation, it is necessary for the disk to transport angular momentum outward. This can only happen if the truncation radius is outside the co-rotation radius. To satisfy both conditions, theoretical models often assume that $r_{trunc} \sim r_{co\text{-}rot}$ (see e.g. Koenigl 1991; Shu et al. 1994; Bouvier et al. 2007; Bessolaz et al. 2008).

There is an opportunity to test this assumption by measuring the parameters in Eq. 1.4.1 and 1.4.2. For example, GRAVITY Collaboration et al. (2021) have calculated the truncation and co-rotation radii for several cTTs (see Fig. 1.18), assuming a magnetic field strength of $1\,\mathrm{kG}$ [4]. They find that there are 4 stars out of 17 that have their truncation radius outside of the co-rotation radius, although both radii are generally of the same order of magnitude (i.e. a few stellar radii). See also Thanathibodee et al. (2023) for the determination of the truncation radius and a comparison with the

---

[3] The units of Eq. 1.4.1 were chosen by Bessolaz et al. (2008) to represent typical values for cTTs citing Valenti and Johns-Krull (2004) and Bouvier et al. (2007).

[4] As the magnetic field strength was not known for all of the targeted cTTs, they used a fiducial value of 1 kG. Although the validity of this assumption is debatable, it has been made in other cases as well (see e.g. Hartmann et al. 2016).

co-rotation radius of low accretors.
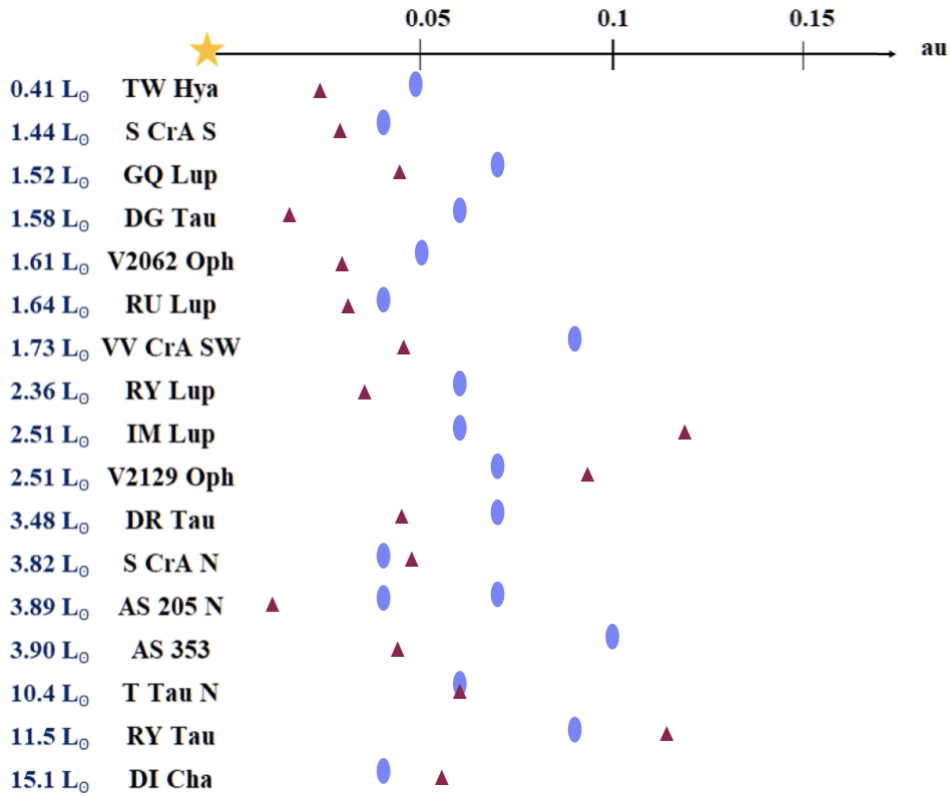


Figure 1.18 – Truncation and co-rotation radii for several cTTs (adapted from GRAVITY Collaboration et al. 2021). The truncation radii are represented by red triangles and the co-rotation radii are pictured by purple ovals.

The locations of the truncation and co-rotation radii compared to each other can also give information on the accretion regime of the star (see Sect. 1.3.2). For simulations with a magnetic obliquity of $\beta = 5°$ (see e.g. Romanova and Owocki 2015; Blinova et al. 2016), the boundary between the stable and unstable accretion regimes occurs when $r_{\text{co-rot}} = 1.4\,r_{\text{trunc}}$. When $r_{\text{co-rot}} > 1.4\,r_{\text{trunc}}$, the star is in the unstable regime. When $r_{\text{trunc}} \leqslant r_{\text{co-rot}} \leqslant 1.4\,r_{\text{trunc}}$, it is in the stable regime. When $r_{\text{co-rot}} < r_{\text{trunc}}$, it is in the propeller regime, in which some of the disk matter can be ejected as an outflow (see e.g. Romanova et al. 2018). Figure 1.19 (see Romanova and Owocki 2015) illustrates these different boundaries.

## 1.4.2 Misalignments of the outer disk axis

The standard models of stellar formation do not predict misalignments between the stellar rotation axis and the outer disk axis. They may however be common. Indeed, they have been observed for several cTTs, including LkCa 15 and DoAr 44 (see Alencar et al. 2018; Bouvier et al. 2020). In addition, GRAVITY Collaboration et al. (2021) report detecting misalignments between the inner and outer disk for four stars (namely GQ Lup, V2062 Oph, RY Lup and AS 205). The cTTs DK Tau (see Sect. 1.5
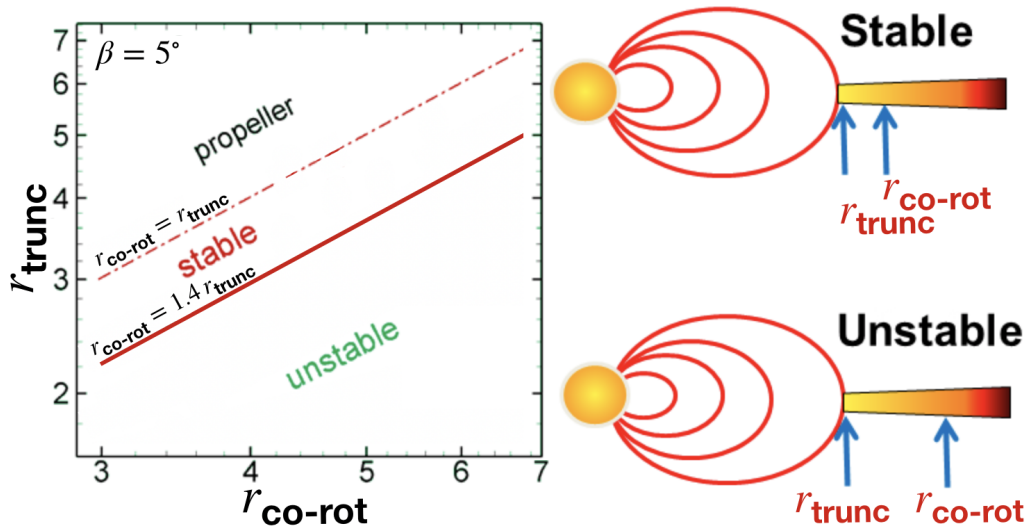
Figure 1.19 – The boundary between the stable and unstable accretion regimes (adapted from Romanova and Owocki 2015), for a magnetic obliquity $\beta = 5°$, is determined by the ratio between the truncation radius ($r_{\text{trunc}}$) and the co-rotation radius ($r_{\text{co-rot}}$).

and Chap. 3) shows signs of having a misaligned outer disk.

Moreover, various dippers display an outer disk with low inclinations (i.e. seen close to pole-on - see e.g. Ansdell et al. 2020; Sicilia-Aguilar et al. 2020). Dippers are stars with flux dips in their lightcurves. The traditional explanation for dipper behavior invokes the crossing of circumstellar material from the inner disk in front of the star, occulting it periodically or aperiodically. There therefore is a requirement for an inner disk with a rather high inclination (i.e. seen close to edge-on - see e.g. McGinnis et al. 2015; Roggero et al. 2021). This is incompatible with the measured low inclination of the outer disk axis.

These observations hint at a more complex stellar formation mechanism than is usually considered. Although it is not clear at this time what gives rise to such misalignments, several potential causes have been suggested. For instance, Sicilia-Aguilar et al. (2020) mention the possibility of two different protostellar collapses. Alencar et al. (2018) suggest the existence of a massive planet inside the disk gap. Whereas Benisty et al. (2018) invoke the effects of a low-mass stellar companion.

## 1.5 Characteristics of DK Tau

This work studies one particular cTTs, DK Tau A. It is a young low-mass star in a wide binary system (i.e. separated by 2.38″ - see Manara et al. 2019), which allows DK Tau A (called "DK Tau" for short hereafter) to be studied on its own. It has a magnetic field, and shows evidence of accretion and ejection processes (see Hartigan et al. 1995; Calvet and Gullbring 1998; Johns-Krull 2007; Fischer et al. 2011; Ingleby et al. 2013),

in particular inner disk winds and a jet. It has a mass loss rate of $3 \times 10^{-9} \, M_\odot \, \mathrm{yr}^{-1}$ (see Hartigan et al. 1995), and a mass accretion rate of $4 \times 10^{-8} \, M_\odot \, \mathrm{yr}^{-1}$ (see Fischer et al. 2011), which leads to the detection of significant veiling in its spectrum (see Johns-Krull 2007; Fischer et al. 2011; Ingleby et al. 2013) as well as broad H$\alpha$ and H$\beta$ line profiles (see McGinnis et al. 2020).

DK Tau is located in the Taurus Molecular Cloud at a distance of 132.6 pc (see Gaia Collaboration et al. 2016, 2018, 2022). It has a K7 spectral type (see Johns-Krull 2007; Fischer et al. 2011). The star has an effective temperature of $4\,150 \pm 110$ K, a rotation period of $8.2 \pm 0.13$ days, a line-of-sight-projected equatorial rotational velocity ($v \sin i$) of $13 \pm 1.3 \, \mathrm{km \, s^{-1}}$, and a radius of $2.48 \pm 0.25 \, R_\odot$ (see Chap. 3 for the derivation of these parameters). Johns-Krull (2007) determined a mass of $0.7 \, M_\odot$. DK Tau has an inclination (i.e. the angle between the line-of-sight and the rotation axis of the star) of 58° (+18)(-11) (see Chap. 3 for the description of this determination). Based on measurements using millimeter data, its outer circumstellar disk has an inclination of 21° ± 3 (see Rota et al. 2022). The outer disk axis is thus misaligned compared to the stellar rotation axis. Table 1.1 summarizes the characteristics of DK Tau.

Table 1.1 – Summary of the characteristics of DK Tau.

| Stellar parameter | Value | Reference |
|---|---|---|
| $i$ (°) | 58 (+18)(-11) | Nelissen et al. (2023a) |
| Outer disk axis inclination (°) | 21 ± 3 | Rota et al. (2022) |
| $P$ (days) | 8.20 ± 0.13 | Nelissen et al. (2023a) |
| $T_{\mathrm{eff}}$ (K) | 4 150 ± 110 | Nelissen et al. (2023a) |
| $v \sin i$ (km s$^{-1}$) | 13.0 ± 1.3 | Nelissen et al. (2023a) |
| $R_\star$ ($R_\odot$) | 2.48 ± 0.25 | Nelissen et al. (2023a) |
| $M_\star$ ($M_\odot$) | 0.7 | Johns-Krull (2007) |

Because DK Tau displays clear signatures of accretion, it is an excellent subject to explore the interaction between stellar magnetic field and accretion from the circumstellar disk. Focusing on a single object allows one not only to determine its characteristics, but the information derived from its analysis is useful to constrain star formation models, in particular regarding outer disk misalignments (see Sect. 3.3.1). In addition, the techniques described in this work (e.g. regarding the removal of veiling in Sect. 3.2.3 or the measurement of the mass accretion rate in Sect. 4.3.2) can be extended to other stars. Finally, the correlations found, in particular regarding the accretion luminosity and veiling (see Sect. 4.3.1), can be explored in additional objects.

## 1.6 Thesis outline

cTTs are young stars that experience magnetospheric accretion. This thesis examines both the magnetic field and the accretion processes in a specific cTTs, DK Tau. In Chapter 1, an introduction to the different relevant concepts was presented. These concepts include low-mass star formation, stellar magnetic fields, accretion processes, circumstellar disks and the characteristics of DK Tau.

In Chapter 2, the observations used in this work are listed. In addition, the instruments that produced these observations are described and the automatic reduction pipeline associated with these instruments is presented.

Chapter 3 is based on the research published in Nelissen et al. (2023a). It focuses on the magnetic field aspect, in particular on the average line-of-sight magnetic field, of DK Tau, in both photospheric absorption lines and accretion-powered emission lines. Moreover, it presents a method of determining and subsequently removing the veiling, a necessary step in order to the study of the magnetic field. Finally, it investigates a potential misalignment of the outer disk axis with respect to the stellar rotation axis.

Chapter 4 is based on the research published in Nelissen et al. (2023b). This time, it focuses on the accretion properties of DK Tau. It compares the mass accretion rates derived from two different procedures. The first one relies on the accretion luminosity via accretion-powered emission lines. The second one uses accretion shock models fitted to the veiling. Furthermore, this chapter presents a correlation between the accretion luminosity and the veiling.

Chapter 5 presents a preliminary study of the large-scale magnetic topology and strength of DK Tau using ZDI on photospheric absorption lines, while underlining the limitations of this approach for cTTs.

Finally, Chapter 6 presents the general conclusions of this work, as well as suggestions for future work.

# 2

# Observations

$\mathcal{T}$HIS second chapter describes the different archival spectropolarimetric datasets used in this work. It also presents the two instruments that obtained the observations. Finally, it explains the data reduction steps undertaken by the automatic pipeline associated with these instruments.

## 2.1 Datasets

The data are comprised of two sets of unpolarized (i.e. Stokes I) and circularly polarized (i.e. Stokes V) spectra of DK Tau, probing two distinct epochs (i.e. periods within 2010 and 2012). They were collected using the high-resolution spectropolarimeters ESPaDOnS (for "Echelle SpectroPolarimetric Device for the Observation of Stars") and NARVAL (see Sect. 2.2). Nine spectra were taken in December 2010 and nine spectra from the end of November to the end of December 2012 with ESPaDOnS. Nine spectra were also taken from the end of November 2010 to January 2011 and nine spectra from November to the end of December 2012 with NARVAL. For the 2010 epoch, a total of 15 observations were collected over 39 days. For the 2012 epoch, a total of 12 observations were collected over 35 days. This was done with the intention of capturing a few rotations cycles of DK Tau (which has a rotation period of 8.2 days - see Sect. 1.5) for each epoch. The two epochs allow one to study the evolution of the magnetic field and of accretion with time.

Table 2.1 lists the characteristics of both datasets. The total exposure time was of 4 996.0 s and 4 800.0 s for each observation taken with ESPaDOnS and NARVAL respectively.

The data had been previously processed at the Canada-France-Hawaii Telescope (CFHT - in the case of the ESPaDOnS observations) and Télescope Bernard Lyot (TBL - in the case of the NARVAL observations) with LibreESpRIT, a fully automatic reduction pipeline (see Donati et al. 1997). It was specifically created for extracting Stokes I and Stokes V spectra from raw data (see Sect. 2.3). It should be noted that the ESPaDOnS and NARVAL spectra are not flux-calibrated.

The datasets are publicly available and were downloaded from the archive of the PolarBase website[1] (see e.g. Petit et al. 2014). The data files are presented in plain `ascii` format and include information about the wavelength, Stokes I (and its error),

---

[1] http://polarbase.irap.omp.eu

Table 2.1 – Log of ESPaDOnS and NARVAL observations of DK Tau.

| Date (yyyy-mm-dd) | Heliocentric Julian date (UTC)* | Rotation cycle** | S/N*** | Airmass | Instrument |
|---|---|---|---|---|---|
| 2010-11-26 | 2 455 527.436 03 | 0.00 | 70 | 1.1 | NARVAL |
| 2010-12-09 | 2 455 540.393 30 | 1.58 | 77 | 1.2 | NARVAL |
| 2010-12-10 | 2 455 541.397 11 | 1.70 | 53 | 1.1 | NARVAL |
| 2010-12-13 | 2 455 544.418 52 | 2.07 | 42 | 1.1 | NARVAL |
| 2010-12-14 | 2 455 544.979 74 | 2.14 | 72 | 1.1 | ESPaDOnS |
| 2010-12-15 | 2 455 545.853 82 | 2.25 | 97 | 1.0 | ESPaDOnS |
| 2010-12-16 | 2 455 546.854 61 | 2.37 | 100 | 1.0 | ESPaDOnS |
| 2010-12-17 | 2 455 547.826 04 | 2.49 | 108 | 1.1 | ESPaDOnS |
| 2010-12-18 | 2 455 548.819 03 | 2.61 | 113 | 1.1 | ESPaDOnS |
| 2010-12-19 | 2 455 549.786 41 | 2.73 | 81 | 1.2 | ESPaDOnS |
| 2010-12-19 | 2 455 550.390 86 | 2.80 | 54 | 1.1 | NARVAL |
| 2010-12-24 | 2 455 554.883 63 | 3.35 | 83 | 1.0 | ESPaDOnS |
| 2010-12-26 | 2 455 557.034 94 | 3.61 | 101 | 1.8 | ESPaDOnS |
| 2010-12-30 | 2 455 560.977 48 | 4.09 | 96 | 1.3 | ESPaDOnS |
| 2011-01-03 | 2 455 565.451 64 | 4.64 | 68 | 1.1 | NARVAL |
| 2012-11-19 | 2 456 250.509 43 | 0.00 | 68 | 1.1 | NARVAL |
| 2012-11-25 | 2 456 256.919 80 | 0.78 | 91 | 1.0 | ESPaDOnS |
| 2012-11-28 | 2 456 259.895 31 | 1.15 | 121 | 1.1 | ESPaDOnS |
| 2012-11-29 | 2 456 260.991 38 | 1.28 | 127 | 1.1 | ESPaDOnS |
| 2012-12-01 | 2 456 262.947 48 | 1.52 | 105 | 1.0 | ESPaDOnS |
| 2012-12-02 | 2 456 263.865 70 | 1.63 | 84 | 1.1 | ESPaDOnS |
| 2012-12-04 | 2 456 265.965 15 | 1.89 | 120 | 1.0 | ESPaDOnS |
| 2012-12-07 | 2 456 268.846 50 | 2.24 | 94 | 1.1 | ESPaDOnS |
| 2012-12-09 | 2 456 271.387 97 | 2.55 | 70 | 1.2 | NARVAL |
| 2012-12-10 | 2 456 271.825 04 | 2.60 | 107 | 1.2 | ESPaDOnS |
| 2012-12-12 | 2 456 273.557 58 | 2.81 | 63 | 1.2 | NARVAL |
| 2012-12-23 | 2 456 284.762 49 | 4.18 | 95 | 1.3 | ESPaDOnS |

* At mid-exposure.

** For an 8.2 day period.

*** Signal to noise ratio at 754 nm.

and Stokes V (and its error). The data is in 1D format, i.e. in the form of a continuous spectrum. The corresponding image files (`.fits`) for the ESPaDOnS data are also available to download from the Canadian Astronomy Data Centre (CADC) website[2].

The spectropolarimetric observations were collected as a result of proposals 10BP12 and 12BP12, with J.-F. Donati as P.I. in both cases. They were part of the Magnetic Protostars and Planets (MaPP) Large Program (LP) at the CFHT, where several cTTs were observed in order to study their magnetic fields (see e.g. Donati et al. 2010, 2011, 2013). The amount of veiling present in the spectra of DK Tau complicated its study and it was consequently left unanalyzed at the time.

## 2.2 ESPaDOnS & NARVAL

The observations were obtained with the instruments ESPaDOnS (see Donati 2003; Donati et al. 2006a) and NARVAL (see Aurière 2003). ESPaDOnS is mounted at the 3.6 m CFHT on Mauna Kea (Hawaii, USA), while NARVAL is installed at the 2 m TBL on the Pic du Midi (southern France). They are twin cross-dispersed echelle spectropolarimeters. They cover the whole optical range (i.e. from 370 to 1 050 nm) in a single exposure, with an average spectral resolution of 65 000 (corresponding to resolved velocity element of $4.6\,\mathrm{km\,s^{-1}}$) in either circular or linear polarization. Each spectropolarimeter essentially consists of two distincts units: a polarimetric unit and a spectroscopic unit.

The polarimetric modules are installed at the Cassegrain focus of their respective telescopes (see Donati et al. 2006a; Petit et al. 2014). Figure 2.1 (see Benton 2005) illustrates the operating principle of a Cassegrain system. The incoming light is first reflected on a concave mirror, then on a convex mirror, before passing through a hole in the center of the first mirror and reaching the Cassegrain focus.
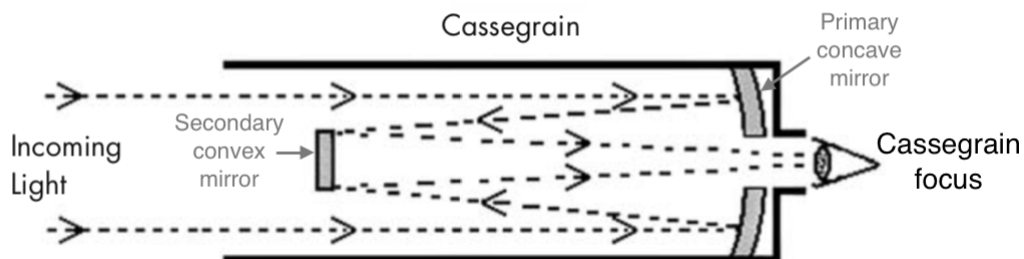


Figure 2.1 – Schematic view of a Cassegrain system. The arrows show the path of the incoming light. The photons first bounce on the primary concave mirror, then on the secondary convex mirror and finally reach the Cassegrain focus (adapted from Benton 2005).

The operating principle of a polarimeter is to measure the polarization of light, i.e. the orientation of the electric field vector in the electromagnetic wave (see e.g.

---

[2]http://www.cadc-ccda.hia-iha.nrc-cnrc.gc.ca/en

Snik and Keller 2013). In the case of ESPaDOnS and NARVAL, the polarimetric module simultaneously measures two orthogonal states of a given polarization. For the observations used in this work, the right ($I_\circlearrowright$) and left circular polarization ($I_\circlearrowleft$) were measured. To this end, the module uses a combination of three Fresnel rhombs (a quarter-wave and two half-wave rhombs) as a retarder and a Wollaston prism as a polarizer (see Donati 2003; Donati et al. 2006a; Petit et al. 2014). Figure 2.2 illustrates the working principle of the polarimetric module.
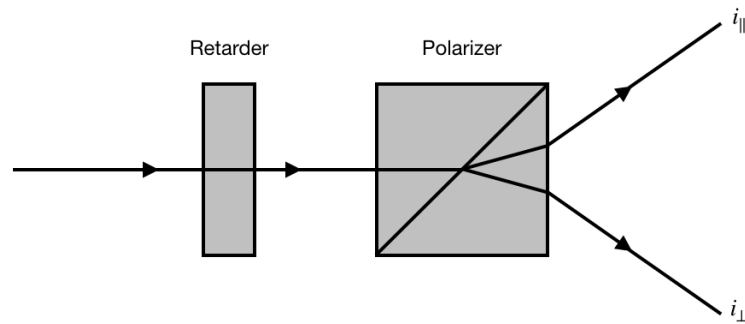


Figure 2.2 – Schematic view of the operating principle of the polarimetric module used by ES-PaDOnS and NARVAL. The polarizer (i.e. the Wollaston prism) splits the incident beam of light in two beams whose polarization states are orthogonal and whose intensities are labelled $i_\parallel$ and $i_\perp$. By rotating the retarder (i.e. the Fresnel rhombs) compared to the polarizer, as well as by rotating both devices compared the direction of propagation of the incident beam, it is possible to measure specific states of polarization.

A retarder is a device that modifies the polarization state of the incident light beam. A quarter-wave retarder can be used to switch between circularly polarized and linearly polarized light. A half-wave retarder can be used to switch between linearly polarized light of different polarization directions. A Wollaston prism is a polarizer that divides the incident beam of light in two orthogonally polarized components. These components propagate along different directions inside the prism. By rotating the retarder and polarizer in the plane that is perpendicular to the direction of propagation of the incident beam, specific states of polarization can be measured (see e.g. Landi Degl'Innocenti and Landolfi 2004; Clarke 2010; Snik and Keller 2013). These are the various states described in Fig. 1.6. During the data reduction process (see the next section), they are combined in order to obtain the Stokes parameters.

Figure 2.3 shows a schematic view of the polarimetric module of ESPaDOnS. In the case of ESPaDOnS and NARVAL, when leaving the polarimeter, the two beams of light from the polarizer are fed into the spectrograph by a double optical fiber (see Donati 2003; Donati et al. 2006a; Petit et al. 2014).

The operating principle of a spectrograph is to disperse the incoming light, by forcing its spectral components to travel in slightly different directions according to their wavelength. This is achieved with a grating, i.e. an optical element etched with (in general) thousands of fine parallel lines (see e.g. Clayton 1996; Oswalt and Bond

INTERFACE

Cassegrain focus

Rotating half-
wave Fresnel
rhomb

Quarter-wave
Fresnel rhomb

Rotating half-
wave- Fresnel
rhomb

Wollaston prism

FIBER LINK
TO SPECTROGRAPH
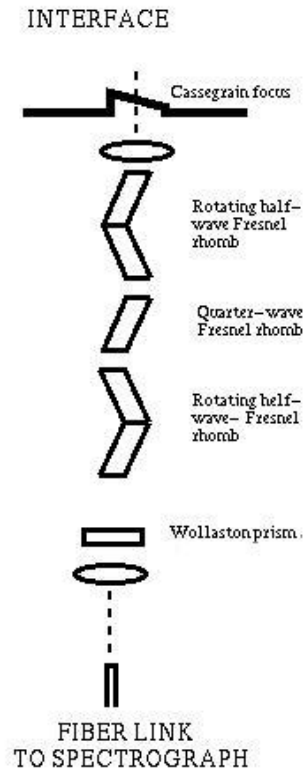
Figure 2.3 – Schematic view of the polarimetric module of ESPaDOnS. It shows the three Fresnel rhombs (a quarter-wave and two half-wave rhombs) acting as a retarder and the Wollaston prism acting as a polarizer (adapted from: https://www.cfht.hawaii.edu/Instruments/Spectroscopy/Espadons/IMAGES/fig_polarimeter.jpg).

2013).

In a spectrograph, constructive interference happens when the light path length is equal to its wavelength multiplied by an integer. This integer is called the order (k - see e.g. Biémont 2006; Oswalt and Bond 2013). When the order is equal to zero, only a central image (corresponding to the non-deflected incoming light) is obtained (see the central panel in Fig. 2.4, with k = 0). For the first order, two spectra appear, one on either side of the central image (see the panels with k = 1 in Fig. 2.4). For the second order, two additional (more dispersed) spectra appear beside the previous two (see the panels with k = 2 in Fig. 2.4). For the third order, two additional (even more dispersed) spectra appear beside the previous two, their ends overlapping (see the panels with k = 3 in Fig. 2.4, the overlapping represented by the gray band).

A higher order is synonymous with a higher resolution. However, as their number increases, the overlap between the orders increases as well. When a spectrograph is used at a very high order, the overlap is so important that it produces white light. There is then a need to separate the optical orders and spread them over the detector. This is done with a cross-disperser, positioned orthogonally to the first grating in such a way that the resulting orders are transversally separated. In this case, the spectrograph acquires the adjective "echelle". Echelle spectrographs use a first grat-
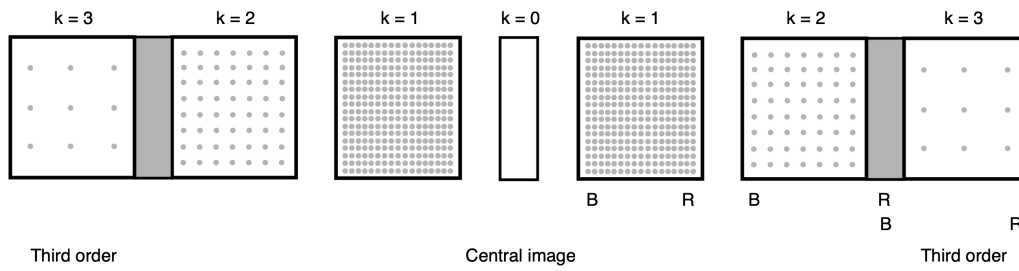
Figure 2.4 – Overlapping of spectral orders, which are denoted by the letter "k". "B" refers to the blue part of the light and "R" to the red (adapted from Biémont 2006).

ing in which the grooves are much further apart than those of a typical grating (see e.g. Clayton 1996; Oswalt and Bond 2013).

Figure 2.5 illustrates the operating principle of an echelle spectrograph. A first grating (on the top left side of the figure) disperses the light. It then arrives on the cross-disperser (on the bottom of the figure), which separates the various orders. The light finally hits the detector (on the top right side of the figure), each order visible.
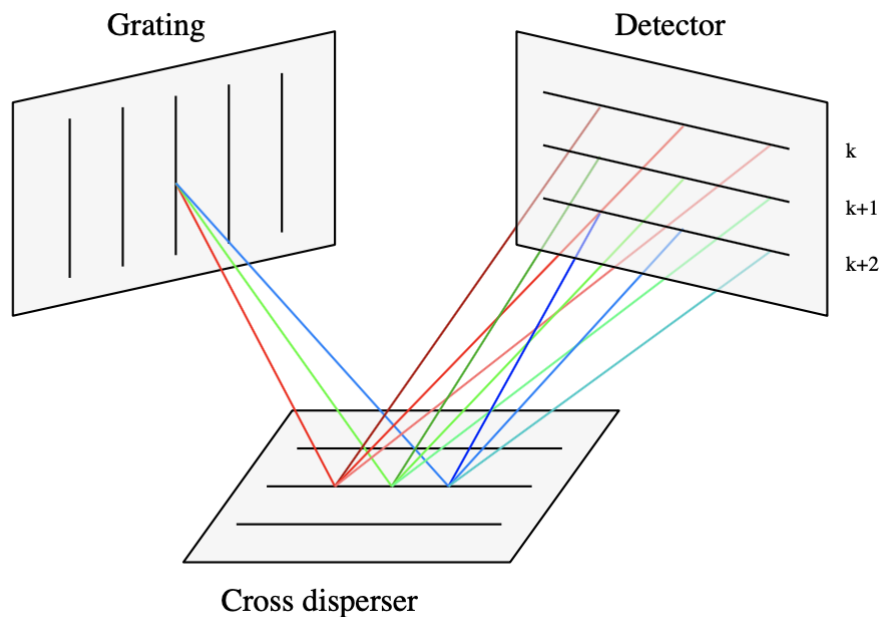


Figure 2.5 – Schematic view of the operating principle of an echelle spectrograph. The orders are denoted by the letter "k". On the detector, the first row corresponds to the red part of the order k. The second row corresponds to the green part of the order k+1. The third row corresponds to the blue part of the order k+2 (by C. Delvaux).

Echelle spectroscopy is interesting because it has a high resolution, it covers a large spectral area and it takes advantage of the (roughly squared) shape of the detector on which it spreads its entire spectrum (the wavelength is spread in one direction, while the different orders are stacked perpendicularly to this direction). Regarding ESPaDOnS and NARVAL, each twin spectropolarimeter records 40 orders (see e.g. Fig. 2.9) and each order is curved. In the case of ESPaDOnS, the first order is k = 22 and is centered at 1 029 nm, while the last one is k = 61 and is centered at

372 nm (see Donati 2003; Donati et al. 2006a).

Figure 2.6 shows a schematic view of the spectroscopic module of NARVAL. It depicts the entry for the optical fibers, the first grating, the cross-disperser and the charge-coupled device (CCD) detector (see the next section for a brief explanation of the operating principle of this type of detector) sitting on an optical bench.
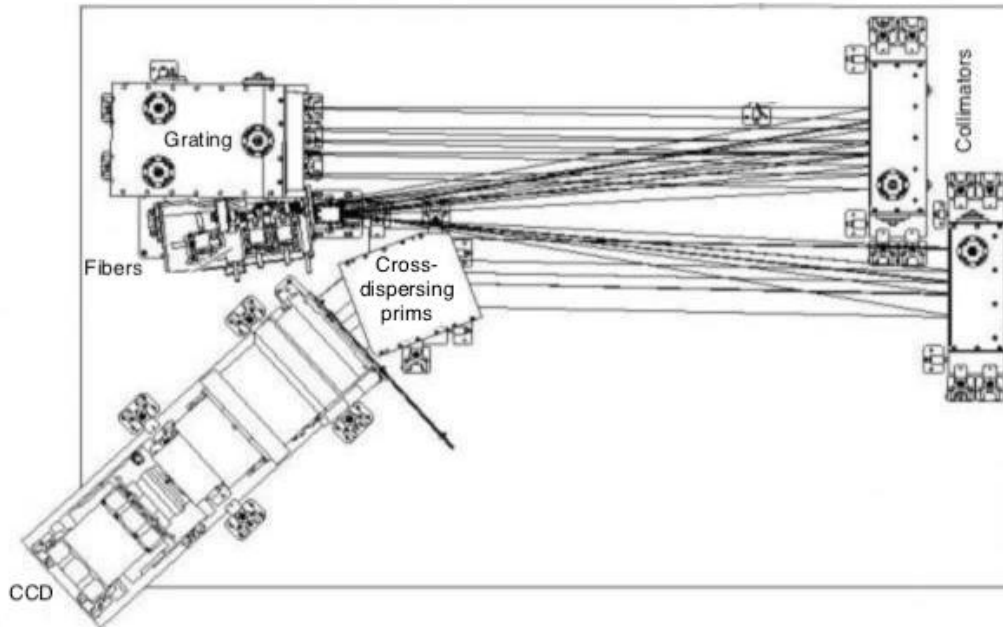


Figure 2.6 – Schematic view of the spectroscopic module of NARVAL. It shows the entry for the optical fibers (on the left), the first grating (on the top left), the cross-disperser (toward the center) and the CCD detector (on the bottom left - adapted from: https://tbl.omp.eu/instruments/aspects-techniques/description-generale).

Regarding the thermal stability of the spectrographs (necessary to avoid thermal noise - see the next section), it is ensured by a thermally stabilised enclosure in the case of ESPaDOnS and a double layer enclosure in the case of NARVAL (see e.g. Donati 2003; Silvester et al. 2012). For additional information on ESPaDOnS and NARVAL, see the dedicated webpages on the CFHT website[3], and on the TBL website[4] respectively.

## 2.3 Data reduction

As mentioned in Sect. 2.1, the LibreESpRIT pipeline installed at the CFHT and TBL automatically reduced the data in real-time. The procedure includes subtracting the bias and the dark frames, adjusting for the variations in sensitivity using flat-field frames, wavelength calibration and continuum normalization. LibreESpRIT was specially developed for ESPaDOnS and NARVAL (see Petit et al. 2014). It is not publicly

---

[3]https://www.cfht.hawaii.edu/Instruments/Spectroscopy/Espadons
[4]https://tbl.omp.eu/instruments/archive-tblnarval/

available. It is based on ESpRIT (for "Echelle Spectra Reduction: an Interactive Tool") and follows roughly the same procedure. ESpRIT is a package that was written for the reduction of echelle spectropolarimetric data with curved orders. For a description of ESpRIT, see Donati et al. (1997); for additional information on LibreESpRIT, see the dedicated webpage on the CFHT website[5]; for a description of echelle data reduction, see for instance Clayton (1996); and for a general description of data reduction, see for instance Oswalt and Bond (2013). Initial steps in the data reduction process are linked to the working principle of CCD detectors. These are the type of detectors used in ESPaDOnS and NARVAL. Their operating principles will be briefly explained in the following paragraphs.

CCDs are made of semiconductors whose atoms have electrons arranged in discrete energy bands. There is a valence and a conduction band (in light gray in Fig. 2.7) separated by a gap (labeled $E_{gap}$ in Fig. 2.7). At absolute zero, the valence band is full and the conduction band is empty. A photon (represented by the dark gray arrow in Fig. 2.7) can be absorbed by transferring its energy to an electron from the valence band, which is then sent to the conduction band. In other words, photons entering the CCD create electron-hole pairs, with the electron being referred to as a photoelectron (represented by the black dot in Fig. 2.7). This is called the photoelectric effect. The number of photoelectrons is proportional to the number of incident photons.
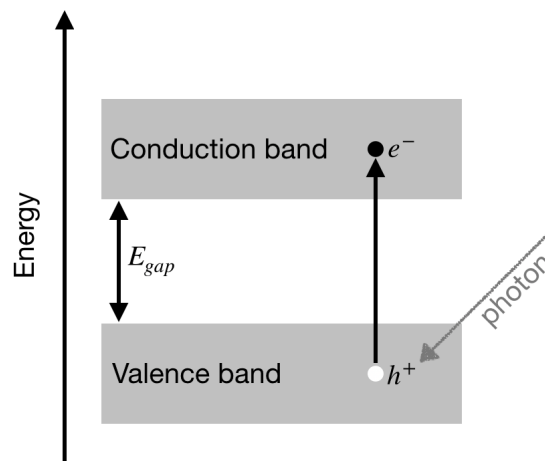


Figure 2.7 – Schematic view of the photoelectric effect. $E_{gap}$ refers to the energy gap between the valence and conduction band. The white dot labeled $h^+$ represents the hole left by the electron in the valence band after the absorption of the photon. This hole acts like a positively charged carrier. The black dot labeled $e^-$ represents the photoelectron that migrated to the conduction band.

Once in the conduction band, the electrons are free to move about. In CCDs, electrodes placed on the surface create potential wells that attract these free electrons in order to collect them. Otherwise, the holes and electrons would recombine.

[5]https://www.cfht.hawaii.edu/Instruments/Spectroscopy/Espadons/Espadons_esprit.html

These electrodes define the pixels of the CCDs.

Kristian and Blouke (1982) proposed the following analogy (illustrated in Fig. 2.8) for the basic working mechanism of CCDs: there is a network of buckets (representing the pixels of the CCD) evenly distributed on a large field (i.e. the focal plane of the telescope) in a square array. Each row of buckets is placed on a stationary conveyer belt. After a heavy rain (i.e. after exposure, where the rain represents the photons), the buckets are full of water (i.e. electrons). Then, the conveyer belts turn on (representing the transfer of charges). At the end of each row, the water is poured into buckets located on a conveyer belt that is at a right angle to the others (i.e. a row of electrodes outside of the photosensitive area of the CCD). At the end of it (i.e. at the corner of the CCD), there is a measuring cylinder (i.e. output amplifier) where the amount of water that was collected in each bucket can be recorded. The spatial distribution of the rainfall over the field (i.e. an image of the incident light) can therefore be known.
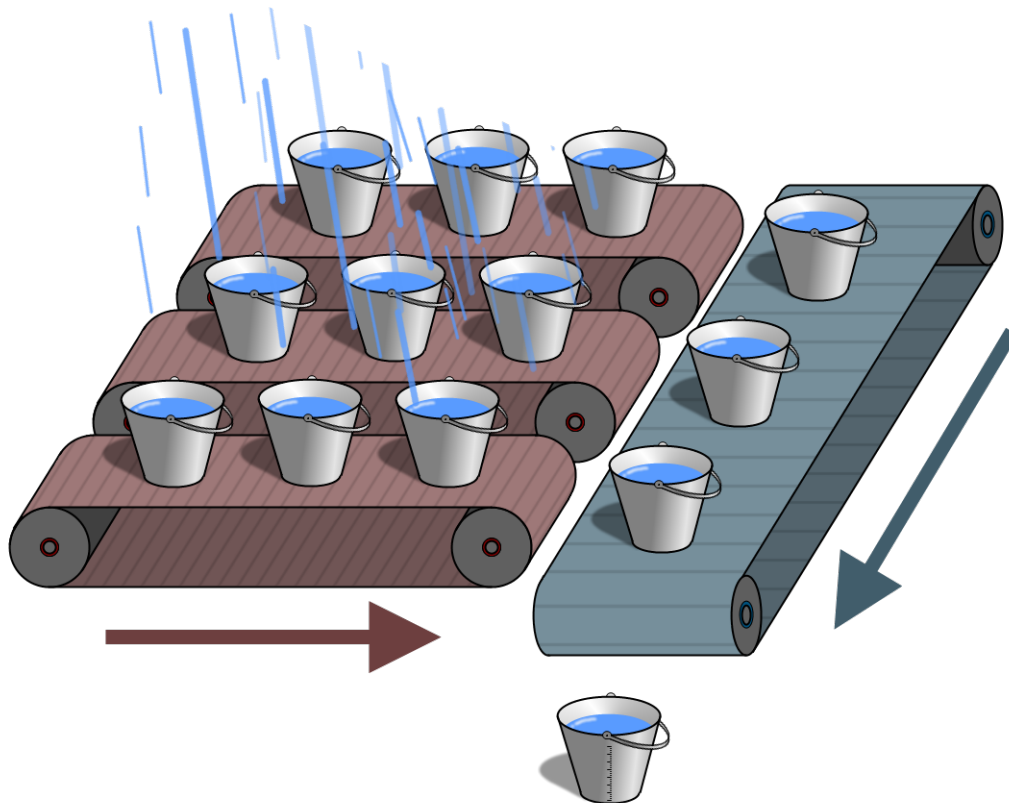


Figure 2.8 – Analogy for the basic working mechanism of CCDs. The rain represents the photons, the buckets represent the pixels of the CCD, the water inside them represents the electrons, the red conveyer belts represent the transfer of charges, the blue conveyer belt represents the row of electrodes outside of the photosensitive area of the CCD, and the bucket with the graduations represents the output amplifier (by C. Delvaux).

When observing with an instrument that uses a CCD detector, it is necessary to collect a number of calibration exposures in order to clean raw observations of contaminations and retrieve useful scientific data. This process is called data reduction.

The first calibration exposures are bias frames. The bias corresponds to the elec-

tronic readout noise from CCDs. Indeed, reading the detectors consist in extracting the photoelectrons from the CCD cells using a voltage.This creates an additional current, and an offset is consequently produced. This offset is different from one pixel to the other on the detector and needs to be measured (by taking an observation in the dark with an exposure time of 0 s) and subsequently subtracted. The Libre-ESpRIT package subtracts the bias averaged over squares of 8 by 8 pixels.

The next calibration frames are dark exposures, which correspond to thermal noise. Despite the thermal enclosures that house the spectrographs, there is a current inside the CCDs due to the energy distribution of electrons above absolue zero allowing a fraction of them to thermally populate the conduction band. Because they are indistinguishable from photoelectrons, these thermal electrons can be interpreted as light sources. To prevent this, the dark current can be determined (by taking an observation with the shutter closed and with an exposure time similar to that of the scientific target) and subtracted from the scientific frames as well.

The flat-field frames inform on the inhomogeneities of the CCDs (i.e. on the sensitivity variations from one pixel to the other) and on the imperfections of the instruments. These variations can be due for instance to dust, defects or damages. In order to obtain flat-field frames, a uniform source of light can be observed in the same conditions as the scientific target. The scientific frames are subsequently divided by the flat-field frames (which have themselves been corrected using the bias and dark frames). In the case of ESPaDOnS and NARVAL, two tungsten lamps (producing composite featureless spectra) are used for flat-field correction. The low-intensity lamp is used with a red filter and the high-intensity lamp is used with a blue filter. This is done to provide a proper illumination level to all orders (see e.g. Donati et al. 2006a; Silvester et al. 2012; Petit et al. 2014).

Regarding the different curved orders produced by echelle specropolarimetry (see the previous section), the path of each of them across the frames needs to be determined. This requires a bright frame from which to trace the orders. LibreESpRIT uses the flat-field frames to derive the position and shape of each order on the CCD (see e.g. Donati et al. 1997). Figure 2.9 shows a flat-field frame taken with ESPaDOnS (using the two tungsten lamps with a red and blue filter), with the orders and their curvature visible.

Generally, the order tracing procedure in the echelle data reduction process involves sampling each order in sections. Then, the center of the order at each sample point is estimated. After an order has been traced in this manner, it is possible to fit a curve to the sample. This curve should represent the real path of the order across the frame. Figure 2.10 (see Clayton 1996) depicts a generic example of order tracing for a single order.
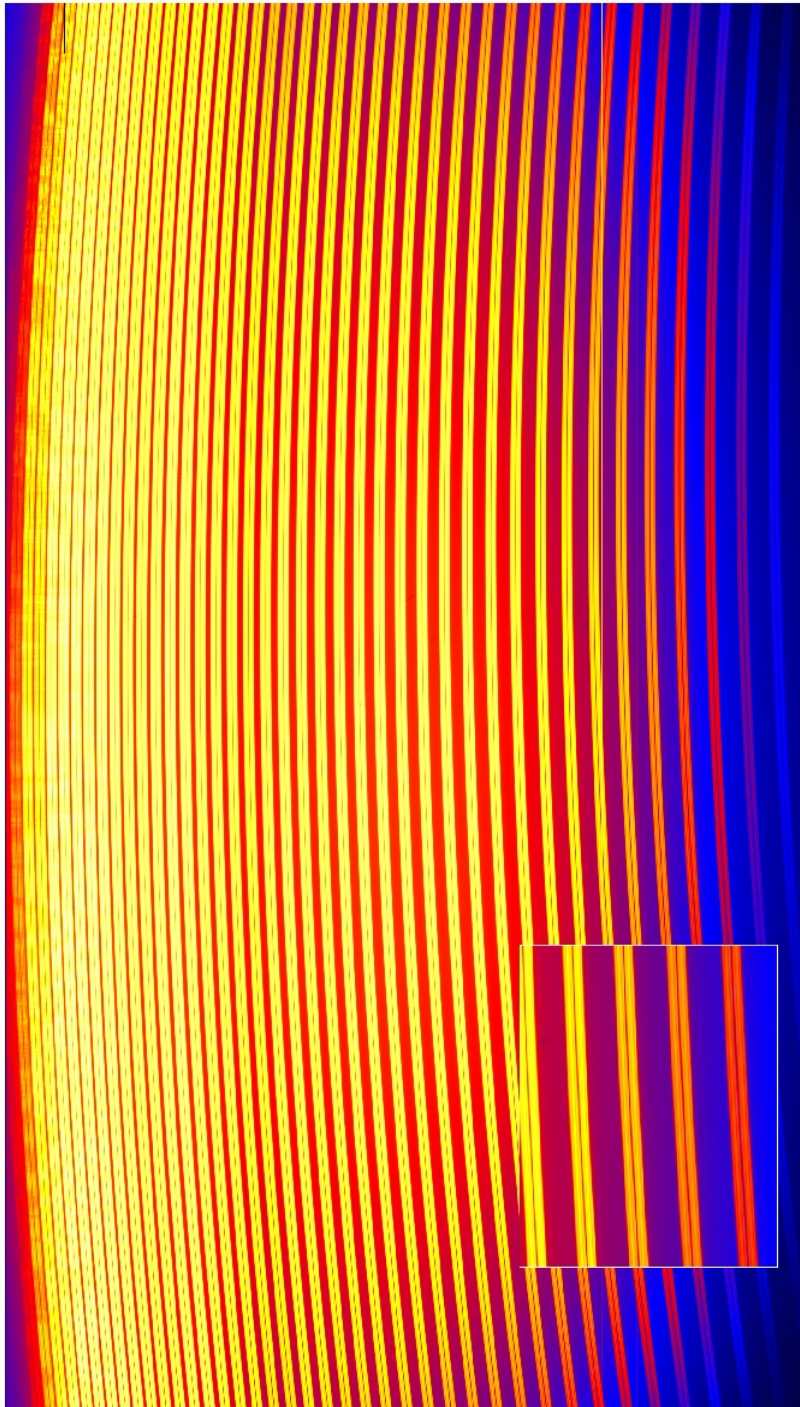
Figure 2.9 – Example of a flat-field frame taken with ESPaDOnS. It was taken with two tungsten lamps, one with a red filter and one with a blue filter. This creates a flat-field frame with flux in the red and blue part of the spectrum. The orders are the bright curved vertical lines and are stacked in order from the left to the right of the CCD. The separation between the orders varies with the wavelength and is largest in the blue (i.e. on the right side of the image). This is to be expected from the use of a cross-disperser (see the previous section). The bottom right part zooms in on the image. It shows that each order has two spectra, one for each orthogonal state of the polarization that is selected to be measured (see the previous section as well). Credit: https://www.cfht.hawaii.edu/Instruments/Spectroscopy/Espadons/IMAGES/colorflatwithzoom.jpg

In practice, to obtain a good fit, some of the sample points may have to be ignored. This is for instance the case if the frame is affected by cosmic ray hits.
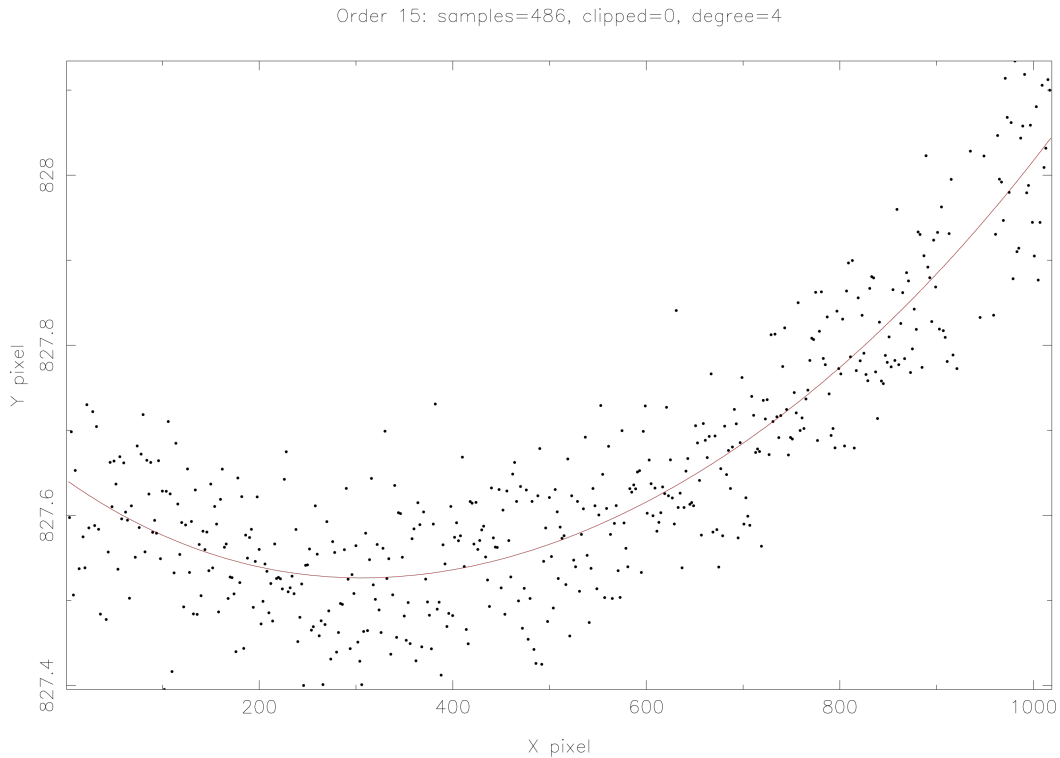


Figure 2.10 – Generic example of order tracing. A polynomial (red solid line) is fitted to the sample points (black dots) of a particular order (Clayton 1996).

Cosmic rays (i.e. high-energy particles from outer space that reach the Earth and pass through its atmosphere, as well as secondary particles subsequently generated), can hit the CCD during exposure, causing the presence of extra signals in the frames. These signals usually cover only a few pixels on the CCD and appear as bright, sometimes saturated spots. If, however, the cosmic ray travelled in a direction that is nearly parallel to the surface of the CCD, then it could cause a streak. Cosmic ray hits need to be identified, as real features in a spectrum can similarly cover only a few pixels in the frames. In the case of LibreESpRIT, the pixels that deviate too much from the average intensity in each order are excluded by the pipeline in order to eliminate cosmic ray hits (see e.g. Donati et al. 1997).

The data reduction process also includes wavelength calibration (i.e. the identification of a number of spectral lines distributed over the observed wavelength range). This uses a comparison lamp containing a mix of gases (a combination of thorium/argon and thorium/neon in the case of ESPaDOnS and NARVAL) that produces a spectrum rich in spectral lines. Because the wavelengths of the lines are well known, they can be used to calibrate lines in the scientific observations. This lead to the determination of the wavelength-to-pixel relation along and across each order. These calibration exposures are taken on each observing night (see e.g. Donati et al. 2006a, 2011; Silvester et al. 2012; Petit et al. 2014).

The common wavelength calibration procedure in echelle data reduction is based on three types of information: the order, the sample number and the intensity. The sample number (as during the order tracing procedure) corresponds to an index for each section along the order. The first stage of the calibration consist in identifying spectral lines of known wavelength in the calibration frames. This is illustrated in Fig. 2.11 (see Clayton 1996). Lists of wavelengths for different spectral lines can be found in various atlases. Next, a polynomial is fitted to the wavelength-to-sample relation from the calibration frames. Finally, this relation is pasted from the calibration frames onto the scientific observations. The wavelength-to-sample relation can be fitted separately for each order. Ideally, each order should feature at least three or four identified spectral lines, with one close to each end of the order and the others dispersed toward the middle of the order.
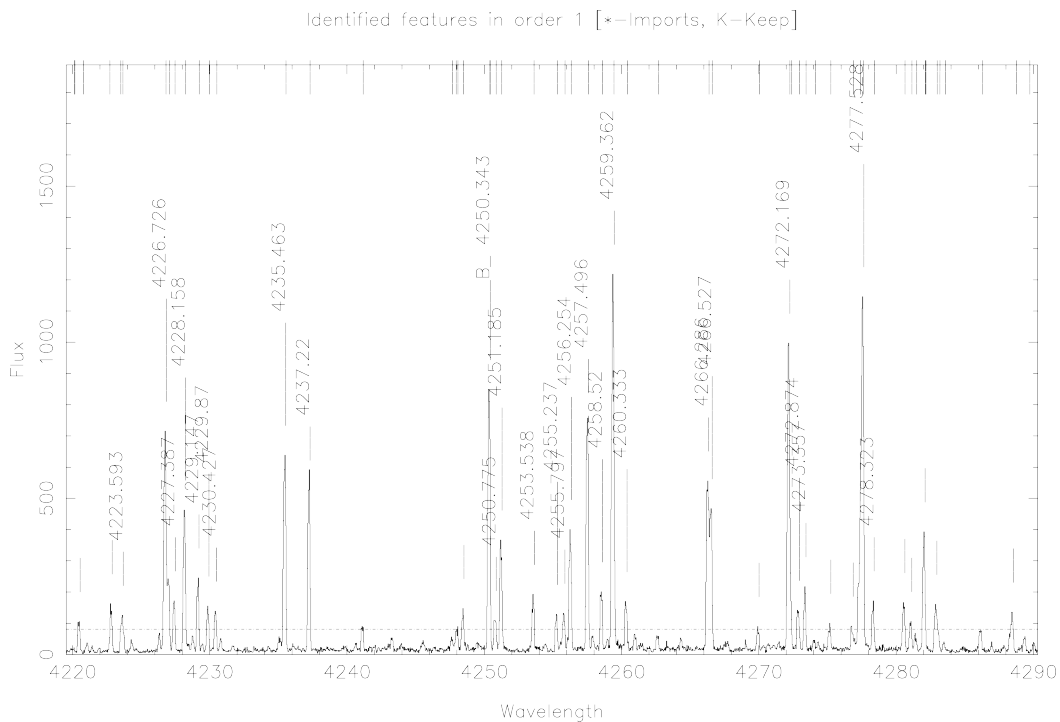


Figure 2.11 – Generic example of spectral line identification for a particular order (Clayton 1996).

In addition to the primary wavelength calibration, the LibreESpRIT pipeline also uses telluric lines to refine the wavelength calibration (see e.g. Donati et al. 2006a, 2011; Silvester et al. 2012; Petit et al. 2014). Telluric lines are spectral lines due to the Earth's atmosphere.

Regarding the polarimetric aspect of the observations, LibreESpRIT combines the exposures of the two orthogonal polarization states in order to obtain the polarized spectra (i.e. Stokes I = $I_\circlearrowright$ + $I_\circlearrowleft$ and Stokes V = $I_\circlearrowright$ - $I_\circlearrowleft$ - see Sect. 1.2.3 and 2.2). It also automatically finds and subtracts any continuum polarization by default, because ESPaDOnS and NARVAL are not optimized to measure it (see e.g. Silvester et al. 2012; Petit et al. 2014).

Additionally, LibreESpRIT normalizes the spectra to the continuum level. In the end, the pipeline produces 1D spectra (stored in a multicolumn `ascii` file) from 2D exposures. The spectra have error bars (on Stokes I and Stokes V) at each wavelength point. These error bars were propagated throughout the reduction process and originate from photon-counting statistics for each CCD pixel (see e.g. Wade et al. 2000; Silvester et al. 2012).

# 3

# Misalignment of the outer disk of DK Tau & a first look at its magnetic field using spectropolarimetry

$\mathcal{T}$HIS chapter is based on the following publication:

## 3.1 Introduction & observations

The current chapter presents the analysis of the average line-of-sight magnetic field of DK Tau (see Sect. 1.5), in both photospheric absorption lines and accretion-powered emission lines. In order to properly measure this, a method was developed to determine the value of veiling as a function of wavelength and to remove its effect from the absorption lines. During this study, inconsistencies regarding the inclination of the rotation axis of DK Tau were identified and are examined as well.

The data collected for this study consist of dual-epoch spectropolarimetric observations taken with ESPaDOnS and NARVAL, collected in 2010 and 2012. More details on the observations and instruments can be found in Chapter 2.

The following section details the analysis and results obtained regarding the stellar parameters, veiling and magnetic characterization. This analysis starts with the normalization of the spectra to the continuum level.

## 3.2 Analysis & results

### 3.2.1 Normalization to continuum level

Continuum normalization of spectra is important to obtain the precise determination of spectral line properties that are essential in a spectropolarimetric study, in particular to achieve a consistent determination of the stellar parameters (see Sect. 3.2.2), as well as the measurement and removal of the veiling (see Sect. 3.2.3). It is a method

that searches for the continuum points, then fits a polynomial through these points, and finally divides the spectrum by the polynomial.

The data from DK Tau were re-normalized to the continuum level, in addition to the LibreESpRIT automatic continuum normalization (see Sect. 2.3), as the automatic procedure is not tailored for stars that display emission lines and it did not properly adjust the continuum.

A spectrum normalizing script written by Folsom et al. (2016) was used for the re-normalization. It allows one to ignore emission lines, which is more appropriate for a cTTs such as DK Tau. In the script, the different orders (see Sect. 2.2), which have sizes of ∼20 nm, were treated individually. The degree of the polynomial that would better fit the continuum points in each order was selected. To determine the location of the continuum, the script ignores the emission and absorption lines by ignoring points above and below a certain threshold. The threshold is a multiple of the calculated average intensity of the whole spectrum. In the calculation of the average, exclusion zones were set to ignore the strong emission lines (e.g. the Balmer lines). In addition, the portion of wavelength below 420 nm was removed (the wavelength of the original data ranged from 370 to 1 050 nm), due to its poor quality: the extreme jitters were causing an aberrant average.

## 3.2.2   Determination of stellar parameters

The continuum-normalized high-resolution spectra of ESPaDOnS and NARVAL were exploited to extract the line-of-sight-projected equatorial rotational velocity ($v \sin i$) and the effective temperature ($T_{\text{eff}}$) of DK Tau.

A mean unpolarized (i.e. Stokes I) spectrum was first obtained by interpolating the four spectra with the least amount of veiling (these are the four spectra with deepest absorption lines) onto the same wavelength array and taking the average value. This was carried out in order to get a better signal to noise ratio of 136, whereas the individual night had a signal to noise ratio of 103 on average. In addition, even though the veiling changes from night to night (see e.g. Fig. 3.3 and Fig. 3.4), its value is not being determined at this point (see Sect. 3.2.3), so this does not affect the results. Furthermore, the line shapes may vary a bit because of, for instance, spots on the stellar surface, and therefore obtaining an average (over time) of several spectra is preferable because it will smooth out this effect.

The stellar parameters were fitted using the ZEEMAN spectrum synthesis program, developed by Landstreet (1988) and Wade et al. (2001) and modified by Folsom et al. (2016). The script solves radiative transfer equations under the assumption of local thermodynamic equilibrium. First a synthetic spectrum is produced using a MARCS stellar atmosphere model (see Gustafsson et al. 2008), picked from a grid,

and an atomic line list (see Sect. 3.2.4). The script then iteratively compares the synthetic spectrum with the observed one, by $\chi^2$ minimization, to determine free model parameters. Veiling ($R$) is included in the model.

Initial values for the stellar parameters were specified, using the ones provided in the literature: a $v \sin i$ of 12.7 km s$^{-1}$ (see e.g. McGinnis et al. 2020), a microturbulence velocity ($v_{\mathrm{mic}}$) of 1 km s$^{-1}$ (as is typically used for cTTs), a macroturbulence velocity ($v_{\mathrm{mac}}$) of 0 km s$^{-1}$ (set at zero due to the value being unknown), a $T_{\mathrm{eff}}$ of 4 000 K (see e.g. Herczeg and Hillenbrand 2014), a logarithmic surface gravity (log $g$) of 4 (in cgs units - as is typically used for cTTs), solar metallicity and a $R$ of 0.1.

First, $v \sin i$, $T_{\mathrm{eff}}$, log $g$ and $R$ were given the initial values mentioned above and selected as free parameters; while the other parameters were fixed (with the values mentioned above). The program was run on a small spectral range with many photospheric lines, in order to get an initial estimate of the free parameter values. Next, using those values as a starting point, the code was run only varying $v \sin i$ and $T_{\mathrm{eff}}$ as free parameters. This time, the spectrum was split in small bins of 10 nm (that ignored emission lines), and the script was operated on each bin individually. Each fit was checked visually to see if the features were well reproduced. When the lines were fitted well, the parameters values were written down.

As was expected, similar values were obtained for each spectral window. The average was subsequently calculated, and the standard deviation of the spread was used as the error bars. A $T_{\mathrm{eff}}$ of 4 150 ± 110 K and a $v \sin i$ of 13.0 ± 1.3 km s$^{-1}$ were obtained. The values are in good agreement with the ones found in the literature (see Herczeg and Hillenbrand 2014; McGinnis et al. 2020).

Next, P. McGinnis carried out the calculation of the stellar luminosity ($L_\star$) in the following manner: first by using the J-band magnitude of Eisner et al. (2007) corrected to remove the contribution of the binary[1], corrected for extinction with the value quoted by Herczeg and Hillenbrand (2014) and corrected for veiling (based on an interpolation of the measurements described in Sect. 3.2.3), then by using the bolometric correction in the J-band from Pecaut and Mamajek (2013), next by converting the magnitude into flux, and finally by deriving the luminosity from the flux (see Eq. 1.3.3). This yields a value of 1.65 ± 0.25 $L_\odot$.

Based on this value for $L_\star$, on the measured value for $T_{\mathrm{eff}}$ and using the Stefan-Boltzmann relation $R_\star^2 = L_\star / (4\pi \sigma_{\mathrm{SB}} T_{\mathrm{eff}}^4)$ with $\sigma_{\mathrm{SB}} = 5.67 \times 10^{-8}$ W m$^{-2}$ K$^{-4}$ the Stefan-Boltzmann constant (see Stefan 1879; Boltzmann 1884), the stellar radius ($R_\star$) was derived. A value of 2.48 ± 0.25 $R_\odot$ was obtained. This agrees with the value of 2.49 $R_\odot$ mentioned by Johns-Krull (2007).

---

[1] DK Tau is a wide binary and this work studies DK Tau A, called "DK Tau" for short throughout this thesis. In the observations used by Eisner et al. (2007), DK Tau A and DK Tau B are not spatially resolved.

Regarding the stellar mass ($M_\star$), Johns-Krull (2007) derive a value of $0.7\,M_\odot$ from PMS evolutionary tracks. When using the Siess et al. (2000) models[2], the values of $T_\mathrm{eff} = 4\,150\,\mathrm{K}$ and $L_\star = 1.65\,L_\odot$ mentioned previously give a slightly higher $M_\star$ than the one of $0.7\,M_\odot$, but it agrees with it within $2\sigma$ (see the gray rectangle in Fig. 3.1).
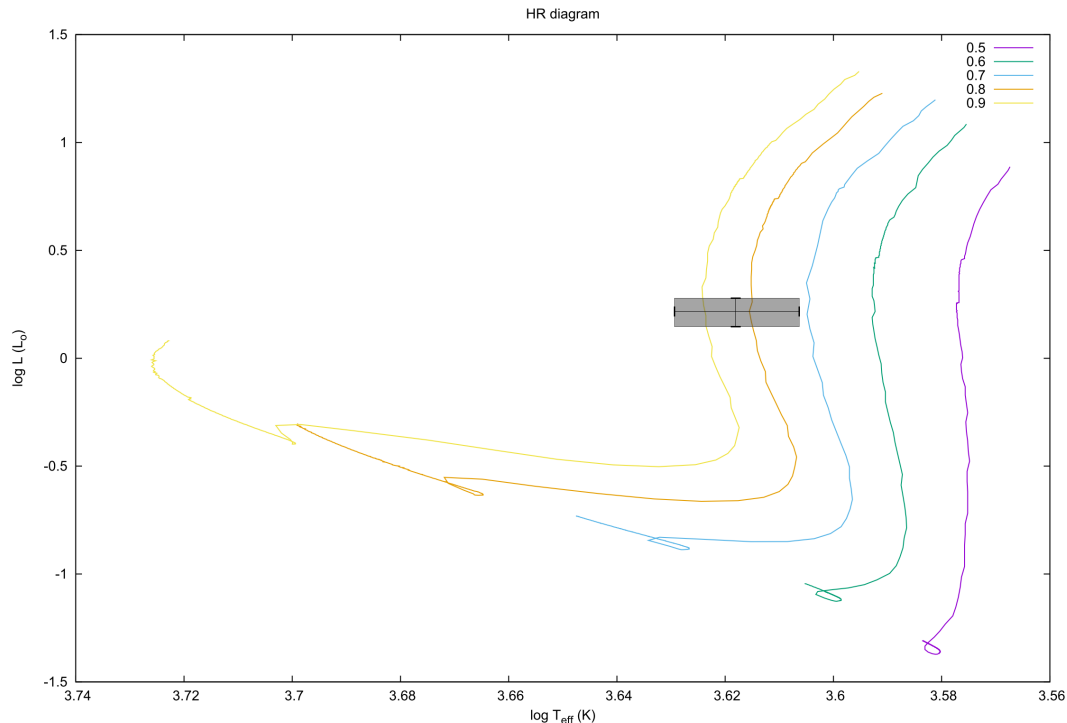


Figure 3.1 – Hertzsprung-Russell (HR) diagram with PMS evolutionary tracks from Siess et al. (2000). The colored lines correspond to different masses (in $M_\odot$). The gray rectangle highlights the values of $T_\mathrm{eff} = 4\,150\,\mathrm{K}$ and $L_\star = 1.65\,L_\odot$ with their error bars.

## 3.2.3   Measurement of veiling

Magnetic field measurement on cTTs, which are actively accreting, are hindered because of the effect of veiling on their spectra, which makes the lines shallower. Yet the study of these stars is very valuable from the perspective of accretion. Therefore, analyzing the magnetic field in active accretors is essential. This section provides a method to determine and remove the veiling from the spectra, in order to use magnetic field measurement techniques on an accreting star. In addition, the measurement of the veiling in itself yields important insights in the study of accretion (see Chapter 4).

The derivation of veiling from the spectrum of a cTTs consist in measuring the amount of excess continuum present. This is done by determining the underlying photospheric contribution, then identifying the amount of deviation displayed by the observed spectrum.

---

[2]http://www.astro.ulb.ac.be/~siess/pmwiki/pmwiki.php?n=WWWTools.PMS

**Photospheric template**

In order to extract the veiling in DK Tau, the spectrum of a wTTs was used as the photospheric template. Indeed, wTTs are believed to be physically similar to cTTs, with the exception that the former are no longer accreting, and therefore experience no veiling. By selecting a wTTs with characteristics that are comparable to the ones of the observed star, this wTTs can be seen as the purely photospheric version of the observed star. This procedure is more robust than using a synthetic spectra built from atmospheric models as a photospheric template, as they are usually based on main sequence stars that are more physically dissimilar to cTTs.

To be able to compare the high-resolution spectra of DK Tau with the spectrum of the wTTs, the latter needed to be an ESPaDOnS spectrum as well (to match the high-resolution of the spectrograph). Four potential candidates that were observed with ESPaDOnS were examined, namely LkCa4, LkCa7, TAP45 and V819 Tau. They all have (in the literature) the same spectral type (and hence the same $T_{\mathrm{eff}}$) as DK Tau (i.e. K7). They also are from the same star forming region, which implies that they would have the same chemical composition and very similar age and $\log g$. It can also be assumed that the $v_{\mathrm{mic}}$ and $v_{\mathrm{mac}}$ should be very similar. In addition, the candidates also have a $v \sin i$ lower than the $v \sin i$ of DK Tau. This is important because the code will need to artificially broaden the wTTs spectrum to match DK Tau; it cannot do so if the wTTs lines are already broader because of rotational broadening.

The candidates normalized spectra were downloaded from the PolarBase archive (see Sect. 2.1). They were re-normalized and the mean spectrum was calculated for each star. Indeed, as a wTTs spectrum should not vary significantly from night to night, this will only increase the signal to noise ratio, making it a better template than the spectrum from one individual night. Furthermore, since the shape of the absorption lines can vary (because of spots on the stellar surface), the mean spectrum will smooth out this effect.

Each of the mean wTTs spectra was then used as a template for the mean DK Tau spectrum, looking at four spectral windows (ones with several good photospheric lines), in order to see which wTTs worked best. The reason for this is that even though they supposedly have the same $T_{\mathrm{eff}}$, there might be small differences (and differences with $\log g$) that make one specific wTTs more suitable as a template for DK Tau. This also helps to avoid the use of a wTTs that could have been slightly misclassified in terms of spectral type. Ultimately, TAP45 (which has a $v \sin i$ of 11.5 km s$^{-1}$ - see Feigelson et al. 1987; Bouvier et al. 1993) was selected as the photospheric template.

**Derivation of veiling**

Using a script written by P. McGinnis, the absorption lines of TAP45 were first broadened to adjust for the stellar rotation of DK Tau. This rotational broadening is carried out by convolving the TAP45 spectrum by a Doppler rotational profile as described in Gray (2008). In addition, the code applies an extra continuum to the TAP45 spectrum to simulate veiling, in order to fit the veiled absorption lines of DK Tau at the lowest $\chi^2$ level. Figure 3.2 shows an example of the fitting of the rotationally broadened and artificially veiled TAP45 spectrum (in red) to the spectrum of DK Tau (in black), for one night in particular and one spectral window.
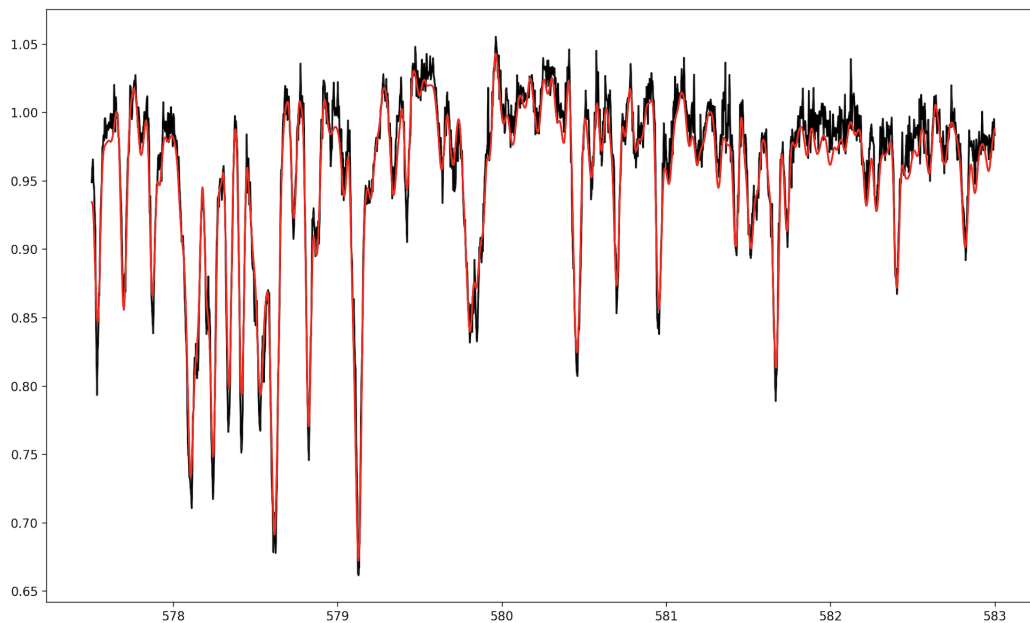


Figure 3.2 – Example of the derivation of veiling for one spectral window. The observed (and veiled) spectrum is in black. The rotationally broadened and artificially veiled template is in red. The x-axis represents the wavelengths in nm. The y-axis represents the intensity and is in arbitrary units.

Each normalized DK Tau spectrum was analyzed individually, and examined in bins of about 5 nm along the wavelength range, to acquire a value for veiling in each spectral window (excluding emission lines and telluric lines from the fit). The fit between the DK Tau spectra and the rotationally broadened and artificially veiled TAP45 mean spectrum was visually checked each time (to see if the absorption lines were well reproduced). The veiling values obtained were discarded when the fit was poor, i.e. when the $\chi^2$ was high and the particular point differed too much from the general trend. The window at 617.50 nm generally displayed the best fit between the observations and the photospheric template, it is thus used throughout this work to summarize the veiling for each night (see e.g. Fig. 3.5).

Once the value of the veiling as a function of wavelength was obtained, a linear relation was fitted through the points, using a least squares polynomial fit. This is the $R(\lambda)$ function and it was interpolated into the wavelength array of the spectrum. This

allows to study the variability of veiling for DK Tau, not only from night to night, but across the different spectra, which cover the optical range. Figures 3.3 and 3.4 show the veiling values (in gray) as a function of the wavelength, as well as the best fit (in blue), for the 2010 and 2012 observations. The standard deviation (of the spread of points compared to the fit) is used as the uncertainty of the fit (light blue shaded region).

For the 2010 epoch, the peak values of veiling (at ~550 nm) range from 0.2 to 1.8. For the 2012 epoch, the peak values range from 0.2 to 1.3 (lower than the values from two years before). For both epochs, the slope of the fit as a function of wavelength steepens when the peak values of veiling increase. Figure 3.5 shows the veiling at 617.50 nm folded in time with the stellar rotation phase. For the 2010 epoch, the veiling folds well with the stellar rotation phase, whereas for the 2012 epoch it does not. This probably stems from the accretion being more intrinsically variable in 2012. This variability of veiling is studied in more detail in Chapter 4.

**Removal of veiling**

For a normalized spectrum, the veiling can be expressed using the following equation:

$$I_{\text{veiled}}(\lambda) = [I_{\text{ph}}(\lambda) + R(\lambda)] \, N(\lambda) \tag{3.2.1}$$

with $I_{\text{veiled}}(\lambda)$ the veiled intensity at wavelength $\lambda$, $I_{\text{ph}}(\lambda)$ the intensity of the photosphere at wavelength $\lambda$, $R(\lambda)$ the veiling at wavelength $\lambda$ and $N(\lambda)$ a normalization constant at wavelength $\lambda$.

For a hypothetical star with no veiling, a normalized spectrum would have its continuum at 1. When $R$ is added to this spectrum, it is shifted upward, its continuum no longer at 1. Therefore, one must divide by $1 + R$ to reposition the continuum at 1:

$$N(\lambda) = 1/[1 + R(\lambda)] \tag{3.2.2}$$

Next, Eq. 3.2.1 is inverted into:

$$[1 + R(\lambda)] \, I_{\text{veiled}}(\lambda) - R(\lambda) = I_{\text{ph}}(\lambda) \tag{3.2.3}$$

Finally, Eq. 3.2.2 is applied on the Stokes I values in order to subtract the veiling.

With the veiling-corrected spectra, it is then possible to begin the analysis of the stellar magnetic field. This starts with obtaining LSD profiles (see Sect. 3.2.5). The next section describes the creation of the line mask needed to recover the LSD profiles.
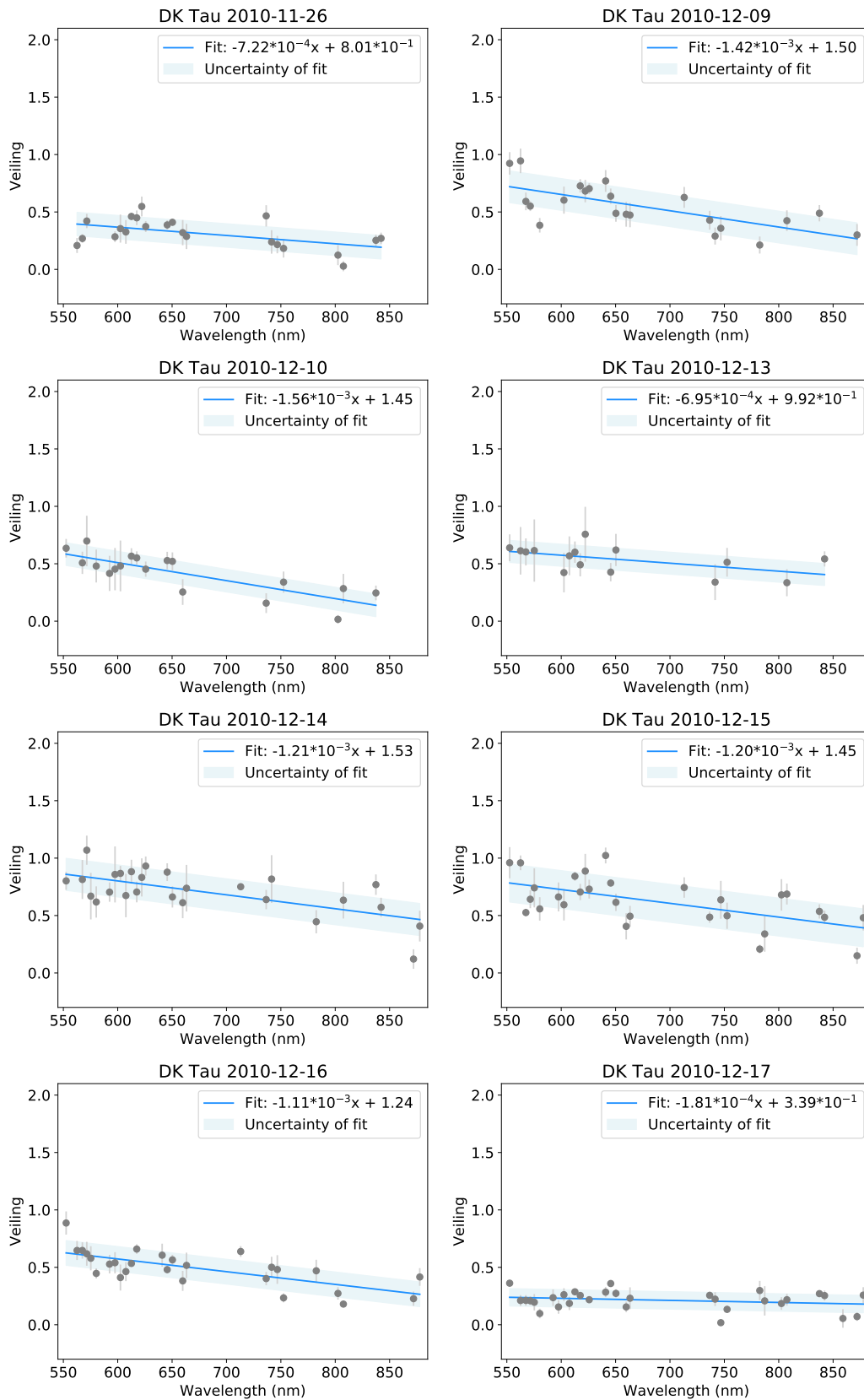
Figure 3.3 – Veiling (gray dots), the best linear fit (blue line) and the standard deviation (light blue shaded region) as a function of wavelength for the 2010 observations.
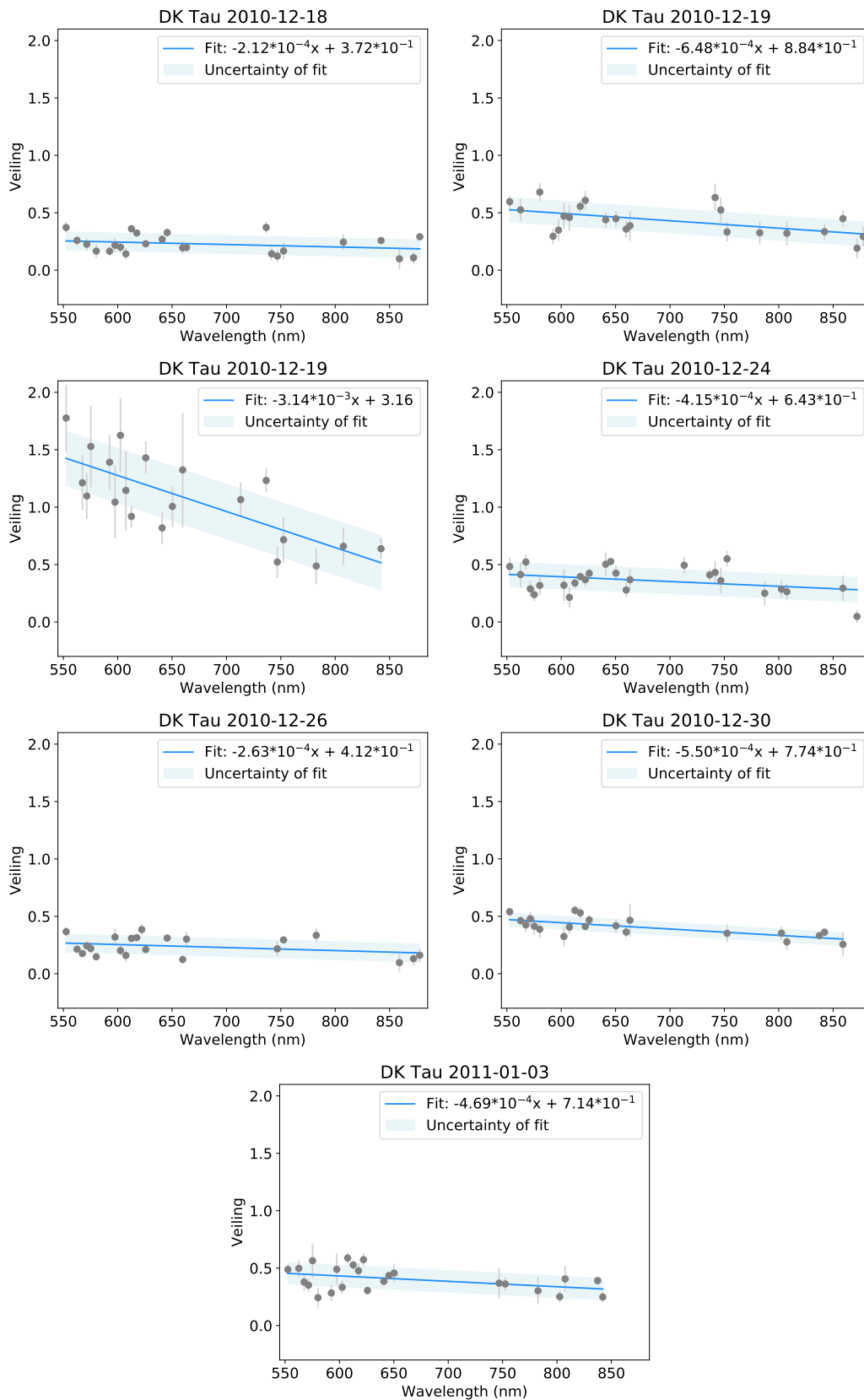
Figure 3.3 – continued.
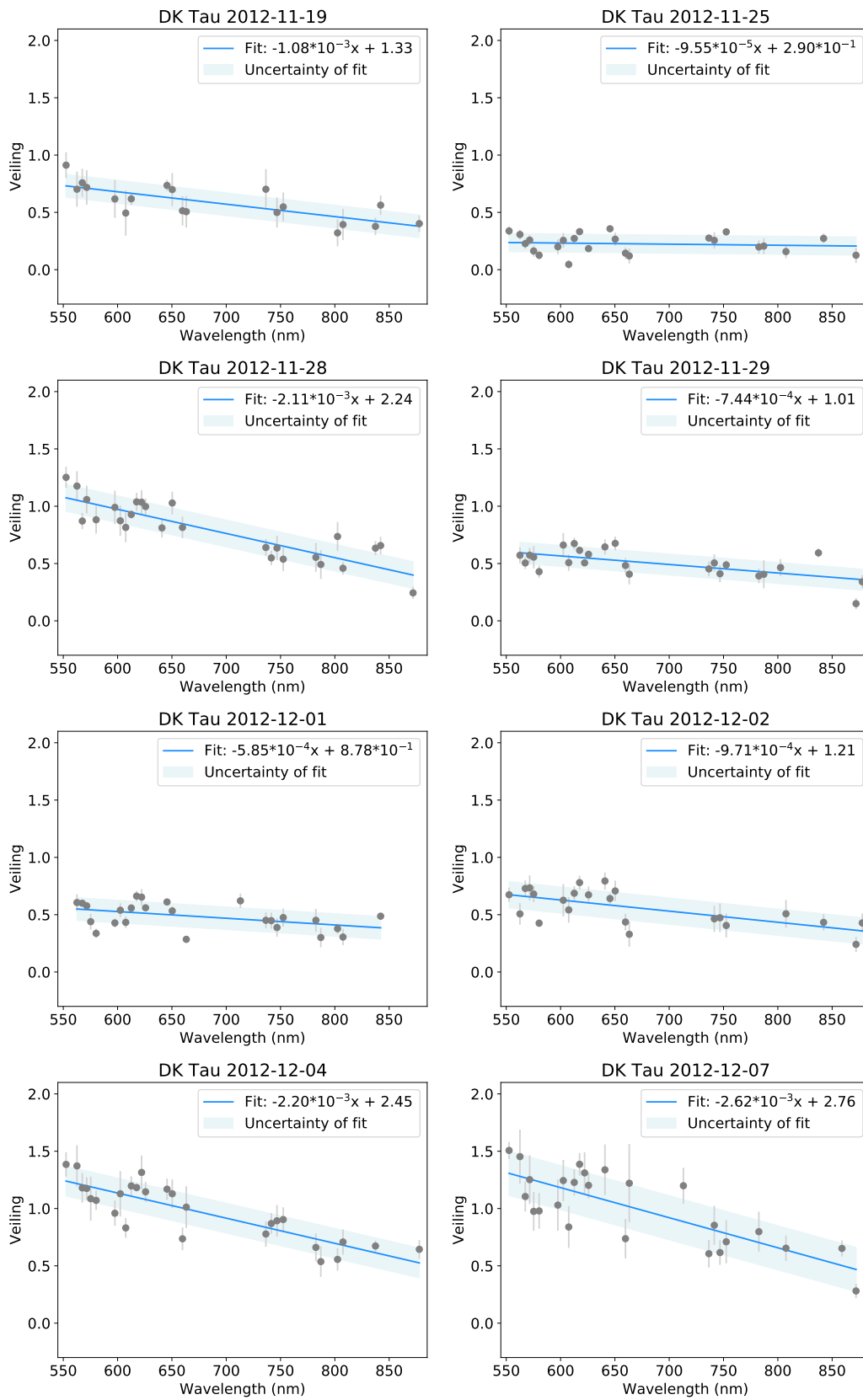
Figure 3.4 – Same as Fig. 3.3, for the 2012 observations.
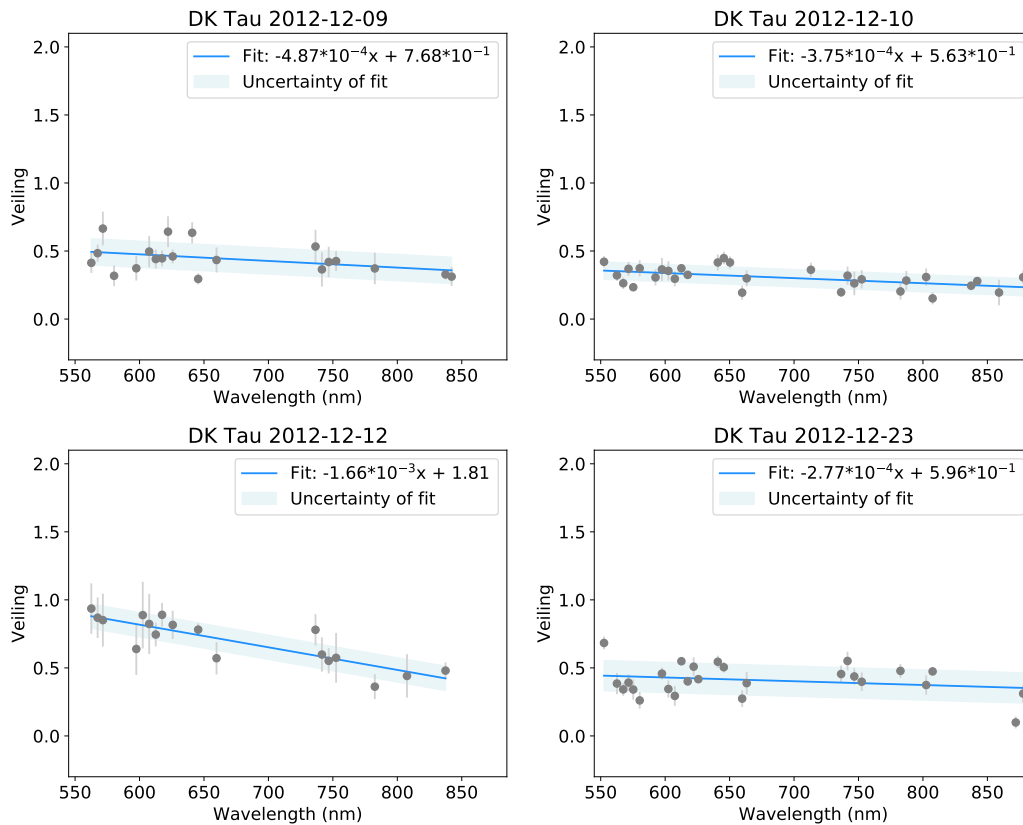
Figure 3.4 – continued.

### 3.2.4  Acquisition of line lists & creation of line mask

A line mask describes the position and depth of chosen lines, and in the case of Stokes V also the Landé factor. In practice, the mask is used to select only the lines that have to be analyzed in a spectrum. This allows one to ignore noisy regions, telluric lines and emission lines. Line masks were used to determine the stellar parameters (see Sect. 3.2.2) and to use LSD (see Sect. 3.2.5).

The first step to obtain a line mask is to acquire a continuous atomic line list. The Vienna Atomic Line Database (VALD) website[3] allows one to do just that (see Ryabchikova et al. 2015). On the VALD website, the appropriate wavelength range (for the observed data) and the desirable minimal line depth can be set. It is necessary to specify the properties of the targeted star: e.g. $v_{\mathrm{mic}}$, $T_{\mathrm{eff}}$, $\log g$, the chemical composition, etc. It is also possible to only select lines which have a non-zero Landé factor (and hence select only lines that are sensitive to the magnetic field).

In the case of DK Tau, the following properties were selected: a starting wavelength of 400 nm and an ending wavelength of 1 000 nm (based on the range of the spectra), a detection threshold of 0.01, a $v_{\mathrm{mic}}$ of 1 km s$^{-1}$ (as is typically used for cTTs), a $T_{\mathrm{eff}}$ of 4 000 K (see e.g. Herczeg and Hillenbrand 2014), a $\log g$ of 4 (in cgs units - as is typically used for cTTs) and a solar metallicity. For the line list ultimately

---

[3]http://vald.astro.uu.se
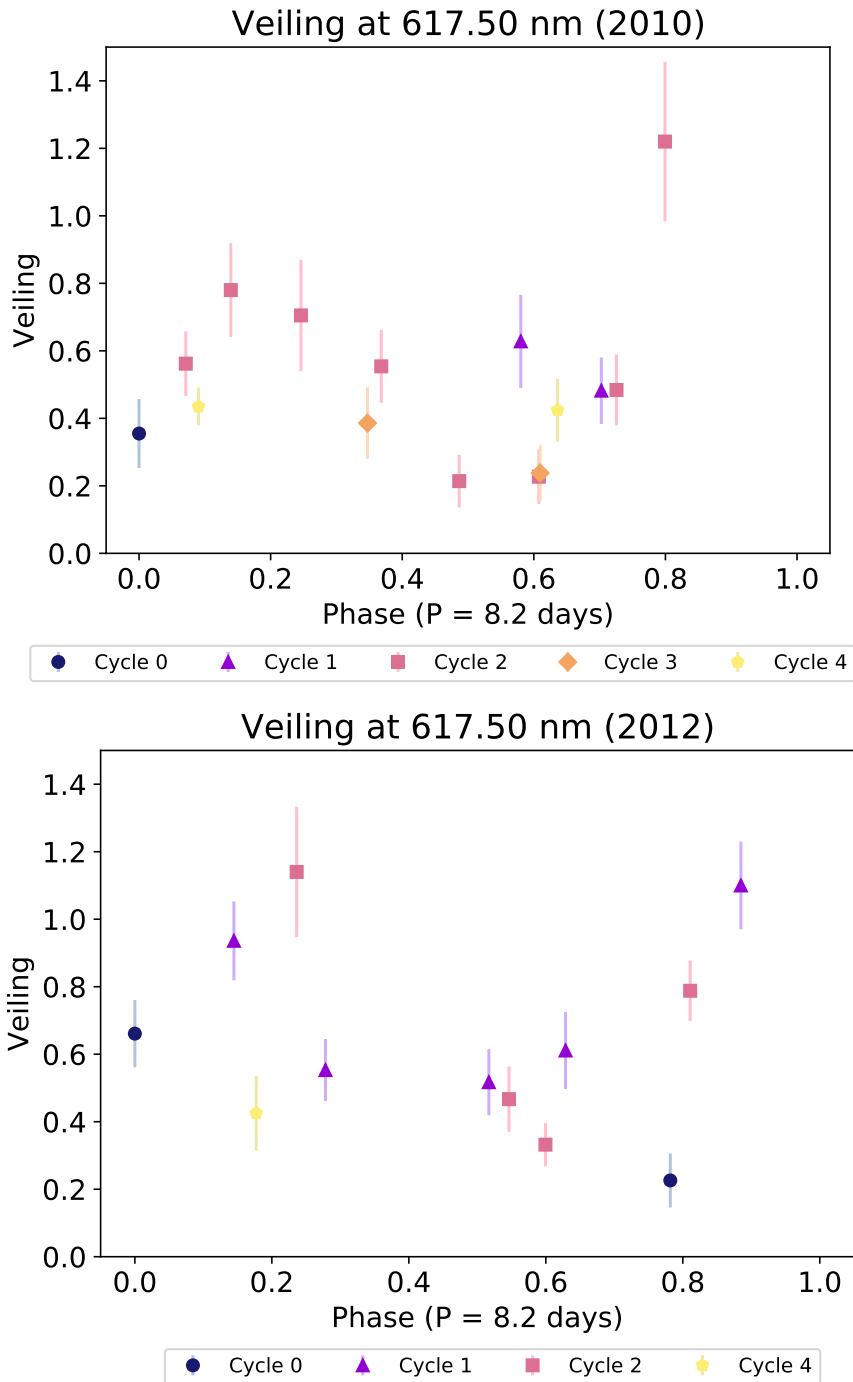
Figure 3.5 – Veiling at 617.50 nm over time, shown folded in phase with an 8.2 day period, for the 2010 (top panel) and 2012 observations (bottom panel). Different colors and symbols represent different rotation cycles.

used for LSD, lines with a non-zero Landé factor were selected, while for the line list used to obtain stellar parameters they were not.

Next, in the case of the line list intended for LSD, a line mask was created with a script written by J. Morin and using the VALD line list. This script assumes an ATLAS9 stellar atmosphere model (see Kurucz 1993) and allows one to ignore telluric and emission lines.

## 3.2.5 Recovering the LSD profiles of absorption lines

A spectrum can be viewed as the convolution of a line mask with the LSD profile (see Sect. 1.2.4). Here the goal is to recover the LSD profiles of the photospheric absorption lines, which means that the spectra need to be deconvolved by the line mask. The program used to obtain the LSD profiles was written by Donati et al. (1997). The selected wavelength range started at 500 nm and ended at 1 000 nm, excluding the blue edge of the spectra because of excess noise. The code allows to ignore parts of the spectrum, so regions with telluric and emission lines were excluded. The lines most affected by accretion were excluded as well. They were identified by comparing with the spectrum of RU Lup, a cTTs of the same spectral type as DK Tau but presenting with a higher mass accretion rate. Indeed, the spectrum of RU Lup has many lines in emission due to the stronger accretion. The lines that are in emission in the spectrum of RU Lup were chosen to be excluded, since they are clearly very sensitive to accretion (see Stock et al. 2022, for an example of the spectrum of RU Lup).

An LSD profile is normalized by three parameters: the equivalent Landé factor ($\overline{g}$), the equivalent line depth ($\overline{d}$) and the equivalent wavelength ($\overline{\lambda}$ - see e.g. Kochukhov et al. 2010). As they affect how the depth and amplitude of the Stokes I and Stokes V LSD profiles are scaled, for the magnetic field measurements to be correct, these parameters have to be representative of the lines that are used in the computations. $\overline{\lambda}$ is set to a value that roughly corresponds to the average wavelength of the lines in the mask, whereas the values of $\overline{g}$ and $\overline{d}$ are manually adjusted until the weights used to normalize Stokes I and Stokes V are both equal to one. These parameters are then used consistently in LSD and ZDI (See Sect 5.2.1). Ultimately, for DK Tau, the parameters were set to $\overline{g}$ = 1.41, $\overline{d}$ = 0.47 and $\overline{\lambda}$ = 650.0 nm for all the nights and LSD was applied to each veiling-corrected spectrum. The LSD profiles were then normalized to be at the same equivalent width. The latter was done in order to correct for the residual effects of veiling.

**Moonlight contamination**

The Stokes I LSD profiles of the ESPaDOnS and NARVAL observations made on 19 December 2010 presented a small absorption feature blueward of the main absorption line (see bottom panel in Fig. 3.6), while the other nights all showed a single photospheric absorption line. This small absorption feature is due to scattered moonlight. Indeed, the full Moon was close to DK Tau on that night (with an angular separation of $\sim 8°$). Furthermore, the contamination is at the expected lunar radial velocity in the heliocentric rest frame[4]. This type of contamination has been observed before (see e.g. Donati et al. 2011).
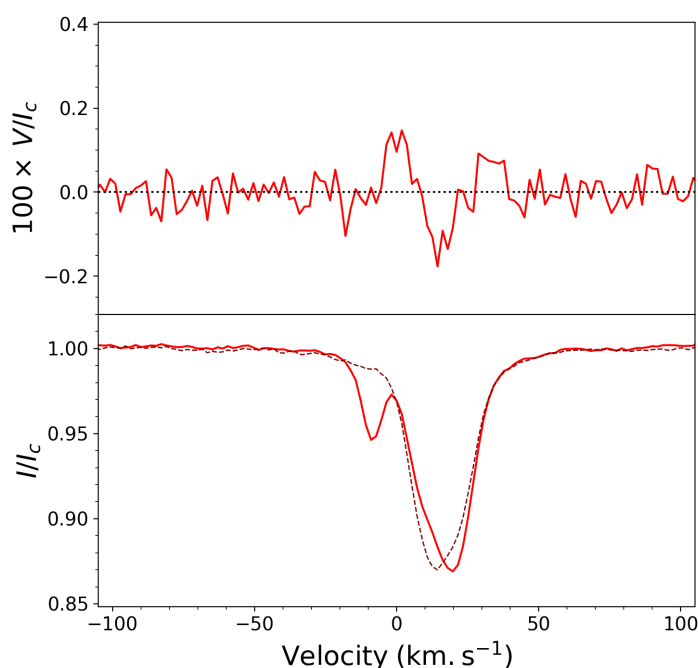


Figure 3.6 – LSD profile (in the heliocentric velocity frame) for the sixth night of the 2010 ESPaDOnS observations (red line). The top panel displays the Stokes V parameter and the bottom panel the Stokes I parameter, normalized to the continuum. On this night, scattered light from the Moon caused the small blueward absorption feature in Stokes I. For comparison, the Stokes I parameter of the seventh night of the 2010 ESPaDOnS observations (maroon dashed line), which did not suffer from moonlight contamination, is shown.

In order to manually remove the contamination, the wing of the main absorption feature was fitted with that of a Voigt profile. Figure 3.7 shows the LSD profiles of the photospheric absorption lines for the 2010 and 2012 epoch (in gray) and their averages (in red).

---

[4]The online applet at https://astroutils.astronomy.osu.edu/exofast/barycorr.html and based on Wright and Eastman (2014) can be used to calculate the correction to apply to geocentric observations in order to transpose them in the heliocentric rest frame. In this case, the correction is -8.8 km s$^{-1}$. Applied to the Moon's radial velocity of 0 km s$^{-1}$ in the geocentric rest frame, this translates into a radial velocity of -8.8 km s$^{-1}$ in the heliocentric rest frame.

Figure 3.7 – Stokes V and Stokes I profiles (in gray) and average (in red) of the photospheric absorption lines, for the 2010 (top panel) and 2012 (bottom panel) observations.

## 3.2.6 Calculation of the average line-of-sight magnetic field in absorption lines & determination of the stellar period

Magnetic fields are ubiquitous in star formation and play different important roles (see Sect. 1.2.1). Consequently, magnetic field studies are essential in order to further the current understanding of star formation. The large-scale magnetic fields associated with the non-accreting areas of the stellar surface are traced by the Stokes V parameters of photospheric absorption lines (see e.g. Donati et al. 2007). The average line-of-sight magnetic field ($B_{los}$ - see Sect. 1.2.5) linked to non-accreting regions was thus derived from the LSD profiles of photospheric absorption lines using Eq. 1.2.4. In comparison to a ZDI map (see Sect. 1.2.7), $B_{los}$ provides less information, but in return depends much less on stellar parameters (see Sect. 5.2.1).

In 2010, $B_{los}$ ranges from -0.19 ± 0.05 kG to 0.20 ± 0.03 kG. In 2012, it ranges from -0.13 ± 0.02 kG to 0.08 ± 0.02 kG. Table 3.1 lists the values of the $B_{los}$ for the photospheric absorption lines for both epochs. Figure 3.8 shows these values folded with the stellar rotation phase. It should be noted that, since $B_{los}$ represents a signed average over the visible stellar hemisphere, regions of opposite polarities partly cancel out.

**Determination of the stellar rotation period**

In order to determine the stellar rotation period, a phase dispersion minimization (PDM - see Stellingwerf 1978) technique was applied to the values of $B_{los}$ for the photospheric absorption lines for the 2010 epoch. This yielded a period of 8.20 ± 0.13 days. In essence, the PDM technique folds the observational points for a given period and measures the amount of jitters. This was done for periods ranging from 2 to 32 days, with bins of 0.1 days. The best fitting period is the one with the least amount of jitters. The error bars were calculated using a Monte Carlo method: each $B_{los}$ value was randomly varied within its error bars (assuming a gaussian distribution) and the PDM technique was applied each time. The standard deviation of the PDM results was then taken as the errors bars on the period.

As this is the period of the modulation of the stellar magnetic field, it accurately represents the stellar rotation period. In addition, it is consistent with values found in the literature and based on photometry: 8.4 days from Bouvier et al. (1993), and 8.18 days from Percy et al. (2010) and Artemenko et al. (2012). Small discrepancies could be explained by differential rotation: different measurements tracking features at various latitudes.

Figure 3.8 – $B_{\mathrm{los}}$ for the photospheric absorption lines over time, shown folded in phase with the derived 8.2 day period, for the 2010 (top panel) and 2012 (bottom panel) epochs. Different colors and symbols represent different rotation cycles.

Table 3.1 – $B_{los}$ for the photospheric absorption lines.

| Date (yyyy-mm-dd) | Rotation cycle (8.2 day period) | $B_{los}$ (G) |
|---|---|---|
| 2010-11-26 | 0.00 | -148.49 |
| 2010-12-09 | 1.58 | 131.92 |
| 2010-12-10 | 1.70 | 16.08 |
| 2010-12-13 | 2.07 | -185.01 |
| 2010-12-14 | 2.14 | -186.52 |
| 2010-12-15 | 2.25 | -90.83 |
| 2010-12-16 | 2.37 | 30.36 |
| 2010-12-17 | 2.49 | 205.23 |
| 2010-12-18 | 2.61 | 87.10 |
| 2010-12-19 | 2.73 | 31.08 |
| 2010-12-19 | 2.80 | 6.72 |
| 2010-12-24 | 3.35 | 10.11 |
| 2010-12-26 | 3.61 | 100.33 |
| 2010-12-30 | 4.09 | -148.73 |
| 2011-01-03 | 4.64 | 93.22 |
| 2012-11-19 | 0.00 | -29.55 |
| 2012-11-25 | 0.78 | -124.88 |
| 2012-11-28 | 1.15 | -17.76 |
| 2012-11-29 | 1.28 | 81.99 |
| 2012-12-01 | 1.52 | -15.75 |
| 2012-12-02 | 1.63 | -78.84 |
| 2012-12-04 | 1.89 | -74.67 |
| 2012-12-07 | 2.24 | -5.17 |
| 2012-12-09 | 2.55 | -87.57 |
| 2012-12-10 | 2.60 | -102.34 |
| 2012-12-12 | 2.81 | -35.25 |
| 2012-12-23 | 4.18 | 26.34 |

### 3.2.7 Study of accretion-powered emission lines

After analyzing the photospheric absorption lines, emission lines associated with accretion shocks were also investigated, in particular the narrow component of the 587.6 nm He$\iota$ line and of the Ca$\iota\iota$ infrared triplet (IRT - at 849.8 nm, 854.2 nm and 866.2 nm). Since they are tracers of the fields present at the footpoints of accretion columns (see e.g. Johns-Krull et al. 1999; Donati et al. 2007), they can be used to get more information on the magnetic field. These lines are known to have various components (see e.g. Beristain et al. 2001; McGinnis et al. 2020), often containing a narrow component (NC), which originates from the accretion shock, and a much broader component (or components), which presumably forms farther out in the accretion columns or in outflows.

P. McGinnis carried out the preparation of the lines by fitting them with two or more Gaussians to isolate the NC (by subtracting the other components), then by averaging

the three NCs of the Ca$_{II}$ lines into a single LSD-like profile. This was done in order to increase the signal to noise ratio, as it has been done in other studies (see e.g. Donati et al. 2007, 2008, 2012).

Figures 3.9 and 3.10 show the Stokes I and Stokes V profiles of the He$_I$ emission line and the Ca$_{II}$ IRT, for the 2010 and 2012 epochs. The various nights are represented in gray, while the averages are shown in red. The Stokes V profiles of the emission lines show similar signatures with phase. This indicates that the accretion spots are mostly likely located at a high enough latitude to be visible with the same polarity at all times.

**Calculation of the average line-of-sight magnetic field in emission lines**

The average line-of-sight magnetic field ($B_{\text{los}}$ - see Sect. 1.2.5) was measured in the accretion-powered emission lines using Eq. 1.2.4. This allows one to recreate a picture of the component of the stellar magnetic field that dominates the accretion process. For the He$_I$ line, $B_{\text{los}}$ ranges from $0.20 \pm 0.51$ kG to $1.77 \pm 0.08$ kG in 2010, and from $0.48 \pm 0.09$ kG to $1.99 \pm 0.09$ kG in 2012. For the Ca$_{II}$ IRT, $B_{\text{los}}$ ranges from $0.34 \pm 0.04$ kG to $0.95 \pm 0.02$ kG in 2010, and from $0.26 \pm 0.02$ kG to $1.41 \pm 0.05$ kG in 2012. Table 3.2 lists the values of $B_{\text{los}}$ for the emission lines for both epochs. Figures 3.11 and 3.12 shows these values folded in phase, for the He$_I$ line and the Ca$_{II}$ IRT respectively.

For both the He$_I$ line and the Ca$_{II}$ IRT, the peak values of $B_{\text{los}}$ are higher in 2012. The values measured through the Ca$_{II}$ IRT are lower than the ones measured through the He$_I$ line. While the He$_I$ line is believed to be generated at the base of the accretion column, the Ca$_{II}$ IRT is thought to probe both the accretion region and the non-accreting chromosphere. The lower values of $B_{\text{los}}$ for the Ca$_{II}$ IRT could stem from the dilution of the emission from the accretion shock by chromospheric emission (see e.g. Donati et al. 2010, 2019), resulting in the Stokes V and Stokes I profiles being shallower for the Ca$_{II}$ IRT than for the He$_I$ line.

The peak values of $B_{\text{los}}$ in the emission lines are one order of magnitude larger than the peak values of $B_{\text{los}}$ derived from the LSD profiles of the photospheric absorption lines (see Fig. 3.8), showing strong fields in the accretion shocks. This is consistent with the current magnetospheric accretion paradigm, in which the accretion shocks are compact regions with some of the strongest magnetic fields. In addition, this is consistent with the values measured for other cTTs (see e.g. Donati et al. 2007, 2008), where the $B_{\text{los}}$ from accreting regions usually reach several kG, whereas the $B_{\text{los}}$ linked to non-accreting areas only reach a few hundred G. This is believed to be related to the magnetic geometry: accreting regions would display a simple magnetic geometry; while non-accreting photospheric magnetic fields would display a geom-
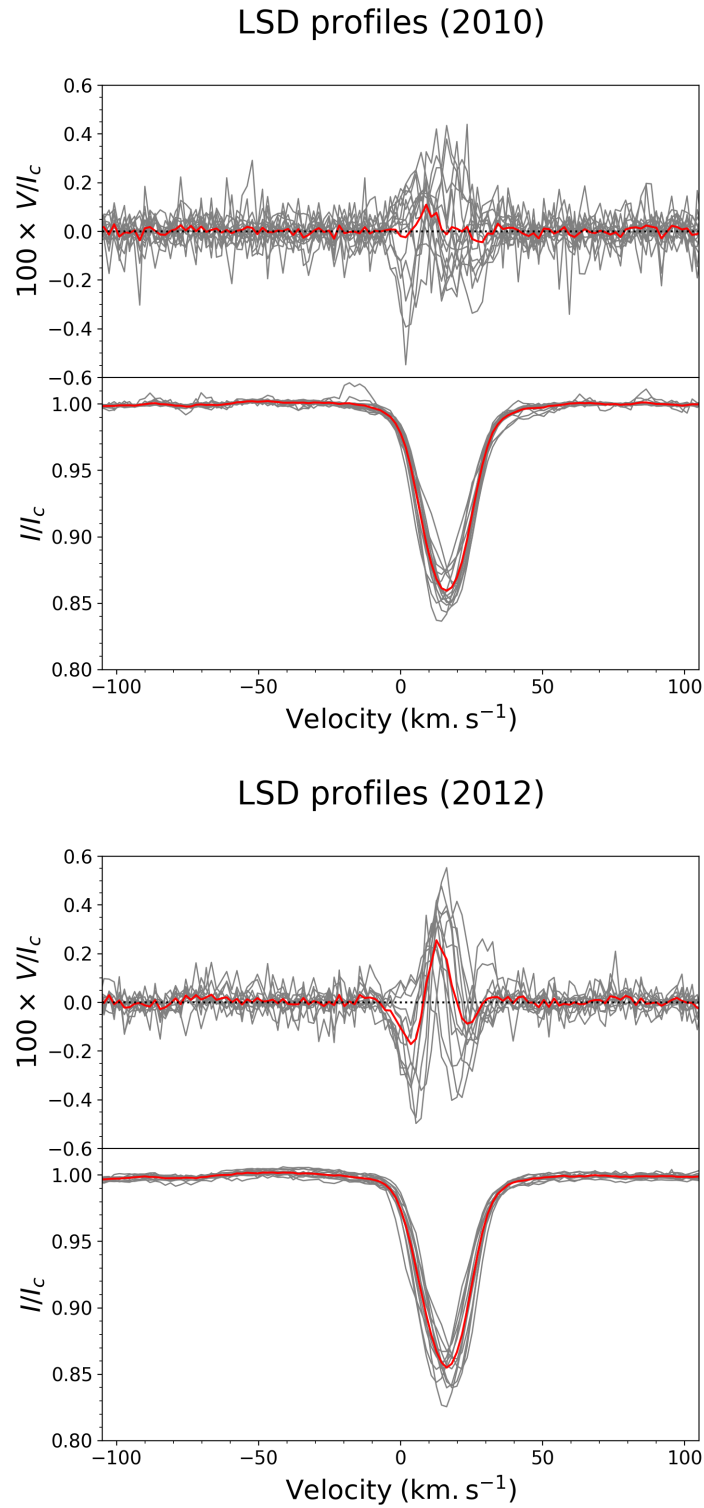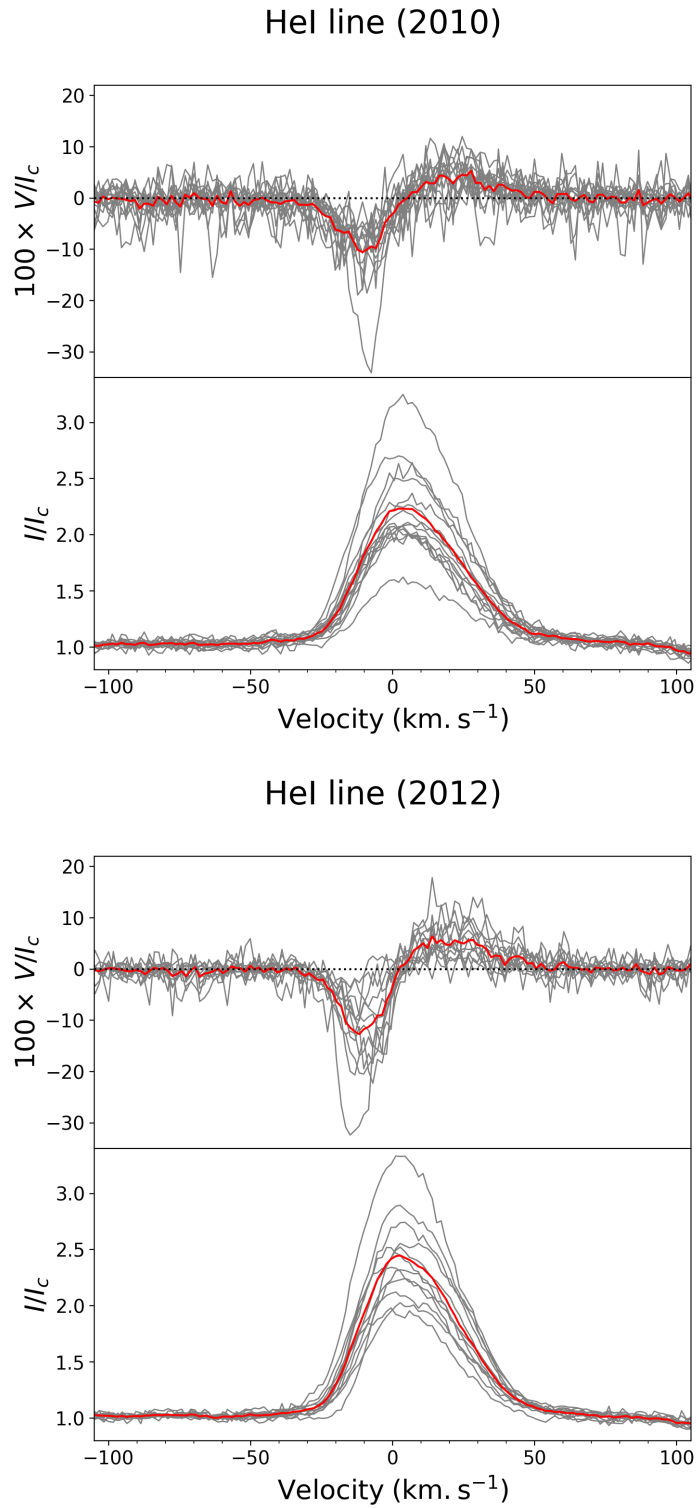
Figure 3.9 – Stokes V and Stokes I profiles (in gray) and average (in red) of the Heɪ emission line, for the 2010 (top panels) and 2012 (bottom panels) observations.
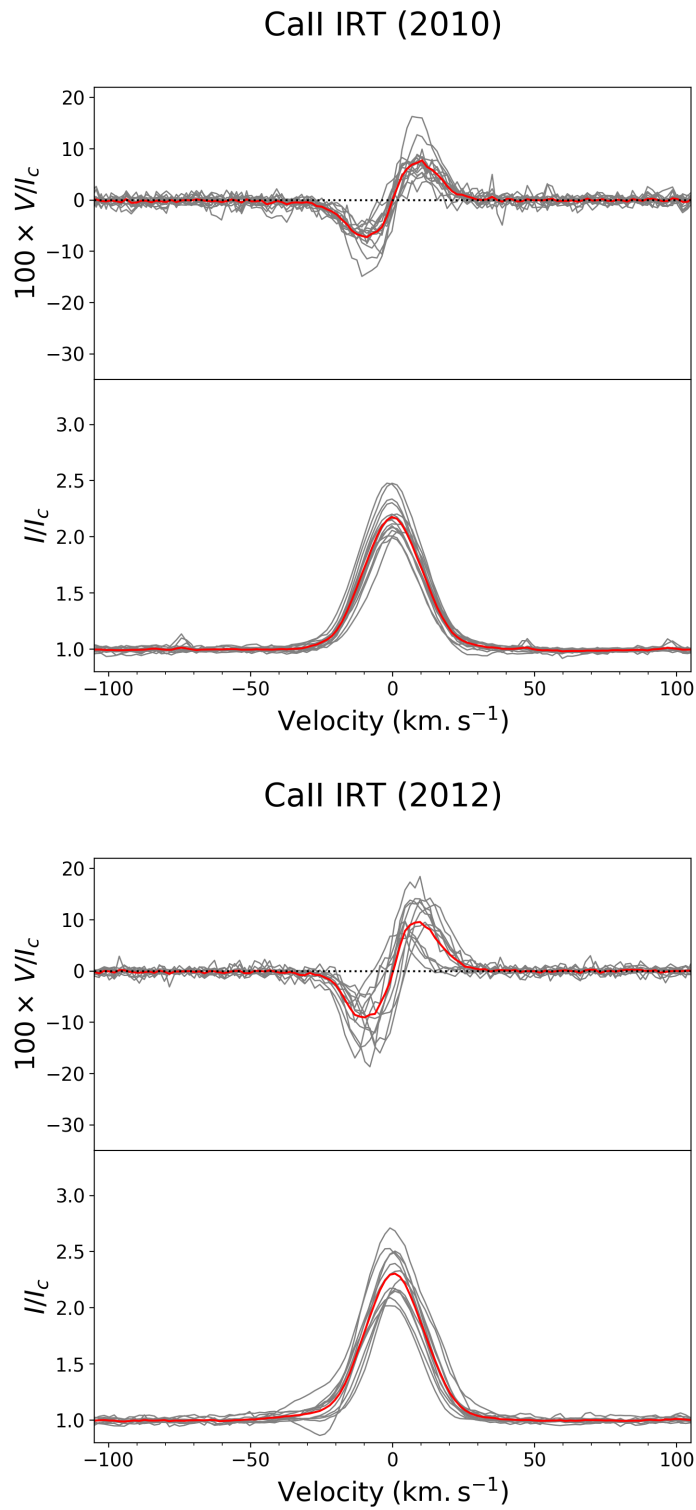
Figure 3.10 – Same as Fig. 3.9, for the Ca II IRT.
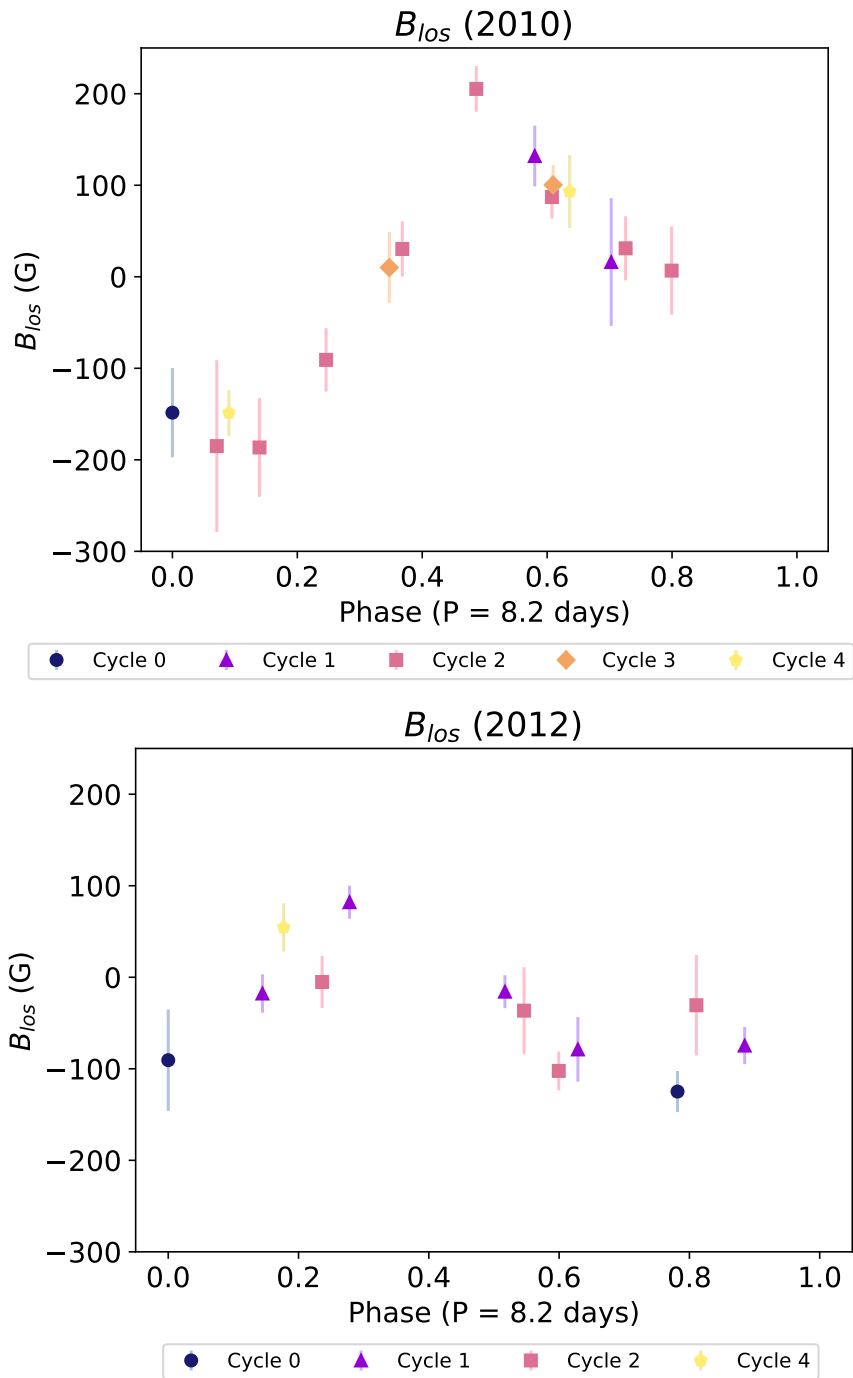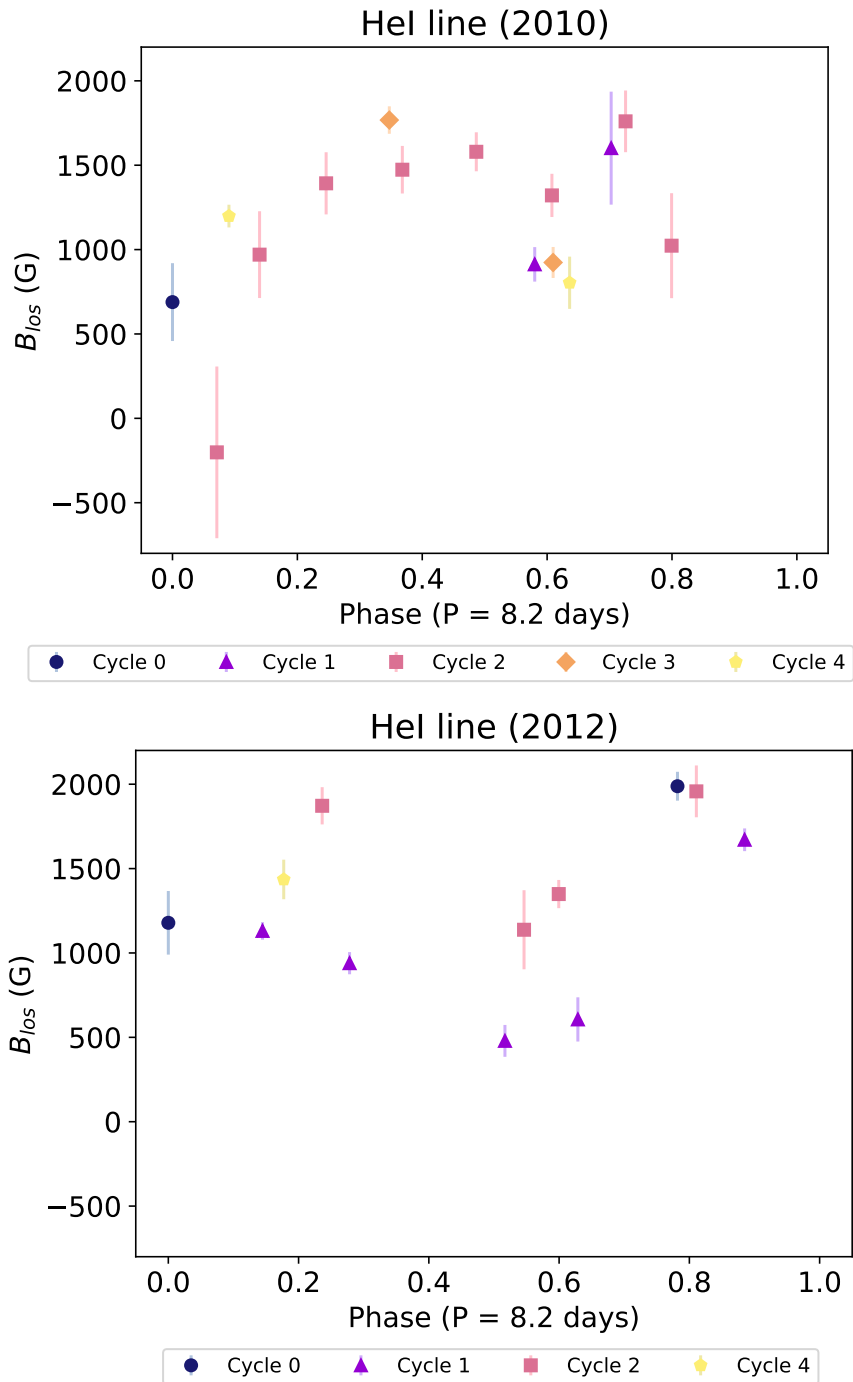
Figure 3.11 – $B_{los}$ for the HeI line over time, shown folded in phase with an 8.2 day period, for the 2010 (top panel) and 2012 (bottom panel) epochs. Different colors and symbols represent different rotation cycles.
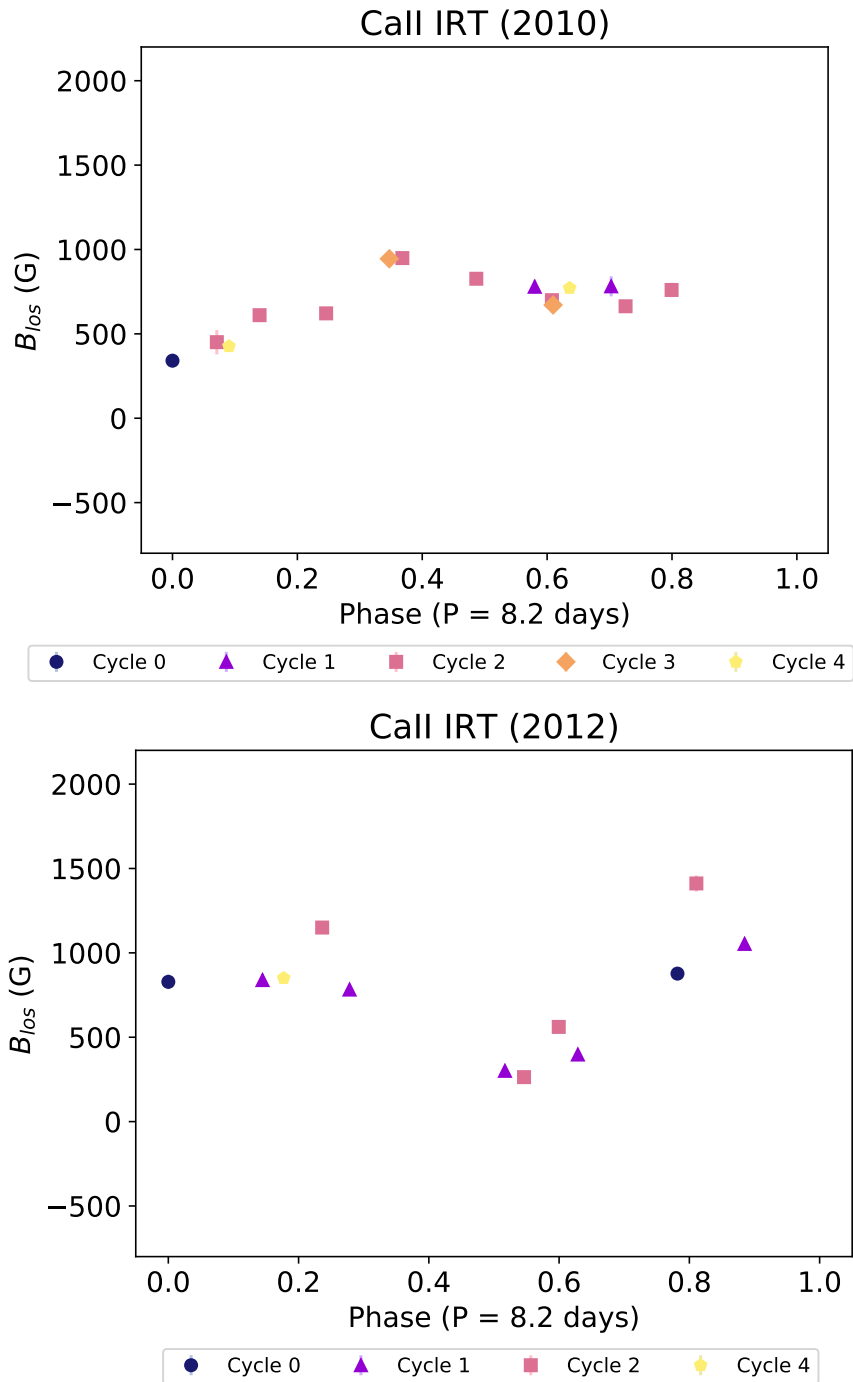
Figure 3.12 – Same as Fig. 3.11, for the Caɪɪ IRT.

Table 3.2 – $B_{los}$ for the accretion-powered emission lines.

| Date (yyyy-mm-dd) | Rotation cycle (8.2 day period) | $B_{los}$ for He I (G) | $B_{los}$ for Ca II (G) |
|---|---|---|---|
| 2010-11-26 | 0.00 | 688.77 | 341.07 |
| 2010-12-09 | 1.58 | 912.45 | 778.92 |
| 2010-12-10 | 1.70 | 1601.15 | 781.50 |
| 2010-12-13 | 2.07 | -201.64 | 450.74 |
| 2010-12-14 | 2.14 | 970.06 | 610.67 |
| 2010-12-15 | 2.25 | 1392.66 | 621.40 |
| 2010-12-16 | 2.37 | 1473.35 | 949.06 |
| 2010-12-17 | 2.49 | 1579.56 | 826.53 |
| 2010-12-18 | 2.61 | 1321.08 | 699.57 |
| 2010-12-19 | 2.73 | 1759.99 | 663.43 |
| 2010-12-19 | 2.80 | 1023.12 | 760.05 |
| 2010-12-24 | 3.35 | 1767.61 | 944.87 |
| 2010-12-26 | 3.61 | 923.56 | 671.05 |
| 2010-12-30 | 4.09 | 1198.59 | 426.48 |
| 2011-01-03 | 4.64 | 803.45 | 771.46 |
| 2012-11-19 | 0.00 | 1957.62 | 1411.28 |
| 2012-11-25 | 0.78 | 1988.06 | 876.93 |
| 2012-11-28 | 1.15 | 1130.63 | 838.51 |
| 2012-11-29 | 1.28 | 939.35 | 782.20 |
| 2012-12-01 | 1.52 | 479.01 | 300.70 |
| 2012-12-02 | 1.63 | 606.14 | 397.38 |
| 2012-12-04 | 1.89 | 1670.70 | 1052.93 |
| 2012-12-07 | 2.24 | 1872.10 | 1149.95 |
| 2012-12-09 | 2.55 | 1178.70 | 828.18 |
| 2012-12-10 | 2.60 | 1349.05 | 561.12 |
| 2012-12-12 | 2.81 | 1137.52 | 263.62 |
| 2012-12-23 | 4.18 | 1435.56 | 850.50 |

etry that is tangled (which leads to cancelation effects) and more complex than a dipole, with often a strong octupole component (see Donati and Landstreet 2009).

The values of $B_{los}$ in the emission lines in 2012 do not fold well in phase. This may be due to the location of the accretion shocks being more dynamic and/or the accretion being more complex, with more than one accretion shock. This is also observed in the variability of veiling in 2012 (see Fig. 3.5), which does not fold well with the stellar rotation phase.

## 3.2.8  Measurement of the magnetic obliquity

Using Eq. 1.2.5, an inclination $i$ of 58° (see Sect. 3.3.1) and the extreme values found for $B_{los}$ in the accretion-powered emission lines (see Sect. 3.2.7), an estimate of the magnetic obliquity ($\beta$ - see Sect. 1.2.6) was calculated. This equation assume a pure dipole, a simplification of the magnetic field present in the accretion shocks. The

estimate is not the magnetic obliquity of the entirety of DK Tau's magnetic field, as it is based solely on the average line-of-sight magnetic field present in the accretion shocks. In addition, the calculation uses the extreme values for $B_{los}$ and does not account for variability between nights. The magnetic obliquity was calculated using the accretion-powered emission lines because it is assumed that the magnetic field present in the accretion shocks is the one that reaches the circumstellar disk. Thus, the derived magnetic obliquity can be seen as an acceptable reflection of the real dipole present above the stellar surface. For the He I line, $\beta$ = 26° in 2010 and 21° in 2012. For the Ca II IRT, $\beta$ = 16° in 2010 and 23° in 2012. These estimates are consistent with the Stokes V signatures of the emission lines (see Sect. 3.2.7), confirming that DK Tau experiences nearly poleward accretion.

These estimates are also consistent with the magnetic obliquity of 18° (+8)(-7) derived by McGinnis et al. (2020) for DK Tau in 2011, using the radial velocity variability of the He I line and assuming one accretion spot. There is thus an agreement between the values derived from the magnetic field that drives the accretion and the value derived from a result of accretion.

### 3.2.9 Truncation & co-rotation radii

The values of $B_{los}$ in the emission lines can also help in estimating the location of the truncation radius (see Sect. 1.4.1). In order to calculate the values of this radius, several quantities are needed. First, the stellar mass accretion rate (see Sect. 1.3.4) was calculated. For this, the equivalent width (EW) of several emission lines was measured. These lines were H$\alpha$, H$\beta$, H$\gamma$, the He I lines at 447.1 nm, 667.8 nm and 706.5 nm, as well as the Ca II IRT at 849.8 nm, 854.2 nm and 866.2 nm. The EW were subsequently corrected for veiling using Eq. 1.3.5. As the ESPaDOnS and NARVAL spectra are not flux-calibrated, the EW were flux-calibrated using a photospheric template and Eq. 1.3.4, resulting in line fluxes.

The photospheric template was created using a script written by P. McGinnis (based on a code originally written by W. Landsman). The template is based on a VLT/X-shooter spectrum of SO879, a wTTs with a K7 spectral type (see Stelzer et al. 2013). The code first corrects the spectrum for extinction, using the reddening curve from Cardelli et al. (1989), with the update from O'Donnell (1994). The script then scales the wTTs spectrum to have the same luminosity (i.e. 1.65 $L_\odot$ - see Nelissen et al. 2023a) and be at the same distance (i.e. 132.6 pc - see e.g. Gaia Collaboration et al. 2016, 2018, 2022) as DK Tau. Finally, it extracts the continuum by removing absorption and emission lines in the same manner as the spectrum normalizing script written by Folsom et al. (2016) (see Sect. 3.2.1).

To clarify, when measuring the values of veiling (see Sect. 3.2.3), an ESPaDOnS

spectrum of the wTTs TAP45 was used because of its high resolution. As ESPaDOnS spectra are not flux-calibrated, that spectrum could not be used to extract the photospheric continuum of DK Tau. Conversely, the X-shooter spectrum of SO879 could not be used to derive the veiling because of its lower resolution. In the absence of an appropriate wTTs spectrum to use as a template in both circumstances, both TAP45 (for the determination of veiling only) and SO879 (for the determination of the accretion luminosity only) were used in this work.

After obtaining the line fluxes, the luminosity in each line was derived using Eq. 1.3.3. Next, the relations in Table B.1. from Alcalá et al. (2017) were used to calculate the accretion luminosity in each line (see Eq. 1.3.2). The obtained values were subsequently averaged for each night. The average over all nights in each epoch was then taken as the accretion luminosity, and the standard deviation of the spread in the values found from different nights were taken as the error bars. This yields $L_{acc} = 0.26 \pm 0.18\,L_\odot$ for the 2010 epoch and $L_{acc} = 0.49 \pm 0.42\,L_\odot$ for the 2012 epoch. These values are similar, within the error bars, to the ones found for instance by Fischer et al. (2011) (i.e. $0.17\,L_\odot$) or by Fang et al. (2018) (i.e. $0.16\,L_\odot$).

Using Eq. 8 from Gullbring et al. (1998), the accretion luminosity was then converted into mass accretion rate (see Eq. 1.3.1). For this, the values of $R_\star = 2.48\,R_\odot$ (see Sect. 3.2.2), $M_\star = 0.7\,M_\odot$ (see Johns-Krull 2007), and $R_{in} = 5\,R_\star$ (as is typically used) were adopted. This yields $\log(\dot{M}_{acc}[M_\odot\,yr^{-1}]) = -7.43$ in 2010, and $\log(\dot{M}_{acc}[M_\odot\,yr^{-1}]) = -7.15$ in 2012. These values are consistent with the one of $-7.42$ quoted by Gullbring et al. (1998).

Next, Eq. 6 from Bessolaz et al. (2008) was used to estimate the truncation radius (see Eq. 1.4.1). This equation assumes an axisymmetric dipole, which is a simplification of the magnetic topology of DK Tau. It also uses the dipolar field calculated at the equator as $B_{eq}$. Considering the equatorial value is half of the value at the pole, the latter was estimated using the extreme values of $B_{los}$ (see Preston 1967) in the emission lines. This is an approximation, as part of the $B_{los}$ could come from higher order multipoles, in particular from the octupole, rather than the dipole. The magnetic field derived from the accretion-powered emission lines was used considering it will dominate over the magnetic field derived from the photospheric absorption lines at the distance of the truncation radius. The estimated values for the truncation radius are $r_{trunc} \sim 5.2 \pm 1.1\,R_\star$ for the He I emission line in 2010, $r_{trunc} \sim 3.9 \pm 0.8\,R_\star$ for the Ca II IRT in 2010, $r_{trunc} \sim 4.7 \pm 1.2\,R_\star$ for the He I emission line in 2012, and $r_{trunc} \sim 3.9 \pm 1.0\,R_\star$ for the Ca II IRT in 2012. The estimates are lower when using the Ca II IRT. This stems from the lower values found for $B_{los}$ in those lines (see Sect. 3.2.7).

The co-rotation radius was calculated as well, using Kepler's third law (see Sect. 1.4.2), with $M_\star = 0.7\,M_\odot$ (see Johns-Krull 2007) and $P = 8.2$ days (see Sect. 3.2.6). This yields $r_{co\text{-}rot} = 6.1\,R_\star$.

It is found that the truncation radius estimates are consistent with the co-rotation radius value. This implies that DK Tau is unlikely to be in the propeller regime (see Sect. 1.3.2 and 1.4.1), an unstable accretion regime, as the truncation radius is not farther than the co-rotation radius (see Romanova et al. 2018).

For the 2010 epoch, DK Tau may be in the stable accretion accretion regime, since the $B_{\mathrm{los}}$ and veiling seem fairly periodic. The truncation radius being slightly smaller than the co-rotation radius is consistent with this as well (see e.g. Romanova and Owocki 2015; Blinova et al. 2016).

## 3.3 Discussion

In this section, two points in particular will be discussed. The first one concerns inconsistencies regarding the inclination of the stellar rotation axis when using the value for the inclination of the outer disk axis. The second one relates to the description of the magnetic field derived from the accretion-powered emission lines.

### 3.3.1 Inconsistencies regarding the rotation axis inclination

One might assume that the inclination angle $i$ of the stellar rotation axis with respect to the line-of-sight is 21° based on the inclination of the outer disk axis (see Rota et al. 2022). Yet DK Tau's lightcurve classifies the star as a dipper (see Roggero et al. 2021). The traditional explanation invokes circumstellar material passing in front of the star and occulting it (see Sect. 1.4.2). If the disk is seen close to edge-on, matter lifted above the disk plane could cause these occultations. However, DK Tau's outer disk is seen nearly pole-on, which is inconsistent with this scenario, unless the stellar rotation axis is at a very different angle than that of the outer disk axis. Moreover, based on the stellar rotational properties derived in this chapter (i.e. $P = 8.20 \pm 0.13\,\mathrm{days}$, $v \sin i = 13.0 \pm 1.3\,\mathrm{km\,s^{-1}}$, $R_\star = 2.48 \pm 0.25\,R_\odot$) and using the following relation

$$v \sin i = \frac{2\pi R_\star}{P} \sin i \qquad (3.3.1)$$

a much higher rotation axis inclination of i = 58° (+18)(-11) is derived. Consequently, if DK Tau is in fact seen nearly pole-on with a rotation axis inclination of i = 21°, then $P$, $v \sin i$ and $R_\star$ are not consistent with each other. The accuracy of each one of these parameters therefore needs to be investigated.

It is possible that the stellar radius may have been underestimated, as it is the most uncertain of these parameters. This is because it depends on an accurate determination of the effective temperature and stellar luminosity. Both can be subject to fairly large uncertainties, particularly the luminosity for a star with a dipper lightcurve

which likely suffers from variable extinction. However, when considering that $P$, $v \sin i$ and $i$ are accurately determined, then it is required that $R_\star = 6 \pm 1 \, R_\odot$ for this formula to agree, which is unrealistically large for a TTs.

Another possibility is that the period or $v \sin i$ may be inaccurate. Regarding $v \sin i$, the measured value agrees within error bars with the one derived by McGinnis et al. (2020), despite using two different assessment methods. It is therefore a value that can be trusted. This leaves the stellar rotation period.

In the literature, the stellar rotation period of DK Tau has been measured using photometry with values ranging from 8.18 days (see Percy et al. 2010; Artemenko et al. 2012) to 8.4 days (see Bouvier et al. 1993). However, since the photometry is dominated by flux dips that might be due to extinction events (Roggero et al. 2021), it is possible that these dips are caused by circumstellar material that is not located at the co-rotation radius. In that case, the measured period would not be the same as the stellar rotation period.

In Sect. 3.2.6, the period was derived from the rotational modulation of the average line-of-sight magnetic field in absorption lines, which should accurately represent the stellar rotation period. In the context of exoplanet search programs, $B_{los}$ is indeed often considered as the most reliable indicator of stellar rotation period (see e.g. Hébrard et al. 2016). Additionally, the value of $8.20 \pm 0.13$ days that is derived is consistent with those found in the literature from photometry. The value for the period can therefore be trusted.

Furthermore, this rotation period can be seen in a number of datasets. For example, P. McGinnis computed bidimensional periodograms of the intensity of the He ɪ emission line, and the Stokes I/V LSD profiles of the photospheric absorption lines (see Nelissen et al. 2023a). The He ɪ line comes from the accretion shock and should therefore vary with the stellar rotation period. In 2010, a period around 8 days is found for the He ɪ line, however this period is very uncertain. The Stokes V profile also shows a period near 8.5 days, but again the uncertainty is large. The Stokes I profile does not show a clear period. In 2012, there is no clear period found from the He ɪ line, likely because accretion is more intrinsically variable in this epoch than two years prior. Again, no clear period is observed from the Stokes I profile, but the Stokes V profile shows a possible periodicity at around 8 days (albeit with a large uncertainty, as in 2010).

In addition, the variation of the 2010 veiling as a function of time is also consistent with an 8.2 day period (see Fig. 3.5). The variation of the 2012 veiling as a function of time, however, does not seem to follow any trend with the period. This is consistent with the intensity of the HeI line not showing a clear correlation with period in this epoch, since both are tracing accretion. This is another indication that there must

be some intrinsic variability in the mass accretion rate in 2012, which masks any rotational modulation of the accretion spot(s).

Looking at the possibility of the rotation period or $v \sin i$ being inaccurate shows evidence to the contrary. Because their values appear to be accurate, it can be deduced that it is the value for the inclination that is problematic. The conclusion is that the inclination measured for the outer circumstellar disk axis must not represent the inclination of the rotation axis of the star. This suggests that there is a considerable misalignment between the rotation axis of DK Tau and its outer disk axis. As previously mentioned, when calculating the rotation axis inclination of DK Tau based on its rotational properties using Eq. 3.3.1, it is found that $i = 58°$ (+18)(-11). It follows that the outer disk axis of DK Tau is likely misaligned compared to its rotation axis. Figure 3.13 illustrates this misalignment. The observer is represented by the telescope and the line-of-sight by the gray line. The stellar rotation axis is in red and is inclined by 58° compared to the line-of-sight. The outer disk axis is in blue and is inclined by 21° compared to the line-of-sight.
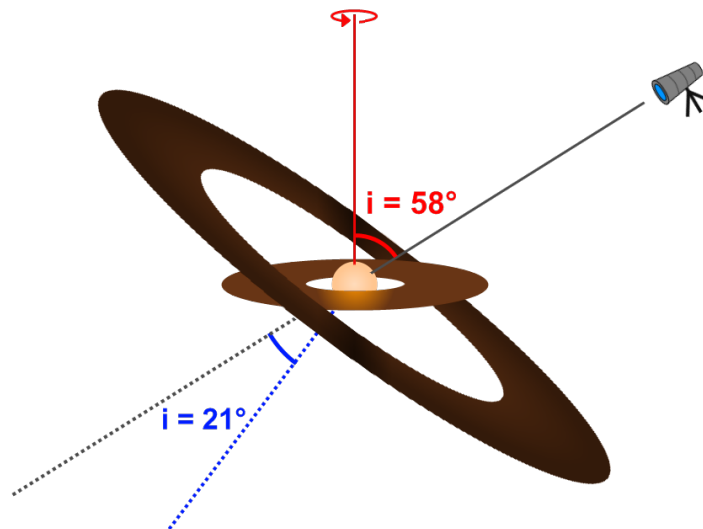


Figure 3.13 – Sketch (not to scale) showing DK Tau in the center, surrounded first by its inner disk, then by its outer disk which is considerably misaligned. The rotation axis at 58° is in red, the outer disk axis at 21° is in blue, and the line-of-sight axis is in gray (by C. Delvaux).

Misalignments between the inner and outer circumstellar disk axes of TTs are starting to be more commonly observed, when combining near infrared interferometric VLTI/GRAVITY data and millimeter interferometric ALMA data (see e.g. Ansdell et al. 2020; Bouvier et al. 2020), or with shadows observed with VLT/SPHERE (see

e.g. Benisty et al. 2018; Sicilia-Aguilar et al. 2020), or with VLTI/GRAVITY (see e.g. Bohn et al. 2022). This work has found a misalignment between the outer disk axis and the rotation axis. What of the inner disk axis? In young dippers like DK Tau, the material that causes the dips is believed to be located in the inner accretion disk (see Bouvier et al. 2007; McGinnis et al. 2015), which needs to be observed at high inclinations in order for the material to cross the line-of-sight to produce the dips. Therefore an inclination of 21° for the inner disk of DK Tau is difficult to reconcile with its dipper lightcurve. Moreover, the inner disk axis is normally expected to be aligned with the stellar rotation axis. It is therefore very likely that the inner disk axis of DK Tau has the same inclination of $i = 58°$ as was calculated for its rotation axis. This inclination is sufficiently high to support the dipper behavior and there are other cases of dippers with similar inclinations (see e.g. McGinnis et al. 2015; Roggero et al. 2021). DK Tau is one more example of a TTs with a misalignment between its inner and outer circumstellar disk axes.

DK Tau is also a wide binary system (with the subject of this work being DK Tau A), and the misalignment could stem from the binary formation mechanism. Indeed, turbulent fragmentation might produce disk axes that are more randomly oriented. It is however interesting to note as well that the outer disk axis of DK Tau B is inclined by 64° compared to the line-of-sight (see Rota et al. 2022). This could suggest a quasi-alignment of the inner disk axis of DK Tau A (at 58° compared to the line-of-sight) with the outer disk axis of DK Tau B. However, this hypothesis assumes that they are not only aligned compared to the line-of-sight, but that the orientation of their nodes are aligned as well, which is unknown.

### 3.3.2 Magnetic field in the accretion-powered emission lines

The $B_{los}$ derived from the photospheric absorption lines (see Sect. 3.2.6), provides a partial view of the magnetic field of DK Tau that exclude the accreting regions, because photospheric absorption lines and accretion-powered emission lines form in different regions of the stellar surface. It is the magnetic field present in these accreting regions that is understood to best probe the global stellar magnetic field that reaches to the circumstellar disk. The magnetic obliquity derived from the accretion-powered emission lines is thus likely to be close to the actual value. The low magnetic obliquity that is calculated (see Sect. 3.2.8), as well as the unchanging polarity of the $B_{los}$ in the emission lines (see Sect. 3.2.7), are consistent with the presence of an accretion spot always visible and close to the pole. This is where the accretion columns connecting DK Tau to its circumstellar disk would be anchored. This is similar to what has been found for several other cTTs (see e.g. Johnstone et al. 2014; McGinnis et al. 2020).

For the 2010 epoch, it can be noted that the magnetic field in the Ca II IRT (and in the He I line - see Fig. 3.11 and 3.12) is at a maximum close to the same phase (i.e. around phase 0.3) as the maximum in the veiling (see Fig. 3.5), which is when the accretion shock is in the line-of-sight. Around phase 0.5, there is a small redshifted absorption in the Hα line (see Appendix A1), indicating that the accretion column is in the line-of-sight. Since this is directly after the maximum of the magnetic field in the emission lines and the increase in veiling, it is probably directly after the accretion shock was in the line-of-sight. This indicates a spatial connection between the magnetic maximum, the accretion shock and the accretion columns.

## 3.4 Conclusions

This chapter presented the study of DK Tau, a low-mass cTTs with significant veiling. The analysis was carried out using dual-epoch spectropolarimetric observations (i.e. collected in 2010 and 2012). A $T_{\text{eff}}$ of $4\,150 \pm 110\,\text{K}$ and a $v \sin i$ of $13.0 \pm 1.3\,\text{km}\,\text{s}^{-1}$ are derived, in agreement with the literature. Peak values of veiling in the optical ($\sim$550 nm) ranging from 0.2 to 1.8 in 2010, and from 0.2 to 1.3 in 2012 are found.

The $B_{\text{los}}$ from the photospheric absorption lines (linked to non-accreting regions) was derived. Values ranging from -0.19 $\pm$ 0.05 kG to 0.20 $\pm$ 0.03 kG in 2010 and from -0.13 $\pm$ 0.02 kG to 0.08 $\pm$ 0.02 kG in 2012 are found.

A rotation period of $8.2 \pm 0.13$ days was recovered using the values of $B_{\text{los}}$ in the photospheric absorption lines for the 2010 dataset. This period was confirmed by analyzing the variation of veiling as a function of time in 2010. It also agrees with the values of period given in the literature from photometry.

Several inconsistencies related to the inclination of the stellar rotation axis with respect to the line-of-sight are found. The measurement of the outer circumstellar disk axis inclination gives a value of 21° ± 3 (see Rota et al. 2022). The lightcurve of DK Tau, however, classifies it as a dipper (see Roggero et al. 2021), for which the simplest explanation involves a star seen close to edge-on. Additionally, Eq. 3.3.1 shows that the inclination of 21°, the period, $v \sin i$ and the radius are not consistent with each other. When using the values of period, $v \sin i$ and stellar radius that were derived in this work to estimate the inclination of the stellar rotation axis, a value of $i = 58°$ (+18)(-11) is found. Consequently, a substantial misalignment between the rotation axis of DK Tau (at 58°) and its outer disk axis (at 21°) is likely.

To complement the partial picture of the $B_{\text{los}}$ derived from the photospheric absorption lines, emission lines that are tracers of the magnetic fields present in the accretion shocks were analyzed. The narrow component of the 587.67 nm He I emission line and of the Ca II infrared triplet (IRT - at at 849.8 nm, 854.2 nm and 866.2 nm)

were examined and the values of $B_{los}$ were measured. Values ranging from 0.92 $\pm$ 0.09 kG to 1.77 $\pm$ 0.08 kG for Heɪ in 2010, from 0.48 $\pm$ 0.09 kG to 1.99 $\pm$ 0.09 kG for Heɪ in 2012, from 0.42 $\pm$ 0.02 kG to 0.95 $\pm$ 0.02 kG for Caɪɪ in 2010, from 0.30 $\pm$ 0.01 kG to 1.15 $\pm$ 0.02 kG for Caɪɪ in 2012 were found. They are consistent with only seeing one pole, suggesting that DK Tau experiences nearly poleward accretion. This geometry is similar to what has been found for other cTTs (see e.g. Johnstone et al. 2014; McGinnis et al. 2020).

An estimate of the magnetic obliquity was derived from the accretion-powered emission lines using the third equation of Preston (1967). This equation assumes a pure dipole, which is a simplification of the magnetic field present in the accretion shocks. It is the field present in these accretion shocks that is presumed to best probe the global stellar field that extend to the circumstellar disk. The magnetic obliquities derived from the accretion-powered emission lines are thus a reasonable reflection of the real dipole present above the surface of the star. For the Heɪ line, a magnetic obliquity of 26° for the 2010 epoch, and of 21° for the 2012 epoch are found. For the Caɪɪ IRT, a magnetic obliquity of 16° for the 2010 epoch, and of 23° for the 2012 epoch are found. These estimates are consistent with the magnetic obliquity of 18° (+8)(-7) in 2011 derived by McGinnis et al. (2020), using the Heɪ line and assuming one accretion spot.

The truncation radius was also estimated using the values of $B_{los}$ in the emission lines. This yields $r_{trunc} \sim 5.2 \pm 1.1\,R_\star$ for the Heɪ line in 2010, $r_{trunc} \sim 3.9 \pm 0.8\,R_\star$ for the Caɪɪ IRT in 2010, $r_{trunc} \sim 4.7 \pm 1.2\,R_\star$ for the Heɪ line in 2012, and $r_{trunc} \sim 3.9 \pm 1.0\,R_\star$ for the Caɪɪ IRT in 2012. The co-rotation radius was calculated as well: $r_{co\text{-}rot}$ = 6.1 $R_\star$. The truncation radius values are consistent with the co-rotation radius.

In conclusion, DK Tau, presenting with significant veiling, has similar magnetic properties as the more moderately accreting cTTs studied so far. Additionally, its outer disk axis is likely to be misaligned compared to its rotation axis. This poses questions with regards to standard models of circumstellar disk formation. More observations of cTTs are needed to better understand the prevalence of such misalignments.

4

# Correlation between the optical veiling & accretion properties:
# A case study of DK Tau

$\mathcal{T}$HIS chapter is based on the following publication:

## 4.1  Introduction & observations

The current chapter presents the investigation into the accretion properties and variability in DK Tau. To this end, the mass accretion rates ($\dot{M}_{\rm acc}$ - see Sect. 1.3.4) for each night were derived, using two different methods for comparison purposes. The first procedure is based on the extraction of the accretion luminosity ($L_{\rm acc}$) using accretion-powered emission lines. The second compares accretion shock models with the variability of the observed veiling in the optical range in order to determine the mass accretion rates. Additionally, the optical veiling can also be used to infer the values of the accretion luminosity. Furthermore, the evolution with time, as the star rotates, of various accretion-related quantities can offer more insight into the accretion process.

Observations taken in 2010 and 2012 with the ESPaDOnS spectropolarimeter (see Sect. 2.1) were used for this purpose. Both epochs respectively cover 17 and 29 days. On 19 December 2010, the full Moon was close to DK Tau (see Sect. 3.2.5). Because of the resultant scattered light, this night was ignored in the analysis.

The next section describes the analysis and the obtained results. It begins with the recapitulation of the veiling data available. This is followed by an explanation of the derivation of the photospheric continuum for this project. Finally, both methods of determining the mass accretion rates and their outcomes are detailed.

## 4.2 Analysis & results

### 4.2.1 Recapitulation of the veiling data

The veiling data used for this project is the same as in the first project (see Sect. 3.2.3), focusing on the ESPaDOnS observations. It consists of values of veiling from night to night and across the visible wavelength range. Using these values of veiling as a function of the wavelength, and working in the logarithmic plane this time, a linear relation was fitted through the points. This was done using a least squares polynomial fit. The standard deviation (of the spread of points compared to the fit) was used as the uncertainty of the fit. A list of the coefficients of the fits (i.e. from $y = ax + b$, with $a$ being the slope and $b$ the vertical intercept) can be found in Table 4.1.

Table 4.1 – Coefficients of the best linear fits to the observed veiling values

| Date (yyyy-mm-dd) | $a$ (err) | $b$ (err) |
|---|---|---|
| 2010-12-14 | -1.69 (0.45) | 4.61 (1.28) |
| 2010-12-15 | -1.67 (0.45) | 4.48 (1.27) |
| 2010-12-16 | -1.83 (0.37) | 4.83 (1.03) |
| 2010-12-17 | -1.05 (0.71) | 2.24 (2.01) |
| 2010-12-18 | -0.85 (0.51) | 1.73 (1.45) |
| 2010-12-24 | -1.35 (0.63) | 3.33 (1.79) |
| 2010-12-26 | -0.95 (0.54) | 2.03 (1.52) |
| 2010-12-30 | -1.00 (0.21) | 2.41 (0.61) |
| 2012-11-25 | -0.15 (0.70) | -0.25 (1.97) |
| 2012-11-28 | -2.09 (0.27) | 5.80 (0.76) |
| 2012-11-29 | -1.29 (0.36) | 3.34 (1.01) |
| 2012-12-01 | -0.85 (0.36) | 2.07 (1.01) |
| 2012-12-02 | -1.36 (0.34) | 3.56 (0.97) |
| 2012-12-04 | -1.68 (0.21) | 4.73 (0.58) |
| 2012-12-07 | -2.19 (0.36) | 6.15 (1.00) |
| 2012-12-10 | -0.90 (0.30) | 2.03 (0.84) |
| 2012-12-23 | -0.71 (0.50) | 1.60 (1.41) |

Figure 4.1 shows the veiling at 617.50 nm folded in time with the stellar rotation phase, for the 2010 and 2012 epochs. The error bars are the uncertainty of the fits. The veiling folds well in phase for the 2010 observations. There is however more scatter for the 2012 dataset. This is likely due to the veiling being modulated by higher accretion activity and not only by the stellar rotation in this epoch.
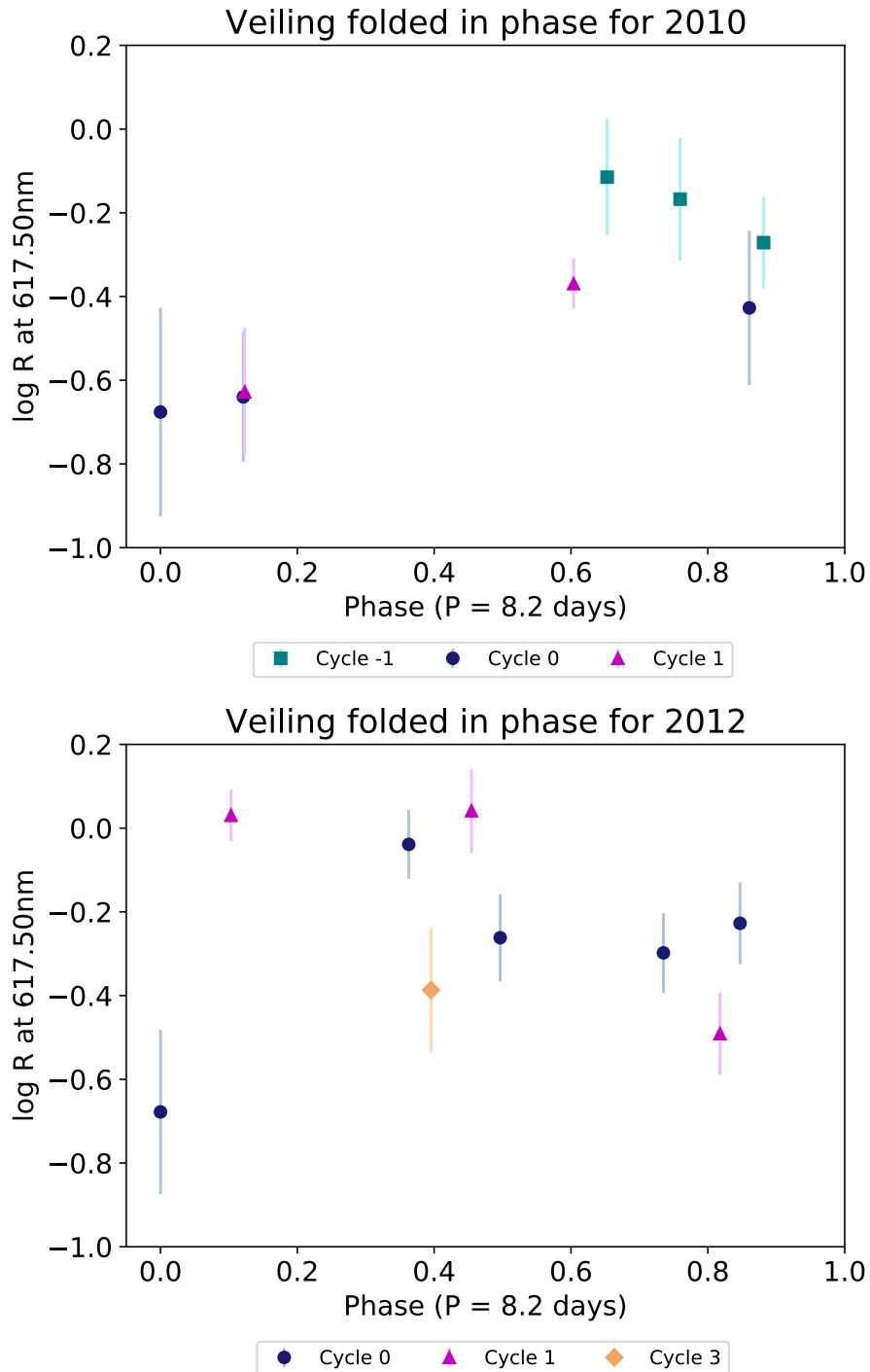
Figure 4.1 – Veiling at 617.50 nm over time, shown folded in phase with an 8.2 day period, for the 2010 (top panel) and 2012 epoch (bottom panel). Cycle 0 for the 2010 observations begins on December 17, while for the 2012 observations it begins on the first observation of 2012. This was done in order to display the minimum at the same phase for both epochs. Different colors and symbols represent different rotation cycles.

## 4.2.2 Derivation of the photospheric continuum

Because ESPaDOnS spectra are not flux-calibrated, it was necessary to use a photospheric template. An improved version of the template creation procedure described in the first project (see Sect. 3.2.9) was used here.

In this project, DK Tau's photospheric continuum was derived from a high-resolution spectrum taken in 2018 by Gangi et al. (2022) at the Telescopio Nazionale Galileo (TNG) using HARPS-N. The spectrum was first corrected for extinction using a value of $A_V$ = 1.2 mag from Gangi et al. (2022). They estimated the extinction by calculating the ratio of a flux-calibrated Asiago spectrum (see the next paragraph) and an artificially reddened template of the same spectral type. In comparison, Herczeg and Hillenbrand (2014) quote a value of $A_V$ = 0.7 mag, whereas Fischer et al. (2011) quote a value of $A_V$ = 1.83 mag. The variability of the extinction is probably linked to the dipper behavior of DK Tau (see Sect. 1.4.2 and Roggero et al. 2021). Next, the veiling was measured as in Sect. 3.2.3. This yielded a small value with a flat dependence on wavelength in the optical (i.e. R~ 0.2 with $a$ < -0.90). The spectrum was then deveiled.

Figure 4.2 plots the extinction-corrected and veiling-corrected HARPS-N spectrum (in red). Unfortunately, it does not cover the entirety of the wavelength range used in this project (i.e. from 550 nm to 900 nm). Consequently, a lower resolution spectrum which extends to slightly longer wavelengths was also plotted (in maroon). This spectrum was used by Gangi et al. (2022), who obtained it at the Asiago telescope[1] almost simultaneously to the HARPS-N data, for flux-calibration of the HARPS-N spectrum. Finally, in order to cover the whole region of interest in terms of wavelength, the photospheric continuum of the wTTs SO879 (in black) was used. As in Sect. 3.2.9, this is based on a VLT/X-shooter spectrum. As in Sect. 3.2.9 again, the spectrum was first corrected for extinction. It was then scaled to the distance and luminosity of DK Tau, that is $d$ = 132.6 pc (see e.g. Gaia Collaboration et al. 2016, 2018, 2022) and $L$ = 0.65 $L_\odot$ (with the luminosity value being derived from the flux-calibrated HARPS-N spectrum).

Because the SO879 continuum is a good description of the DK Tau continuum in the spectral range where they overlap, it was adopted as a good representation of the photospheric continuum over the whole range of the ESPaDOnS spectra.

In summary, as in the first project (see Sect. 3.2.3 and 3.2.9), two photospheric templates were used at two different stages of the analysis. In order to determine the values of veiling (see Sect. 3.2.3), an ESPaDOnS spectrum of the wTTs TAP45 was used because of its high resolution. However, that spectrum could not be used to

---

[1]The Asiago spectrum was flux-calibrated by Gangi et al. (2022) using spectroscopic and photometric observations of standards taken on the same night.
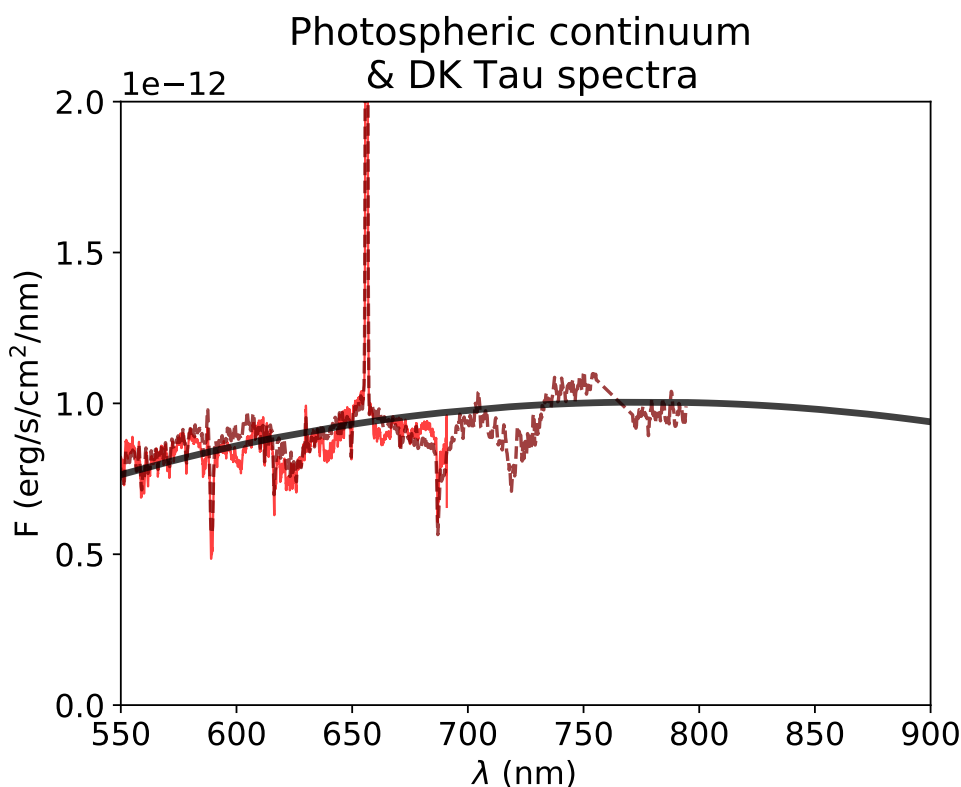
Figure 4.2 – Template of DK Tau's photospheric continuum (thick continuous black line) as a function of wavelength. The thin lines show the flux-calibrated spectra of DK Tau taken with HARPS-N (continuous red line) and the Asiago Telescope (maroon dashed line), both corrected for extinction and deveiled (see Gangi et al. 2022).

derive DK Tau's photospheric continuum because ESPaDOnS spectra are not flux-calibrated. An X-shooter spectrum of the wTTs SO879 was used instead. The latter could not be used the measure the veiling because of its lower resolution.

## 4.2.3   Calculating the accretion luminosity from emission lines

As mentioned in Sect. 1.3.4 and 3.2.9, one method of determining the mass accretion rate is by using the accretion luminosity, knowing the stellar mass and radius. In the first project, an average value of $\dot{M}_{acc}$ was calculated for each epoch. In this project, the mass accretion rate is calculated for each night, using the improved photospheric template described in the previous section. The various steps taken in order to obtain the values of $L_{acc}$, and then of $\dot{M}_{acc}$, are the same as the ones detailed in Sect. 1.3.4 and 3.2.9. As before, the values of $R_\star = 2.48\,R_\odot$ (see Sect. 3.2.2) and $M_\star = 0.7\,M_\odot$ (see Johns-Krull 2007) were adopted.

Plots of the accretion luminosities, for each night and for each emission line, can be found in Appendix A2. Figure 4.3 shows the accretion luminosity values averaged over the various emission lines and folded in phase. The weighted average was calculated and the weighted standard deviation of the spread in the accretion luminosity

values from the various emission lines was used as the error bars. For the 2010 epoch, the accretion luminosity changes with time by a factor of up to approximately 4. For the 2012 epoch, it changes with time by a factor of up to approximately 6. It changes in phase with the stellar rotation in the 2010 observations, but less clearly in the 2012 observations. The values for each night are listed in Table 4.2.

Figure 4.4 shows that the accretion luminosity correlates with the veiling in an almost linear fashion (see Sect. 4.3.1 for a discussion of the correlation). The error bars are the same as in Fig. 4.1 and 4.3 (i.e. the uncertainty of the fits for the veiling and the weighted standard deviation of the spread for the accretion luminosity).

Figure 4.5 shows the mass accretion rate onto the star for each night, folded in time with the stellar rotation phase. These values were calculated using the values of the accretion luminosities (and of the stellar mass and radius - see Sect. 1.3.4 and 3.2.9). The error bars on $\dot{M}_{acc}$ were taken as being the same as the ones on $L_{acc}$ because the mass accretion rate is proportional to the accretion luminosity. Additionally, this project is focusing on the variability of the accretion and the error bars on $M_\star$ and $R_\star$ do not change from night to night. The values for each night are listed in Table 4.2.

For the accretion luminosity, the values range from $\log(L_{acc}[L_\odot]) = -1.36$ to $\log(L_{acc}[L_\odot]) = -0.57$. This leads to mass accretion rate values ranging from $\log(\dot{M}_{acc}[M_\odot\,\mathrm{yr}^{-1}]) = -8.20$ to $\log(\dot{M}_{acc}[M_\odot\,\mathrm{yr}^{-1}]) = -7.40$. This agrees with the values found for DK Tau in the literature. Indeed, in comparison, Fischer et al. (2011) find $\log(\dot{M}_{acc}[M_\odot\,\mathrm{yr}^{-1}]) = -7.40$, a value that is in agreement with the higher end of the range. Gullbring et al. (1998) and Ingleby et al. (2013) quote similar values of $\log(\dot{M}_{acc}[M_\odot\,\mathrm{yr}^{-1}]) = -7.42$ and $-7.47$. The results are also in agreement with the value quoted by Fang et al. (2018) of $\log(\dot{M}_{acc}[M_\odot\,\mathrm{yr}^{-1}]) = -7.86$, a value approximately in the middle of the range. Gangi et al. (2022) find $\log(\dot{M}_{acc}[M_\odot\,\mathrm{yr}^{-1}]) = -8.33$. This agrees within the error bars of the lower end of the range.

### 4.2.4 Calculating the mass accretion rate using accretion shock models

A second method of determining the mass accretion rate involves accretion shock models. A description of these models can be found in Sect. 1.3.5.

C. Pittman carried out the construction of shock models using DK Tau's parameters: a distance $d = 132.6\,\mathrm{pc}$, a stellar luminosity $L = 0.65\,L_\odot$, a radius $R_\star = 2.48\,R_\odot$, an effective temperature $T_{\mathrm{eff}} = 4\,000\,\mathrm{K}$ and a mass $M_\star = 0.7\,M_\odot$. Each model has a different energy flux, namely $\mathcal{F} = 1\times10^9\,\mathrm{erg\,s^{-1}\,cm^{-2}}$, $\mathcal{F} = 3\times10^9\,\mathrm{erg\,s^{-1}\,cm^{-2}}$, $\mathcal{F} = 1\times10^{10}\,\mathrm{erg\,s^{-1}\,cm^{-2}}$, $\mathcal{F} = 3\times10^{10}\,\mathrm{erg\,s^{-1}\,cm^{-2}}$, $\mathcal{F} = 1\times10^{11}\,\mathrm{erg\,s^{-1}\,cm^{-2}}$
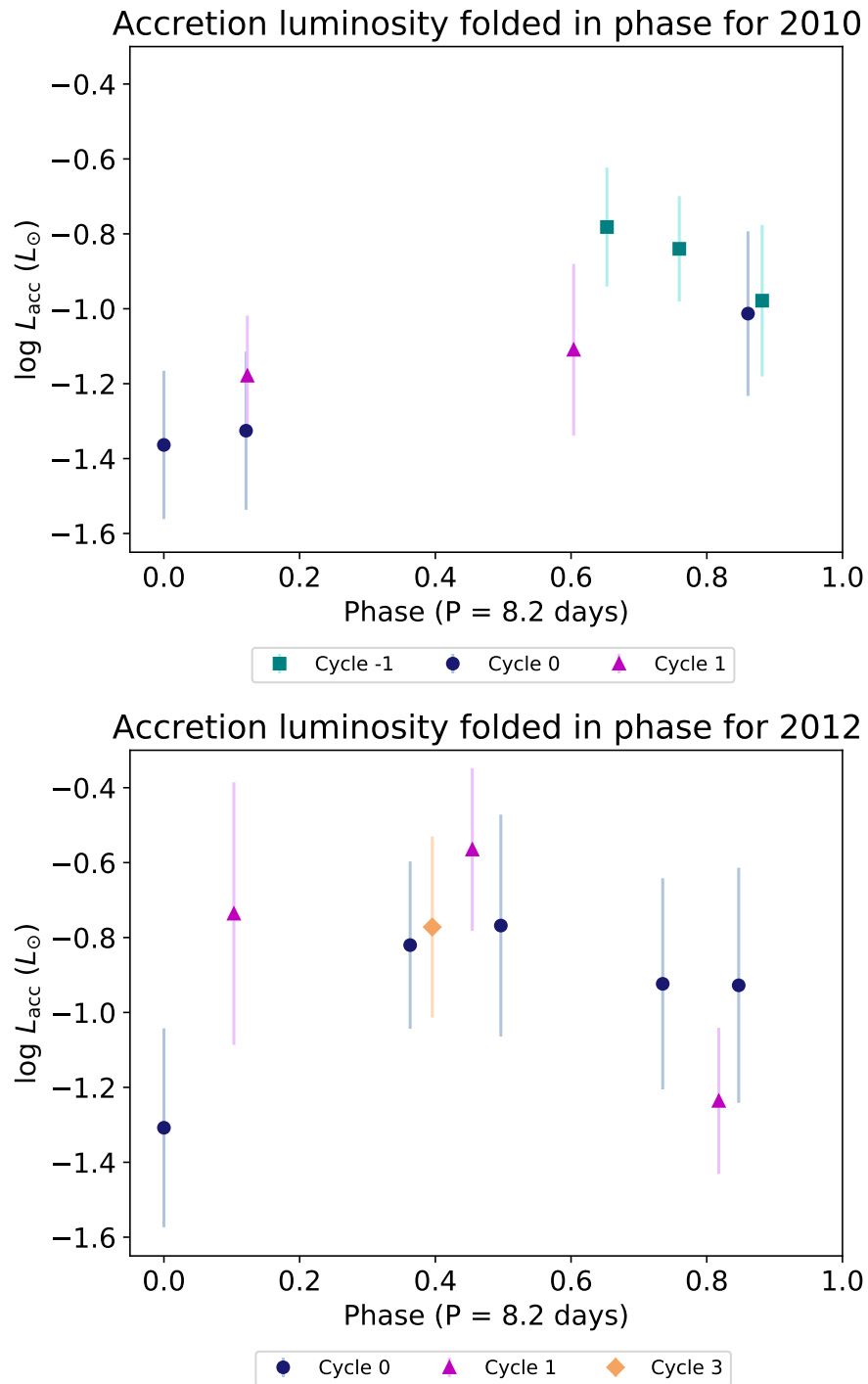
Figure 4.3 – Accretion luminosity over time, shown folded in phase with an 8.2 day period, for the 2010 (top panel) and 2012 epoch (bottom panel). Cycle 0 for the 2010 observations begins on December 17, while for the 2012 observations it begins on the first observation of 2012, as in previous figures. Different colors and symbols represent different rotation cycles.
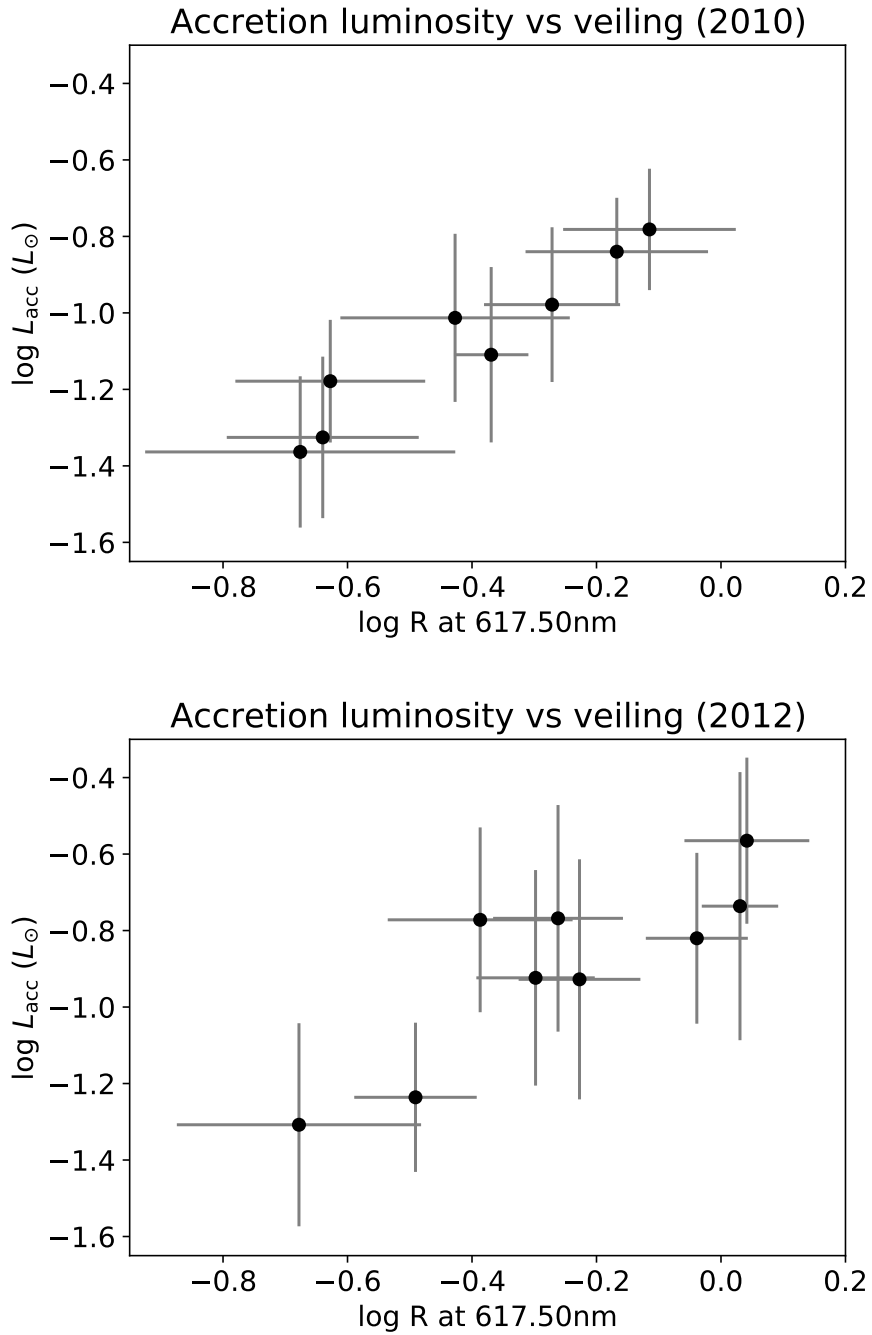
Figure 4.4 – Accretion luminosity as a function of the veiling at 617.50 nm, for the 2010 (top panel) and 2012 epoch (bottom panel).
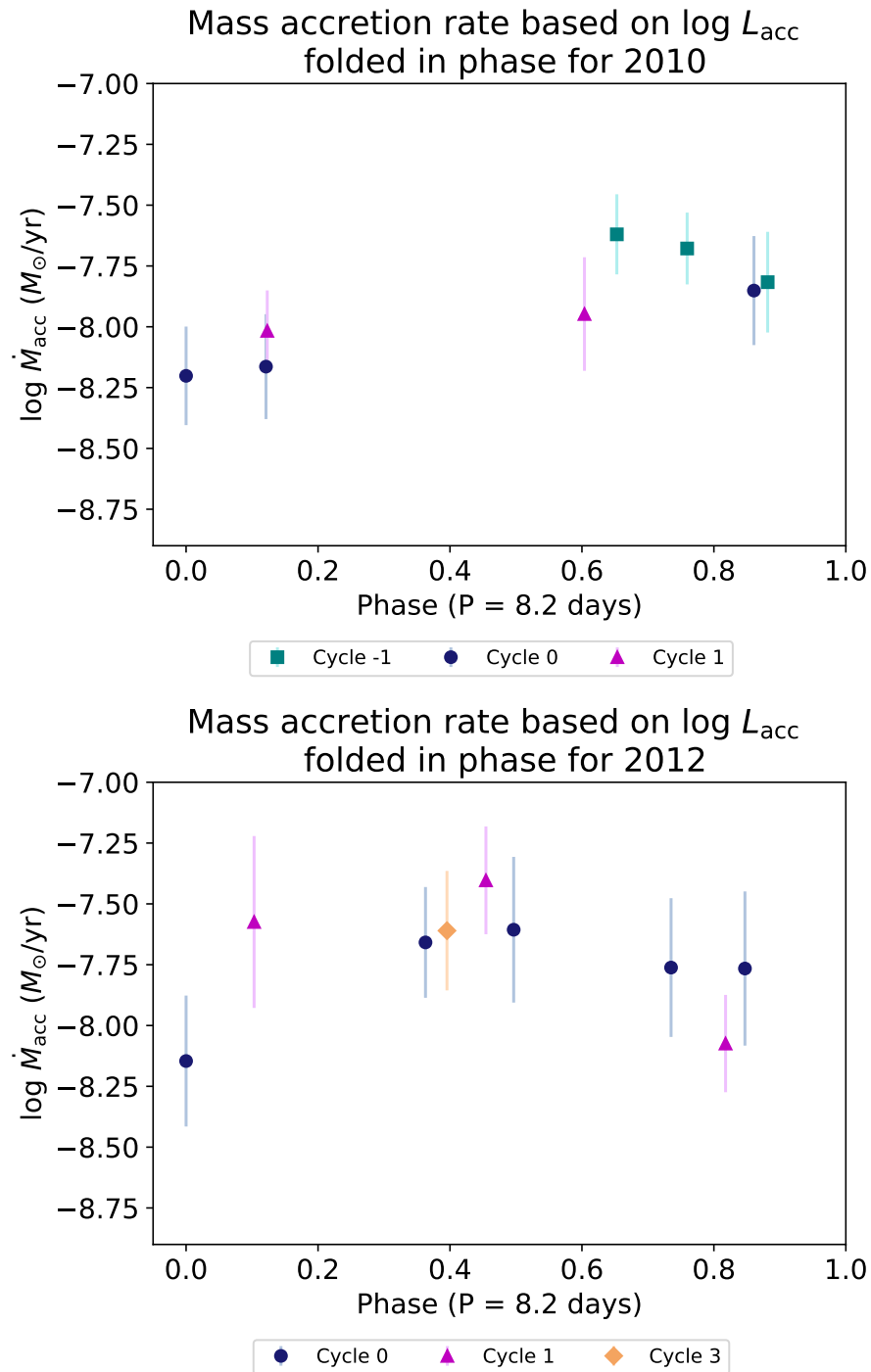
Figure 4.5 – Mass accretion rate based on the accretion luminosity over time, shown folded in phase with an 8.2 day period, for the 2010 (top panel) and 2012 epoch (bottom panel). Cycle 0 for the 2010 observations begins on December 17, while for the 2012 observations it begins on the first observation of 2012, as in previous figures. Different colors and symbols represent different rotation cycles.

and $\mathscr{F} = 3 \times 10^{11} \, \mathrm{erg \, s^{-1} \, cm^{-2}}$.

The top panel of Fig. 4.6 shows the various shock models (in rainbow colors), as well as DK Tau's photospheric continuum (in black - see Sect. 4.2.2). They are expressed as fluxes (i.e. $F$) in units of $\mathrm{erg \, s^{-1} \, cm^{-2} \, nm^{-1}}$ as a function of the wavelength in nm. Each model is defined by its energy flux (i.e. $\mathscr{F}$, not to be confused with $F$) in units of $\mathrm{erg \, s^{-1} \, cm^{-2}}$.

The shock models were used to acquire values of model-predicted veiling as a function of wavelength. This was done by calculating the ratio between the various modeled accretion shock fluxes (i.e. $F$) and the photospheric continuum flux. Indeed, the veiling is defined as the ratio between the accretion shock flux and the stellar photospheric flux (see Sect. 1.3.3). The modeled values of veiling are displayed on the bottom panel of Fig. 4.6. As for the shock models, each modeled veiling is defined by its energy flux (i.e. $\mathscr{F}$). In the present wavelength range (i.e. the optical), the slope of the modeled veiling increases monotonically with the energy flux. Therefore, the energy flux seems to univocally characterize the slope of the modeled veiling. This means that a specific value of $\mathscr{F}$ can be assigned to a specific slope for the modeled veiling. In turn, by fitting the modeled veiling onto the observed veiling, it is possible to assign a specific value of $\mathscr{F}$ to a specific slope for the observed veiling.

The slopes of the modeled veiling were computed in the same manner as the slopes of the observed veiling (see Sect. 4.2.1). Both types of slopes (i.e. $a$) were then plotted as a function of the veiling at 617.50 nm in Fig. 4.7. The error bars on the y-axis are the errors on $a$, while the error bars on the x-axis are the uncertainties of the fits (i.e. the fits from the veiling measurements - see Sect. 4.2.1). Next, the values of the slopes, of the veiling at 617.50 nm, and of the energy fluxes were linearly interpolated between the six available models. However, only these six models are displayed in Fig. 4.7 for clarity. The modeled veiling values are represented by the rainbow diamonds (with each color depicting a different value of $\mathscr{F}$). The observed veiling values are represented by the black dots. The latter follow the aforementioned trend of a higher slope with higher veiling values (see Sect. 3.2.3). This trend is highlighted by the gray dotted line, which represents a linear fit of the observed data points.

Regarding the modeled veiling values, they are scaled by the filling factors (i.e. $f$) which are free parameters. In Fig. 4.7, $f$ was adjusted in order for the values of modeled veiling (i.e. the rainbow diamonds) to coincide with the linear fit from the observations (i.e. the gray dotted line).

As mentioned previously, in the optical range, the slopes of the modeled veiling are only dependent on the value of the energy flux and independent of the filling factors. Therefore, the best value of the energy flux for each observation was derived
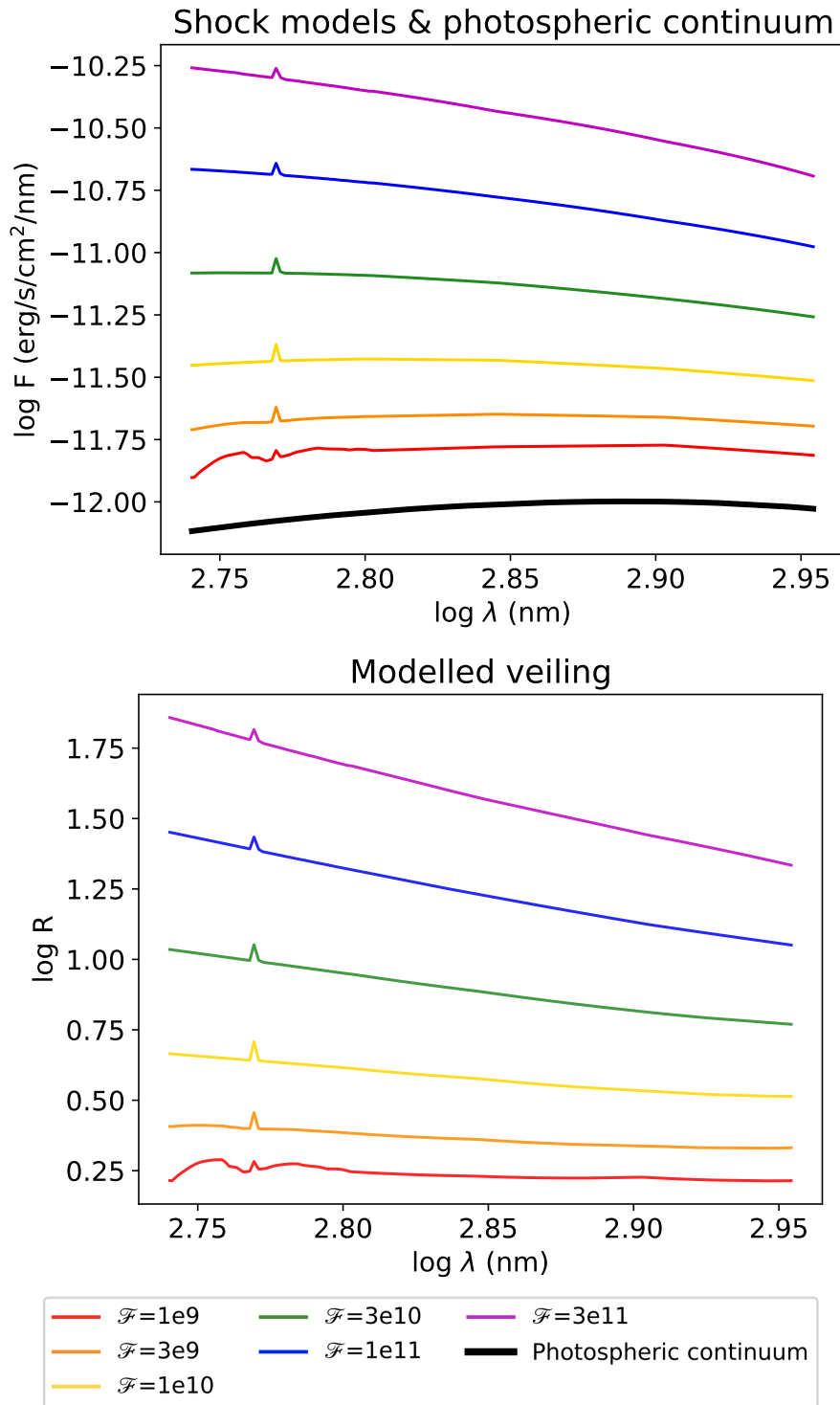
Figure 4.6 – Models of the excess flux from accretion shocks (in rainbow colors) and photospheric continuum (in black) as a function of wavelength (top panel). Modeled veiling (in rainbow colors) computed from the various shock models and the photospheric continuum as a function of wavelength (bottom panel).
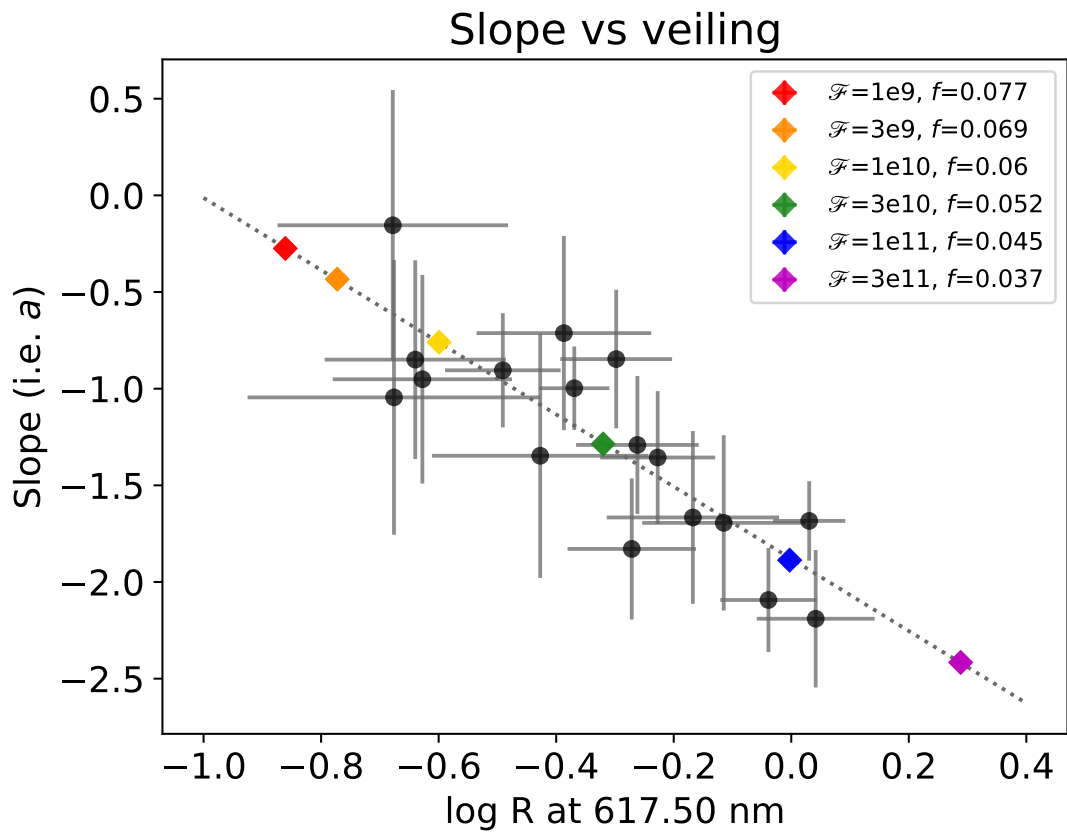
Figure 4.7 – Slope of the veiling for the different models (diamonds in rainbow colors), and for the 2010 and 2012 observations (black dots) as a function of the veiling value at 617.50 nm. The vertical error bars are the errors on *a*, the horizontal ones are the uncertainties of the fits. The gray dotted line represents the linear fit of the observations.

by matching the slope of the modeled veiling with the slope of the observational veiling. In other words, matching along the y-axis.

Next, adjusting the values of the filling factors shifts the modeled veiling values along the x-axis only. The models were consequently aligned with the the observations by varying the filling factors. The energy flux and the appropriate filling factor for that energy flux were thus derived for each night. Two examples of the overlap between the observed and modeled veiling can be found in Appendix A3.

As mentioned previously (see Sect. 1.3.5), in the literature (see e.g. Ingleby et al. 2013; Robinson and Espaillat 2019; Espaillat et al. 2022; Pittman et al. 2022), it is usually a combination of several energy fluxes, each with its own filling factor, that are used to fit a single observation, with each energy flux better constrained by different regions of the spectrum. Generally, the lower energy fluxes peak in the optical, and the higher energy fluxes peak in the UV. However, this work focuses on a narrower wavelength range (i.e. from 550 nm to 900 nm) that excludes the UV. Consequently, a single energy flux with its assigned filling factor are used for each observation. Nevertheless, it is still possible to constrain the models to the data adequately. This leads to the approximation that, for a given observation, one homogeneous accretion spot, characterized by a single value of $\mathscr{F}$ and $f$, is dominating the optical emission.

The values of the energy fluxes that were derived range from $1.00 \times 10^9$ to $2.15 \times 10^{11}$ erg s$^{-1}$ cm$^{-2}$. For these various energy fluxes, the filling factors range from 0.026 to 0.117. This implies that the accretion spots cover from 2.6% to 11.7% of the stellar surface. These numbers are comparable to the ones listed in the literature for other cTTs. It should however be noted, as mentioned before, that the various authors use a multicolumn approach, whereas this work assumes the presence of a single column and spot. There are several examples that use three accretion columns with $\mathscr{F} = 1 \times 10^{10}$ erg s$^{-1}$ cm$^{-2}$, $\mathscr{F} = 1 \times 10^{11}$ erg s$^{-1}$ cm$^{-2}$ and $\mathscr{F} = 1 \times 10^{12}$ erg s$^{-1}$ cm$^{-2}$. For instance, Robinson and Espaillat (2019) find filling factors ranging from $5.00 \times 10^{-5}$ to 0.39 for the low-mass cTTs DM Tau, GM Aur, SZ 45, TW Hya and VW Cha. Espaillat et al. (2021) mention filling factors ranging from $5.30 \times 10^{-5}$ to 0.18 for the cTTs GM Aur. And Pittman et al. (2022) find filling factors ranging from $4.85 \times 10^{-5}$ to 0.23 for the cTTs CVSO 58, CVSO 90, CVSO 104, CVSO 107, CVSO 109A, CVSO 146, CVSO 165A, CVSO 165B and CVSO 176.

The values of the energy fluxes and corresponding filling factors that were derived for each night are listed in Table 4.2. They are anticorrelated: higher energy fluxes are paired with smaller filling factors. Conversely, filling factors increase when the energy fluxes decrease, in order to match the observed veiling. This is to be expected for a constant accretion rate, as the product of the energy flux by the filling factor is proportional to the mass accretion rate (see Sect. 1.3.5). In other words, in order to produce the same amount of flux, lower energy fluxes must be paired with larger

filling factors (see e.g. Calvet and Gullbring 1998; Ingleby et al. 2013).

Figure 4.8 shows the energy fluxes folded in phase, while Fig. 4.9 shows the filling factors folded in phase. Both quantities seem to vary in phase with the stellar rotation, notably for the 2010 epoch.

Next, using the derived values for the energy fluxes and filling factors, and using Eq. 11 from Calvet and Gullbring (1998), the corresponding mass accretion rates were calculated for each observation (see Eq. 1.3.8). For this, the values of $R_\star =$ 2.48 $R_\odot$ (see Sect. 3.2.2) and $M_\star = 0.7\,M_\odot$ (see Johns-Krull 2007) were used, as before. This yields values ranging from $\log{(\dot{M}_{\mathrm{acc}}[M_\odot\,\mathrm{yr}^{-1}])} = -8.78$ to $\log{(\dot{M}_{\mathrm{acc}}[M_\odot\,\mathrm{yr}^{-1}])}$ $= -7.04$. A list of the values for each night can be found in Table 4.2.

Figure 4.10 shows the mass accretion rate for each night, obtained via $\mathscr{F}$ and $f$, folded in phase. The uncertainties on the product of the energy fluxes $\mathscr{F}$ and the filling factors $f$, translate into uncertainties on the mass accretion rate. They were estimated by comparing different models with the distribution of points for the observed veiling. They were found to range from a factor 2 (or lower for some nights) to a factor 5 (on the nights where the scatter on the observed veiling is the largest). An example of the estimation of the uncertainty can be found in Appendix A3.

Over the range of observations, there is a significant range of values for $\mathscr{F}$, the energy flux of the column that impinges on the star, as it varies by two orders of magnitude. This is due to the range of slopes displayed by the observational veiling. The product of $\mathscr{F}$ and $f$ varies over a smaller range, because the mass accretion rate does not change as much as the energy flux.

## 4.3 Discussion

In the following section, a correlation between the veiling and the accretion properties will be discussed. Next, the variability in relation to stellar rotation and accretion spots will be considered as well. Finally, the main conclusions will be presented in the last section of this chapter.

### 4.3.1 Accretion luminosity and optical veiling

Figure 4.11 shows the accretion luminosities measured from accretion-powered emission lines (see Sect. 4.2.3) as a function of the veiling at 617.50 nm (see Sect. 4.2.1). The plot incorporates both the 2010 and 2012 observations (represented by the black dots). The error bars on the veiling are the uncertainty of the fits. The error bars on the accretion luminosity are the weighted standard deviation of the spread of individual emission lines. A power-law correlation (i.e. a linear correlation between
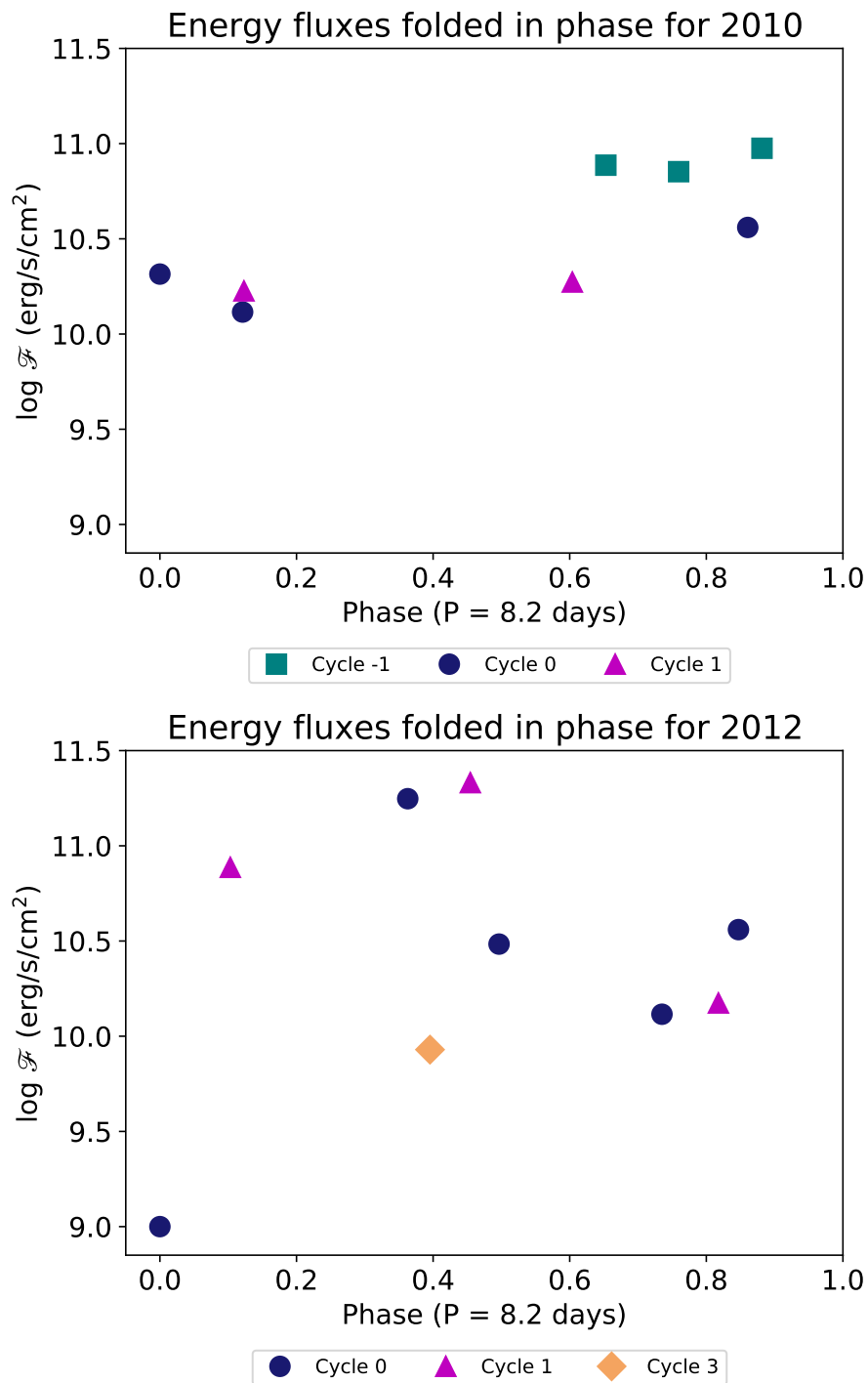
Figure 4.8 – Energy fluxes over time, shown folded in phase with an 8.2 day period, for the 2010 (top panel) and 2012 epoch (bottom panel). Cycle 0 for the 2010 observations begins on December 17, while for the 2012 observations it begins on the first observation of 2012, as in previous figures. Different colors and symbols represent different rotation cycles.

## Filling factors folded in phase for 2010



## Filling factors folded in phase for 2012
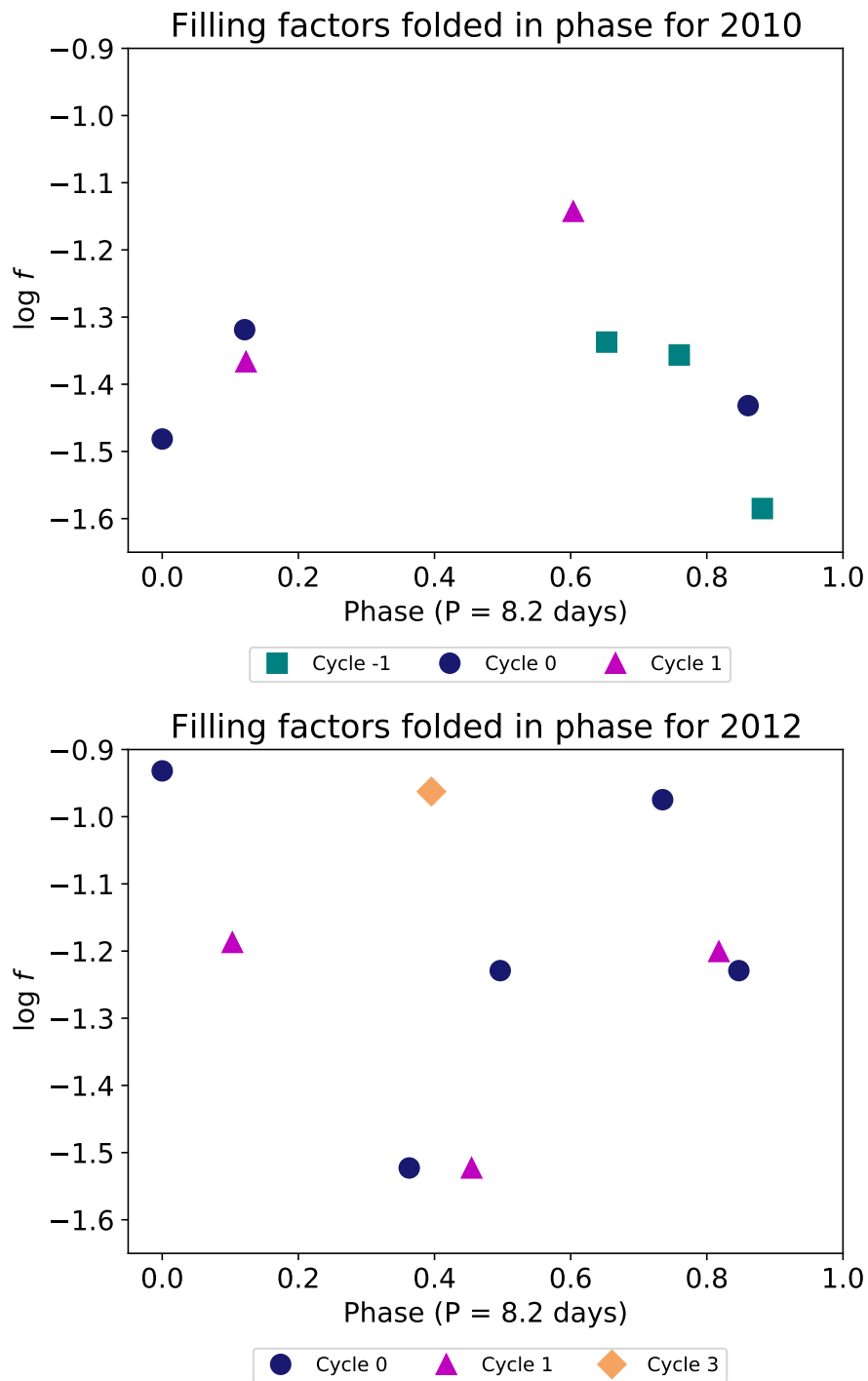
Figure 4.9 – Filling factors over time, shown folded in phase with an 8.2 day period, for the 2010 (top panel) and 2012 epoch (bottom panel). Cycle 0 for the 2010 observations begins on December 17, while for the 2012 observations it begins on the first observation of 2012, as in previous figures. Different colors and symbols represent different rotation cycles.
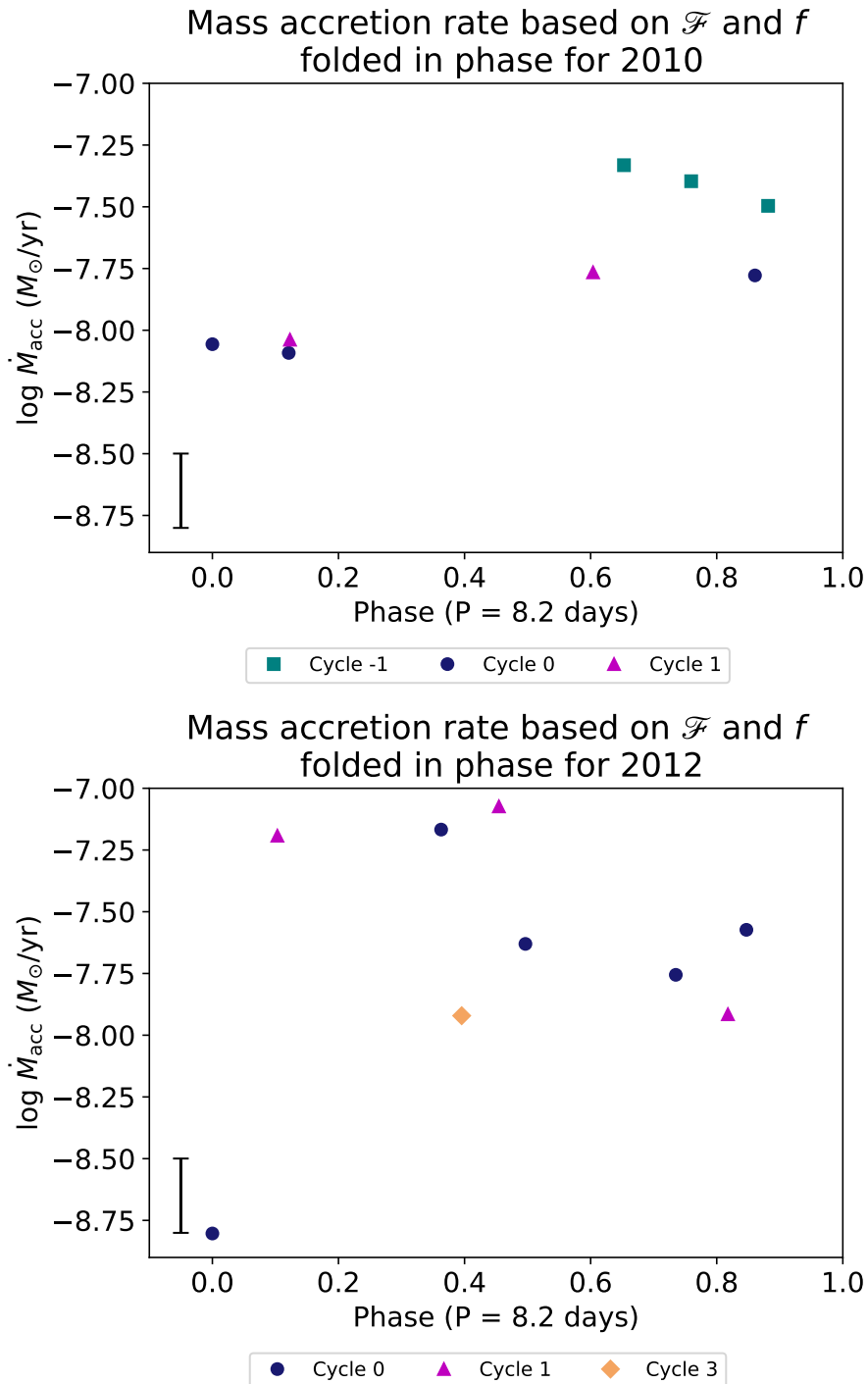
Figure 4.10 – Mass accretion rate based on $\mathscr{F}$ and $f$ over time, shown folded in phase with an 8.2 day period, for the 2010 (top panel) and 2012 epoch (bottom panel). Cycle 0 for the 2010 observations begins on December 17, while for the 2012 observations it begins on the first observation of 2012, as in previous figures. Different colors and symbols represent different rotation cycles. The uncertainty on the y-axis is shown on the lower left (see text for details).

94

Table 4.2 – Accretion luminosities, mass accretion rates based on $L_{acc}$, energy fluxes, filling factors and mass accretion rates based on $\mathscr{F}$ and $f$ for the 2010 and 2012 epochs.

| Date (yyyy-mm-dd) | log $L_{acc}$ (err) ($L_\odot$) | log $\dot{M}_{acc}$ (err) ($M_\odot$ yr$^{-1}$) based on $L_{acc}$ | $\mathscr{F}$ (erg s$^{-1}$ cm$^{-2}$) | $f$ | log $\dot{M}_{acc}$ ($M_\odot$ yr$^{-1}$) based on $\mathscr{F}$ and $f$ |
|---|---|---|---|---|---|
| 2010-12-14 | -0.78 (0.16) | -7.62 (0.16) | $7.71 \times 10^{10}$ | 0.046 | -7.29 |
| 2010-12-15 | -0.84 (0.14) | -7.68 (0.14) | $7.12 \times 10^{10}$ | 0.044 | -7.35 |
| 2010-12-16 | -0.98 (0.20) | -7.82 (0.20) | $9.45 \times 10^{10}$ | 0.026 | -7.45 |
| 2010-12-17 | -1.36 (0.20) | -8.20 (0.20) | $2.06 \times 10^{10}$ | 0.033 | -8.01 |
| 2010-12-18 | -1.33 (0.21) | -8.16 (0.21) | $1.30 \times 10^{10}$ | 0.048 | -8.05 |
| 2010-12-24 | -1.01 (0.22) | -7.85 (0.22) | $3.63 \times 10^{10}$ | 0.037 | -7.72 |
| 2010-12-26 | -1.18 (0.16) | -8.02 (0.16) | $1.68 \times 10^{10}$ | 0.043 | -7.98 |
| 2010-12-30 | -1.11 (0.23) | -7.95 (0.23) | $1.87 \times 10^{10}$ | 0.072 | -7.71 |
| 2012-11-25 | -1.31 (0.27) | -8.15 (0.27) | $1.00 \times 10^{9}$ | 0.117 | -8.78 |
| 2012-11-28 | -0.82 (0.22) | -7.66 (0.22) | $1.77 \times 10^{11}$ | 0.030 | -7.12 |
| 2012-11-29 | -0.77 (0.30) | -7.61 (0.30) | $3.04 \times 10^{10}$ | 0.059 | -7.59 |
| 2012-12-01 | -0.92 (0.28) | -7.76 (0.28) | $1.30 \times 10^{10}$ | 0.106 | -7.70 |
| 2012-12-02 | -0.93 (0.31) | -7.77 (0.31) | $3.63 \times 10^{10}$ | 0.059 | -7.51 |
| 2012-12-04 | -0.74 (0.35) | -7.57 (0.35) | $7.71 \times 10^{10}$ | 0.065 | -7.14 |
| 2012-12-07 | -0.57 (0.22) | -7.40 (0.22) | $2.15 \times 10^{11}$ | 0.030 | -7.04 |
| 2012-12-10 | -1.24 (0.20) | -8.07 (0.20) | $1.49 \times 10^{10}$ | 0.063 | -7.87 |
| 2012-12-23 | -0.77 (0.24) | -7.61 (0.24) | $8.50 \times 10^{9}$ | 0.109 | -7.88 |

both quantities expressed in the logarithmic plane) is found. This correlation is quite good, showing that the optical veiling traces the accretion luminosity very well. This is notably interesting and useful, as the two quantities are measured in two considerably different ways. Indeed, the veiling is measured at a single wavelength. The accretion luminosity, on the other hand, is a global quantity in terms of wavelength. Consequently, within the uncertainties, by measuring the veiling (i.e. by simply comparing the depth of observed absorption lines to a photospheric template) at one wavelength (in the optical in this case), one can infer the accretion luminosity, despite the fact that it is mostly emitted in the UV range and not at optical wavelengths.

This correlation between the accretion luminosity and the veiling is similar to the one found by Stock et al. (2022) for RU Lup[2]. The latter is a cTTs which experiences higher accretion (i.e. log ($L_{acc}[L_\odot]$) $\sim$ - 0.3) than DK Tau. In their Fig. 8, Stock et al. (2022) show a power-law correlation between the accretion luminosity and the veiling from the Li I line. They find a slope of 1.22 ($\pm$ 0.26) over a range of log $R$ going from 0.40 to 0.65. This is represented in Fig. 4.11 by the continuous maroon line. The maroon dashed line represents the trend extended to a larger range. In comparison, for DK Tau and using the optical veiling from the photospheric absorption lines, this project finds a slope of 0.91 ($\pm$ 0.11) over a range of log $R$ going from -0.70 to 0.10.

---

[2]See also Fig. 4 by Muzerolle et al. (1998) for a correlation between the mass accretion rate and veiling for various cTTs.
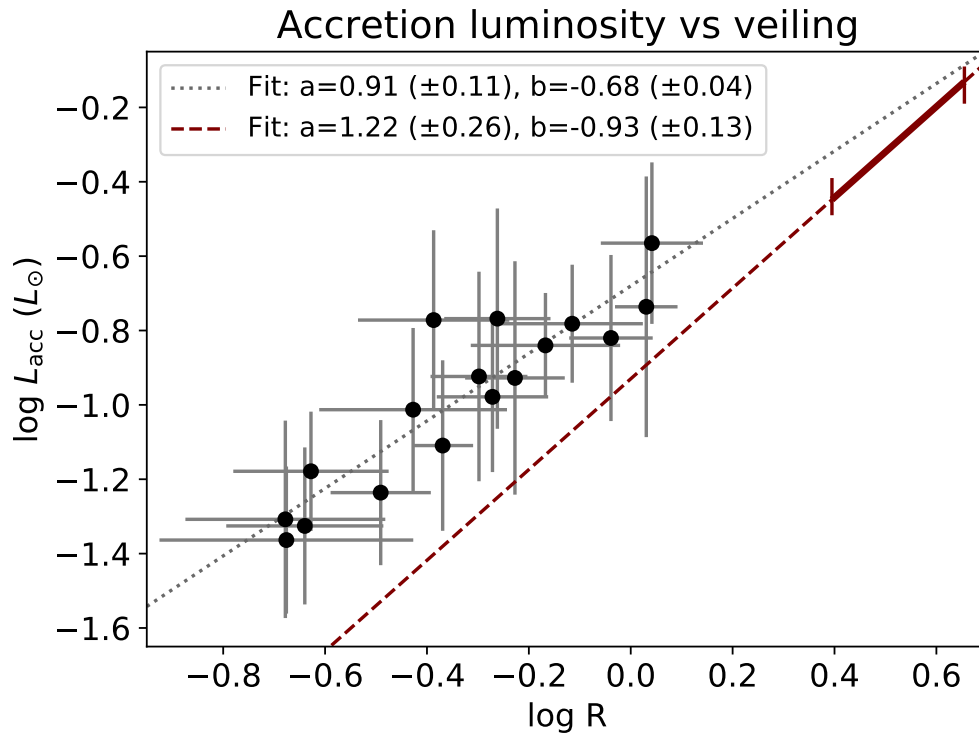
Figure 4.11 – Accretion luminosity as a function of the veiling at 617.50 nm, for the 2010 and 2012 epochs. The black dots show the range of values for DK Tau and the gray dotted line is their trend. The maroon dashed line shows the trend found for RU Lup by Stock et al. (2022), with the continuous maroon line highlighting their range of values.

This is represented by the gray dotted line. The slopes of the correlation for RU Lup and DK Tau agree within their error bars. Combined, they cover a large range of accretion luminosities, going from $\log\left(L_{\mathrm{acc}}[L_\odot]\right)$ = -0.10 to $\log\left(L_{\mathrm{acc}}[L_\odot]\right)$ = -1.40. The vertical intercept varies between the two stars, with b = -0.93 ($\pm$ 0.13) for RU Lup and b = -0.68 ($\pm$ 0.04) for DK Tau.

The discrepancy between the correlations could stem from the comparison of the veiling from the photospheric absorption lines[3] (for DK Tau) with the veiling derived from a single line, the Li I line (for RU Lup). This line suffers from differences in the abundance between RU Lup and the adopted template. Stock et al. (2022) have applied a correction, but note that it has large uncertainties, which could cause a systematic shift in their numbers.

It would be very interesting to investigate the relation between $L_{\mathrm{acc}}$ and the veiling in other stars. It would also be interesting to study the relation for a larger range of veiling values. If a similar relation is found for different stars, this could be a great tool when working on deriving quantities from limited data.

The correlation shown in Fig. 4.11 between the accretion luminosity and the optical veiling is also potentially very interesting when applied to stars with large and

---

[3]Summarized by the value of the fit (from the veiling measurements) at 617.50 nm (see Sect. 3.2.3).

uncertain extinction values. Indeed, the veiling does not depend on the extinction, while any method to measure the accretion luminosity does (see also Muzerolle et al. 1998; Stock et al. 2022).

## 4.3.2 Mass accretion rates

The mass accretion rate for each night was derived via two different procedures. The first method uses the accretion luminosity based on accretion-powered emission lines (see Sect. 4.2.3). The second technique compares the observed veiling in the optical with accretion shock models to derive values of the energy flux and filling factor (see Sect. 4.2.4). The values of $\dot{M}_{acc}$ that were obtained are listed in Table 4.2. They agree within a factor 2 for most nights, which is within the error bars. Figure 4.12 shows the two sets of mass accretion rates for both epochs. The errors bars on the mass accretion rate based on $L_{acc}$ are the error bars on $L_{acc}$ (see Sect. 4.2.3). The errors bars on the mass accretion rate based on $\mathscr{F}$ and $f$ are the uncertainties on the product of $\mathscr{F}$ and $f$ (see Sect. 4.2.4).
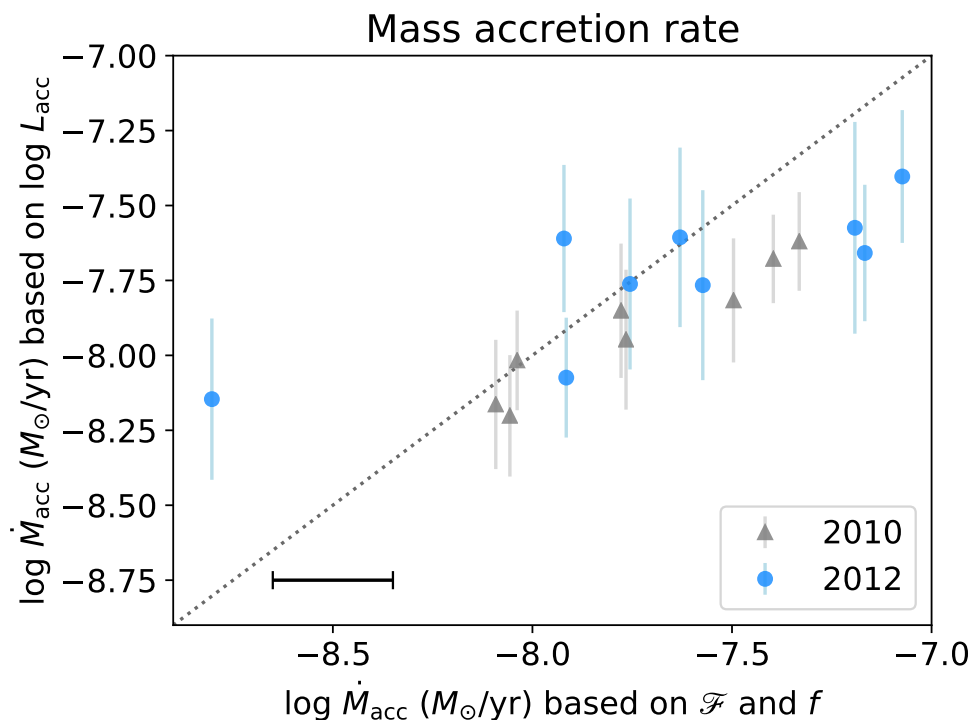


Figure 4.12 – Mass accretion rate based on the accretion luminosity as a function of the mass accretion rate based on $\mathscr{F}$ and $f$, for the 2010 and 2012 epochs. The gray dotted line shows a one-to-one relationship. The uncertainty on the x-axis is shown on the lower left (see text for details). It should be noted that the accretion shock model method finds almost systematically higher accretion rates than does the accretion luminosity method.

There is a trend close to a one-to-one relationship, showing that both methods of estimating the mass accretion rate are comparable. The discrepancy is probably systematic. Indeed, the mass accretion rate derived using the accretion shock models is

almost systematically higher than the one calculated using the accretion luminosity. This may be due to the calibration of the relations between the accretion luminosity and the line luminosity from Alcalá et al. (2017). Similarly, Pittman et al. (2022)[4] have found consistently higher mass accretion rate from accretion shock models than from the Hα luminosity. They mention systematic effects in the modeling methods as the probable cause.

As mentioned before, previous studies have used accretion shock models to derive the values of $\dot{M}_{acc}$ by working in a wavelength range going from he UV to the visible. In these instances, the observed excess emission generated by the accretion shock was fitted by a combination of shocks models of various $\mathscr{F}$ and $f$ (see e.g. Ingleby et al. 2013; Espaillat et al. 2021). In this project, working with DK Tau, it was found that a single shock model, with the $\mathscr{F}$ and $f$ values constrained only by the observed excess emission at optical wavelengths, reproduces quite well the values of $\dot{M}_{acc}$ obtained from the intensity of the emission lines. This is only possible when a single shock dominates the observed excess emission at all wavelengths. This is indeed the case not only in DK Tau but in 15 of the 21 TTs modeled by Ingleby et al. (2013). It is important to note that, as will be discussed in Sect. 4.3.4, this result does not rule out models where a single spot has a complex structure (see e.g. Robinson and Espaillat 2019; Espaillat et al. 2021).

### 4.3.3 Variability properties

The variation of several quantities with the stellar rotation were investigated. Although it should be noted that eight and nine points (for the 2010 and 2012 dataset respectively) are low numbers to detect a trend. The modulation of several of them, such as the accretion luminosity (see Fig. 4.3), the mass accretion rate derived from it (see Fig. 4.5), the value of the veiling at 617.50 nm (see Fig. 4.1), and the mass accretion rate derived from the shock models (see Fig. 4.10) seem to be dominated by the stellar rotation for the 2010 epoch. This is less clear for the 2012 epoch, which experiences some perturbation. As mentioned in Sect. 3.2.9, DK Tau may be in the stable accretion regime (see Sect. 1.3.2) in 2010. This difference between epochs might be linked to the accretion being less stable in 2012, when the mass accretion rate is higher.

The accretion luminosity (see Fig. 4.3) and the energy flux (see Fig. 4.8) seem to be varying in phase for the 2010 epoch. Therefore, the filling factor has to adjust to the energy flux and the mass accretion rate. This is because both methods of calculating the mass accretion rate (via the accretion luminosity or via the accretion

---

[4]Pittman et al. (2022) include the UV in their determination of the accretion luminosity. Other ground-based methods do not.

shock models) yield similar results (see the previous section) that are varying in phase (see Fig. 4.5 and 4.10). As will be discussed in the following section, the apparent variability of the filling factor with the phase can be used to estimate the location of the accretion spot.

### 4.3.4 Accretion spot

Figure 4.13 depicts the rotation of a star. The star is seen edge-on. In other words, the observer is looking at the page, while the stellar rotation axis is vertical and in the plane of the page. The star presents with an accretion spot a the equator (with this location chosen for illustrative purposes). As the star rotates, the spot is first invisible, then a portion of it becomes visible, next the whole spot is in view, until it gradually disappears again behind the star. This illustration assumes a single and stable accretion spot.
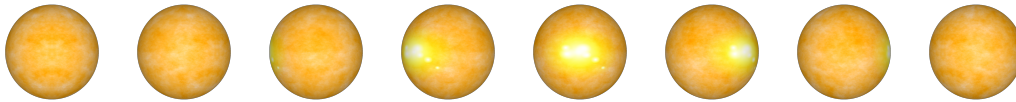


Figure 4.13 – Sketch (not to scale) showing an accretion spot at the equator of a star that is rotating. The star is seen edge-on (by C. Delvaux).

Next, Fig. 4.14 depicts an accretion spot, at a random fixed location on the stellar surface, for different inclinations of the star. The inclination is the angle between the stellar rotation axis and the line of sight of the observer. The second case is closest to the one corresponding to DK Tau's inclination of 58°. This illustrates that the inclination of the star influences not only the portion of the accretion spot that might be visible, but it also affects the perceived area of the spot. For instance, the area of the spot seems to be smaller for an inclination of 60° (the second case) compared to an inclination of 90° (the first case), despite both being in full view. This is a geometrical effect, the true area of the spot remains unchanged.

In the case of DK Tau, the effects depicted on Fig. 4.13 and Fig. 4.14 are combined. This means that there are times during the stellar rotation when the spot is invisible to the observer, and times when it starts being visible. When it is visible, it is with a perceived area that is varying with the stellar rotation, and the maximum perceived area depends on the inclination of the stellar rotation axis.

Assuming a point-like accretion spot, Fig. 4.15 plots the projected surface of the spot as a function of the stellar rotation phase. In this case, the stellar inclination is of 58°. The various colors represents various latitudes for the spot. The projected surface corresponds to the perceived area of the spot ($A$) divided by the true area of the spot ($A_{\text{tot}}$). When $A/A_{\text{tot}} = 1$, the observer sees the spot in full. Approximating

Figure 4.14 – Sketch (not to scale) showing a star presenting with an accretion spot and seen with various inclinations (namely 90° or edge-on, 60°, 30° and 0° or pole-one). The arrow represents the rotation axis. The case corresponding to DK Tau (i.e. 58°) is closest to the second one (by C. Delvaux).

the accretion spot as an ideal lambertian surface, the light it emits in the direction of the line-of-sight obeys Lambert's law:

$$I_L = I_{L,\text{tot}} \frac{A}{A_{\text{tot}}} = I_{L,\text{tot}} \cos \alpha \qquad (4.3.1)$$

where $I_L$ and $I_{L,\text{tot}}$ are respectively the perceived and the true luminous intensity of the bright accretion spot. $\alpha$ is the angle between the center of the visible stellar disk and the accretion spot. It depends on the inclination $i$ of the star, on the latitude $\Phi$ of the spot and on the stellar rotation phase $\varphi$ via

$$\sin \alpha = \sin i \sin \Phi + \cos i \cos \Phi \cos \varphi. \qquad (4.3.2)$$

The shapes of the curves in Fig. 4.15 hold under the assumption of a point-like spot. An extended spot would have the effect of enlarging the wings of the curves, especially the sharp ones.

The curves in Fig. 4.15 were compared with the shape of the curve for the filling factors folded in phase (see Fig. 4.9). Because of the low number of datapoints available, they were compared by eye. The filling factors represent the area of the star covered by an accretion spot (see Sect. 1.3.5 and 4.2.4). Assuming that observed variation of the filling factors are caused by the stellar rotation only, the comparison can lead to an estimate of the location of the accretion spot.
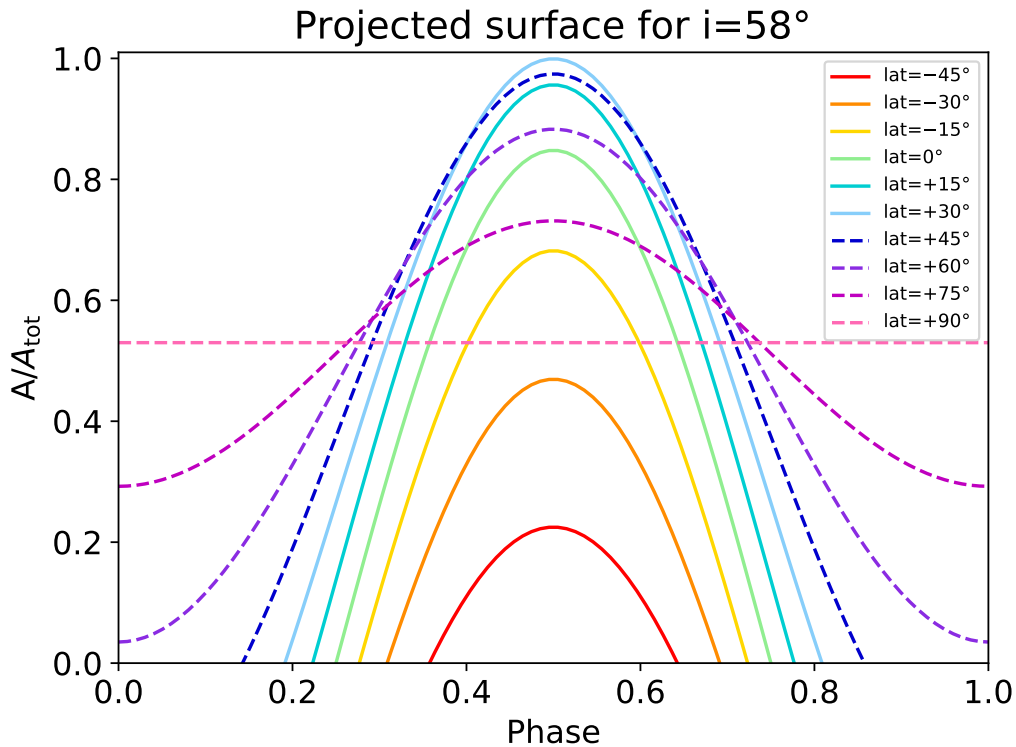
Figure 4.15 – Projected surface of an accretion spot as a function of the rotation phase for a star inclined by 58°. Different colors correspond to different locations in latitude for the spot.

As mentioned before, this comparison is made under the assumption of a single, stable and point-like accretion spot. In addition, the assumption is that the variation in filling factors depends only on the perceived change of area due to rotation. In other words, that it is only due to a geometrical effect, and is not due to the area of the spot truly changing. The curves in Fig. 4.15 that best ressemble the curve for the filling factors folded in phase for the 2010 dataset correspond to latitudes ranging from +45° to +75°. Consequently, it is inferred that the accretion spot would be located between +45° and +75° in latitude for the 2010 epoch. While the hypotheses made are a simplification of a likely more complex configuration, the curves in Fig. 4.15 do seem to reproduce the curve in Fig. 4.9. For the 2012 epoch, however, the perturbation to the rotational modulation prevents a comparison between Fig. 4.15 and Fig. 4.9.

Based on the current magnetospheric accretion paradigm (see Sect. 1.3.1), the magnetic pole is thought to be found at a similar location as the accretion spot. This is where the matter would accrete because the magnetic field lines channel the circumstellar material into accretion columns. Indeed, in the magnetohydrodynamic simulations done by Espaillat et al. (2021) for GM Aur, for example, the accretion spot is a few degrees away from the magnetic pole. By assuming that the accretion spot is close to the magnetic pole, the approximate location of the magnetic pole of DK Tau can be inferred. For the 2010 epoch, it would be located between +45° and +75° in latitude. This translate into a magnetic obliquity (i.e. the orientation of the magnetic field axis compared to the stellar rotation axis - see Sect. 1.2.6) ranging from

15° to 45°. As mentioned previously, this estimation rests on several hypotheses, including the assumption that the observed variation of the filling factors are caused by the stellar rotation only. In addition, it is based on a low number of datapoints. Nevertheless, it can be noticed that this estimated range is consistent with the one of 16° to 26° estimated for the same epoch in Sect. 3.2.8. This estimation was based on measurements of the average line of sight magnetic field. The estimated range is also consistent with the magnetic obliquity of 18° for 2011 measured by McGinnis et al. (2020) and based on the radial velocity variability of the He ɪ line. In comparison, obliquities ranging from 5° to 60° have been measured for other TTs (see e.g. Johnstone et al. 2014; Alencar et al. 2018; McGinnis et al. 2020; Pouilly et al. 2020; Donati et al. 2020a; Finociety et al. 2023).

Regarding the structure of the accretion spots, the current consensus is that a lower-density area encircles a denser center (see Espaillat et al. 2021). However, a combination of at least two energy fluxes and the corresponding filling factors are required in order to trace two density areas for a single observation. In this project, since each observational veiling was fitted with a single accretion shock model defined by one value of the energy flux and filling factor (see Sect. 4.2.4), the accretion spot structure is approximated by a single-density region solely. Extrapolating from previous studies, where the high-density region dominates in the UV range (see e.g. Ingleby et al. 2013; Espaillat et al. 2021), it can be speculated that the optical range used in this work traces the low-density part of the spot. This is supported by the fact that the highest energy flux of $\mathscr{F} = 2.15 \times 10^{11}\ \mathrm{erg\,s^{-1}\,cm^{-2}}$ that was found here is lower than the value of $1.00 \times 10^{12}\ \mathrm{erg\,s^{-1}\,cm^{-2}}$ usually used in the literature for the high-density region (see e.g. Espaillat et al. 2021; Pittman et al. 2022). By not taking the UV emission into account, the total energy flux may therefore be underestimated.

## 4.4 Conclusions

In this chapter, the accretion onto DK Tau was investigated using ESPaDOnS spectra from 2010 and 2012. First, the mass accretion rates for each observation were calculated using accretion-powered emission lines and computing the accretion luminosities. Values were found ranging from $\log{(\dot{M}_{\mathrm{acc}}[M_\odot\ \mathrm{yr}^{-1}])} = $ -8.20 to $\log{(\dot{M}_{\mathrm{acc}}[M_\odot\ \mathrm{yr}^{-1}])}$ = -7.62 in 2010, and from $\log{(\dot{M}_{\mathrm{acc}}[M_\odot\ \mathrm{yr}^{-1}])} = $ -8.15 to $\log{(\dot{M}_{\mathrm{acc}}[M_\odot\ \mathrm{yr}^{-1}])}$ = -7.40 in 2012. These values agree with the ones mentioned in the literature (see e.g. Gullbring et al. 1998; Fischer et al. 2011; Ingleby et al. 2013; Fang et al. 2018; Gangi et al. 2022).

Additionally, as Stock et al. (2022) have found for the cTTs RU Lup (see also Muzerolle et al. 1998, for other cTTs), a power-law correlation between the accretion luminosity and the optical veiling was found for DK Tau. This means that, within

the uncertainties, by measuring the veiling at a single wavelength, one can infer the accretion luminosity, which is a global quantity in terms of wavelength. If a similar correlation is found for additional stars, it could be a helpful means of verifying the estimation of the accretion luminosity. Because the veiling does not depend on extinction, it could be particularly useful for high extinction regions.

The mass accretion rates onto DK Tau and for each night were also derived by fitting the optical veiling with accretion shock models. The values of $\dot{M}_{\mathrm{acc}}$ extracted from both methods agree within a factor of 2 for most observations. The accretion shock models used are characterized by an energy flux and a filling factor. The energy fluxes range from $1.30 \times 10^{10}\ \mathrm{erg\,s^{-1}\,cm^{-2}}$ to $9.45 \times 10^{10}\ \mathrm{erg\,s^{-1}\,cm^{-2}}$ in 2010, and from $1.00 \times 10^{9}\ \mathrm{erg\,s^{-1}\,cm^{-2}}$ to $2.15 \times 10^{11}\ \mathrm{erg\,s^{-1}\,cm^{-2}}$ in 2012. And the filling factors range accordingly from 4.8 % to 2.6 % in 2010, and from 11.7 % to 3.0 % in 2012. For each observation, a single energy flux with its assigned filling factor was used, making the approximation that one homogeneous accretion spot is dominating the optical emission. The values of $\mathscr{F}$ and $f$ that were found are comparable to the ones mentioned in the literature for other stars and using multiple sets of $\mathscr{F}$ and $f$ (see e.g. Robinson and Espaillat 2019; Espaillat et al. 2021; Pittman et al. 2022).

Several quantities, including the values of veiling at 617.50 nm, the accretion luminosity, and the mass accretion rate seem to be rotationally modulated. This is more apparent for the 2010 epoch. The accretion might be more intrinsically variable in the 2012 observations. Using the 2010 dataset, the values of the filling factors folded in phase were compared with curves of the projected surface of a theoretical single, stable and point-like accretion spot for a star with DK Tau's inclination. Consequently, it was estimated that the spot could be located between +45° and +75° in latitude, under the hypothesis that the observed variation of the filling factors are caused by the stellar rotation only. Assuming that the position of the accretion spot is found at a similar location as with the magnetic pole, a magnetic obliquity ranging from 15° to 45° was inferred. This is consistent with the obliquities estimated in Sect. 3.2.8 and by McGinnis et al. (2020).

<div style="border:1px solid #900; padding:1em;">

# 5

# Magnetic mapping of DK Tau

</div>

$\mathcal{A}$ preliminary study of the large-scale magnetic field configuration and of the photospheric brightness distribution of DK Tau is described in this chapter. This is based on Zeeman-Doppler Imaging (ZDI) reconstruction.

## 5.1 Introduction & observations

The current chapter presents a preliminary analysis of the large-scale magnetic topology and strength (linked to non-accreting regions), and of the relative photospheric brightness of DK Tau. In addition, it describes their evolution with time. This work was done using ZDI on the photospheric absorption lines and the limitations of this approach for cTTs is discussed as well.

The dataset consist of two sets of dual-epoch spectra, from 2010 and 2012, taken with ESPaDOnS and NARVAL (see Sect. 2.1). The data covers at least one stellar rotation cycle in both epochs, which allows one to examine the full configuration of DK Tau's magnetic field at those times. The day to day changes observed in the magnetic field should stem only from the stellar rotation phase, since the magnetic field is not expected to display substantial variability during the timescale of each set of observations. ZDI is therefore investigating a single magnetic topology over different phases. It should however be noted that the accretion pattern is subject to strong variability during the timescale of an observation set, and that the photospheric brightness reflects accretion. Examining the magnetic field for more than one epoch allows one to study the variation of the topology with time.

The subsequent section details the analysis and results for the ZDI reconstruction based on photospheric absorption lines. It is followed by an examination of DK Tau's parameters using ZDI.

## 5.2 Analysis & results

### 5.2.1 Applying ZDI on the photospheric absorption lines

The large-scale magnetic field configuration of a star, as well as its photospheric brightness distribution, can be recovered using ZDI (see Sect. 1.2.7). The ZDI imple-

mentation described by Folsom et al. (2018) was used on the photospheric absorption lines. It is based on the ZDI method of Semel (1989), Donati and Brown (1997) and Donati et al. (2006b). It models the magnetic field using a combination of spherical harmonics (see Sect. 1.2.8) following Donati et al. (2006b), and provides fits that minimize $\chi^2$ and maximize entropy following Skilling and Bryan (1984). Because there are multiple magnetic configurations that can fit a set of observations for a given $\chi^2$ level, a unique reconstruction is reached by selecting the maximum entropy solution (i.e. which contains the least amount of information), while the target reduced $\chi^2$ is set by the user. First the surface brightness was fitted using the Stokes I LSD profiles (see Sect. 1.2.4 and 3.2.5), then the magnetic field was fitted using the Stokes V LSD profiles and the surface brightness result as an input. The following paragraphs will present the details of the various operations.

ZDI was run on both the ESPaDOnS and NARVAL Stokes I/V LSD profiles using the parameters that were derived previously: $i$ = 58° (see Sect. 3.3.1), $P$ = 8.2 days (see Sect. 3.2.6) and $v \sin i$ = 13.03 km s$^{-1}$ (see Sect. 3.2.2). The code requires that several additional input parameters be specified. As when obtaining the LSD profiles (see Sect. 3.2.5), the normalization parameters were set to $\overline{g}$ = 1.40 and $\overline{\lambda}$ = 650.0 nm. In addition, $\overline{d}$ was set to 0.78. Indeed, after a first run, ZDI offers a value for $\overline{d}$, that might differ from the one used with LSD. It was the case here and that value was subsequently used for all the nights.

The width of the Gaussian line profile was set to 2.5 km s$^{-1}$, and the Lorentzian width for the line to 1.4 × the Gaussian width. The Gaussian and Lorentzian widths are chosen in order to set the Voigt profile, which represents the intrinsic line profile (i.e. the intrinsic LSD profile) without magnetic field and rotational broadening (i.e. a symmetric and narrow profile). Initial values were chosen based on studies of similar stars, and consequently varied until they gave the best fit between the artificially broadened Voigt profile created by ZDI and the observational mean line profile produced by LSD.

The maximum degree of the spherical harmonic coefficients ($\ell_{max}$ - see Sect. 1.2.8) was fixed to 15. Because the differential rotation value is unknown, it was set at zero (as was done for other stars in the literature). The radial velocity for the center of the line was set to 16.5 km s$^{-1}$, the starting and ending velocities (which denote the range that will be used for the ZDI fit) were set to -35.0 and 35.0 km s$^{-1}$ respectively, based on the average Stokes I LSD profile (see Fig. 3.7). The Heliocentric Julian date were specified for each night (see Table 2.1). Because ZDI operates on the assumption of a rotating star (see Sect. 1.2.7), it needs to know the rotation period of said star and the dates at which the observations were taken.

It should be noted that the code does not take the uncertainties associated with the input parameters into account. It also does not constrain the input variables. If

the user wants to vary a specific parameter about its uncertainties, they need to run the code with a different parameter value each time, and compare the results in order to estimate the best value.

In both epochs, there were nights that could not be well fit by ZDI. For the 2010 epoch, these were the first night for the Stokes I and Stokes V LSD profiles in the ESPaDOnS data; the third, fourth and fifth night in Stokes I, the third and sixth night in Stokes V in the NARVAL data. For the 2012 epoch, these were the third night in Stokes I and the seventh night in Stokes V in the ESPaDOnS data; the first two nights in Stokes I and the first night in Stokes V in the NARVAL data. These nights seem to present some non-rotational intrinsic variability most likely driven by accretion, which cannot be fit correctly by ZDI since it assumes that any variability stems from rotational modulation only[1]. These LSD profiles were therefore removed from the fits, as the impact of systematic errors, due to this unaccounted for variability, would distort the maps worse than the loss of phase coverage. Figures 5.1 and 5.3 show the ZDI fits (in red) on the Stokes I and Stokes V LSD profiles (in black) for the 2010 and 2012 epoch respectively.

When using a target reduced $\chi^2$ of 1, there was intense overfitting with brightness map values close to zero. This is probably due to a high signal to noise ratio in the LSD profiles and strong variability. Therefore small imperfections in the model, as well as small underestimates in the uncertainties, could lead to large reduced $\chi^2$ values. The target reduced $\chi^2$ was consequently increased in order to obtain a more reliable fit. For the 2010 dataset, a target reduced $\chi^2$ of 5.5 for Stokes I and of 1.0 for Stokes V were used. For the 2012 epoch, a target reduced $\chi^2$ of 9.0 for Stokes I and of 1.5 for Stokes V were used. Although, in theory, a reduced $\chi^2$ of 1 would indicate that the synthetic profiles produced by ZDI perfectly fit the observations, this can result in overfitting, producing physically unrealistic solutions (e.g. maps with little to no features). Consequently, in practice, the target reduced $\chi^2$ provided by the user can be larger than 1 (see e.g. Donati et al. 2010, 2011; Finociety and Donati 2022). The target reduced $\chi^2$ chosen in this project correspond to the lowest values that did not lead to overfitting in the form of featureless maps.

The ZDI maps for 2010 and 2012 can be seen in Fig. 5.2 and 5.4. The stellar spherical surface is shown as a strip of the latitude as a function of rotational phase (which is used as a proxy for the longitude). The first map represents DK Tau's relative brightness across the stellar surface. A value of 1.0 refers to the undisturbed photosphere (and the invisible portion of the star is set at this default value), while 0.0 means complete darkness. The next four maps show the magnetic field of DK Tau in units of G. The first of these maps represents the total magnetic field, whereas the

---

[1]During an initial ZDI run with an inclination of 21° (the inclination of the outer disk axis), these same nights could not be well fit by ZDI, strengthening the argument of intrinsic variability driven by accretion regardless of the inclination.

last three maps represent the different vector components of the stellar magnetic field (see Sect. 1.2.8). In order, these are the radial field (away from the center of the star), the azimuthal field (along the east-west direction) and the meridional field (along the north-south direction). In 2010, a portion of the rotational phase (between 0.80 and 1.00) is not covered by the observations, so the information there is extrapolated by ZDI. Similarly, in 2012, there is a gap (between 0.28 and 0.52) in the coverage.
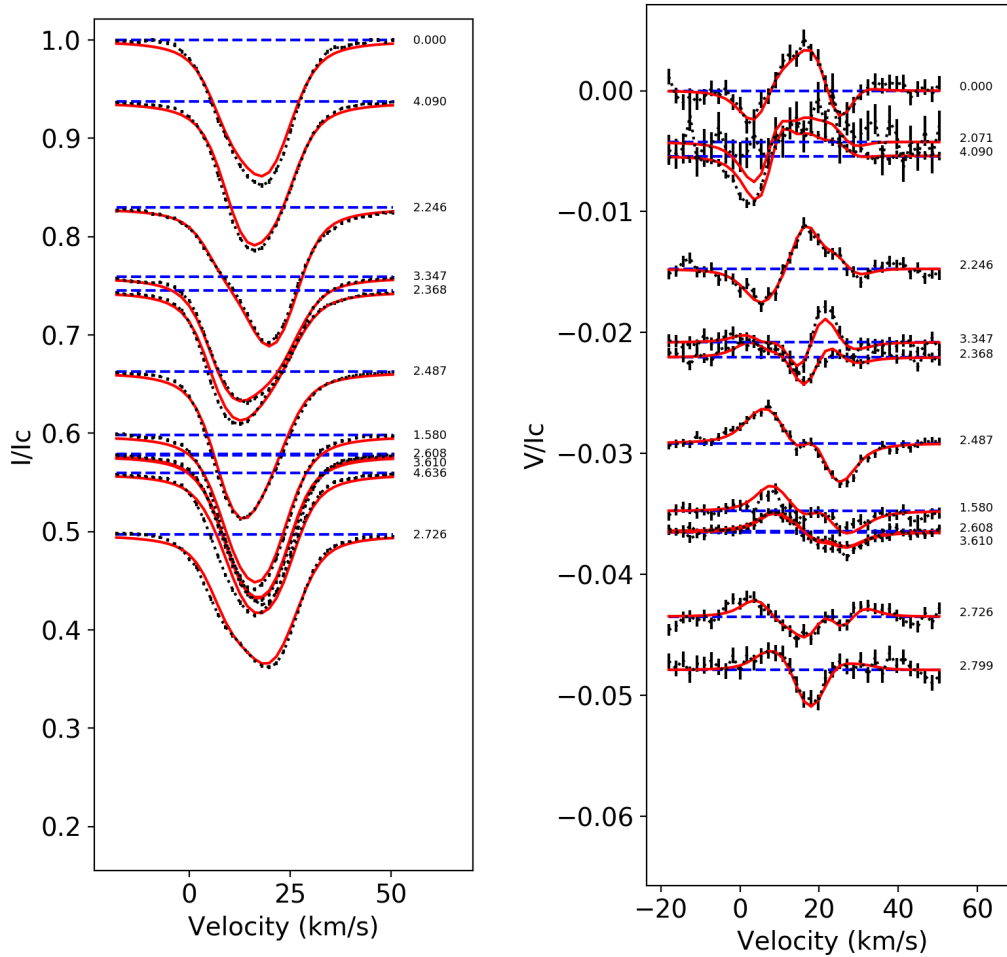


Figure 5.1 – ZDI fits on the Stokes I (let panel) and Stokes V (right panel) LSD profiles for the 2010 epoch. Both are normalized to the continuum ($I_c$) and shown as a function of the velocity. The observations (i.e. the LSD profiles of the photospheric absorption lines) are represented by the black dots and have been shifted vertically, by rotation phase, for clarity. The fit is the red line. The continuum is pictured as the blue dashed line. The numbers to the right of the curves show the rotation cycle of the observation, relative to the first observation.

Regarding the 2010 reconstructed large-scale magnetic strength (see Sect. 1.2.8), ZDI finds that DK Tau has a mean magnetic field ($\langle B \rangle$ - the magnitude of the magnetic vector averaged over the visible hemisphere) of 0.62 kG and a maximal field of 4.02 kG located close to the equator. Regarding the large-scale magnetic configuration, it is described through fractions of the magnetic energy (which is proportional to $B^2$). The poloidal component[2] (approximately directed

---

[2]The poloidal and toroidal components are another decomposition of the magnetic field compared to the radial, azimuthal and meridional components (see Sect. 1.2.8).
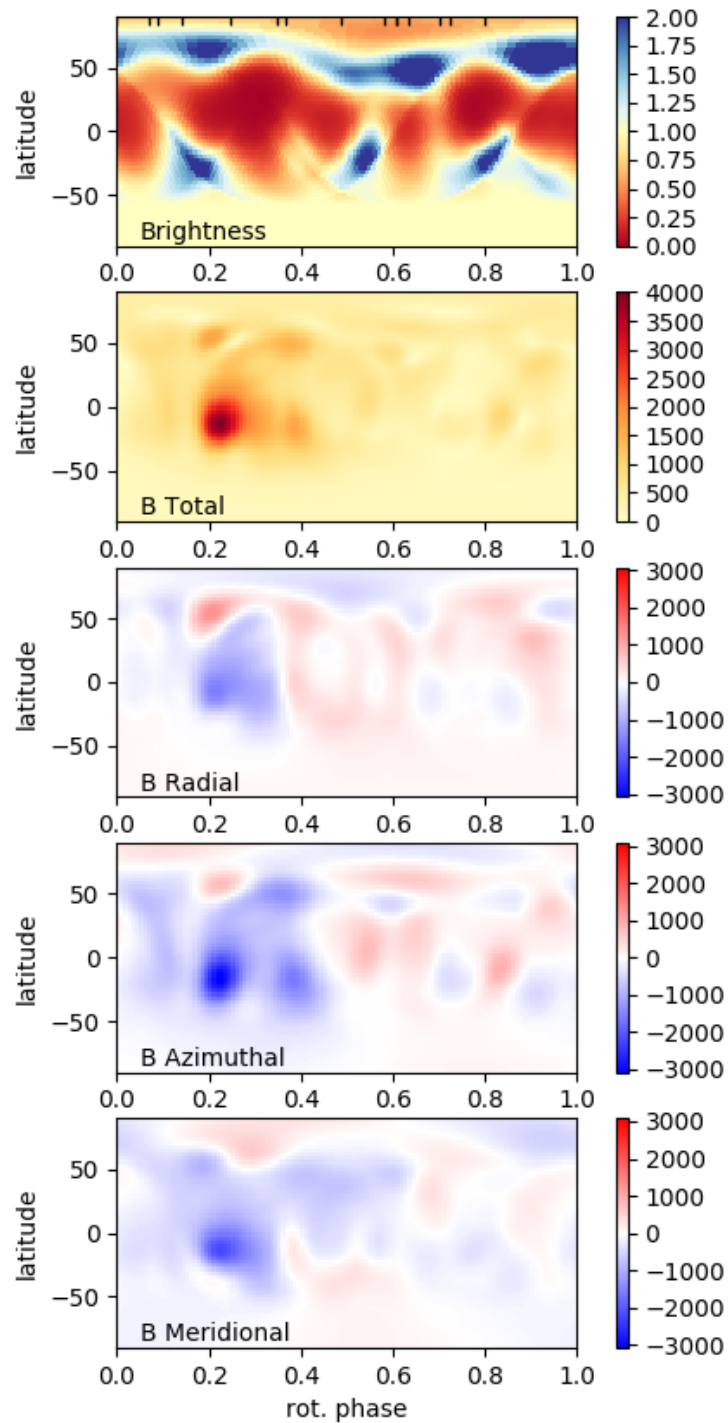
Figure 5.2 – ZDI maps (based on the photospheric absorption lines) for the 2010 epoch. The stellar spherical surface is shown as a strip of the latitude as a function of rotational phase (which is used as a proxy for the longitude). The first map represents DK Tau's relative brightness across the stellar surface. The ticks at the top indicate the phases at which the spectra have been obtained. The last four maps represent the different components of the magnetic field (i.e. the total, radial, azimuthal and meridional magnetic field) associated with the photospheric absorption lines, in units of G.
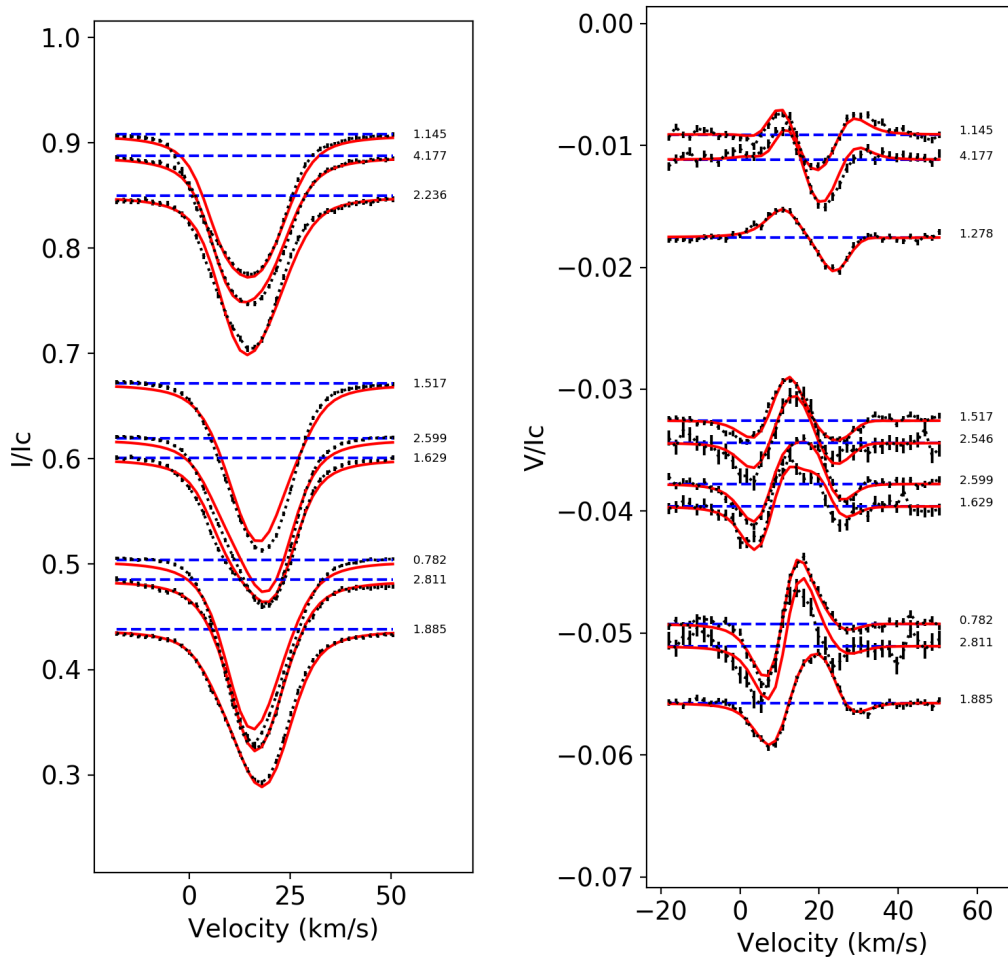
Figure 5.3 – Same as Fig. 5.1, for the 2012 epoch.
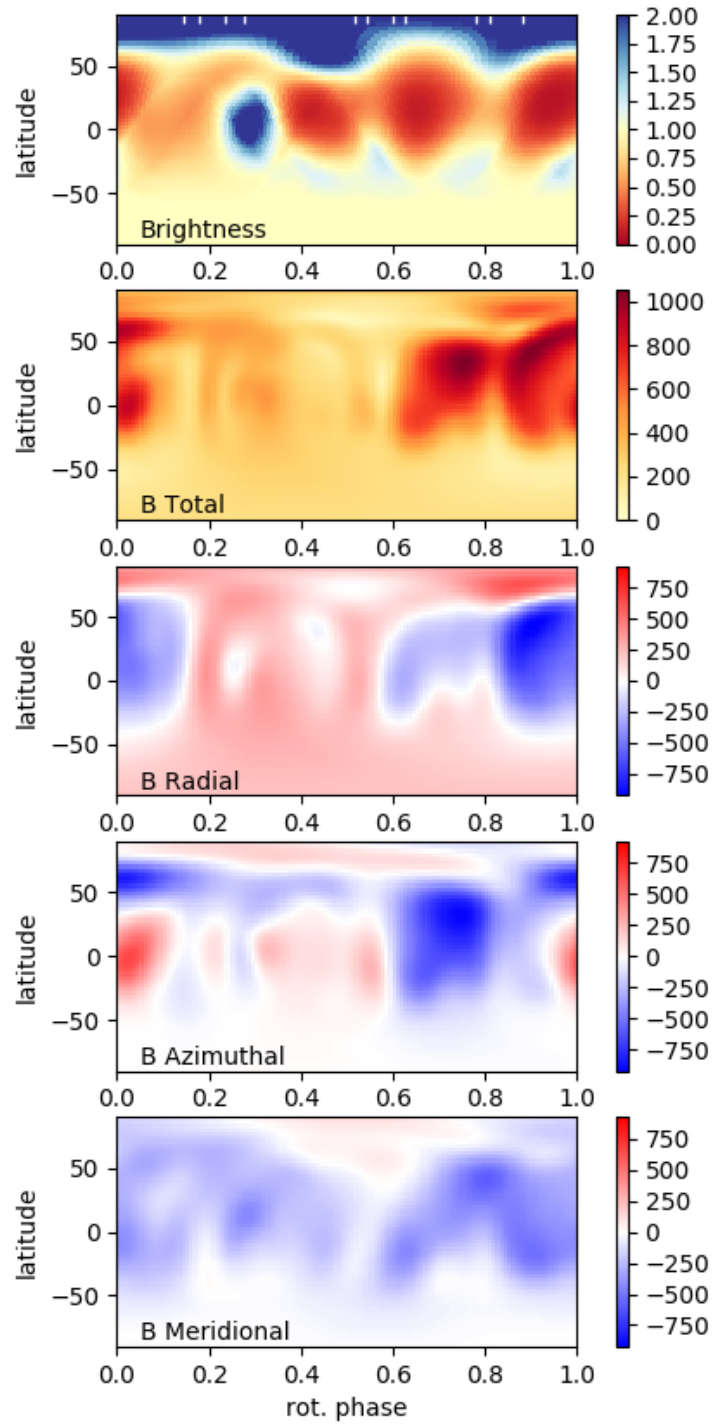
Figure 5.4 – Same as Fig. 5.2, for the 2012 epoch.

vertically) is dominant, accounting for 68 % of the magnetic energy, while the toroidal component (approximately directed horizontally) accounts for only 32 % of the total magnetic energy. Within the poloidal field, the dipolar component is strongest (at 46 %), followed by a quadrupolar component (at 18 %). Within the toroidal field, the $\ell = 1$ component dominates as well (at 37 %), followed by the $\ell = 2$ component (at 27 %). The total axisymmetric component (i.e. the symmetry about the stellar rotation axis, when $m = 0$ in the spherical harmonic coefficients) is at 22%, and the axisymmetry of the poloidal field component is at 17%.

In 2010, in the distribution of relative photospheric brightness reconstructed by ZDI, the higher latitudes are dominated by brighter areas, with a few bright areas near the equator as well. These do not refer to bright/hot spots, which are due to accretion shocks, as accretion-powered emission lines are the ones tracing the bright spots and ZDI was used on the photospheric absorption lines. The brighter areas are surrounded by dark/cool spots, which are due to the magnetic field lines emerging at the surface of the star.

Two years later, ZDI finds that DK Tau has a mean magnetic field of 0.41 kG and a maximal field of 1.05 kG located between 0° and 50° in latitude. The mean value is similar to the one measured previously, while the maximum is lower and covers a larger area. The poloidal component of the magnetic field dominates at 80 % (a higher percentage than two years prior), while the toroidal component accounts for only 20 % of the total magnetic energy. Within the poloidal field, the dipolar component is the dominating one (at 59 %), followed by a quadrupolar component (at 23 %). Within the toroidal field, unlike two years prior, the $\ell = 2$ component is strongest this time (at 36 %), followed by the $\ell = 1$ component (at 26 %). The total axisymmetric component is at 37%, and the axisymmetry of the poloidal field component is at 35%. As in other TTs (see e.g. Gregory et al. 2012), the magnetic field changes between the epochs, which supports the dynamo-generated field theory. Table 5.1 summarizes the ZDI-recovered magnetic properties of DK Tau for both epochs.

In the distribution of relative photospheric brightness obtained for the 2012 epoch, there is one brighter area at around 50° in latitude. Dark spots populate the lower latitudes.

Regarding the accuracy of ZDI maps, it should be noted that they are unable to recover the small-scale magnetic field components, i.e. they have a lower resolution than solar maps. This is inherent to ZDI, as the technique suffers from flux cancellation effects (see e.g. Morin et al. 2008; See et al. 2019). The maps produced are thus tracing the large-scale magnetic field components only.

ZDI has been used reliably for many years, and multiple studies have demonstrated its robustness (see e.g. Donati and Brown 1997; Hussain et al. 2000;

Table 5.1 – Summary of the ZDI-recovered magnetic properties of DK Tau based on the photospheric absorption lines

|  | 2010 | 2012 |
| --- | --- | --- |
| $\langle B \rangle$ (kG) | 0.62 | 0.41 |
| $B_{max}$ (kG) | 4.02 | 1.05 |
| Poloidal component (% total) | 68 | 80 |
| Toroidal component (% total) | 32 | 20 |
| Dipolar component (% poloidal) | 46 | 59 |
| Quadrupolar component (% poloidal) | 18 | 23 |
| $\ell$=1 component (% toroidal) | 37 | 26 |
| $\ell$=2 component (% toroidal) | 27 | 36 |
| Axisymmetry (% total) | 22 | 37 |
| Axisymmetry (% poloidal) | 17 | 35 |

Kochukhov and Piskunov 2002; Morin et al. 2008, 2010; Yadav et al. 2015).

However, there are limitations to this technique. First, the spacial resolution of the reconstruction depends on the stellar $v \sin i$, with the highest available $\ell$ degree of the spherical harmonic coefficients being proportional to $v \sin i$ (see e.g. Morin et al. 2010; Folsom et al. 2018).

Next, for stars with low inclinations (i.e. stars that are seen close to pole-on), the reconstruction of the magnetic field at low latitudes can be challenging, or inaccessible in the case of a constantly obscured hemisphere (see e.g. Donati and Brown 1997).

In addition, by comparing with the magnetic field measured by Zeeman broadening, several studies have found that ZDI usually retrieves between 10 % and 25 % of $\langle B \rangle$ (see e.g. Reiners and Basri 2009; Morin et al. 2010; Kochukhov and Shulyak 2019; See et al. 2019). While ZDI is able to map the large-scale magnetic field geometry, but is subject to cancellation effects, the Zeeman broadening technique is insensitive to the field geometry, but does not suffer from cancellation effects (see e.g. Reiners 2012; See et al. 2019).

Lehmann et al. (2019) explored the capabilities of ZDI by using synthetic observations. They used 3D photospheric magnetic field simulations of slowly rotating sun-like stars with weak activity. Regarding the stellar parameters, the simulations assumed a stellar inclination of either 20° or 60°, and $v \sin i$ values ranging from 0.64 to 2.58 km s$^{-1}$. For each simulation, 25 phases evenly sampling the stellar rotation period were used. The simulated magnetic field strength varied and went up to 8 G. Lehmann et al. (2019) used the simulations as input in ZDI, then compared the recovered ZDI maps with the simulations. They did not use the fully resolved simulations for the comparison, but restricted them to their large-scale components instead, by only considering $\ell \leqslant 7$. This was done in order to allow for a direct comparison, given the flux cancellation limitations of ZDI. Lehmann et al. (2019) found that ZDI reason-

ably reproduces the large-scale magnetic geometry of the simulations. Furthermore, ZDI provides better results for more active stars with high $v \sin i$ values and high inclinations (i.e. stars that are seen close to edge-on). However, Lehmann et al. (2019) also found that ZDI underestimates the field strengths, by approximately an order of magnitude for the low-$\ell$ field modes, although there was less discrepancy for simulations with a higher magnetic field strength. The authors explain that this is due to the fitting routine that minimizes $\chi^2$ and maximizes entropy. Indeed, because the LSD profiles can be fitted with a range of magnetic field values for a given $\chi^2$ level, and the maximum entropy solution searches for the lowest energy solution, this means that the simulated magnetic field can be underestimated while there still is an equally good fit to the LSD profiles. They observe that the level of underestimation varies, in particular with the stellar activity, inclination and $v \sin i$ value. Consequently, they are not able to determine a general correction factor for the field strengths provided by ZDI. They therefore advice caution when using the absolute values for the field strength, but note that the fractions of the individual field components recovered by ZDI are generally in agreement with the simulations within 20 %.

Regarding the estimated uncertainties of the ZDI maps that are presented in this project, a few specific elements can be noted. The inclination of 58° for the rotation axis of DK Tau, as well as its $v \sin i$ value of 13.03 km s$^{-1}$ and its magnetic field strength of the order of the kG are an advantage for the ZDI reconstruction. On the contrary, the low phase coverage is a limiting factor.

## 5.2.2 Inclination estimate using ZDI, stellar period & $v \sin i$ confirmation

To confirm the hypothesis of a substantial misalignment between the rotation axis of DK Tau and its outer disk axis (see Sect. 3.3.1), the full range of possible inclinations was tested on the ESPaDOnS data with ZDI. A grid of models of varying inclinations (covering the whole parameter interval) was run. The final entropy calculated for each model that converged was compared, in a search for which inclination results in the maximum entropy. The results are consistent with the higher inclination hypothesis (see Figures 5.5 and 5.6), though it is not possible to pinpoint a precise value of inclination from them. It can however be noted that the results strongly disfavor the possibility of an inclination of 21° for the rotation axis of DK Tau.

Next, using the best entropy value from the grid search as a target for the models (see e.g. Petit et al. 2002; Folsom et al. 2018), the grid of different inclination values was repeated, this time comparing the resulting values of reduced $\chi^2$. The reduced $\chi^2$ was thus plotted as a function of the inclination for that entropy (see Figures 5.7 and 5.8). This yields four measurements of the inclination derived from ZDI, with two

Figure 5.5 – Entropy as a function of the inclination for the Stokes I (top panel) and Stokes V (bottom panel) LSD profiles of the photospheric absorption lines for the 2010 ESPaDOnS data. The models are converging for inclinations higher than 20°. The curves argue for an inclination that is at least higher than 40°, with a best value between 60° and 70°.
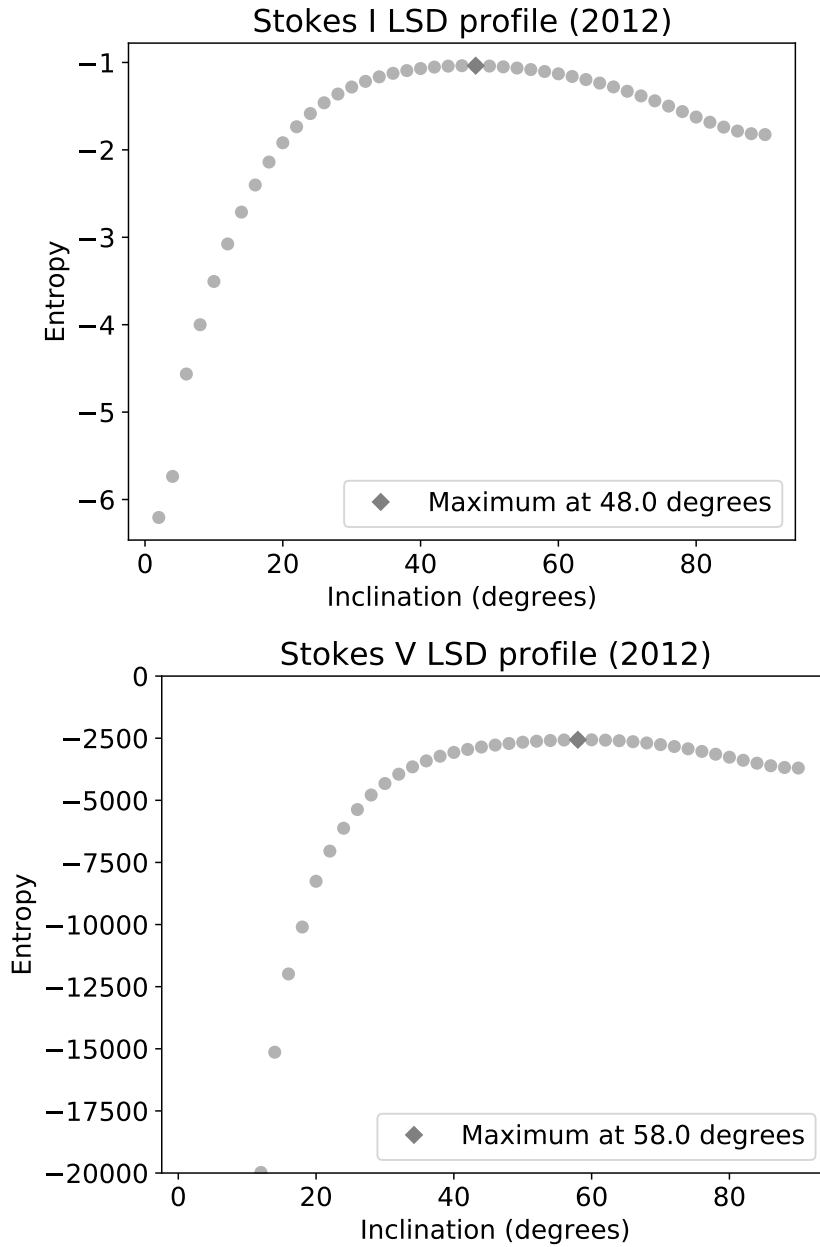
Figure 5.6 – Same as Fig. 5.5, for the 2012 epoch. For the Stokes I (top panel) LSD profiles, the models are converging for an inclination higher than 4°. For the Stokes V (bottom panel) LSD profiles, the models are converging for an inclination higher than 20°. The plots are consistent with the ones based on the 2010 dataset. They also argue that an inclination between 40° and 80° yields higher entropy.

properly independent datasets (i.e. for 2010 and 2012), and Stokes I and Stokes V LSD profiles information for each set. The best inclination was estimated by taking the average of the values, and the range of values on either side of the average as the uncertainty: $i = 61°$ (+11)(-13). Four values is a low number for statistics, however, in order to use the variation in reduced $\chi^2$ about a minimum to determine the uncertainty on the inclination, there is the difficulty of establishing the number of free parameters, as it is not well defined in a regularized fitting process. Additionally, the method of using the average should incorporate some systematic uncertainties, making it plausibly more realistic than any formal uncertainty that could be calculated. The inclination estimated using ZDI agrees, within the error bars, with the value of 58° derived in Sect. 3.3.1. Moreover, it was possible to set a lower target reduced $\chi^2$ without overfitting when using an inclination of 58° than when using an inclination of 21° (the inclination of the outer disk axis), for both Stokes I/V and for both epochs. Allowing the rotation axis of DK Tau to be misaligned with its outer disk provides a better fit for ZDI.

**Stellar period and $v \sin i$ confirmation using ZDI**

In addition to the inclination, ZDI was also used to confirm the values of the stellar period and of $v \sin i$ derived in Chapter 3. A range of possible periods was tested using the ESPaDOnS Stokes I LSD profiles. Unfortunately, using the Stokes V LSD profiles did not give probative results. A grid of models was run, varying the period. The entropy was compared for models that converged. Periods of 8.1 and 8.3 days maximize the entropy for the 2010 and 2012 datasets respectively. These values are close to the 8.2 days value calculated in Sect. 3.2.6. The $v \sin i$ was also varied around the derived value and it was found that different values did not give a better fit with ZDI.

## 5.3 Discussion

In this section, two points in particular will be discussed. The first one relates to the comparison of the ZDI maps of DK Tau between the two epochs, as well as with maps of other stars referenced in the literature. The second one concerns the limitations of using ZDI on the photospheric absorption lines only.

### 5.3.1 ZDI maps based on photospheric absorption lines

In the ZDI magnetic maps computed from the photospheric absorption lines, there are qualitative similarities in the two epochs (see Sect. 5.2.1). They are both

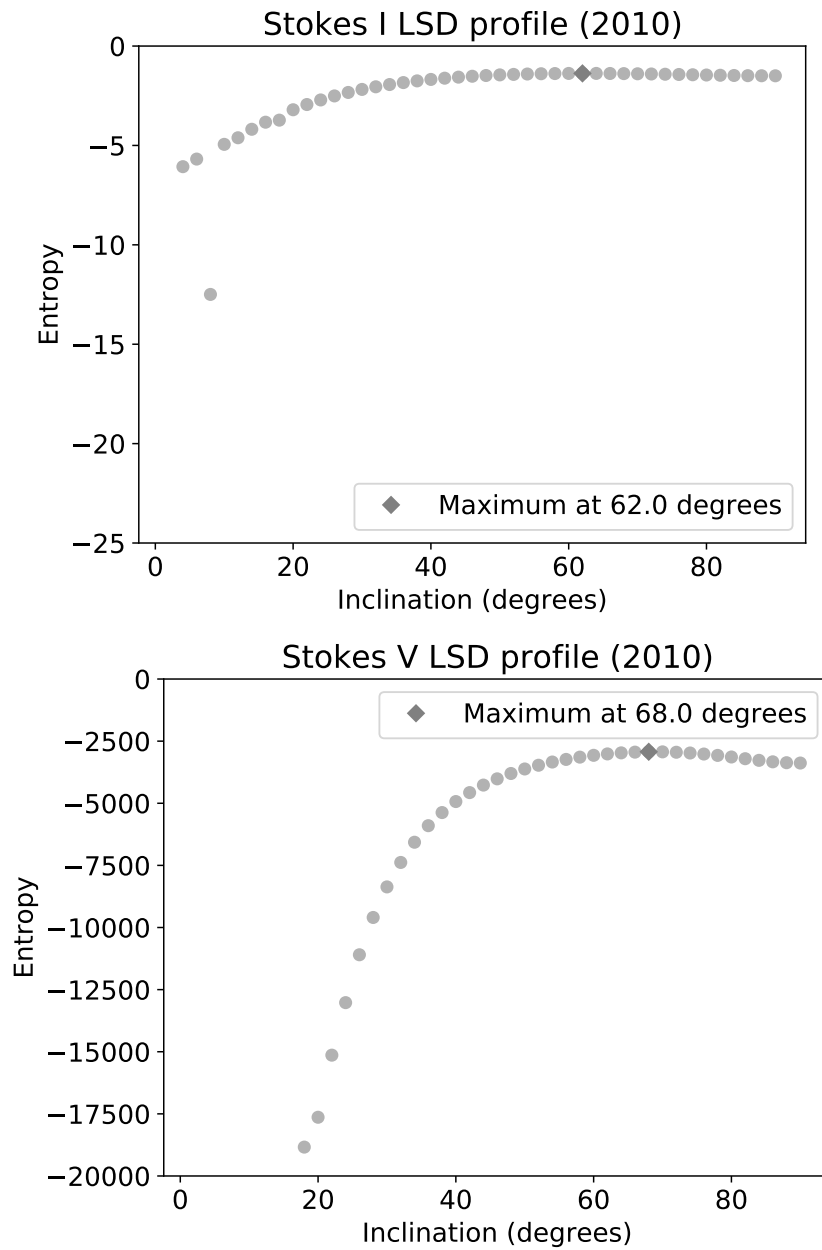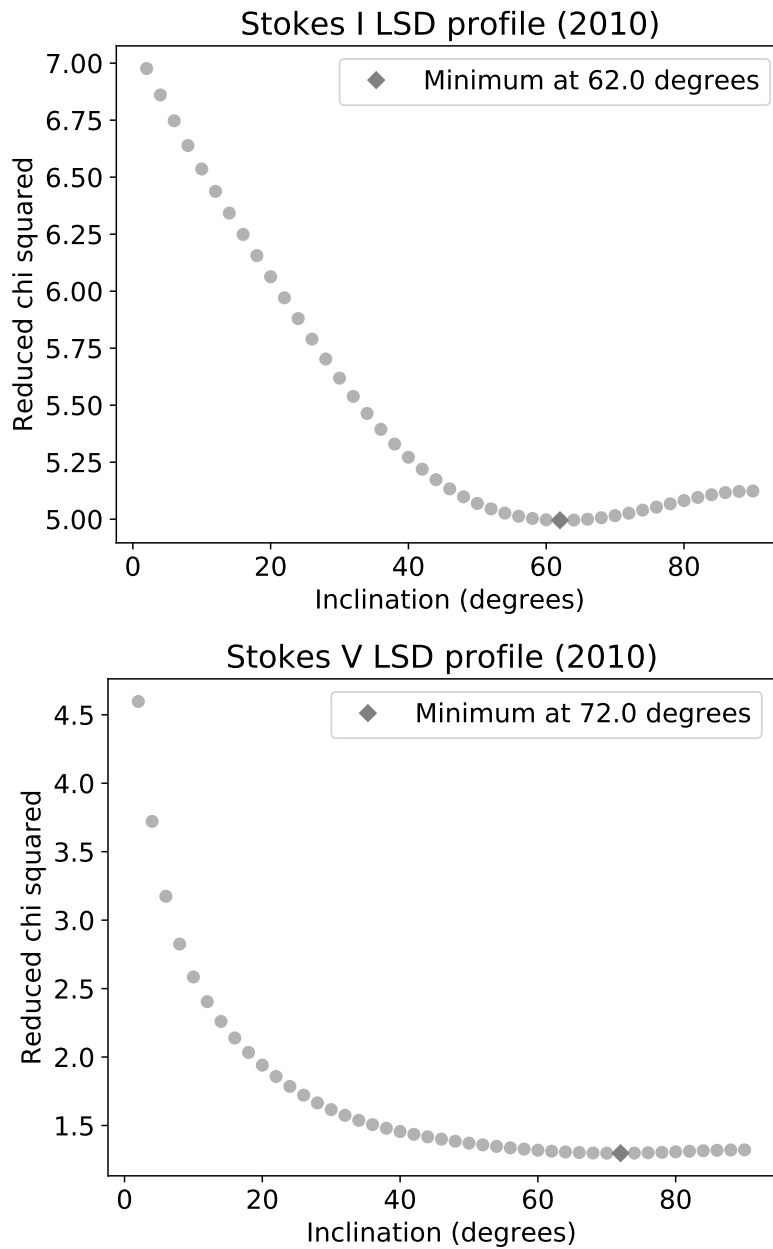Figure 5.7 – Reduced $\chi^2$ as a function of the inclination for the Stokes I (top panel) and Stokes V (bottom panel) LSD profiles of the photospheric absorption lines for the 2010 ESPaDOnS data.
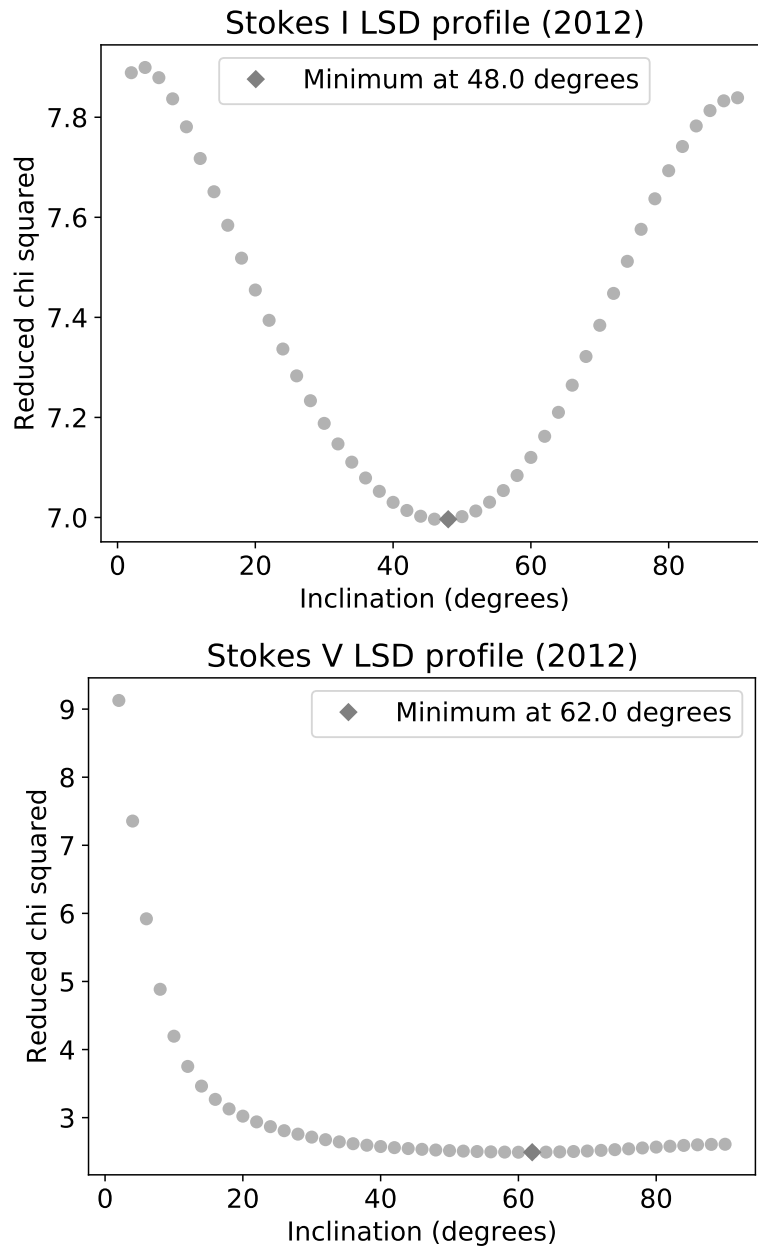
Figure 5.8 – Same as Fig. 5.7, for the 2012 epoch.

largely poloidal, with a strong poloidal dipolar component, and more modest poloidal quadrupolar components. They are also largely non-axisymmetric. Thus while the details of the magnetic field have changed, the large-scale geometry has not radically altered over two years. In the brightness maps, a high latitude brighter area seems to be qualitatively consistent between the two epochs, although the exact position and extent of it have changed. There are also qualitative similarities in the large darker regions at lower latitudes.

Regarding connections between the brightness and magnetic field structures derived from ZDI using the photospheric absorption lines, there is a correlation between dark/cool spots and regions of strong magnetic fields, as expected since the latter are causing the dark spots. As ZDI was used on the photospheric absorption lines, and not emission lines sensitive to accretion shocks, it is not surprising that there is no correlation between brighter areas (which are not bright/hot spots due to accretion) and regions of high field strength.

Compared to other cTTs, there are similar levels of complexity in DK Tau's radial maps as for example for CR Cha and CV Cha (see Hussain et al. 2009; Johnstone et al. 2014), or V807 Tau (see Pouilly et al. 2021), whose ZDI maps were also computed from photospheric absorption lines only. Regarding the photospheric brightness distribution, the maps for DK Tau are more complex and contrasted as the one for V807 Tau. The mean magnetic fields (averaged over the visible hemisphere) derived from ZDI are twice as large as the ones for CR Cha and CV Cha, and approximately ten times the ones for V807 Tau. They are however nearly half the values found for example for V2129 Oph (see Donati et al. 2007, 2011), BP Tau (see Donati et al. 2008), or GQ Lup (see Donati et al. 2012), whose ZDI maps were simultaneously derived from photospheric absorption lines and accretion proxies. The ZDI analysis of the photospheric absorption lines finds that DK Tau has a mostly poloidal field, in the same manner as V807 Tau, V2129 Oph, BP Tau and GQ Lup; and largely non-axisymmetric, as V807 Tau, but unlike V2129 Oph, BP Tau and GQ Lup. It can also be noted that many cTTs that have been observed so far (see e.g. Donati et al. 2007, 2011, 2012; Hussain and Alecian 2014; Johnstone et al. 2014) present with octupolar-dominant fields and not dipolar-dominant fields.

## 5.3.2 Partial picture of the magnetic field

The photospheric absorption lines give a partial view of the magnetic topology of DK Tau, as it is a cTTs that experiences accretion. The magnetic field deduced from the photospheric absorption lines is a representation of the large-scale field existing at the surface of the star, excluding the regions of strongest accretion. Indeed, because the shocks are at a higher temperature than the photosphere, the information on

these regions is missing in the photospheric absorption lines. Whereas the accretion-powered emission lines give the information on the magnetic field at the regions of the accretion shocks. According to the current magnetospheric accretion paradigm (see Sect. 1.3.1), it is the field present in these accreting regions that is thought to be the strongest component of the global stellar magnetic field and to extend to the circumstellar disk.

In this work, the photospheric absorption lines (see Sect. 5.2.1) and the accretion-powered emission lines (see Sect. 3.2.7) were analyzed separately. There is a caveat with this method, as Donati et al. (2007) have shown for V2129 Oph, a cTTs with low veiling. The ZDI maps obtained when analyzing both types of lines simultaneously differ from the maps computed from the photospheric absorption lines alone, in particular for the radial field and its intensity.

This means that the ZDI analysis of the photospheric absorption lines is a preliminary study of the magnetic field of DK Tau. Although it provides exploratory information on the magnetic topology that pertains to the surface magnetic field, it does not provide information on the topology of the strongest component of the magnetic field that is linked to accretion. Regarding the magnetic intensity, the values derived from ZDI are likely an underestimation of the intensity of the global magnetic field, since they do not take into account the field in the accretion shocks. This can be observed from the values of $B_{\text{los}}$, the average line-of-sight magnetic field, in the photospheric absorption lines (see Sect. 3.2.6) compared to the values of $B_{\text{los}}$ in the emission lines (see Sect. 3.2.7), which are one order of magnitude larger. In addition, the brightness maps displayed here do not provide information on the location of accretion spots, which are traced by accretion-powered emission lines. In order to retrieve this information, the LSD profiles of photospheric absorption lines need to be modeled simultaneously with an accretion-tracing profile (see e.g. Donati et al. 2010).

Furthermore, it would be valuable to be able to compare the ZDI maps based solely on the photospheric absorption lines with ZDI maps based on both photospheric absorption lines and accretion proxies. In particular, it would be useful to see if the later method could improve the fits. This could unfortunately not be done as the ZDI implementation that was used in this work cannot take emission lines into account.

This is the main limitation of this implementation and a useful improvement would be to be able to choose to run ZDI on photospheric absorption lines only, or on photospheric absorption lines and accretion-powered emission lines simultaneously. In addition, one potential small improvement would be to allow the user to vary the input parameters (about their uncertainties) within the code itself and be presented with best-fit values. With the current implementation, the user is able to do this manually, by running ZDI each time they change a parameter. Another potential upgrade

could be to add a routine extrapolating the magnetic field (determined from both photospheric absorption lines and accretion proxies) that reaches the truncation radius and creating 3D maps of the field lines (see e.g. Fig. 11 by Johnstone et al. 2014).

## 5.4 Conclusions

ZDI was run on the ESPaDOnS and NARVAL LSD profiles of the photospheric absorption lines in order to derive the associated large-scale magnetic fields (linked to non-accreting regions). In 2010, ZDI finds a mean magnetic field (averaged over the visible hemisphere) of 0.62 kG and a maximal field of 4.02 kG located close to the equator. The reconstructed magnetic field is largely poloidal (68 % of the magnetic energy). Within the poloidal field, the dipolar component is strongest (at 46 %). The magnetic topology presents a total axisymmetry (i.e. symmetry about the stellar rotation axis) of 22 %. The distribution of relative photospheric brightness displays brighter areas at higher latitudes, and a few bright areas close to the equator. They are surrounded by dark/cool spots.

Two years later, the large-scale geometry of the magnetic field is not radically altered. In 2012, ZDI finds that DK Tau has a mean magnetic field of 0.41 kG and a maximal field of 1.05 kG located between 0° and 50° in latitude. The field is still largely poloidal (80 % of the magnetic energy), with a strong poloidal dipolar component (at 59 %). It is also still non-axisymmetric (with a total axisymmetry of 37 %). Similar levels of complexity are found in the radial maps as for other cTTs (see e.g. Hussain et al. 2009; Johnstone et al. 2014; Pouilly et al. 2021). In the brightness maps, one high latitude brighter area is qualitatively consistent between the two epochs, whereas dark spots populate the lower latitudes.

The derived rotation period of 8.2 days (see Sect. 3.2.6) and the value of $v \sin i$ (see Sect. 3.2.2) were confirmed using ZDI. In addition, the full range of possible inclinations was tested with ZDI: significantly lower values of reduced $\chi^2$ were achieved with a higher inclination, strongly favoring a value of i = 58° over i = 21° (see Sect. 3.3.1).

In conclusion, in this preliminary analysis of the large-scale magnetic field linked to non-accreting regions, DK Tau, presenting with considerable veiling, is found to have similar magnetic properties as the more moderately accreting cTTs studied so far. It should however be noted that there is a caveat in computing ZDI maps from photospheric absorption lines alone when studying an active accretor, as it provides a partial picture of the magnetic field that exclude the accretion regions, which are believed to be the strongest component of the global stellar field.

# 6
# Conclusions and perspectives

$\mathscr{I}$N this chapter, the general conclusions of the thesis will be presented. In addition, suggestions for future work will be discussed.

## 6.1 Conclusions

This thesis examined DK Tau, a low-mass cTTs that experiences magnetospheric accretion. In particular, it studied the magnetic field and investigated the accretion processes in this specific cTTs.

The first project (see Chapter 3) focused on DK Tau's magnetic field. In order to measure the magnetic field, it presented a method of determining and subsequently removing the effect of veiling from the spectropolarimetric observations. These consist of ESPaDOnS and NARVAL data from 2010 and 2012. The values of veiling were determined from night to night and across each spectra, with peak values (at ∼550 nm) ranging from 0.2 to 1.8. Next, $B_{\mathrm{los}}$, the average line-of-sight magnetic field, was determined, on both the photospheric absorption lines and accretion-powered emission lines. The latter has peak values of ∼1.5 kG. In addition, its signatures suggest that DK Tau experiences nearly poleward accretion. This is consistent with the estimate of the magnetic obliquity (i.e. the angle between the stellar rotation and magnetic field axes) of ∼20°. It was derived using the $B_{\mathrm{los}}$ from the emission lines. A rotation period of 8.2 days was recovered, using the $B_{\mathrm{los}}$ as well, this time from the absorption lines for the 2010 dataset. Additional stellar parameters were extracted from the data. These include $T_{\mathrm{eff}}$ = 4 150 ± 110 K and $v \sin i$ = 13.0 ± 1.3 km s$^{-1}$. The truncation radius was estimated at ∼4.5 $R_{\star}$ and the co-rotation radius was calculated at 6.1 $R_{\star}$. In general, DK Tau has magnetic properties that are comparable to the ones of the more moderately accreting cTTs that have been studied so far. Finally, inconsistencies regarding the inclination of the rotation axis of DK Tau, when using the value for the inclination of the outer disk axis, were examined. In particular, its dipper lightcurve is incompatible with a nearly pole-on inclination. It was found that a misalignment between the rotation axis and the outer disk axis is likely. Based on the derived stellar rotational properties, an inclination of 58° (+18)(-11) was calculated for the stellar rotation axis. This is significantly different from the outer disk axis inclination of 21° given in the literature. As misalignments have been found for several cTTs, this poses questions with regards to the classic theories of circumstellar disk formation.

The second project (see Chapter 4) was devoted to the investigation into the accretion processes in DK Tau. It used dual-epoch spectropolarimetric data from ESPaDOnS, collected in 2010 and 2012. The mass accretion rates for each night were derived, using two different procedures in order to compare their results. The first method consisted of calculating $\dot{M}_{\rm acc}$ based on the accretion luminosity obtained via accretion-powered emission lines. This yielded values ranging from $\log(\dot{M}_{\rm acc}[M_\odot\,{\rm yr}^{-1}]) = -8.20$ to $\log(\dot{M}_{\rm acc}[M_\odot\,{\rm yr}^{-1}]) = -7.40$. In addition, a power-law correlation between the values of the accretion luminosity and the optical veiling was identified. This implies the possibility of inferring the accretion luminosity (which is mostly emitted in the UV range) by measuring the veiling at a single wavelength in the optical. The second approach for extracting the values of $\dot{M}_{\rm acc}$ relied on the fitting of accretion shock models to the optical veiling. It produced results similar to the first method. The shock models are characterized by an energy flux and a corresponding filling factor. The latter represent the fraction of the stellar surface covered by an accretion spot. By comparing the filling factor values derived from the shock model with theoretical curves of the apparent area of the spot, the location of the spot was estimated. These theoretical curves are based on the assumptions of a single, stable, point-like accretion spot. An additional hypothesis is that the observed variations of the filling factors with time are only due to the motion of the spot relative to the observer as the star rotates. For the 2010 epoch, the accretion spot was inferred to be located between +45° and +75° in latitude. This translate into an estimated magnetic obliquity ranging from 15° to 45°, in agreement with the value derived during the first project.

The third part of this work (see Chapter 5) presented a preliminary magnetic mapping of DK Tau, using ZDI on the photospheric absorption lines only. The data consist of ESPaDOnS and NARVAL spectropolarimetric observations from 2010 and 2012. In 2010, ZDI finds that DK Tau hosts a mainly poloidal large-scale magnetic field. The mean value (averaged over the visible hemisphere) is of 0.62 kG. The maximal value is of 4.02 kG and located close to the equator. Two years later, DK Tau is found to have a mean magnetic field of 0.41 kG. The maximal field is of 1.05 kG and located between 0° and 50° in latitude. The poloidal component is the dominant component in this epoch as well. Regarding the evolution of the magnetic field with time, while the details of the field have changed, the large-scale topology has not radically changed over two years. With ZDI, it was confirmed that DK Tau's rotation axis is likely misaligned comparent to its outer disk axis. Lastly, the limitations of this approach were underlined. Using ZDI solely on the photospheric absorption lines when mapping an actively accreting star gives a partial picture of the magnetic field that exclude the accretion shock regions.

## 6.2 Perspectives

### 6.2.1 Applying ZDI on both absorption and emission lines

Chapter 5 presents a preliminary investigation of the magnetic topology of DK Tau using the photospheric absorption lines. It also describes the limitations of this method. Indeed, excluding the accretion-powered emission lines from the ZDI reconstruction will only provide a partial view of the magnetic topology of the star. This is because this omits the magnetic field at the regions of the accretion shocks. In order to carry out a complete analysis of the magnetic field, ZDI needs to be applied to both the photospheric absorption lines and emission lines, as Donati et al. (2007) have done for V2129 Oph. This would allow the reconstruction of the total magnetic topology of DK Tau, including the part of the magnetic field that extends to the circumstellar disk. In addition, this would allow to compare both sets of ZDI maps and to measure the importance of using both types of lines with ZDI when studying a cTTs.

### 6.2.2 Observing DK Tau with SPIRou and SPIP

The work presented in this thesis was based on spectropolarimetric data in the optical range (see Chapter 2). SPIRou (for "SPectropolarimètre InfraRouge") is a second generation version of ESPaDOnS. It is a near-infrared (nIR) echelle spectropolarimeter at the CFHT. In a single exposure, it covers the domain ranging from 0.95 to 2.55 $\mu$m and has a resolving power of 70 000. SPIRou mainly consists of two distinct units: a polarimetric unit (mounted at the Cassegrain focus of the CFHT) and a cryogenic spectroscopic unit (cooled down to 80 K). They are linked via two optical fibers (see Donati et al. 2018, 2020b). Figure 6.1 shows a schematic view of the units. SPIRou features a reduction pipeline, APERO (for "A PipelinE to Reduce Observations"), that has been optimized by the SPIRou team (see Cook et al. 2022). For additional information on SPIRou, see its official website[1], as well as the dedicated webpage on the CFHT website[2].

The SPIRou Legacy Survey (SLS) was a LP allocated on the CFHT with SPIRou. It included a work package focusing on the study of the magnetic topologies of young stars. The program was allocated 300 nights of observations over 4 years (from 2019 to 2022 - see Donati et al. 2018, 2020b). This was followed by a new LP called SPICE (for "Consolidating & Enhancing the SPIRou Legacy Survey"). This program started in 2022 and was allocated 174.28 nights of observations over 2 years (see e.g. Donati et al. 2023).

---

[1] https://spirou.omp.eu
[2] https://www.cfht.hawaii.edu/Instruments/SPIRou
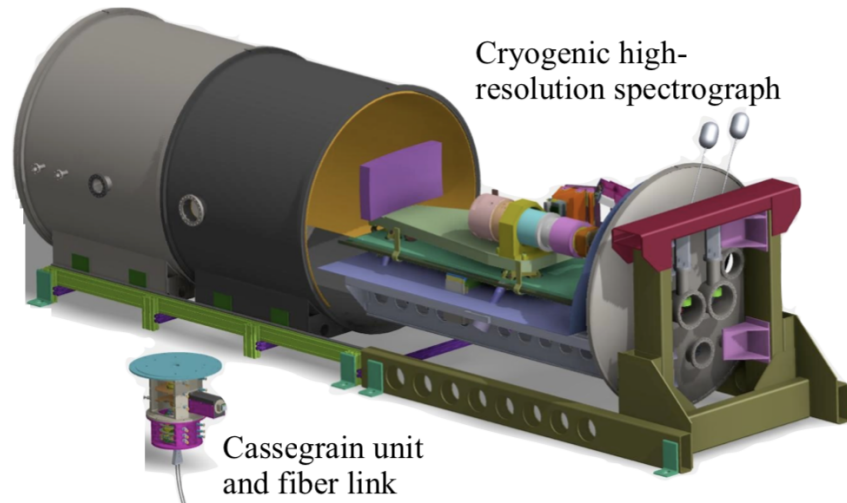
Figure 6.1 – Schematic view of SPIRou. It mainly consists of a polarimetric unit at the Cassegrain focus, and of a fiber-fed spectroscopic unit (adapted from Donati et al. 2018).

Similarly to the construction of NARVAL as a twin of ESPaDOnS at the TBL, a twin of SPIRou was constructed at the TBL as well. It is called SPIP (for "SPectropolarimètre Infrarouge Pyrénéen" - see Donati et al. 2018). There are plans to extend the compatibility of APERO to SPIP (see Cook et al. 2022). For additional information on SPIP, see its official website[3], as well as the dedicated webpage on the TBL website[4].

SPIRou and SPIP have the same scientific objectives, which include exploring the impact of magnetic fields on stellar and planetary formation. One goal is to detect and characterize the magnetic fields of different types of YSOs, including evolved protostars, cTTs, wTTs and inner circumstellar disks. In addition, another objective is to investigate the potential presence of hot Jupiters (i.e. massive planets located close to their stars) orbiting young stars and within the inner circumstellar disks (see Donati et al. 2018, 2020b).

It would be interesting to observe DK Tau in the nIR with SPIRou and SPIP in order to study its magnetic field. Indeed, magnetic fields are detected through the Zeeman effect on spectral lines and this effect is more pronounced at nIR wavelengths compared to optical wavelengths. This is because the Zeeman broadening is proportional to the square of the central wavelength that is studied (see Eq. 1.2.1). Consequently, investigating magnetic fields at nIR wavelengths is more efficient than in the visible. There are thousands of atomic and molecular spectral lines in the nIR, presenting a large range of magnetic sensitivities. For instance, the three Ti I lines at 2.221, 2.223 and 2.227 $\mu$m (with Landé factors of 2.08, 1.66 and 1.58 respectively) and the Sc I line at 2.226 $\mu$m (with a Landé factor of 0.50) are often used to estimate magnetic field strengths in young stars (see e.g. Johns-Krull 2007; Johns-Krull et al.

---

[3]https://spip.omp.eu
[4]https://tbl.omp.eu/instruments/spip

2009; Donati et al. 2020b).

In addition, the veiling of photospheric absorption lines caused by accretion shocks is weaker in the nIR, simplifying the study of the magnetic field. Furthermore, given the amount of magnetically sensitive spectral lines featured in the nIR, the LSD and ZDI techniques are straightforwardly adaptable at these wavelengths, which makes the comparison with ESPaDOnS and NARVAL analyses simple (see e.g. Donati et al. 2020b; Klein et al. 2021; Finociety et al. 2023). This would make it possible to study the evolution with time of DK Tau on longer timescales than those investigated in this thesis by adding another epoch to the 2010 and 2012 observations. This has been done for other young stars (see e.g. Sousa et al. 2021; Finociety et al. 2023).

Moreover, magnetic field in the inner regions of circumstellar disks can be probed at nIR wavelengths (see e.g. Johns-Krull 2007) or at optical wavelengths. And, as mentioned before, the Zeeman sensitivity is stronger in the nIR than in the optical range. It would therefore be interesting to study the inner circumstellar disk of DK Tau in the nIR with SPIRou and SPIP. Exploring the magnetic field in inner circumstellar disks in general is useful to examine their impact on the formation and migration of protoplanets (see e.g. Terquem 2003; Fromang 2005; Vidotto et al. 2009; Donati et al. 2020b).

It would also be interesting to study the accretion experienced by DK Tau in the nIR. There are several accretion-powered lines at these wavelengths. For instance, the 1.28 $\mu$m Pa$\beta$, 1.09 $\mu$m Pa$\gamma$ and 2.17 $\mu$m Br$\gamma$ lines are reliable tracers of accretion (see e.g. Kurosawa et al. 2005; Donati et al. 2020b). In particular, it would be interesting to explore the relation between the accretion luminosity and the veiling in the nIR in order to confirm or invalidate the relation described in Sect. 4.3.1.

## 6.2.3 Investigating the magnetic fields and accretion processes for multiple cTTs

The analysis of the magnetic field described in this thesis can be extended to other PMS. In the case of wTTs, as they do not experience veiling, the study of their magnetic field is direct. In the case of cTTs, the method of determining and removing veiling described in Sect. 3.2.3 can be applied before measuring the magnetic field. Regarding accretion, the relation between the accretion luminosity and the veiling found for DK Tau and RU Lup (see Sect. 4.3.1) could be investigated for multiple cTTs. If generalized, it would be a useful tool for deriving quantities from limited data, particularly non-flux-calibrated data. Furthermore, as the veiling does not depend on extinction, it could be particularly useful for high-extinction regions.

# Bibliography

J. M. Alcalá, C. F. Manara, A. Natta, A. Frasca, L. Testi, B. Nisini, B. Stelzer, J. P. Williams, S. Antoniucci, K. Biazzo, E. Covino, M. Esposito, F. Getman, and E. Rigliaco. X-shooter spectroscopy of young stellar objects in Lupus. Accretion properties of class II and transitional objects. *A&A*, 600:A20, Apr 2017. doi: 10.1051/0004-6361/201629929.

J. M. Alcalá, M. Gangi, K. Biazzo, S. Antoniucci, A. Frasca, T. Giannini, U. Munari, B. Nisini, A. Harutyunyan, C. F. Manara, and F. Vitali. GIARPS High-resolution Observations of T Tauri stars (GHOsT). III. A pilot study of stellar and accretion properties. *A&A*, 652:A72, August 2021. doi: 10.1051/0004-6361/202140918.

S. H. P. Alencar, J. Bouvier, J. F. Donati, E. Alecian, C. P. Folsom, K. Grankin, G. A. J. Hussain, C. Hill, A. M. Cody, A. Carmona, C. Dougados, S. G. Gregory, G. Herczeg, F. Ménard, C. Moutou, L. Malo, M. Takami, and Matysse Collaboration. Inner disk structure of the classical T Tauri star LkCa 15. *A&A*, 620:A195, Dec 2018. doi: 10.1051/0004-6361/201834263.

ALMA Partnership, C. L. Brogan, L. M. Pérez, T. R. Hunter, W. R. F. Dent, A. S. Hales, R. E. Hills, S. Corder, E. B. Fomalont, C. Vlahakis, Y. Asaki, D. Barkats, A. Hirota, J. A. Hodge, C. M. V. Impellizzeri, R. Kneissl, E. Liuzzo, R. Lucas, N. Marcelino, S. Matsushita, K. Nakanishi, N. Phillips, A. M. S. Richards, I. Toledo, R. Aladro, D. Broguiere, J. R. Cortes, P. C. Cortes, D. Espada, F. Galarza, D. Garcia-Appadoo, L. Guzman-Ramirez, E. M. Humphreys, T. Jung, S. Kameno, R. A. Laing, S. Leon, G. Marconi, A. Mignano, B. Nikolic, L. A. Nyman, M. Radiszcz, A. Remijan, J. A. Rodón, T. Sawada, S. Takahashi, R. P. J. Tilanus, B. Vila Vilaro, L. C. Watson, T. Wiklind, E. Akiyama, E. Chapillon, I. de Gregorio-Monsalvo, J. Di Francesco, F. Gueth, A. Kawamura, C. F. Lee, Q. Nguyen Luong, J. Mangum, V. Pietu, P. Sanhueza, K. Saigo, S. Takakuwa, C. Ubach, T. van Kempen, A. Wootten, A. Castro-Carrizo, H. Francke, J. Gallardo, J. Garcia, S. Gonzalez, T. Hill, T. Kaminski, Y. Kurono, H. Y. Liu, C. Lopez, F. Morales, K. Plarre, G. Schieven, L. Testi, L. Videla, E. Villard, P. Andreani, J. E. Hibbard, and K. Tatematsu. The 2014 ALMA Long Baseline Campaign: First Results from High Angular Resolution Observations toward the HL Tau Region. *ApJ*, 808(1):L3, July 2015. doi: 10.1088/2041-8205/808/1/L3.

Philippe Andre, Derek Ward-Thompson, and Mary Barsony. Submillimeter Continuum Observations of rho Ophiuchi A: The Candidate Protostar VLA 1623 and Prestellar Clumps. *ApJ*, 406:122, March 1993. doi: 10.1086/172425.

M. Ansdell, E. Gaidos, C. Hedges, M. Tazzari, A. L. Kraus, M. C. Wyatt, G. M. Kennedy, J. P. Williams, A. W. Mann, I. Angelo, G. Dûchene, E. E. Mamajek, J. Carpenter, T. L. Esplin, and A. C. Rizzuto. Are inner disc misalignments common? ALMA reveals an isotropic outer disc inclination distribution for young dipper stars. *MNRAS*, 492(1):572–588, February 2020. doi: 10.1093/mnras/stz3361.

S. A. Artemenko, K. N. Grankin, and P. P. Petrov. Rotation effects in classical T Tauri stars. *Astronomy Letters*, 38(12):783–792, December 2012. doi: 10.1134/S1063773712110011.

M. Aurière. Stellar Polarimetry with NARVAL. In J. Arnaud and N. Meunier, editors, *EAS Publications Series*, volume 9 of *EAS Publications Series*, page 105, January 2003.

Jaehan Bae, Andrea Isella, Zhaohuan Zhu, Rebecca Martin, Satoshi Okuzumi, and Scott Suriano. Structured Distributions of Gas and Solids in Protoplanetary Disks. *arXiv e-prints*, art. arXiv:2210.13314, October 2022. doi: 10.48550/arXiv.2210.13314.

Steven A. Balbus and John F. Hawley. A Powerful Local Shear Instability in Weakly Magnetized Disks. I. Linear Analysis. *ApJ*, 376:214, July 1991. doi: 10.1086/170270.

M. Benisty, A. Juhász, S. Facchini, P. Pinilla, J. de Boer, L. M. Pérez, M. Keppler, G. Muro-Arena, M. Villenave, S. Andrews, C. Dominik, C. P. Dullemond, A. Gallenne, A. Garufi, C. Ginski, and A. Isella. Shadows and asymmetries in the T Tauri disk HD 143006: evidence for a misaligned inner disk. *A&A*, 619:A171, November 2018. doi: 10.1051/0004-6361/201833913.

Julius L. Benton. *Saturn and How to Observe It*. 2005. doi: 10.1007/b137452.

Edwin A. Bergin and Mario Tafalla. Cold Dark Clouds: The Initial Conditions for Star Formation. *ARA&A*, 45(1):339–396, Sep 2007. doi: 10.1146/annurev.astro.45.071206.100404.

Georgina Beristain, Suzan Edwards, and John Kwan. Helium Emission from Classical T Tauri Stars: Dual Origin in Magnetospheric Infall and Hot Wind. *ApJ*, 551(2):1037–1064, April 2001. doi: 10.1086/320233.

N. Bessolaz, C. Zanni, J. Ferreira, R. Keppens, and J. Bouvier. Accretion funnels onto weakly magnetized young stars. *A&A*, 478(1):155–162, Jan 2008. doi: 10.1051/0004-6361:20078328.

K. Biazzo, J. M. Alcalá, E. Covino, A. Frasca, F. Getman, and L. Spezzi. The Chamaeleon II low-mass star-forming region: radial velocities, elemental abun-

dances, and accretion properties ⋆. *A&A*, 547:A104, November 2012. doi: 10.1051/0004-6361/201219680.

Émile Biémont. *Spectroscopie atomique: Instrumentation et structures atomiques*. de boeck, 2006.

A. A. Blinova, M. M. Romanova, and R. V. E. Lovelace. Boundary between stable and unstable regimes of accretion. Ordered and chaotic unstable regimes. *MNRAS*, 459(3):2354–2369, July 2016. doi: 10.1093/mnras/stw786.

A. J. Bohn, M. Benisty, K. Perraut, N. van der Marel, L. Wölfer, E. F. van Dishoeck, S. Facchini, C. F. Manara, R. Teague, L. Francis, J. P. Berger, R. Garcia-Lopez, C. Ginski, T. Henning, M. Kenworthy, S. Kraus, F. Ménard, A. Mérand, and L. M. Pérez. Probing inner and outer disk misalignments in transition disks. Constraints from VLTI/GRAVITY and ALMA observations. *A&A*, 658:A183, February 2022. doi: 10.1051/0004-6361/202142070.

Ludwig Boltzmann. Ableitung des Stefan'schen Gesetzes, betreffend die Abhängigkeit der Wärmestrahlung von der Temperatur aus der electromagnetischen Lichttheorie. *Annalen der Physik*, 258(6):291–294, January 1884. doi: 10.1002/andp.18842580616.

J. Bouvier, S. Cabrit, M. Fernandez, E. L. Martin, and J. M. Matthews. COYOTES I. Multisite UBVRI photometry of 24 pre-main-sequence stars of the Taurus-Auriga cloud. *A&AS*, 101:485–498, November 1993.

J. Bouvier, S. H. P. Alencar, T. J. Harries, C. M. Johns-Krull, and M. M. Romanova. Magnetospheric Accretion in Classical T Tauri Stars. In Bo Reipurth, David Jewitt, and Klaus Keil, editors, *Protostars and Planets V*, page 479, Jan 2007.

J. Bouvier, S. P. Matt, S. Mohanty, A. Scholz, K. G. Stassun, and C. Zanni. Angular Momentum Evolution of Young Low-Mass Stars and Brown Dwarfs: Observations and Theory. In Henrik Beuther, Ralf S. Klessen, Cornelis P. Dullemond, and Thomas Henning, editors, *Protostars and Planets VI*, page 433, Jan 2014. doi: 10.2458/azu_uapress_9780816531240-ch019.

J. Bouvier, K. Perraut, J. B. Le Bouquin, G. Duvert, C. Dougados, W. Brandner, M. Benisty, J. P. Berger, and E. Alécian. Probing the magnetospheric accretion region of the young pre-transitional disk system DoAr 44 using VLTI/GRAVITY. *A&A*, 636:A108, April 2020. doi: 10.1051/0004-6361/202037611.

S. F. Brown, J. F. Donati, D. E. Rees, and M. Semel. Zeeman-Doppler imaging of solar-type and AP stars. IV. Maximum entropy reconstruction of 2D magnetic topologies. *A&A*, 250:463, Oct 1991.

Nuria Calvet and Erik Gullbring. The Structure and Emission of the Accretion Shock in T Tauri Stars. *ApJ*, 509(2):802–818, Dec 1998. doi: 10.1086/306527.

Jason A. Cardelli, Geoffrey C. Clayton, and John S. Mathis. The Relationship between Infrared, Optical, and Ultraviolet Extinction. *ApJ*, 345:245, October 1989. doi: 10.1086/167900.

F. F. Chen. Introduction to Plasma Physics and Controlled Fusion. pages 1–421, 1984.

David Clarke. *Stellar Polarimetry*. Wiley-VCH, 2010.

Martin Clayton. Introduction to Echelle Spectroscopy. *Starlink Guide*, 9:9, January 1996.

Neil James Cook, Étienne Artigau, René Doyon, Melissa Hobson, Eder Martioli, François Bouchy, Claire Moutou, Andres Carmona, Chris Usher, Pascal Fouqué, Luc Arnold, Xavier Delfosse, Isabelle Boisse, Charles Cadieux, Thomas Vandal, Jean-François Donati, and Ariane Deslières. APERO: A PipelinE to Reduce Observations-Demonstration with SPIRou. *PASP*, 134(1041):114509, November 2022. doi: 10.1088/1538-3873/ac9e74.

G. Costigan, Jorick S. Vink, A. Scholz, T. Ray, and L. Testi. Temperaments of young stars: rapid mass accretion rate changes in T Tauri and Herbig Ae stars. *MNRAS*, 440(4):3444–3461, June 2014. doi: 10.1093/mnras/stu529.

J. F. Donati. ESPaDOnS: An Echelle SpectroPolarimetric Device for the Observation of Stars at CFHT. In Javier Trujillo-Bueno and Jorge Sanchez Almeida, editors, *Solar Polarization*, volume 307 of *Astronomical Society of the Pacific Conference Series*, page 41, January 2003.

J. F. Donati and S. F. Brown. Zeeman-Doppler imaging of active stars. V. Sensitivity of maximum entropy magnetic maps to field orientation. *A&A*, 326:1135–1142, Oct 1997.

J. F. Donati and J. D. Landstreet. Magnetic Fields of Nondegenerate Stars. *ARA&A*, 47(1):333–370, September 2009. doi: 10.1146/annurev-astro-082708-101833.

J. F. Donati, M. Semel, B. D. Carter, D. E. Rees, and A. Collier Cameron. Spectropolarimetric observations of active stars. *MNRAS*, 291(4):658–682, Nov 1997. doi: 10.1093/mnras/291.4.658.

J. F. Donati, C. Catala, J. D. Landstreet, and P. Petit. *ESPaDOnS: The New Generation Stellar Spectro-Polarimeter. Performances and First Results*, volume 358 of *Astronomical Society of the Pacific Conference Series*, page 362. 2006a.

J. F. Donati, I. D. Howarth, M. M. Jardine, P. Petit, C. Catala, J. D. Landstreet, J. C. Bouret, E. Alecian, J. R. Barnes, T. Forveille, F. Paletou, and N. Manset. The surprising magnetic topology of $\tau$ Sco: fossil remnant or dynamo output? *MNRAS*, 370(2):629–644, August 2006b. doi: 10.1111/j.1365-2966.2006.10558.x.

J. F. Donati, M. M. Jardine, S. G. Gregory, P. Petit, J. Bouvier, C. Dougados, F. Ménard, A. Collier Cameron, T. J. Harries, S. V. Jeffers, and F. Paletou. Magnetic fields and accretion flows on the classical T Tauri star V2129 Oph. *MNRAS*, 380 (4):1297–1312, October 2007. doi: 10.1111/j.1365-2966.2007.12194.x.

J. F. Donati, M. M. Jardine, S. G. Gregory, P. Petit, F. Paletou, J. Bouvier, C. Dougados, F. Ménard, A. Collier Cameron, T. J. Harries, G. A. J. Hussain, Y. Unruh, J. Morin, S. C. Marsden, N. Manset, M. Aurière, C. Catala, and E. Alecian. Magnetospheric accretion on the T Tauri star BP Tauri. *MNRAS*, 386(3):1234–1251, May 2008. doi: 10.1111/j.1365-2966.2008.13111.x.

J. F. Donati, M. B. Skelly, J. Bouvier, S. G. Gregory, K. N. Grankin, M. M. Jardine, G. A. J. Hussain, F. Ménard, C. Dougados, Y. Unruh, S. Mohanty, M. Aurière, J. Morin, R. Farès, and MAPP Collaboration. Magnetospheric accretion and spin-down of the prototypical classical T Tauri star AA Tau. *MNRAS*, 409(4):1347–1361, December 2010. doi: 10.1111/j.1365-2966.2010.17409.x.

J. F. Donati, J. Bouvier, F. M. Walter, S. G. Gregory, M. B. Skelly, G. A. J. Hussain, E. Flaccomio, C. Argiroffi, K. N. Grankin, M. M. Jardine, F. Ménard, C. Dougados, and M. M. Romanova. Non-stationary dynamo and magnetospheric accretion processes of the classical T Tauri star V2129 Oph. *MNRAS*, 412(4):2454–2468, Apr 2011. doi: 10.1111/j.1365-2966.2010.18069.x.

J. F. Donati, S. G. Gregory, S. H. P. Alencar, G. Hussain, J. Bouvier, C. Dougados, M. M. Jardine, F. Ménard, and M. M. Romanova. Magnetometry of the classical T Tauri star GQ Lup: non-stationary dynamos and spin evolution of young Suns. *MNRAS*, 425(4):2948–2963, October 2012. doi: 10.1111/j.1365-2966.2012.21482.x.

J. F. Donati, S. G. Gregory, S. H. P. Alencar, G. Hussain, J. Bouvier, M. M. Jardine, F. Ménard, C. Dougados, M. M. Romanova, and MaPP Collaboration. Magnetospheric accretion on the fully convective classical T Tauri star DN Tau. *MNRAS*, 436(1):881–897, November 2013. doi: 10.1093/mnras/stt1622.

J. F. Donati, J. Bouvier, S. H. Alencar, C. Hill, A. Carmona, C. P. Folsom, F. Ménard, S. G. Gregory, G. A. Hussain, K. Grankin, C. Moutou, L. Malo, M. Takami, G. J. Herczeg, and MaTYSSE Collaboration. The magnetic propeller accretion regime of LkCa 15. *MNRAS*, 483(1):L1–L5, Feb 2019. doi: 10.1093/mnrasl/sly207.

J. F. Donati, J. Bouvier, S. H. Alencar, C. Moutou, L. Malo, M. Takami, F. Ménard, C. Dougados, G. A. Hussain, and Matysse Collaboration. The magnetic field and

accretion regime of CI Tau. *MNRAS*, 491(4):5660–5670, February 2020a. doi: 10.1093/mnras/stz3368.

J. F. Donati, D. Kouach, C. Moutou, R. Doyon, X. Delfosse, E. Artigau, S. Baratchart, M. Lacombe, G. Barrick, G. Hébrard, F. Bouchy, L. Saddlemyer, L. Parès, P. Rabou, Y. Micheau, F. Dolon, V. Reshetov, Z. Challita, A. Carmona, N. Striebig, S. Thibault, E. Martioli, N. Cook, P. Fouqué, T. Vermeulen, S. Y. Wang, L. Arnold, F. Pepe, I. Boisse, P. Figueira, J. Bouvier, T. P. Ray, C. Feugeade, J. Morin, S. Alencar, M. Hobson, B. Castilho, S. Udry, N. C. Santos, O. Hernandez, T. Benedict, P. Vallée, G. Gallou, M. Dupieux, M. Larrieu, S. Perruchot, R. Sottile, F. Moreau, C. Usher, M. Baril, F. Wildi, B. Chazelas, L. Malo, X. Bonfils, D. Loop, D. Kerley, I. Wevers, J. Dunn, J. Pazder, S. Macdonald, B. Dubois, E. Carrié, H. Valentin, F. Henault, C. H. Yan, and T. Steinmetz. SPIRou: NIR velocimetry and spectropolarimetry at the CFHT. *MNRAS*, 498(4):5684–5703, November 2020b. doi: 10.1093/mnras/staa2569.

J. F. Donati, P. I. Cristofari, B. Finociety, B. Klein, C. Moutou, E. Gaidos, C. Cadieux, E. Artigau, A. C. M. Correia, G. Boué, N. J. Cook, A. Carmona, L. T. Lehmann, J. Bouvier, E. Martioli, J. Morin, P. Fouqué, X. Delfosse, R. Doyon, G. Hébrard, S. H. P. Alencar, J. Laskar, L. Arnold, P. Petit, Á. Kóspál, A. Vidotto, C. P. Folsom, and the S L S collaboration. The magnetic field and multiple planets of the young dwarf AU Mic. *MNRAS*, 525(1):455–475, October 2023. doi: 10.1093/mnras/stad1193.

Jean-François Donati, D. Kouach, M. Lacombe, S. Baratchart, R. Doyon, X. Delfosse, Étienne Artigau, Claire Moutou, G. Hébrard, François Bouchy, J. Bouvier, S. Alencar, L. Saddlemyer, L. Parès, P. Rabou, Y. Micheau, F. Dolon, G. Barrick, O. Hernandez, S. Y. Wang, V. Reshetov, N. Striebig, Z. Challita, A. Carmona, S. Tibault, E. Martioli, P. Figueira, I. Boisse, and Francesco Pepe. *SPIRou: A NIR Spectropolarimeter/High-Precision Velocimeter for the CFHT*. Springer International Publishing AG, 2018. doi: 10.1007/978-3-319-55333-7_107.

C. P. Dullemond and J. D. Monnier. The Inner Regions of Protoplanetary Disks. *ARA&A*, 48:205–239, September 2010. doi: 10.1146/annurev-astro-081309-130932.

J. A. Eisner, L. A. Hillenbrand, R. J. White, J. S. Bloom, R. L. Akeson, and C. H. Blake. Near-Infrared Interferometric, Spectroscopic, and Photometric Monitoring of T Tauri Inner Disks. *ApJ*, 669(2):1072–1084, November 2007. doi: 10.1086/521874.

C. C. Espaillat, C. E. Robinson, M. M. Romanova, T. Thanathibodee, J. Wendeborn, N. Calvet, M. Reynolds, and J. Muzerolle. Measuring the density structure of an

accretion hot spot. *Nature*, 597(7874):41–44, September 2021. doi: 10.1038/s41586-021-03751-5.

C. C. Espaillat, G. J. Herczeg, T. Thanathibodee, C. Pittman, N. Calvet, N. Arulanantham, K. France, Javier Serna, J. Hernández, Á. Kóspál, F. M. Walter, A. Frasca, W. J. Fischer, C. M. Johns-Krull, P. C. Schneider, C. Robinson, Suzan Edwards, P. Ábrahám, Min Fang, J. Erkal, C. F. Manara, J. M. Alcalá, E. Alecian, R. D. Alexander, J. Alonso-Santiago, Simone Antoniucci, David R. Ardila, Andrea Banzatti, M. Benisty, Edwin A. Bergin, Katia Biazzo, César Briceño, Justyn Campbell-White, L. Ilsedore Cleeves, Deirdre Coffey, Jochen Eislöffel, Stefano Facchini, D. Fedele, Eleonora Fiorellino, Dirk Froebrich, Manuele Gangi, Teresa Giannini, K. Grankin, Hans Moritz Günther, Zhen Guo, Lee Hartmann, Lynne A. Hillenbrand, P. C. Hinton, Joel H. Kastner, Chris Koen, K. Maucó, I. Mendigutía, B. Nisini, Neelam Panwar, D. A. Principe, Massimo Robberto, A. Sicilia-Aguilar, Jeff A. Valenti, J. Wendeborn, Jonathan P. Williams, Ziyan Xu, and R. K. Yadav. The ODYSSEUS Survey. Motivation and First Results: Accretion, Ejection, and Disk Irradiation of CVSO 109. *AJ*, 163(3):114, March 2022. doi: 10.3847/1538-3881/ac479d.

Min Fang, Ilaria Pascucci, Suzan Edwards, Uma Gorti, Andrea Banzatti, Mario Flock, Patrick Hartigan, Gregory J. Herczeg, and Andrea K. Dupree. A New Look at T Tauri Star Forbidden Lines: MHD-driven Winds from the Inner Disk. *ApJ*, 868(1): 28, November 2018. doi: 10.3847/1538-4357/aae780.

E. D. Feigelson, J. M. Jackson, R. D. Mathieu, P. C. Myers, and F. M. Walter. An X-Ray Survey for Pre-Main-Sequence Stars in the Taurus-Auriga and Perseus Molecular Cloud Complexes. *AJ*, 94:1251, November 1987. doi: 10.1086/114561.

Eric D. Feigelson and Thierry Montmerle. High-Energy Processes in Young Stellar Objects. *ARA&A*, 37:363–408, Jan 1999. doi: 10.1146/annurev.astro.37.1.363.

Adam J. Finley and Sean P. Matt. The Effect of Combined Magnetic Geometries on Thermally Driven Winds. I. Interaction of Dipolar and Quadrupolar Fields. *ApJ*, 845 (1):46, August 2017. doi: 10.3847/1538-4357/aa7fb9.

B. Finociety and J. F. Donati. Mapping time-dependent magnetic topologies of active stars. *MNRAS*, 516(4):5887–5906, November 2022. doi: 10.1093/mnras/stac2682.

B. Finociety, J. F. Donati, K. Grankin, J. Bouvier, S. Alencar, F. Ménard, T. P. Ray, Á. Kóspál, and the S. L. S. consortium. The active weak-line T Tauri star LkCa 4 observed with SPIRou and TESS. *MNRAS*, 520(2):3049–3065, April 2023. doi: 10.1093/mnras/stad267.

William Fischer, Suzan Edwards, Lynne Hillenbrand, and John Kwan. Characterizing the IYJ Excess Continuum Emission in T Tauri Stars. *ApJ*, 730(2):73, Apr 2011. doi: 10.1088/0004-637X/730/2/73.

C. P. Folsom, P. Petit, J. Bouvier, A. Lèbre, L. Amard, A. Palacios, J. Morin, J. F. Donati, S. V. Jeffers, S. C. Marsden, and A. A. Vidotto. The evolution of surface magnetic fields in young solar-type stars - I. The first 250 Myr. *MNRAS*, 457(1): 580–607, Mar 2016. doi: 10.1093/mnras/stv2924.

C. P. Folsom, J. Bouvier, P. Petit, A. Lèbre, L. Amard, A. Palacios, J. Morin, J. F. Donati, and A. A. Vidotto. The evolution of surface magnetic fields in young solar-type stars II: the early main sequence (250-650 Myr). *MNRAS*, 474(4):4956–4987, March 2018. doi: 10.1093/mnras/stx3021.

A. Frank, T. P. Ray, S. Cabrit, P. Hartigan, H. G. Arce, F. Bacciotti, J. Bally, M. Benisty, J. Eislöffel, M. Güdel, S. Lebedev, B. Nisini, and A. Raga. Jets and Outflows from Star to Cloud: Observations Confront Theory. In Henrik Beuther, Ralf S. Klessen, Cornelis P. Dullemond, and Thomas Henning, editors, *Protostars and Planets VI*, page 451, Jan 2014. doi: 10.2458/azu_uapress_9780816531240-ch020.

S. Fromang. The effect of MHD turbulence on massive protoplanetary disk fragmentation. *A&A*, 441(1):1–8, October 2005. doi: 10.1051/0004-6361:20053080.

Gaia Collaboration, T. Prusti, J. H. J. de Bruijne, A. G. A. Brown, A. Vallenari, C. Babusiaux, C. A. L. Bailer-Jones, U. Bastian, M. Biermann, D. W. Evans, and et al. The Gaia mission. *A&A*, 595:A1, November 2016. doi: 10.1051/0004-6361/201629272.

Gaia Collaboration, A. G. A. Brown, A. Vallenari, T. Prusti, J. H. J. de Bruijne, C. Babusiaux, and C. A. L. Bailer-Jones. Gaia Data Release 2. Summary of the contents and survey properties. *A&A*, 616, April 2018.

Gaia Collaboration, A. Vallenari, A. G. A. Brown, T. Prusti, J. H. J. de Bruijne, F. Arenou, C. Babusiaux, M. Biermann, O. L. Creevey, C. Ducourant, D. W. Evans, L. Eyer, R. Guerra, A. Hutton, C. Jordi, S. A. Klioner, U. L. Lammers, L. Lindegren, X. Luri, F. Mignard, C. Panem, D. Pourbaix, S. Randich, P. Sartoretti, C. Soubiran, P. Tanga, N. A. Walton, C. A. L. Bailer-Jones, U. Bastian, R. Drimmel, F. Jansen, D. Katz, M. G. Lattanzi, F. van Leeuwen, J. Bakker, C. Cacciari, J. Castañeda, F. De Angeli, C. Fabricius, M. Fouesneau, Y. Frémat, L. Galluccio, A. Guerrier, U. Heiter, E. Masana, R. Messineo, N. Mowlavi, C. Nicolas, K. Nienartowicz, F. Pailler, P. Panuzzo, F. Riclet, W. Roux, G. M. Seabroke, R. Sordoørcit, F. Thévenin, G. Gracia-Abril, J. Portell, D. Teyssier, M. Altmann, R. Andrae, M. Audard, I. Bellas-Velidis, K. Benson, J. Berthier, R. Blomme, P. W. Burgess, D. Busonero, G. Busso,

H. Cánovas, B. Carry, A. Cellino, N. Cheek, G. Clementini, Y. Damerdji, M. Davidson, P. de Teodoro, M. Nuñez Campos, L. Delchambre, A. Dell'Oro, P. Esquej, J. Fernández-Hernández, E. Fraile, D. Garabato, P. García-Lario, E. Gosset, R. Haigron, J. L. Halbwachs, N. C. Hambly, D. L. Harrison, J. Hernández, D. Hestroffer, S. T. Hodgkin, B. Holl, K. Janßen, G. Jevardat de Fombelle, S. Jordan, A. Krone-Martins, A. C. Lanzafame, W. Löffler, O. Marchal, P. M. Marrese, A. Moitinho, K. Muinonen, P. Osborne, E. Pancino, T. Pauwels, A. Recio-Blanco, C. Reylé, M. Riello, L. Rimoldini, T. Roegiers, J. Rybizki, L. M. Sarro, C. Siopis, M. Smith, A. Sozzetti, E. Utrilla, M. van Leeuwen, U. Abbas, P. Ábrahám, A. Abreu Aramburu, C. Aerts, J. J. Aguado, M. Ajaj, F. Aldea-Montero, G. Altavilla, M. A. Álvarez, J. Alves, F. Anders, R. I. Anderson, E. Anglada Varela, T. Antoja, D. Baines, S. G. Baker, L. Balaguer-Núñez, E. Balbinot, Z. Balog, C. Barache, D. Barbato, M. Barros, M. A. Barstow, S. Bartolomé, J. L. Bassilana, N. Bauchet, U. Becciani, M. Bellazzini, A. Berihuete, M. Bernet, S. Bertone, L. Bianchi, A. Binnenfeld, S. Blanco-Cuaresma, A. Blazere, T. Boch, A. Bombrun, D. Bossini, S. Bouquillon, A. Bragaglia, L. Bramante, E. Breedt, A. Bressan, N. Brouillet, E. Brugaletta, B. Bucciarelli, A. Burlacu, A. G. Butkevich, R. Buzzi, E. Caffau, R. Cancelliere, T. Cantat-Gaudin, R. Carballo, T. Carlucci, M. I. Carnerero, J. M. Carrasco, L. Casamiquela, M. Castellani, A. Castro-Ginard, L. Chaoul, P. Charlot, L. Chemin, V. Chiaramida, A. Chiavassa, N. Chornay, G. Comoretto, G. Contursi, W. J. Cooper, T. Cornez, S. Cowell, F. Crifo, M. Cropper, M. Crosta, C. Crowley, C. Dafonte, A. Dapergolas, M. David, P. David, P. de Laverny, F. De Luise, R. De March, J. De Ridder, R. de Souza, A. de Torres, E. F. del Peloso, E. del Pozo, M. Delbo, A. Delgado, J. B. Delisle, C. Demouchy, T. E. Dharmawardena, P. Di Matteo, S. Diakite, C. Diener, E. Distefano, C. Dolding, B. Edvardsson, H. Enke, C. Fabre, M. Fabrizio, S. Faigler, G. Fedorets, P. Fernique, A. Fienga, F. Figueras, Y. Fournier, C. Fouron, F. Fragkoudi, M. Gai, A. Garcia-Gutierrez, M. Garcia-Reinaldos, M. García-Torres, A. Garofalo, A. Gavel, P. Gavras, E. Gerlach, R. Geyer, P. Giacobbe, G. Gilmore, S. Girona, G. Giuffrida, R. Gomel, A. Gomez, J. González-Núñez, I. González-Santamaría, J. J. González-Vidal, M. Granvik, P. Guillout, J. Guiraud, R. Gutiérrez-Sánchez, L. P. Guy, D. Hatzidimitriou, M. Hauser, M. Haywood, A. Helmer, A. Helmi, M. H. Sarmiento, S. L. Hidalgo, T. Hilger, N. Hładczuk, D. Hobbs, G. Holland, H. E. Huckle, K. Jardine, G. Jasniewicz, A. Jean-Antoine Piccolo, Ó. Jiménez-Arranz, A. Jorissen, J. Juaristi Campillo, F. Julbe, L. Karbevska, P. Kervella, S. Khanna, M. Kontizas, G. Kordopatis, A. J. Korn, Á Kóspál, Z. Kostrzewa-Rutkowska, K. Kruszyńska, M. Kun, P. Laizeau, S. Lambert, A. F. Lanza, Y. Lasne, J. F. Le Campion, Y. Lebreton, T. Lebzelter, S. Leccia, N. Leclerc, I. Lecoeur-Taibi, S. Liao, E. L. Licata, H. E. P. Lindstrøm, T. A. Lister, E. Livanou, A. Lobel, A. Lorca, C. Loup, P. Madrero Pardo, A. Magdaleno Romeo, S. Managau, R. G. Mann, M. Manteiga, J. M. Marchant, M. Marconi, J. Marcos, M. M. S. Marcos Santos,

D. Marín Pina, S. Marinoni, F. Marocco, D. J. Marshall, L. Martin Polo, J. M. Martín-Fleitas, G. Marton, N. Mary, A. Masip, D. Massari, A. Mastrobuono-Battisti, T. Mazeh, P. J. McMillan, S. Messina, D. Michalik, N. R. Millar, A. Mints, D. Molina, R. Molinaro, L. Molnár, G. Monari, M. Monguió, P. Montegriffo, A. Montero, R. Mor, A. Mora, R. Morbidelli, T. Morel, D. Morris, T. Muraveva, C. P. Murphy, I. Musella, Z. Nagy, L. Noval, F. Ocaña, A. Ogden, C. Ordenovic, J. O. Osinde, C. Pagani, I. Pagano, L. Palaversa, P. A. Palicio, L. Pallas-Quintela, A. Panahi, S. Payne-Wardenaar, X. Peñalosa Esteller, A. Penttilä, B. Pichon, A. M. Piersimoni, F. X. Pineau, E. Plachy, G. Plum, E. Poggio, A. Prša, L. Pulone, E. Racero, S. Ragaini, M. Rainer, C. M. Raiteri, N. Rambaux, P. Ramos, M. Ramos-Lerate, P. Re Fiorentin, S. Regibo, P. J. Richards, C. Rios Diaz, V. Ripepi, A. Riva, H. W. Rix, G. Rixon, N. Robichon, A. C. Robin, C. Robin, M. Roelens, H. R. O. Rogues, L. Rohrbasser, M. Romero-Gómez, N. Rowell, F. Royer, D. Ruz Mieres, K. A. Rybicki, G. Sadowski, A. Sáez Núñez, A. Sagristà Sellés, J. Sahlmann, E. Salguero, N. Samaras, V. Sanchez Gimenez, N. Sanna, R. Santoveña, M. Sarasso, M. Schultheis, E. Sciacca, M. Segol, J. C. Segovia, D. Ségransan, D. Semeux, S. Shahaf, H. I. Siddiqui, A. Siebert, L. Siltala, A. Silvelo, E. Slezak, I. Slezak, R. L. Smart, O. N. Snaith, E. Solano, F. Solitro, D. Souami, J. Souchay, A. Spagna, L. Spina, F. Spoto, I. A. Steele, H. Steidelmüller, C. A. Stephenson, M. Süveges, J. Surdej, L. Szabados, E. Szegedi-Elek, F. Taris, M. B. Taylo, R. Teixeira, L. Tolomei, N. Tonello, F. Torra, J. Torra, G. Torralba Elipe, M. Trabucchi, A. T. Tsounis, C. Turon, A. Ulla, N. Unger, M. V. Vaillant, E. van Dillen, W. van Reeven, O. Vanel, A. Vecchiato, Y. Viala, D. Vicente, S. Voutsinas, M. Weiler, T. Wevers, L. Wyrzykowski, A. Yoldas, P. Yvard, H. Zhao, J. Zorec, S. Zucker, and T. Zwitter. Gaia Data Release 3: Summary of the content and survey properties. *arXiv e-prints*, art. arXiv:2208.00211, July 2022.

M. Gangi, S. Antoniucci, K. Biazzo, A. Frasca, B. Nisini, J. M. Alcalá, T. Giannini, C. F. Manara, A. Giunta, A. Harutyunyan, U. Munari, and F. Vitali. GIARPS High-resolution Observations of T Tauri stars (GHOsT). IV. Accretion properties of the Taurus-Auriga young association. *A&A*, 667:A124, November 2022. doi: 10.1051/0004-6361/202244042.

GRAVITY Collaboration, K. Perraut, L. Labadie, J. Bouvier, F. Ménard, L. Klarmann, C. Dougados, M. Benisty, J. P. Berger, Y. I. Bouarour, W. Brandner, A. Caratti O Garatti, P. Caselli, P. T. de Zeeuw, R. Garcia-Lopez, T. Henning, J. Sanchez-Bermudez, A. Sousa, E. van Dishoeck, E. Alécian, A. Amorim, Y. Clénet, R. Davies, A. Drescher, G. Duvert, A. Eckart, F. Eisenhauer, N. M. Förster-Schreiber, P. Garcia, E. Gendron, R. Genzel, S. Gillessen, R. Grellmann, G. Heißel, S. Hippler, M. Horrobin, Z. Hubert, L. Jocou, P. Kervella, S. Lacour, V. Lapeyrère, J. B. Le Bouquin, P. Léna, D. Lutz, T. Ott, T. Paumard, G. Perrin, S. Scheithauer, J. Shangguan, T. Shimizu, J. Stadler, O. Straub, C. Straubmeier, E. Sturm, L. Tacconi, F. Vincent, S. von Fellenberg, and F. Widmann. The GRAV-

ITY young stellar object survey. VII. The inner dusty disks of T Tauri stars. *A&A*, 655:A73, November 2021. doi: 10.1051/0004-6361/202141624.

David F. Gray. *The Observation and Analysis of Stellar Photospheres*. 2008.

Thomas Greene. Protostars. *American Scientist*, 89(4):316, August 2001. doi: 10.1511/2001.4.316.

S. G. Gregory. Equation of the field lines of an axisymmetric multipole with a source surface. *American Journal of Physics*, 79(5):461–469, May 2011. doi: 10.1119/1.3549206.

S. G. Gregory, J. F. Donati, J. Morin, G. A. J. Hussain, N. J. Mayne, L. A. Hillenbrand, and M. Jardine. Can We Predict the Global Magnetic Topology of a Pre-main-sequence Star from Its Position in the Hertzsprung-Russell Diagram? *ApJ*, 755 (2):97, August 2012. doi: 10.1088/0004-637X/755/2/97.

Erik Gullbring, Lee Hartmann, Cesar Briceño, and Nuria Calvet. Disk Accretion Rates for T Tauri Stars. *ApJ*, 492(1):323–341, January 1998. doi: 10.1086/305032.

B. Gustafsson, B. Edvardsson, K. Eriksson, U. G. Jørgensen, Å. Nordlund, and B. Plez. A grid of MARCS model atmospheres for late-type stars. I. Methods and general properties. *A&A*, 486(3):951–970, August 2008. doi: 10.1051/0004-6361:200809724.

P. Hartigan, S. Edwards, and L. Ghandour. Disk Accretion and Mass Loss from Young Stars. *ApJ*, 452:736, October 1995. doi: 10.1086/176344.

Patrick Hartigan, Scott J. Kenyon, Lee Hartmann, Stephen E. Strom, Suzan Edwards, Alan D. Welty, and John Stauffer. Optical Excess Emission in T Tauri Stars. *ApJ*, 382:617, December 1991. doi: 10.1086/170749.

L. Hartmann, R. Hewett, and N. Calvet. Magnetospheric accretion models for T Tauri stars. 1: Balmer line profiles without rotation. *ApJ*, 426:669–687, May 1994. doi: 10.1086/174104.

Lee Hartmann. *Accretion Processes in Star Formation: Second Edition*. Published by Cambridge University Press, Cambridge, UK, 2009.

Lee Hartmann, Gregory Herczeg, and Nuria Calvet. Accretion onto Pre-Main-Sequence Stars. *ARA&A*, 54:135–180, Sep 2016. doi: 10.1146/annurev-astro-081915-023347.

É. M. Hébrard, J. F. Donati, X. Delfosse, J. Morin, C. Moutou, and I. Boisse. Modelling the RV jitter of early-M dwarfs using tomographic imaging. *MNRAS*, 461(2):1465–1497, September 2016. doi: 10.1093/mnras/stw1346.

Gregory J. Herczeg and Lynne A. Hillenbrand. An Optical Spectroscopic Study of T Tauri Stars. I. Photospheric Properties. *ApJ*, 786(2):97, May 2014. doi: 10.1088/0004-637X/786/2/97.

Mark Heyer and T. M. Dame. Molecular Clouds in the Milky Way. *ARA&A*, 53:583–629, Aug 2015. doi: 10.1146/annurev-astro-082214-122324.

G. A. J. Hussain, J. F. Donati, A. Collier Cameron, and J. R. Barnes. Comparisons of images derived from independent Zeeman Doppler imaging codes. *MNRAS*, 318 (4):961–973, November 2000. doi: 10.1046/j.1365-8711.2000.03573.x.

G. A. J. Hussain, A. A. van Ballegooijen, M. Jardine, and A. Collier Cameron. The Coronal Topology of the Rapidly Rotating K0 Dwarf AB Doradus. I. Using Surface Magnetic Field Maps to Model the Structure of the Stellar Corona. *ApJ*, 575(2): 1078–1086, August 2002. doi: 10.1086/341429.

G. A. J. Hussain, A. Collier Cameron, M. M. Jardine, N. Dunstone, J. Ramirez Velez, H. C. Stempels, J. F. Donati, M. Semel, G. Aulanier, T. Harries, J. Bouvier, C. Dougados, J. Ferreira, B. D. Carter, and W. A. Lawson. Surface magnetic fields on two accreting TTauri stars: CVCha and CRCha. *MNRAS*, 398(1):189–200, Sep 2009. doi: 10.1111/j.1365-2966.2009.14881.x.

Gaitee A. J. Hussain and Evelyne Alecian. The role of magnetic fields in pre-main sequence stars. In Pascal Petit, Moira Jardine, and Hendrik C. Spruit, editors, *Magnetic Fields throughout Stellar Evolution*, volume 302 of *IAU Symposium*, pages 25–37, Aug 2014. doi: 10.1017/S1743921314001653.

Laura Ingleby, Nuria Calvet, Gregory Herczeg, Alex Blaty, Frederick Walter, David Ardila, Richard Alexander, Suzan Edwards, Catherine Espaillat, Scott G. Gregory, Lynne Hillenbrand, and Alexander Brown. Accretion Rates for T Tauri Stars Using Nearly Simultaneous Ultraviolet and Optical Spectra. *ApJ*, 767(2):112, April 2013. doi: 10.1088/0004-637X/767/2/112.

Christopher M. Johns-Krull. The Magnetic Fields of Classical T Tauri Stars. *ApJ*, 664 (2):975–985, Aug 2007. doi: 10.1086/519017.

Christopher M. Johns-Krull, Jeff A. Valenti, and Christopher Koresko. Measuring the Magnetic Field on the Classical T Tauri Star BP Tauri. *ApJ*, 516(2):900–915, May 1999. doi: 10.1086/307128.

Christopher M. Johns-Krull, Thomas P. Greene, Greg W. Doppmann, and Kevin R. Covey. First Magnetic Field Detection on a Class I Protostar. *ApJ*, 700(2):1440–1448, August 2009. doi: 10.1088/0004-637X/700/2/1440.

C. P. Johnstone, M. Jardine, S. G. Gregory, J. F. Donati, and G. Hussain. Classical T Tauri stars: magnetic fields, coronae and star-disc interactions. *MNRAS*, 437(4): 3202–3220, February 2014. doi: 10.1093/mnras/stt2107.

Alfred H. Joy. T Tauri Variable Stars. *ApJ*, 102:168, September 1945. doi: 10.1086/ 144749.

Baptiste Klein, Jean-François Donati, Claire Moutou, Xavier Delfosse, Xavier Bonfils, Eder Martioli, Pascal Fouqué, Ryan Cloutier, Étienne Artigau, René Doyon, Guillaume Hébrard, Julien Morin, Julien Rameau, Peter Plavchan, and Eric Gaidos. Investigating the young AU Mic system with SPIRou: large-scale stellar magnetic field and close-in planet mass. *MNRAS*, 502(1):188–205, March 2021. doi: 10.1093/mnras/staa3702.

O. Kochukhov and N. Piskunov. Doppler Imaging of stellar magnetic fields. II. Numerical experiments. *A&A*, 388:868–888, June 2002. doi: 10.1051/0004-6361: 20020300.

O. Kochukhov, V. Makaganiuk, and N. Piskunov. Least-squares deconvolution of the stellar intensity and polarization spectra. *A&A*, 524:A5, Dec 2010. doi: 10.1051/ 0004-6361/201015429.

O. Kochukhov, V. Makaganiuk, N. Piskunov, F. Snik, S. V. Jeffers, C. M. Johns-Krull, C. U. Keller, M. Rodenhuis, and J. A. Valenti. First Detection of Linear Polarization in the Line Profiles of Active Cool Stars. *ApJ*, 732(2):L19, May 2011. doi: 10.1088/ 2041-8205/732/2/L19.

Oleg Kochukhov and Denis Shulyak. Magnetic Field of the Eclipsing M-dwarf Binary YY Gem. *ApJ*, 873(1):69, March 2019. doi: 10.3847/1538-4357/ab06c5.

Arieh Koenigl. Disk Accretion onto Magnetic T Tauri Stars. *ApJ*, 370:L39, March 1991. doi: 10.1086/185972.

J. Kristian and M. Blouke. Charge-coupled devices in astronomy. *Scientific American*, 247:66–74, October 1982. doi: 10.1038/scientificamerican1082-66.

Mark R. Krumholz. Notes on Star Formation. *arXiv e-prints*, art. arXiv:1511.03457, November 2015. doi: 10.48550/arXiv.1511.03457.

A. K. Kulkarni and M. M. Romanova. Accretion to magnetized stars through the Rayleigh-Taylor instability: global 3D simulations. *MNRAS*, 386(2):673–687, May 2008. doi: 10.1111/j.1365-2966.2008.13094.x.

A. K. Kulkarni and M. M. Romanova. Possible quasi-periodic oscillations from unstable accretion: 3D magnetohydrodynamic simulations. *MNRAS*, 398(2):701–714, September 2009. doi: 10.1111/j.1365-2966.2009.15186.x.

R. Kurosawa and M. M. Romanova. Spectral variability of classical T Tauri stars accreting in an unstable regime. *MNRAS*, 431:2673–2689, May 2013. doi: 10. 1093/mnras/stt365.

Ryuichi Kurosawa, Tim J. Harries, and Neil H. Symington. Time-series Paschen-$\beta$ spectroscopy of SU Aurigae. *MNRAS*, 358(2):671–683, April 2005. doi: 10.1111/j.1365-2966.2005.08808.x.

Robert Kurucz. ATLAS9 Stellar Atmosphere Programs and 2 km/s grid. *ATLAS9 Stellar Atmosphere Programs and 2 km/s grid. Kurucz CD-ROM No. 13. Cambridge*, 13, Jan 1993.

C. J. Lada and B. A. Wilking. The nature of the embedded population in the rho Ophiuchi dark cloud : mid-infrared observations. *ApJ*, 287:610–621, December 1984. doi: 10.1086/162719.

Charles J. Lada. Star formation: from OB associations to protostars. In Manuel Peimbert and Jun Jugaku, editors, *Star Forming Regions*, volume 115, page 1, January 1987.

S. A. Lamzin. On the structure of the accretion shock wave in the case of young stars. *A&A*, 295:L20–L22, March 1995.

S. A. Lamzin. The structure of shock waves in the case of accretion onto low-mass young stars. *Astronomy Reports*, 42(3):322–335, May 1998. doi: 10.48550/arXiv. 1303.4066.

E. Landi Degl'Innocenti and M. Landolfi. *Polarization in Spectral Lines*, volume 307. 2004. doi: 10.1007/978-1-4020-2415-3.

J. D. Landstreet. The Magnetic Field and Abundance Distribution Geometry of the Peculiar A Star 53 Camelopardalis. *ApJ*, 326:967, March 1988. doi: 10.1086/166155.

L. T. Lehmann, G. A. J. Hussain, M. M. Jardine, D. H. Mackay, and A. A. Vidotto. Observing the simulations: applying ZDI to 3D non-potential magnetic field simulations. *MNRAS*, 483(4):5246–5266, March 2019. doi: 10.1093/mnras/sty3362.

D. Lynden-Bell and J. E. Pringle. The evolution of viscous discs and the origin of the nebular variables. *MNRAS*, 168:603–637, Sep 1974. doi: 10.1093/mnras/168.3. 603.

Eric E. Mamajek. Initial Conditions of Planet Formation: Lifetimes of Primordial Disks. In Tomonori Usuda, Motohide Tamura, and Miki Ishii, editors, *Exoplanets and Disks: Their Formation and Diversity*, volume 1158 of *American Institute of Physics Conference Series*, pages 3–10, August 2009. doi: 10.1063/1.3215910.

C. F. Manara, M. Robberto, N. Da Rio, G. Lodato, L. A. Hillenbrand, K. G. Stassun, and D. R. Soderblom. Hubble Space Telescope Measures of Mass Accretion Rates in the Orion Nebula Cluster. *ApJ*, 755(2):154, August 2012. doi: 10.1088/0004-637X/755/2/154.

C. F. Manara, L. Testi, A. Natta, and J. M. Alcalá. X-Shooter study of accretion in $\rho$-Ophiucus: very low-mass stars and brown dwarfs. *A&A*, 579:A66, July 2015. doi: 10.1051/0004-6361/201526169.

C. F. Manara, D. Fedele, G. J. Herczeg, and P. S. Teixeira. X-Shooter study of accretion in Chamaeleon I. *A&A*, 585:A136, January 2016. doi: 10.1051/0004-6361/201527224.

C. F. Manara, M. Tazzari, F. Long, G. J. Herczeg, G. Lodato, A. A. Rota, P. Cazzoletti, G. van der Plas, P. Pinilla, G. Dipierro, S. Edwards, D. Harsono, D. Johnstone, Y. Liu, F. Menard, B. Nisini, E. Ragusa, Y. Boehler, and S. Cabrit. Observational constraints on dust disk sizes in tidally truncated protoplanetary disks in multiple systems in the Taurus region. *A&A*, 628:A95, Aug 2019. doi: 10.1051/0004-6361/201935964.

C. F. Manara, M. Ansdell, G. P. Rosotti, A. M. Hughes, P. J. Armitage, G. Lodato, and J. P. Williams. Demographics of Young Stars and their Protoplanetary Disks: Lessons Learned on Disk Evolution and its Connection to Planet Formation. In S. Inutsuka, Y. Aikawa, T. Muto, K. Tomida, and M. Tamura, editors, *Protostars and Planets VII*, volume 534 of *Astronomical Society of the Pacific Conference Series*, page 539, July 2023. doi: 10.48550/arXiv.2203.09930.

P. T. McGinnis, S. H. P. Alencar, M. M. Guimarães, A. P. Sousa, J. Stauffer, J. Bouvier, L. Rebull, N. N. J. Fonseca, L. Venuti, L. Hillenbrand, A. M. Cody, P. S. Teixeira, S. Aigrain, F. Favata, G. Fűrész, F. J. Vrba, E. Flaccomio, N. J. Turner, J. F. Gameiro, C. Dougados, W. Herbst, M. Morales-Calderón, and G. Micela. CSI 2264: Probing the inner disks of AA Tauri-like systems in NGC 2264. *A&A*, 577: A11, May 2015. doi: 10.1051/0004-6361/201425475.

Pauline McGinnis, Jérôme Bouvier, and Florian Gallet. The magnetic obliquity of accreting T Tauri stars. *MNRAS*, 497(2):2142–2162, September 2020. doi: 10. 1093/mnras/staa2041.

J. Morin. Magnetic Fields from Low-Mass Stars to Brown Dwarfs. In Céline Reylé, Corinne Charbonnel, and Mathias Schultheis, editors, *EAS Publications Series*, volume 57 of *EAS Publications Series*, pages 165–191, Nov 2012. doi: 10.1051/ eas/1257005.

J. Morin, J. F. Donati, P. Petit, X. Delfosse, T. Forveille, L. Albert, M. Aurière, R. Cabanac, B. Dintrans, R. Fares, T. Gastine, M. M. Jardine, F. Lignières, F. Paletou,

J. C. Ramirez Velez, and S. Théado. Large-scale magnetic topologies of mid M dwarfs. *MNRAS*, 390(2):567–581, October 2008. doi: 10.1111/j.1365-2966.2008. 13809.x.

J. Morin, J. F. Donati, P. Petit, X. Delfosse, T. Forveille, and M. M. Jardine. Large-scale magnetic topologies of late M dwarfs*. *MNRAS*, 407(4):2269–2286, October 2010. doi: 10.1111/j.1365-2966.2010.17101.x.

James Muzerolle, Lee Hartmann, and Nuria Calvet. Emission-Line Diagnostics of T Tauri Magnetospheric Accretion. I. Line Profile Observations. *AJ*, 116(1):455–468, July 1998. doi: 10.1086/300428.

A. Natta, L. Testi, and S. Randich. Accretion in the $\rho$-Ophiuchi pre-main sequence stars. *A&A*, 452(1):245–252, June 2006. doi: 10.1051/0004-6361:20054706.

M. Nelissen, P. McGinnis, C. P. Folsom, T. Ray, A. A. Vidotto, E. Alecian, J. Bouvier, J. Morin, J. F. Donati, and R. Devaraj. Misalignment of the outer disk of DK Tau and a first look at its magnetic field using spectropolarimetry. *A&A*, 670:A165, February 2023a. doi: 10.1051/0004-6361/202245194.

M. Nelissen, A. Natta, P. McGinnis, C. Pittman, C. Delvaux, and T. Ray. Correlation between the optical veiling and accretion properties. A case study of the classical T Tauri star DK Tau. *A&A*, 677:A64, September 2023b. doi: 10.1051/0004-6361/202347231.

James E. O'Donnell. R v-dependent Optical and Near-Ultraviolet Extinction. *ApJ*, 422:158, February 1994. doi: 10.1086/173713.

Terry D. Oswalt and Howard E. Bond. *Planets, Stars and Stellar Systems: Volume 2: Astronomical Techniques, Software and Data*. 2013. doi: 10.1007/978-94-007-5618-2.

Mark J. Pecaut and Eric E. Mamajek. Intrinsic Colors, Temperatures, and Bolometric Corrections of Pre-main-sequence Stars. *ApJS*, 208(1):9, September 2013. doi: 10.1088/0067-0049/208/1/9.

John R. Percy, Sergiy Grynko, Rajiv Seneviratne, and William Herbst. Self-Correlation Analysis of the Photometric Variability of T Tauri Stars. II. A Survey. *PASP*, 122(893):753, Jul 2010. doi: 10.1086/654826.

M. V. Persson. SEDs of the different protostellar evolutionary stages. 2014.

P. Petit, J. F. Donati, and A. Collier Cameron. Differential rotation of cool active stars: the case of intermediate rotators. *MNRAS*, 334(2):374–382, August 2002. doi: 10.1046/j.1365-8711.2002.05529.x.

P. Petit, T. Louge, S. Théado, F. Paletou, N. Manset, J. Morin, S. C. Marsden, and S. V. Jeffers. PolarBase: A Database of High-Resolution Spectropolarimetric Stellar Observations. *PASP*, 126(939):469, May 2014. doi: 10.1086/676976.

Caeley V. Pittman, Catherine C. Espaillat, Connor E. Robinson, Thanawuth Thanathibodee, Nuria Calvet, John Wendeborn, Jesus Hernández, Carlo F. Manara, Fred Walter, Péter Ábrahám, Juan M. Alcalá, Sílvia H. P. Alencar, Nicole Arulanantham, Sylvie Cabrit, Jochen Eislöffel, Eleonora Fiorellino, Kevin France, Manuele Gangi, Konstantin Grankin, Gregory J. Herczeg, Ágnes Kóspál, Ignacio Mendigutía, Javier Serna, and Laura Venuti. Towards a Comprehensive View of Accretion, Inner Disks, and Extinction in Classical T Tauri Stars: An ODYSSEUS Study of the Orion OB1b Association. *AJ*, 164(5):201, November 2022. doi: 10.3847/1538-3881/ac898d.

K. Pouilly, J. Bouvier, E. Alecian, S. H. P. Alencar, A. M. Cody, J. F. Donati, K. Grankin, G. A. J. Hussain, L. Rebull, and C. P. Folsom. Magnetospheric accretion in the intermediate-mass T Tauri star HQ Tauri. *A&A*, 642:A99, October 2020. doi: 10.1051/0004-6361/202038086.

K. Pouilly, J. Bouvier, E. Alecian, S. H. P. Alencar, A. M. Cody, J. F. Donati, K. Grankin, L. Rebull, and C. P. Folsom. Beyond the dips of V807 Tau, a spectropolarimetric study of a dipper's magnetosphere. *A&A*, 656:A50, December 2021. doi: 10.1051/0004-6361/202140850.

George W. Preston. A Statistical Investigation of the Orientation of Magnetic Axes in the Periodic Magnetic Variables. *ApJ*, 150:547, November 1967. doi: 10.1086/149358.

L. M. Rebull, S. C. Wolff, and S. E. Strom. Stellar Rotation in Young Clusters: The First 4 Million Years. *AJ*, 127(2):1029–1051, February 2004. doi: 10.1086/380931.

D. E. Rees and M. D. Semel. Line formation in an unresolved magnetic element: a test of the centre of gravity method. *A&A*, 74(1):1–5, April 1979.

A. Reiners and G. Basri. On the magnetic topology of partially and fully convective stars. *A&A*, 496(3):787–790, March 2009. doi: 10.1051/0004-6361:200811450.

Ansgar Reiners. Observations of Cool-Star Magnetic Fields. *Living Reviews in Solar Physics*, 9(1):1, February 2012. doi: 10.12942/lrsp-2012-1.

Connor E. Robinson and Catherine C. Espaillat. Multiepoch Ultraviolet HST Observations of Accreting Low-mass Stars. *ApJ*, 874(2):129, April 2019. doi: 10.3847/1538-4357/ab0d8d.

Noemi Roggero, Jérôme Bouvier, Luisa M. Rebull, and Ann Marie Cody. The dipper population of Taurus seen with K2. *A&A*, 651:A44, July 2021. doi: 10.1051/0004-6361/202140646.

M. M. Romanova, G. V. Ustyugova, A. V. Koldoba, and R. V. E. Lovelace. Warps, bending and density waves excited by rotating magnetized stars: results of global 3D MHD simulations. *MNRAS*, 430(1):699–724, March 2013. doi: 10.1093/mnras/sts670.

M. M. Romanova, A. A. Blinova, G. V. Ustyugova, A. V. Koldoba, and R. V. E. Lovelace. Properties of strong and weak propellers from MHD simulations. *New Astron.*, 62:94–114, July 2018. doi: 10.1016/j.newast.2018.01.011.

Marina M. Romanova and Stanley P. Owocki. Accretion, Outflows, and Winds of Magnetized Stars. *Space Sci. Rev.*, 191(1-4):339–389, October 2015. doi: 10.1007/s11214-015-0200-9.

A. A. Rota, C. F. Manara, A. Miotello, G. Lodato, S. Facchini, M. Koutoulaki, G. Herczeg, F. Long, M. Tazzari, S. Cabrit, D. Harsono, F. Menard, P. Pinilla, G. van der Plas, E. Ragusa, and H. W. Yen. Observational constraints on disc sizes in protoplanetary discs in multiple systems in the Taurus region. II. Gas disc sizes. *arXiv e-prints*, art. arXiv:2201.03588, January 2022.

T. Ryabchikova, N. Piskunov, R. L. Kurucz, H. C. Stempels, U. Heiter, Yu Pakhomov, and P. S. Barklem. A major upgrade of the VALD database. *Phys. Scr.*, 90(5):054005, May 2015. doi: 10.1088/0031-8949/90/5/054005.

Norbert S. Schulz. *From Dust To Stars Studies of the Formation and Early Evolution of Stars*. Springer-Praxis books in astrophysics and astronomy. Praxis Publishing Ltd, 2005. doi: 10.1007/b138917.

Victor See, Sean P. Matt, Colin P. Folsom, Sudeshna Boro Saikia, Jean-Francois Donati, Rim Fares, Adam J. Finley, Élodie M. Hébrard, Moira M. Jardine, Sandra V. Jeffers, Lisa T. Lehmann, Stephen C. Marsden, Matthew W. Mengel, Julien Morin, Pascal Petit, Aline A. Vidotto, Ian A. Waite, and BCool Collaboration. Estimating Magnetic Filling Factors from Zeeman-Doppler Magnetograms. *ApJ*, 876(2):118, May 2019. doi: 10.3847/1538-4357/ab1096.

M. Semel. Zeeman-Doppler imaging of active stars. I - Basic principles. *A&A*, 225:456–466, Nov 1989.

F. H. Shu. Self-similar collapse of isothermal spheres and star formation. *ApJ*, 214:488–497, June 1977. doi: 10.1086/155274.

Frank Shu, Joan Najita, Eve Ostriker, Frank Wilkin, Steven Ruden, and Susana Lizano. Magnetocentrifugally Driven Flows from Young Stars and Disks. I. A Generalized Model. *ApJ*, 429:781, July 1994. doi: 10.1086/174363.

A. Sicilia-Aguilar, C. F. Manara, J. de Boer, M. Benisty, P. Pinilla, and J. Bouvier. Time-resolved photometry of the young dipper RX J1604.3-2130A. Unveiling the structure and mass transport through the innermost disk. *A&A*, 633:A37, January 2020. doi: 10.1051/0004-6361/201936565.

L. Siess, E. Dufour, and M. Forestini. An internet server for pre-main sequence tracks of low- and intermediate-mass stars. *A&A*, 358:593–599, June 2000.

J. Silvester, G. A. Wade, O. Kochukhov, S. Bagnulo, C. P. Folsom, and D. Hanes. Stokes IQUV magnetic Doppler imaging of Ap stars - I. ESPaDOnS and NARVAL observations. *MNRAS*, 426(2):1003–1030, October 2012. doi: 10.1111/j.1365-2966.2012.21587.x.

J. Skilling and R. K. Bryan. Maximum Entropy Image Reconstruction - General Algorithm. *MNRAS*, 211:111, November 1984. doi: 10.1093/mnras/211.1.111.

Frans Snik and Christoph U. Keller. Astronomical Polarimetry: Polarized Views of Stars and Planets. In Terry D. Oswalt and Howard E. Bond, editors, *Planets, Stars and Stellar Systems. Volume 2: Astronomical Techniques, Software and Data*, page 175. 2013. doi: 10.1007/978-94-007-5618-2_4.

A. P. Sousa, J. Bouvier, S. H. P. Alencar, J. F. Donati, E. Alecian, J. Roquette, K. Perraut, C. Dougados, A. Carmona, S. Covino, D. Fugazza, E. Molinari, C. Moutou, A. Santerne, K. Grankin, É. Artigau, X. Delfosse, G. Hebrard, and SPIRou Consortium. Star-disk interaction in the T Tauri star V2129 Ophiuchi: An evolving accretion-ejection structure. *A&A*, 649:A68, May 2021. doi: 10.1051/0004-6361/202140346.

J. Stefan. Über die Beziehung zwischen der Wärmestrahlung und der Temperatur. *Sitzungsberichte der Mathematisch-naturwissenschaftlichen Classe der Kaiserlichen Akademie der Wissenschaften*, pages 391–428, 1879.

R. F. Stellingwerf. Period determination using phase dispersion minimization. *ApJ*, 224:953–960, September 1978. doi: 10.1086/156444.

B. Stelzer, A. Frasca, J. M. Alcalá, C. F. Manara, K. Biazzo, E. Covino, E. Rigliaco, L. Testi, S. Covino, and V. D'Elia. X-shooter spectroscopy of young stellar objects. III. Photospheric and chromospheric properties of Class III objects. *A&A*, 558:A141, October 2013. doi: 10.1051/0004-6361/201321979.

C. Stock, P. McGinnis, A. Caratti o Garatti, A. Natta, and T. P. Ray. Accretion variability in RU Lup. *A&A*, 668:A94, December 2022. doi: 10.1051/0004-6361/202244315.

G. G. Stokes. On the Change of Refrangibility of Light. *Philosophical Transactions of the Royal Society of London Series I*, 142:463–562, January 1852.

Jonathan Tennyson. *Astronomical spectroscopy : an introduction to the atomic and molecular physics of astronomical spectra*, volume 2. London: Imperial College Press, 2005. doi: 10.1142/p371.

Caroline E. J. M. L. J. Terquem. Stopping inward planetary migration by a toroidal magnetic field. *MNRAS*, 341(4):1157–1173, June 2003. doi: 10.1046/j.1365-8711.2003.06455.x.

B. Tessore, A. Lèbre, J. Morin, P. Mathias, E. Josselin, and M. Aurière. Measuring surface magnetic fields of red supergiant stars. *A&A*, 603:A129, July 2017. doi: 10.1051/0004-6361/201730473.

Thanawuth Thanathibodee, Brandon Molina, Javier Serna, Nuria Calvet, Jesús Hernández, James Muzerolle, and Ramiro Franco-Hernández. A Census of the Low Accretors. II. Accretion Properties. *ApJ*, 944(1):90, February 2023. doi: 10.3847/1538-4357/acac84.

Jeff A. Valenti and Christopher M. Johns-Krull. Observations of Magnetic Fields on T Tauri Stars. *Ap&SS*, 292(1):619–629, August 2004. doi: 10.1023/B:ASTR.0000045068.34836.cf.

L. Venuti, J. Bouvier, E. Flaccomio, S. H. P. Alencar, J. Irwin, J. R. Stauffer, A. M. Cody, P. S. Teixeira, A. P. Sousa, G. Micela, J. C. Cuillandre, and G. Peres. Mapping accretion and its variability in the young open cluster NGC 2264: a study based on u-band photometry. *A&A*, 570:A82, October 2014. doi: 10.1051/0004-6361/201423776.

A. A. Vidotto. The magnetic field vector of the Sun-as-a-star. *MNRAS*, 459(2):1533–1542, June 2016. doi: 10.1093/mnras/stw758.

A. A. Vidotto, M. Opher, V. Jatenco-Pereira, and T. I. Gombosi. Simulations of Winds of Weak-Lined T Tauri Stars: The Magnetic Field Geometry and the Influence of the Wind on Giant Planet Migration. *ApJ*, 703(2):1734–1742, October 2009. doi: 10.1088/0004-637X/703/2/1734.

G. A. Wade, J. F. Donati, J. D. Landstreet, and S. L. S. Shorlin. High-precision magnetic field measurements of Ap and Bp stars. *MNRAS*, 313(4):851–867, April 2000. doi: 10.1046/j.1365-8711.2000.03271.x.

G. A. Wade, S. Bagnulo, O. Kochukhov, J. D. Landstreet, N. Piskunov, and M. J. Stift. LTE spectrum synthesis in magnetic stellar atmospheres. The interagreement of three independent polarised radiative transfer codes. *A&A*, 374:265–279, July 2001. doi: 10.1051/0004-6361:20010735.

J. T. Wright and J. D. Eastman. Barycentric Corrections at 1 cm s$^{-1}$ for Precise Doppler Velocities. *PASP*, 126(943):838, September 2014. doi: 10.1086/678541.

Rakesh K. Yadav, Ulrich R. Christensen, Julien Morin, Thomas Gastine, Ansgar Reiners, Katja Poppenhaeger, and Scott J. Wolk. Explaining the Coexistence of Large-scale and Small-scale Magnetic Fields in Fully Convective Stars. *ApJ*, 813(2):L31, November 2015. doi: 10.1088/2041-8205/813/2/L31.

C. Zanni and J. Ferreira. MHD simulations of accretion onto a dipolar magnetosphere. II. Magnetospheric ejections and stellar spin-down. *A&A*, 550:A99, February 2013. doi: 10.1051/0004-6361/201220168.

P. Zeeman. Over de invloed eener magnetisatie op den aard van het door een stof uitgezonden licht. *Verslagen en Mededeelingen der Kon. Academie van Wetenschappen, Afd. Natuurkunde*, 5:181–184, January 1896.

# A1    Hα lines

Figure A1.1 shows the Hα line for the fourth and fifth night of the 2010 ESPaDOnS observations, corresponding to phase ~0.5. For both nights, there is a small red-shifted absorption, indicating that the accretion column is in the line-of-sight.
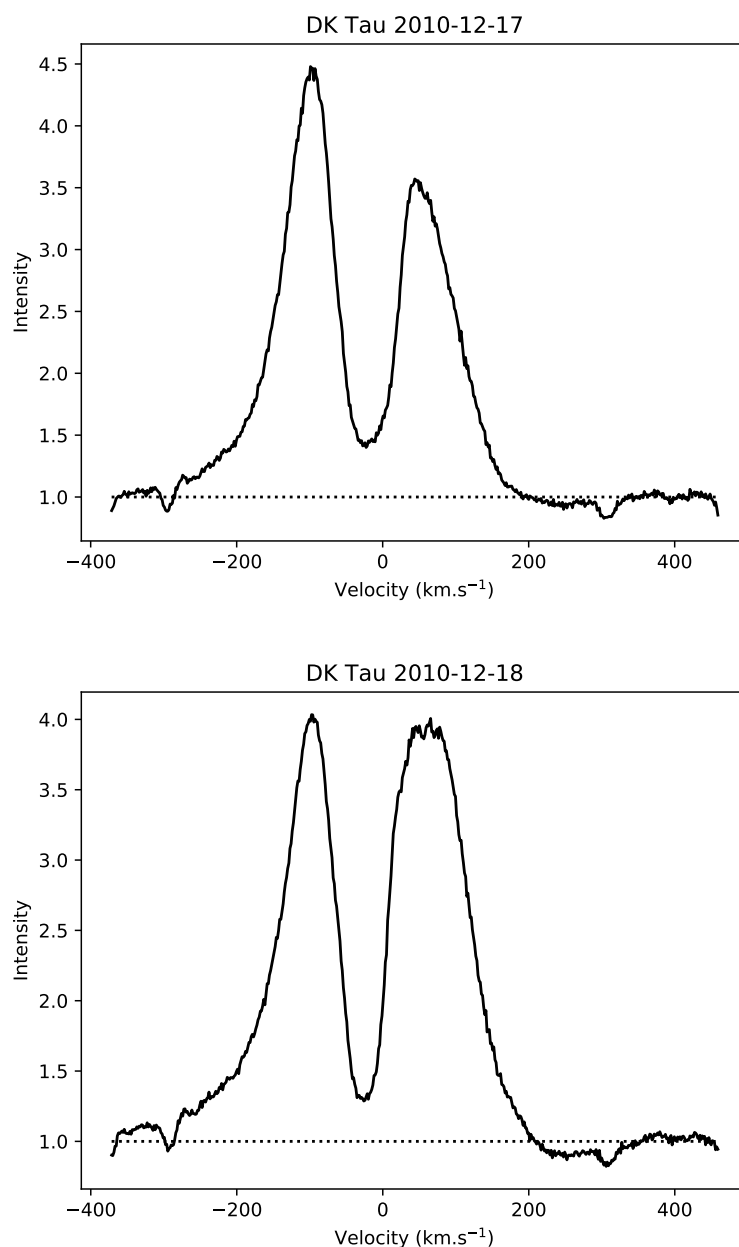


Figure A1.1 – Hα line for the fourth night (top panel) and the fifth night (bottom panel) of the 2010 ESPaDOnS observations. The dotted line highlights the continuum.

# A2     Accretion luminosity

Figure A2.1 and A2.2 show the accretion luminosity as a function of wavelength for each night in 2010 and 2012. The continuous black line shows the weighted average and the gray dashed line shows the spread of values. The weighted standard deviation of the values from the different lines was taken as the spread.
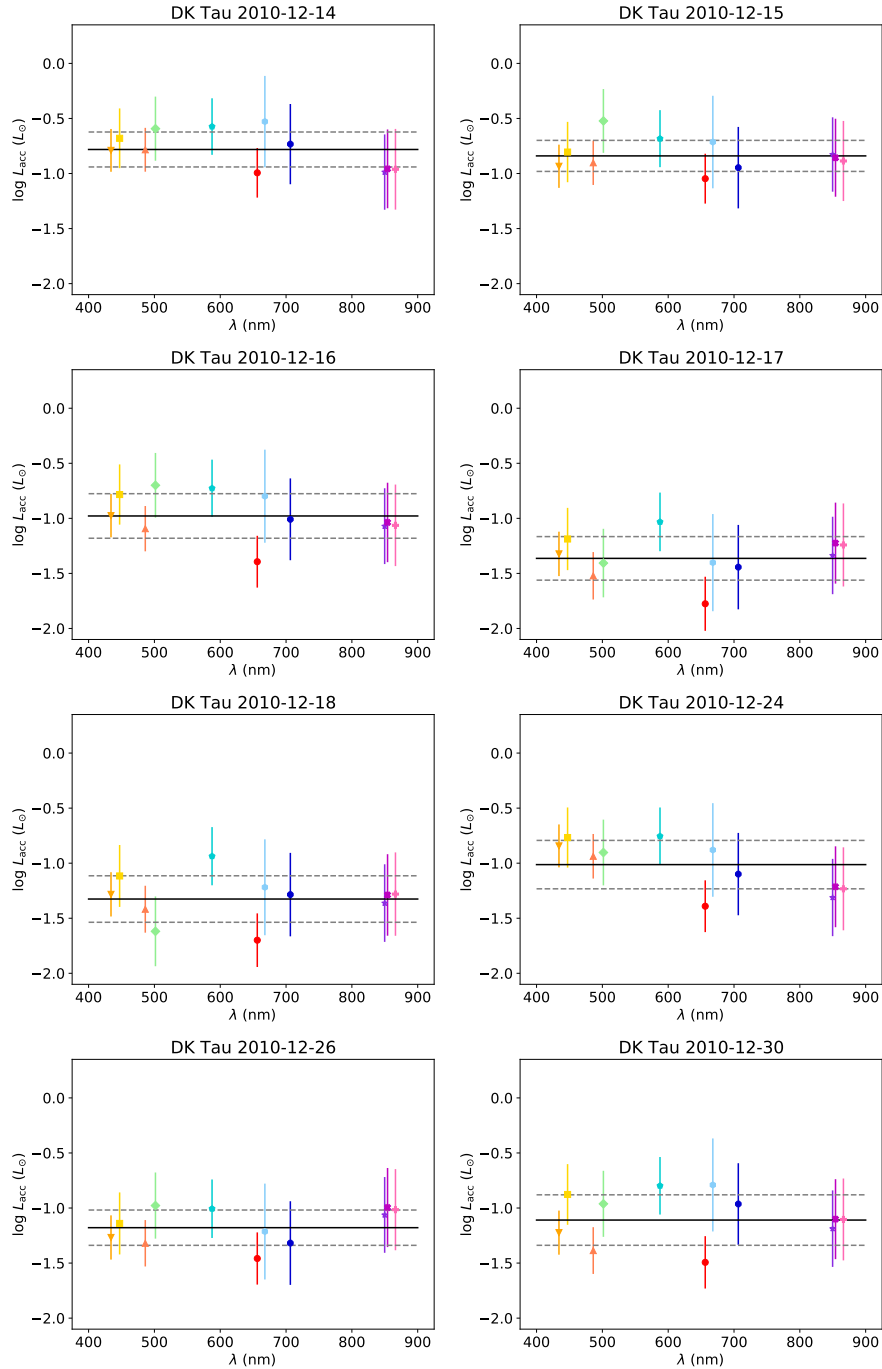


Figure A2.1 – Accretion luminosity (colored points), the weighted average (continuous black line) and the spread of values (gray dotted line) as a function of wavelength for the 2010 observations.
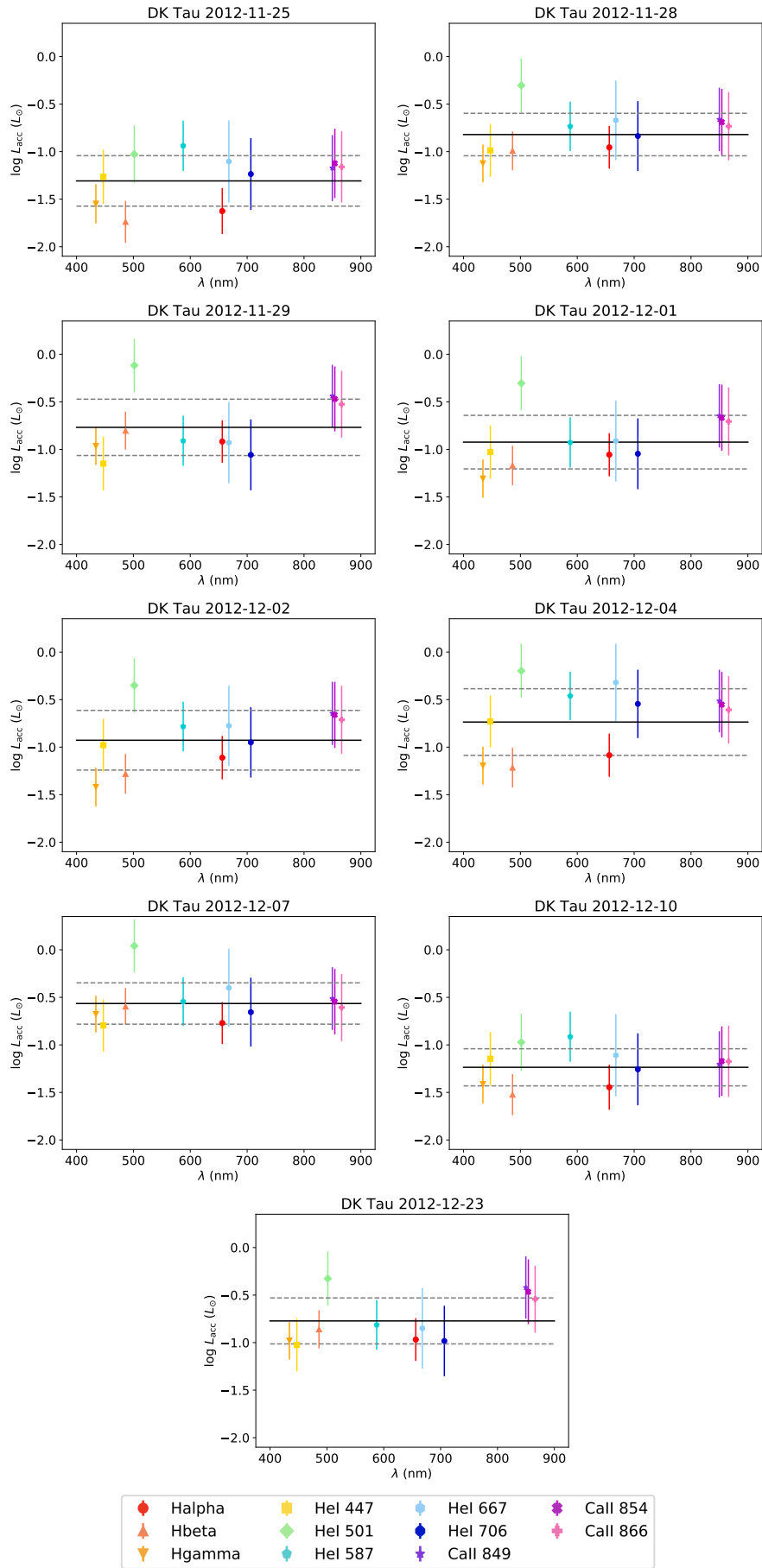
Figure A2.2 – Same as Fig. A2.1, for the 2012 observations.

# A3  Accretion shock models

Figure A3.1 overlaps the observational veiling (gray dots and their best linear fit in black) with its corresponding modeled veiling (in colors). The modeled veiling is based on an accretion shock model, itself characterized by an energy flux ($\mathscr{F}$) and scaled by a filling factor ($f$). Two examples are given, one with low veiling and one with higher veiling.
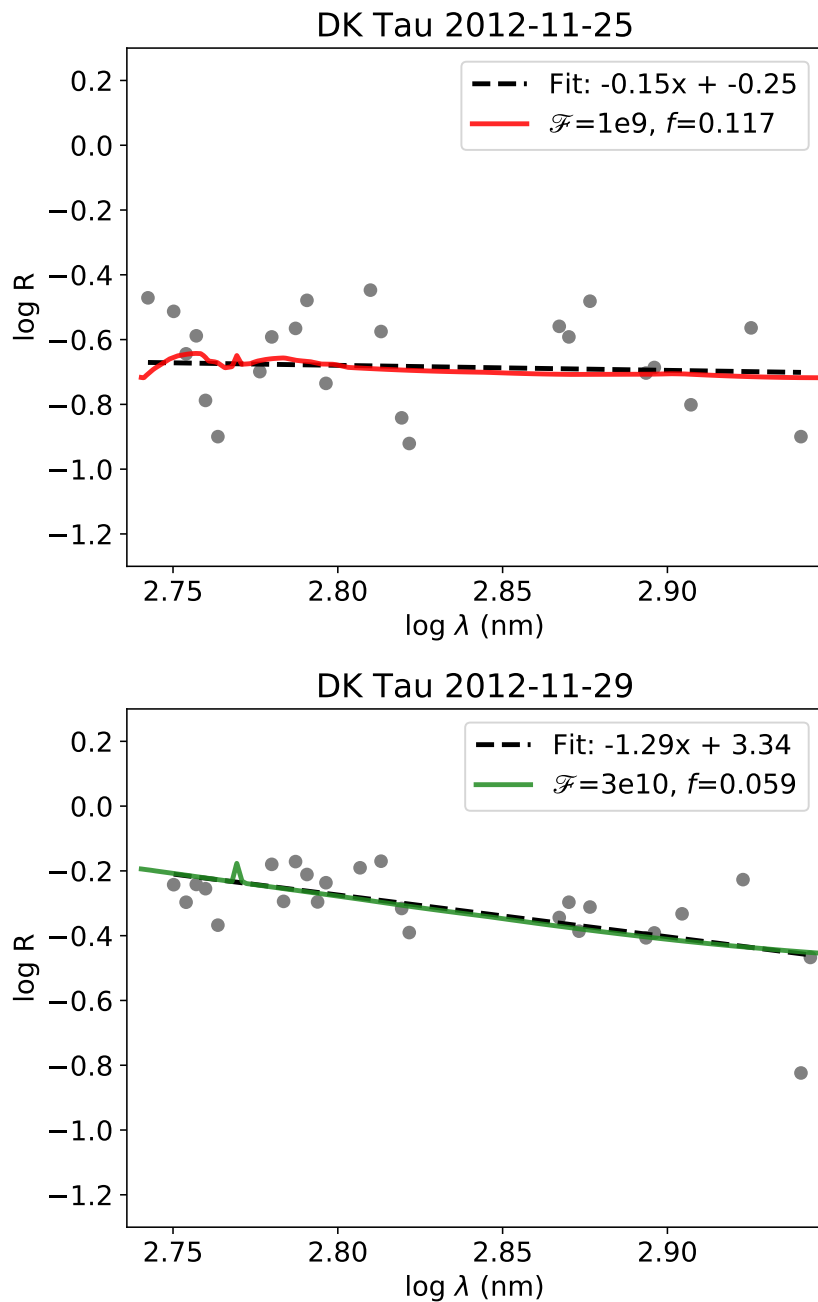


Figure A3.1 – Observed veiling (gray dots), the best linear fit (black dashed line) and corresponding modeled veiling (continuous colored line) as a function of wavelength for two examples.

Figure A3.2 depicts an example of the estimation of the uncertainty on the product of $\mathscr{F}$ and $f$ for one observation. The gray dots represent the observed veiling and the black dashed line represent its best fit. The continuous green line represents the corresponding modeled veiling (i.e. the one best matching the data). It is characterized by $\mathscr{F} = 3 \times 10^{10}$ erg s$^{-1}$ cm$^{-2}$ and $f = 0.059$. In order to estimate the uncertainty, the two models with a value of $\mathscr{F}$ framing the value of $\mathscr{F}$ of the model that is evaluated were also plotted. In other words, one model with a higher value of $\mathscr{F}$, and one with a lower value. They are characterized by $\mathscr{F} = 1 \times 10^{10}$ erg s$^{-1}$ cm$^{-2}$ and $f = 0.126$ (in yellow), and $\mathscr{F} = 1 \times 10^{11}$ erg s$^{-1}$ cm$^{-2}$ and $f = 0.025$ (in blue). Their corresponding filling factors were chosen in order to overlap with the best fit at 617.50 nm. When looking at the product of $\mathscr{F}$ and $f$ for the yellow or the blue model, there is a factor 1.4 difference compared to the green model. This factor 1.4 is then considered an estimation of the uncertainty for that observation.
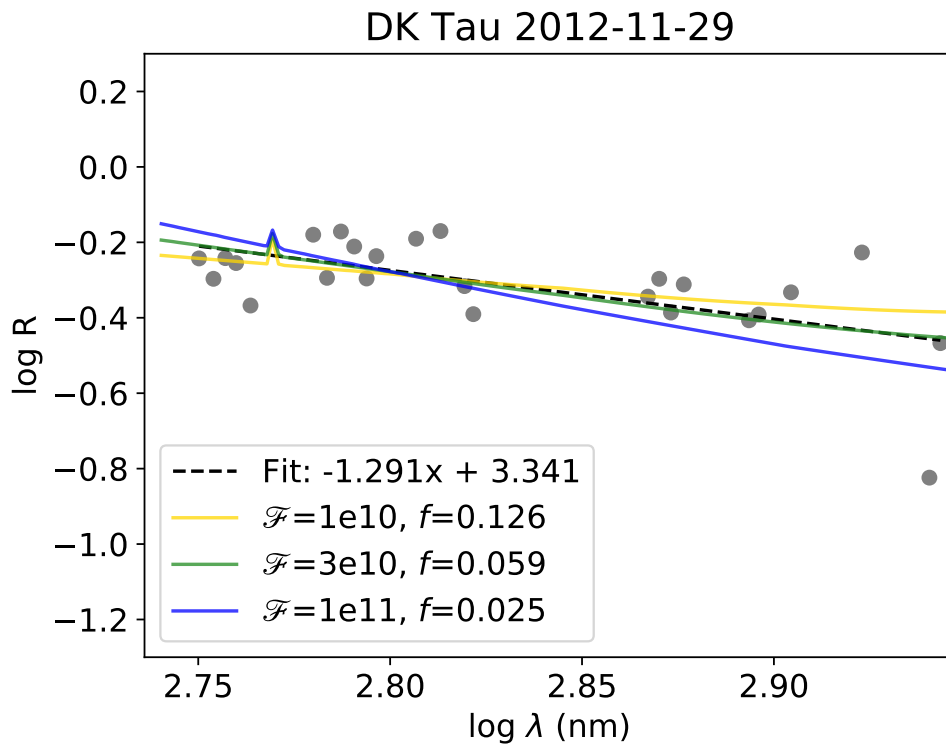


Figure A3.2 – Example of the estimation of the uncertainty on the product of $\mathscr{F}$ and $f$ for one observation. The observed veiling is represented by the gray dots and its best linear fit is represented by the black dashed line. Three different modeled veiling are represented by the continuous colored lines. They are plotted as a function of the wavelength.

# Acknowledgements

This thesis was officially supervised by Tom Ray and officially co-supervised partially by Aline Vidotto. It was unofficially partially supervised by Pauline McGinnis and Antonella Natta. The author worked at the Dublin Institute for Advanced Studies, while they were registered at Trinity College Dublin.

The work described in Chapters 3 and 4 has been published with the participation of the various co-authors.

## Remerciements

Merci à ma famille en Belgique. Merci à mes amis pour leur soutien. Ein besonderer Dank geht an Hana, Zazou und Namnam. To the people on Thursdays at 2 pm: thank you for being there and thank you for being you. Lastly, thank you, dear reader, for taking the time to read this thesis.